ABSTRACT

Title of dissertation: Experimental Investigation into Unsteady Force Transients on Rapidly Maneuvering Wings

Peter Mancini, Doctor of Philosophy, 2017

Dissertation directed by: Professor Anya R. Jones
Department of Aerospace Engineering

Small-scale aircraft, such as biological fliers and micro air vehicles, typically operate in a low Reynolds number flight regime, $Re \sim \mathcal{O}(10^2 - 10^5)$, that is known to contain massive flow separation and unsteady force production. This work conducts comprehensive experimental campaigns on a flat plate undergoing three simple wing motions typical of low Reynolds number flight: surging from rest, pitching in a constant free stream, and deflection of a large trailing edge flap. Water tunnel tests were performed in collaboration between the University of Maryland (UMD) and the Air Force Research Laboratory (AFRL). Unsteady force measurements and time-resolved velocity fields were obtained for a wide range of incidence angles and motion rates, spanning cases of fully attached flow to those of massively separated flow. Experiments were conducted at Reynolds number $Re = 20{,}000$ over an extensive breadth of reduced frequencies ($0.06 \leq k \leq 3$) representative of the conditions found in small biological fliers. Detailed investigations into rapidly surging and pitching wings illustrated the direct relationship between observable vortex dynamics and force/moment coefficients during the transient acceleration and subsequent relaxation to steady state. It was

shown that circulation strength is proportional to motion rate, and faster acceleration transients produce stronger, more coherent leading edge vortices. Experiments were also performed on a hinged wing with a 50%-chord trailing edge flap. Dynamically pitching the wing was shown to generate instantaneous lift response upon motion onset regardless of initial flow attachment. Additionally, direct measurement of wing component forces and numerical simulations using an unsteady panel method confirmed the production of considerable unsteady forces on the stationary fore element of the hinged wing. Using a modified aerodynamic model that accurately predicts force histories on the hinged wing, it was determined that the largest discrepancy between Theodorsen's classical solution and the measured forces is due to its over-prediction of steady circulatory lift.

Experimental Investigation into Unsteady Force Transients on Rapidly Maneuvering Wings

by

Peter Mancini

Dissertation submitted to the Faculty of the Graduate School of the
University of Maryland, College Park in partial fulfillment
of the requirements for the degree of
Doctor of Philosophy
2017

Advisory Committee:
Professor Anya Jones, Chair/Advisor
Professor James Baeder
Professor Inderjit Chopra
Professor Alison Flatau
Professor Ken Kiger, Dean's Representative

Acknowledgments

I would first like to thank my advisor, Dr. Anya Jones. It has been an extreme pleasure to work under her guidance, and the opportunities she has provided me are far more than I could have asked for from an advisor. She is a true inspiration to all of her students. Her work ethic and constant inquiry for "what's next" have kept all of us driven and steadily growing over the course of my time at the University of Maryland.

I am also grateful for the opportunity to have worked with Dr. Michael Ol, from whom I draw inspiration as both a technical researcher as well as an eloquent communicator. Although occasionally misconstrued as grandiloquent, his speech and writing veritably demonstrated his unique ability to artfully articulate his arguments. He taught by example how to perform sound research and put in the extra preparatory effort to do things right the first time. Hold your work to a high standard and always seek to answer the hard questions. Along the way, you are bound to stumble across answers to smaller, sometimes un-asked, questions, and that serendipitous journey has made for an incredibly enjoyable academic experience.

Of course, a huge thanks to all of my ultimate frisbee teammates, coaches, and players over the past five years. You inspire me every day to push myself harder and reach for a stronger, faster, smarter version of myself. You have shown me that there is always a higher level to strive for and to never be satisfied giving anything shy of your best.

Arguably the best part of this entire graduate journey has been collaborating with the amazing group of people that make up our lab. From sitting through countless

practice presentations or off-the-wall ideas frantically drawn on white boards to providing a second set of hands to hold a calibration plate while someone focuses the high-speed camera, every member of our lab is committed to helping each other succeed. Most notably, I should first thank my partners in crime, Field Manar and Gino Perrotta. I simply could not ask for better officemates. Andrew Lind, our tool-stealing guardian angel, has been an invaluable resource, teaching by example how to perform quality research, master PowerPoint presentations, and just appreciate the academic process, recognizing every hurdle as an opportunity for growth.

In lieu of recounting a story for everybody who impacted my career at UMD, I would just like to thank a few of those who made my time here so great: Max Cassell, Tim Kreutzfeldt, Nate Beals, Dave Mayo, Tom Pillsbury, Vera Klimchenko, Stacy Sidle, Luke Smith, Jonathan Lefebvre, Hülya Biler, Zach Smith, Girguis Sedky, Phil Kirk, Albert Medina, and Karen Mulleners.

Finally, I would like to thank my parents, who have supported me in every way possible through my many journeys and have always pushed me to shoot for the stars.

Table of Contents

List of Figures

Nomenclature

a	Chordwise distance between mid-chord and pitch axis
AR	Aspect ratio
b	Semi-chord
c	Chord length
C_L	Lift coefficient
C_D	Drag coefficient
C_M	Moment coefficient
$C(k)$	Theodorsen's function
$\hat{\mathbf{e}}_\mathbf{n}$	Unit normal vector to line, s, in vortex impulse calculation
f	Sampling frequency, Hz
h/c	Non-dimensional plunge distance
J	Impulse
j	Panel index
k	Reduced frequency
L	Lift
P	Horizontal impulse
p	Pressure
Q	Vertical impulse
Re	Reynolds number
S	Planform area or area of integration in γ_1 calculation
s	Convective distance, chord-lengths
s	Distance between vortices (used in vortex impulse calculation)

s/c	Non-dimensional convective distance
s_a	Acceleration distance, chord-lengths
s_a/c	Non-dimensional acceleration distance
t	Time
t^*	Convective time, $t^* = \frac{tU}{c}$
t/c	Thickness-to-chord ratio
x	Non-dimensional chordwise position
U	Streamwise velocity
$V_{\|\|}$	Plate-parallel velocity
$V_\perp$	Plate-normal velocity
X'	Plate-parallel direction
Y'	Plate-normal direction

Greek Symbols

α	Angle of attack
α_{LE}	Angle of attack of leading edge element
β	Flap deflection angle
δ	Flap deflection angle
δ_0	Initial flap deflection angle
δ_F	Final flap deflection angle
$\Delta\delta$	Flap amplitude
Γ	Circulation

γ_1	Vortex center, $\frac{\mathrm{m}^2}{\mathrm{s}}$
μ	Dynamic viscosity
ϕ	Velocity potential
$\phi(s)$	Wagner's function
ρ	Density
ω	Vorticity ($\nabla \times V$), 1/s

Subscripts

∞	Free stream
$+$	Vortex with positive vorticity
$-$	Vortex with negative vorticity
b	Bound
C	Circulatory
cent	Centroid
meas	Experimental
NC	Non-circulatory
wake	Trailing edge wake

List of Abbreviations

AFRL	Air Force Research Laboratory
CFD	Computational Fluid Dynamics
KJ	Kutta-Joukowski

LE	Leading edge
LEV	Leading edge vortex
MAV	Micro air vehicle
NACA	National Advisory Committee for Aeronautics
PIV	Particle Image Velocimetry
TEV	Trailing edge vortex
UMD	University of Maryland
VI	Vortex impulse

Chapter 1

Introduction

1.1 Motivation

Whether in natural flyers [1, 2] or for man-made vehicles [3, 4], the application of rapidly maneuvering wings has been of interest among biologists and engineers alike for over half a century [5]. Observation of natural fliers, especially those capable of hover, has provided insight into efficient flight mechanics within the low Reynolds number flight regime in which they operate. Of principal interest for flight-control applications is understanding the extent to which lift history is quasi-steady with motion history [6]. For the past four decades, despite a concerted effort to develop more accurate models, unsteady aerodynamic prediction tools have consisted mostly of linear methods largely derived for attached flow regimes [7]. At present, most of these methods remain rooted in inviscid theory and are thus inherently incapable of capturing the viscous effects associated with low Re flight regimes without some degree of empirical correction or robust computing power. Advancements in computational fluid dynamics (CFD) [8–10] and analytical solvers [11, 12] have brought forth powerful tools for capturing complex

flow physics and accurately quantifying 2D and 3D aerodynamic behavior. However, the large computational cost of higher order solvers typically makes them unsuitable for controller applications. Low-order models provide reasonably accurate force predictions at a drastically lower run time. The most universally used low-order models are those of classical, inviscid airfoil theory, most notably the solutions of Wagner [13] and Theodorsen [14]. Their widespread use is largely because they provide simple, low-order analytical models based entirely on motion history and provide reasonable results even for separated flow [15]. The field of unsteady low Reynolds number aerodynamics contains a wealth of knowledge yet to be discovered regarding quantification of separated flow development and accurate modeling of the underlying flow physics. The present work helps fill a void regarding the fundamental understanding of individual sources of lift and the accuracy with which current modeling methods predict lift on rapidly maneuvering wings.

1.2 Problem Statement

Present literature is densely populated with over a century's worth of detailed studies on high Reynolds number, fixed-wing aircraft and the classical aerodynamic theories which model their steady low angle of attack flight [16]. An abundance of prior work exists that is aimed toward understanding the underlying flow physics of large-scale commercial and military aircraft. This is in direct contrast with the more recent prominence of small scale aircraft of comparable size to biological fliers. These aircraft operate in the low Reynolds number regime, $Re = \mathcal{O}(10^2 - 10^5)$, and have a relatively

much larger degree of flow unsteadiness. Cai et al. [17] provided a survey of recent advances and future development trends of small-scale unmanned vehicles, highlighting two particular gaps in the literature that the present work aims to address: 1) a need for documentation of aggressive flight conditions and envelopes for small-scale fixed-wing aircraft and 2) improved dynamics modeling based on first-principles and application of model-based linear control.

Identically replicating all of the intricacies of flapping wing flight still eludes the aerodynamics community, despite significant advancements over the past two decades [18]. This is in part due to the large number of geometric and kinematic parameters that can be varied. Studies mapping the in-flight wing kinematics of natural fliers [19, 20] have found that the kinematics can be composed of a combination of translational, rotational, and pitching motions. It is common to isolate the individual wing motions to analyze them separately for in-depth studies of the fundamental fluid mechanics of such flight. The present work considers the components of rectilinear pitch and translational (surge) acceleration over a range of rates and incidence angles (see Figure 1.1), building upon the rich literature of accelerating finite wings in the low Reynolds number flight regime [21–25]. There are still many complex flow phenomena occuring in this flight regime that are not presently well understood. The exact contributions to lift from the leading edge vortex is presently unclear, despite the large body of work on its qualitative size and kinematics.

The objective of this work is to provide a comprehensive experimental characterization of wings undergoing a wide range of incidence angles and motion rates for surge acceleration from rest (Figure 1.1a) and pitch in a constant free stream (Figure 1.1b) in

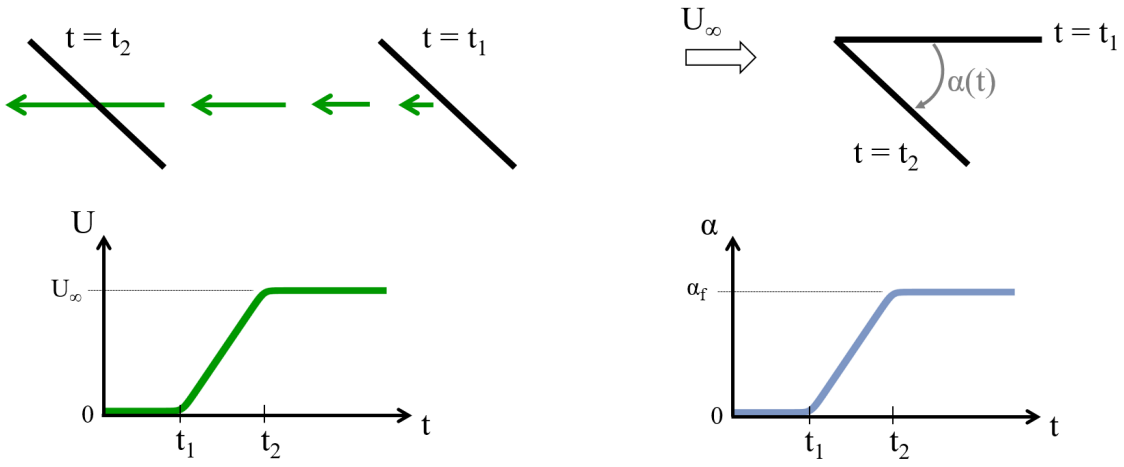

(a) Surge

(b) Pitch

Figure 1.1: Illustrative examples of the two pure rectilinear motions considered in this work.

an effort to improve the understanding of flow topology and circulation history and their effect on lift force. The study of single-element flat plates will be followed by the case of a large, rapidly deflecting trailing edge flap in an effort to 1) quantify lift histories and flow topologies for a wide, novel parameter space of deflection rates and flap angles and 2) apply classical unsteady aerodynamic models and address their accuracy to measured lift.

The present work does not aim to create a new predictive model; it aims to address the accuracy of each term that comprises Theodorsen's model to either justify or invalidate its use within the examined parameter space. Experimental studies facilitated the understanding of physical phenomena, which led to improvements to the current state of predictive modeling. There are certainly more complex low-order models that go to great lengths to more accurately represent the flow physics present in

this flight regime [26], but the novelty in a model like that of Theodorsen is its sole dependence on motion history and linear superpositional terms. This work provides an assessment of the applicability of several existing inviscid modeling techniques to low Reynolds number flight and presents adapted models of Lamb's vortex impulse method and Theodorsen's solution to predict forces on the hinged plate in good agreement with force measurements.

1.3 Background

1.3.1 Reynolds Number and Reduced Frequency

The flight mechanics and fundamental mechanisms of lift production for flapping wing vehicles are fundamentally characterized by two important non-dimensional quantities: *Reynolds number* and *reduced frequency*. The Reynolds number of a flow is a non-dimensional parameter that describes the ratio of inertial to viscous forces:

$$Re = \frac{\rho U c}{\mu}. \tag{1.1}$$

This parameter can also be interpreted as the ratio of convection time-scale over diffusion time-scale for a standard transport distance [27]. A higher Reynolds number means faster downstream convection of a fluid structure relative to its rate of diffusion. Conversely, lower Reynolds number flows are typically more heavily influenced by effects of shear and vorticity due to the slower rate of convection and longer duration of near-wing presence. For a given fluid viscosity, μ, the drastic difference in size (i.e. characteristic length, c) and forward flight velocity, U, results in a several orders of magnitude difference in

Reynolds number between biological fliers and commercial aircraft. Using dimensionless quantities, such as Reynolds number, allows for the scaling of problems that share a dynamic similitude. Comparing time-resolved results also involves non-dimensionalizing wall clock time as a *convective time*, t^*, using the wing's forward velocity (or free stream speed) and chord length with the form $t^* = \frac{tU}{c}$. This describes the duration of motion in terms of the amount of chord-lengths traveled.

Flow unsteadiness is commonly characterized by a different non-dimensional quantity, reduced frequency,

$$k = \frac{\omega c}{2U}, \tag{1.2}$$

where ω is rotation rate, c is wing chord, and U is free stream velocity. Figure 1.2 provides a distribution of flight regimes for a wide variety of fliers. Commercial fixed-wing aircraft fly at high Reynolds number but very low reduced frequency, and so their main flight condition is steady flow. The upward trend in reduced frequency with decreasing Re is demonstrative of the fact that small-scale vehicles increasingly depend on unsteady flow to generate lift as their size decreases. Figure 1.2 also provides a qualitative description of the state of aerodynamics knowledge regarding the present understanding of underlying flow physics in each Reynolds number and reduced frequency flight regime. The present work studies the aerodynamic behavior of wings at $Re = 20,000$ and reduced frequencies $0.06 \leq k \leq 1.4$, which forms a range of kinematic parameters that bridges the well-understood low reduced frequency regime to the highly unsteady high frequency regime.

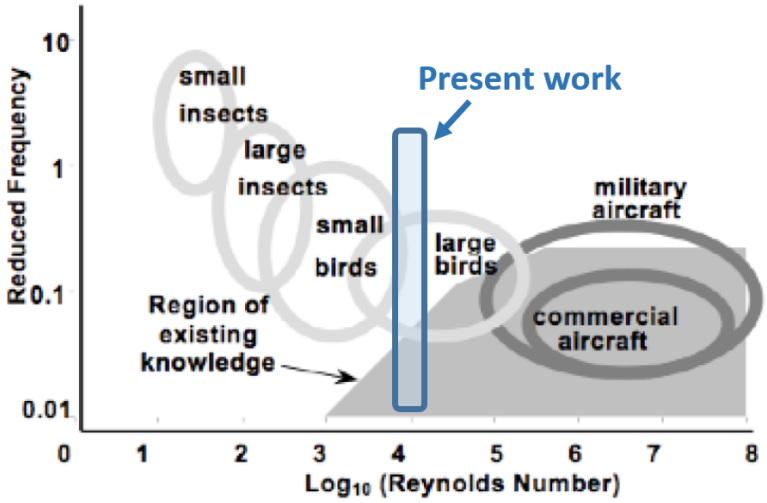

Figure 1.2: Illustration of the various occupants in each reduced frequency vs. Reynolds number flight regime. Figure adapted from Ames et al. [28].

1.3.2 Lift Production in Low Reynolds Number Flight

Figure 1.2 shows that small-scale fliers operate at high reduced frequency and low Reynolds number. The present study, along with decades of prior research, provides an understanding of the physical mechanisms by which lift is produced at the MAV flight scale. It has been established that biological fliers and MAVs produce lift via entirely different mechanisms than conventional aircraft, i.e. rapid flapping vs. steady attached flow. Wings in attached flow produce lift in part due to a pressure distribution normal to the surface along the airfoil and a leading edge suction force [29]. At high incidence angle, flow separates about the leading edge, which leads to a loss of this suction force. However, for rapid motions at high incidence, the formation of large-scale vortices provides lift enhancement that appears to mitigate the loss of a suction

force [30, 31].

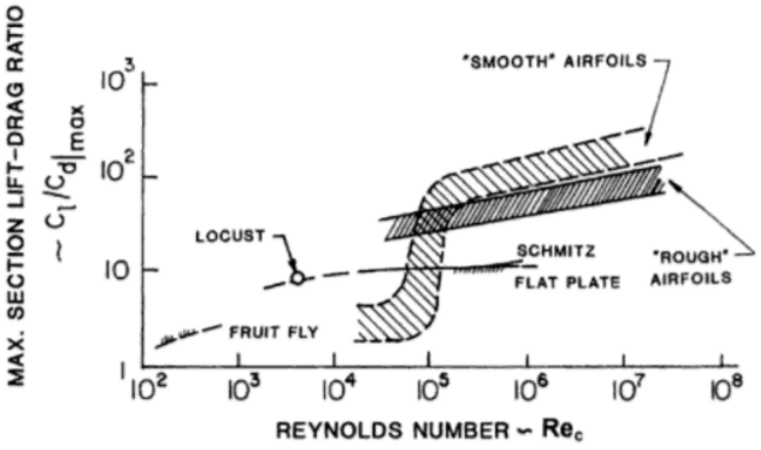

Figure 1.3: Maximum lift-to-drag ratio for a variety of airfoil shapes at Re $\mathcal{O}(10^2 - 10^8)$ [32].

Figure 1.3 shows the degradation in airfoil performance in steady flow with decreasing Re. For $Re < 10^5$, flat plates generate higher lift-to-drag ratios than traditional airfoils. At high Reynolds number, $Re > 10^6$, a turbulent boundary layer forms over the suction side that can withstand a greater adverse pressure gradient, thus maintaining attached flow at higher incidence than at low Re. As Re decreases, the boundary layer remains laminar and can no longer overcome the adverse pressure gradient, especially at high angle of attack. Thus, small-scale fliers rely less on attached flow to generate lift and instead utilize flow separation and viscous phenomena to provide unsteady lift enhancement. To promote flow separation, these vehicles have thinner airfoil sections than do passenger planes and rotorcraft, with thickness-to-chord ratio $t/c \approx 3-6\%$ [33].

The present work aims to study the fluid dynamics of wings operating with kinematics typical of the $Re = \mathcal{O}(10^4)$ flight regime, that is, they contain high levels of

unsteadiness and whose exact lift production methods are presently unclear. It is common to break down the complex motion of flapping wings into isolated motions: rotation, surge, and pitch. The latter two will be studied in the present work and represent a simplified two-dimensional flapping wing. Figure 1.4 provides examples of experimentally obtained wing strokes using high-speed cameras observing fruit flies (Figure 1.4a) and hummingbirds (Figure 1.4b) in hover. Results between the two fliers are very similar, and the breakdown of wing incidence on the right of Figure 1.4a shows a relatively horizontal period of translation, motivating the present surge from rest study, and a rapid pitch upon stroke reversal at the ends of upstroke and downstroke, motivating the present pitch study. Dickinson and Götz [36] also studied the impulsively started wing to draw insights into insect flight force production with the aim of further rejecting the 'quasi-steady state' model, which assumes that steady state forces are produced by the wing at each instantaneous position in the stroke cycle [37]. Dickinson admits that although insect wings move only 2-4 chord lengths each half cycle, it is still of interest to the aerodynamics community to observe the lift history over an extended convective time. For example, these results may also be applied to fixed wing aircraft undergoing rapid maneuvers that will subsequently experience a relaxation period as lift production returns to original state. Dickinson et al. extended the translation after the plate reached constant velocity for a distance of seven chord lengths to observe the wing's relaxation from maximum lift during the acceleration phase to its steady state lift long after startup. They observed the formation, shedding, and reformation of leading edge vortices (LEV), as illustrated in Figure 1.5a and similarly observed experimentally by Stevens et al. in Figure 1.5b for pitching wings. It was hypothesized that leading edge

vortices were a source of considerable lift production. Studying its formation became a major focus of subsequent work [39, 40].

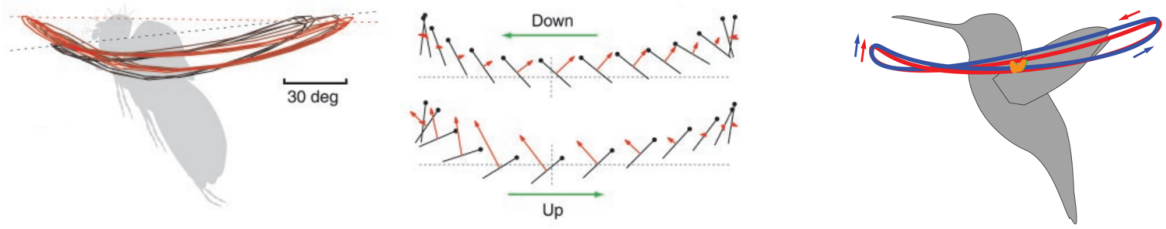

(a) Wing motion and flight forces (red arrows) of fruit fly (*Drosophila melanogaster*) [34]

(b) Experimental wing stroke traces of *Calypte anna* [35].

Figure 1.4: Typical wing strokes of flapping wing fliers in hover.

1.3.3 Effects of Leading Edge Flow Separation

Figure 1.5a provides a schematic illustrating the effect of an LEV on lift, showing a 90° rotation of the suction force vector and additional contribution to the plate-normal force. Panah et al. quantified the effect of a leading edge vortex above a plunging plate and provided time-resolved vorticity and chord-wise pressure measurements that clearly demonstrated the strong suction beneath the LEV (see Figure 1.6) [31]. Previous work has concluded that faster motion rates leads to higher peak lift and LEV circulation strength during the acceleration phase of a maneuver [38, 40]. This motivates the present work to explore the nature by which circulation production is related to motion rates.

It is important to recognize that quantitative differences in circulation production may not necessarily correspond to unique leading and trailing edge wake shape. Granlund et al. [41] showed a qualitative similarity between leading edge vortices cor-

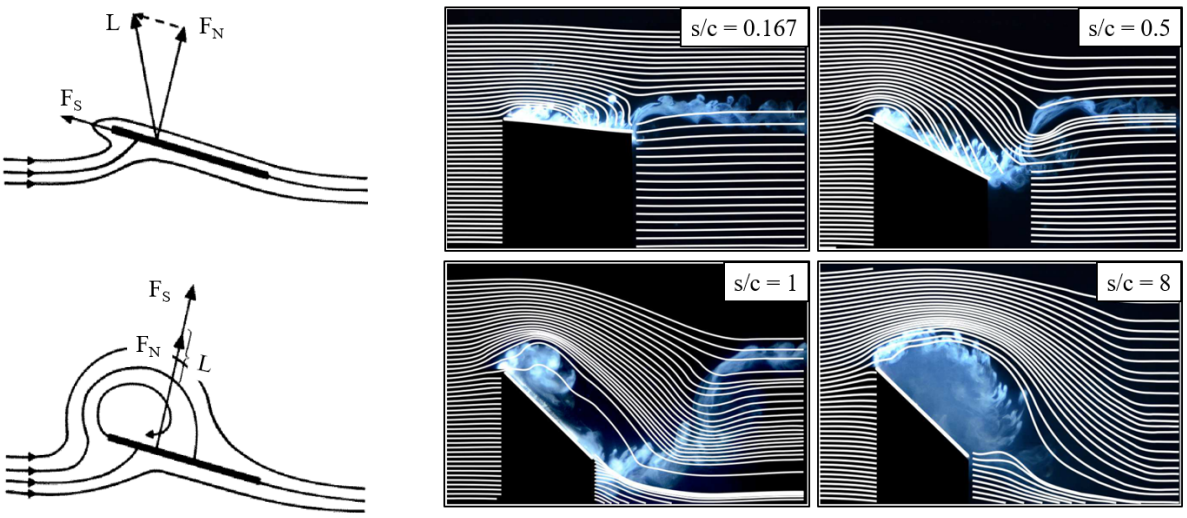

(a) Generation of detached vortex lift on thin wings [36] .

(b) Dye flow visualization with streamlines calculated from velocity fields (LE pitch) [38]

Figure 1.5: (a) (top) Conventional steady lift from potential flow. Rapid change in velocity around sharp edge results in suction vector. (bottom) Development of leading edge vortex and elimination of plate-parallel suction force and instead angles it normal to the plate. (b) Dye visualization and streamlines for a rapidly pitching flat plate in a freestream.

responding to peak lift for several pitch cases at $k = 0.2$. Figure 1.7 provides a pivot axis study for pitching wings that illustrates a significant difference in force production, despite nearly identical flow visualization images at peak lift. This demonstrates that for high motion rates qualitative similarity in flow topology is not sufficient to also ensure similar forces. Without having quantitative flow field measurements, they hypothesized that the difference in aerodynamic force histories was likely due to a difference in circulation production. The present work will support their hypothesis by providing cases

with identical flow field histories (shape and trajectory) containing strikingly different LEV strengths that directly contribute to a difference in force production.

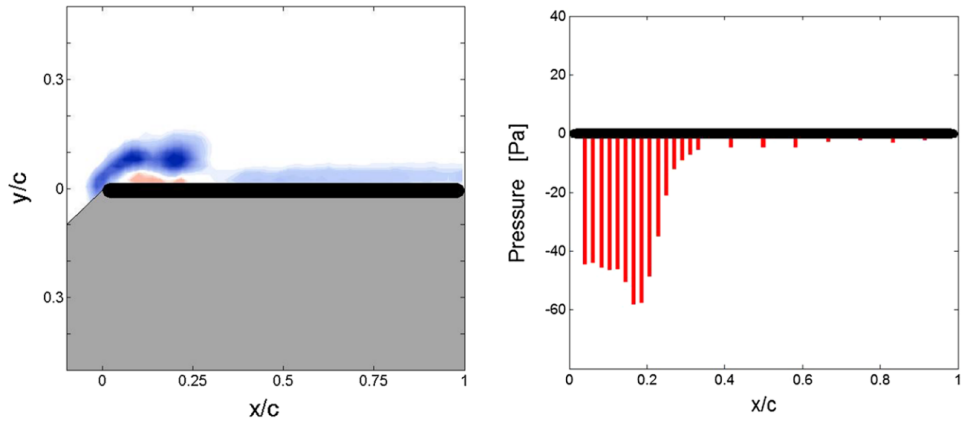

Figure 1.6: Vorticity field and surface pressure distribution on the top surface of a two-dimensional plunging plate with plunge amplitude $h_0/c = 0.3$ and $k = 1.05$. Figure from Panah et al. [39]

1.3.4 Trailing Edge Flaps and Flow Control

Building upon the present study of single-element wings, another major campaign in this work is studying the aerodynamic behavior of a large, rapidly pitching trailing edge flap. A two-element wing utilizes fundamental principles behind pitching wings to provide an actuating lifting surface to increase maneuverability and act as an active flow control device. Present studies into active flow control typically include the use of synthetic jets and other forms of fluidic control. However, Colonius and Williams showed that although fluidic control is remarkably effective at delaying the onset of stall at high angle of attack and increasing steady lift coefficient (see Figure 1.8a), there is a

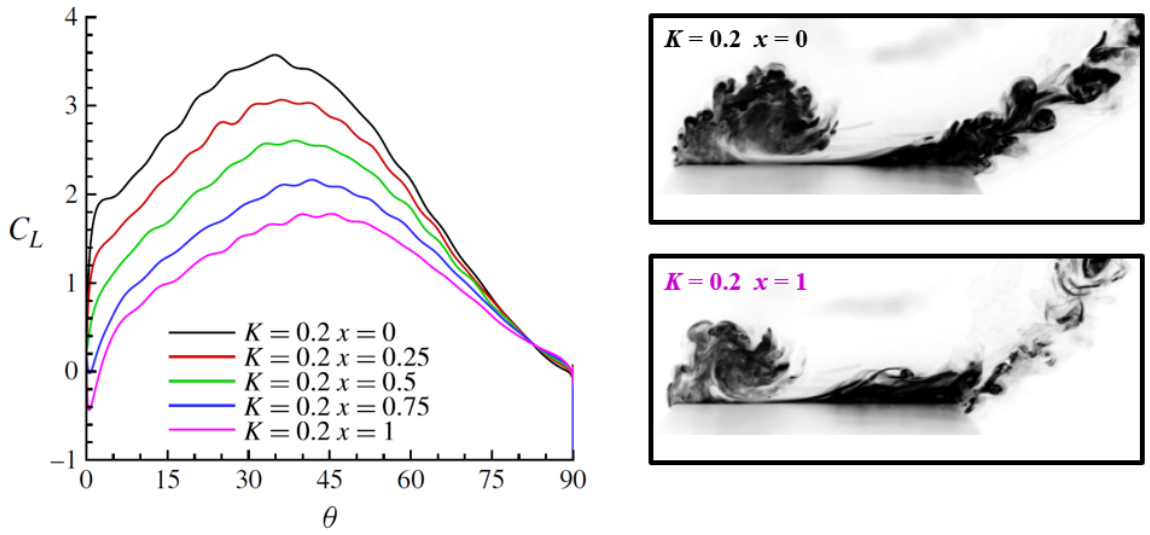

Figure 1.7: Pivot point study on pitching flat plate at reduced frequency $k = 2$ at pivot point, $0 \leq x \leq 1$, with dye visualization snapshots at the point of maximum lift. Notice a qualitative similarity of the flow field despite twice as large force history for the leading edge pitch, $x = 0$, than that of the trailing edge pitch, $x = 1$. Figure adapted from Granlund at al. [41].

time lag or even a reversal in lift history immediately upon actuation (see Figure 1.8b at early t^*) [42]. The benefit of a rapidly deflecting flap is that high force transients due to flap motion are preserved whether the flow is attached or separated - a notable advantage over most fluidic control. More importantly, the additional lift production occurs immediately upon motion onset and without the lift reversal demonstrated in Figure 1.8b.

Present-day flight vehicles typically employ some form of control surface to expand the aircraft's optimal performance envelope, allowing them to fly efficiently in a wide

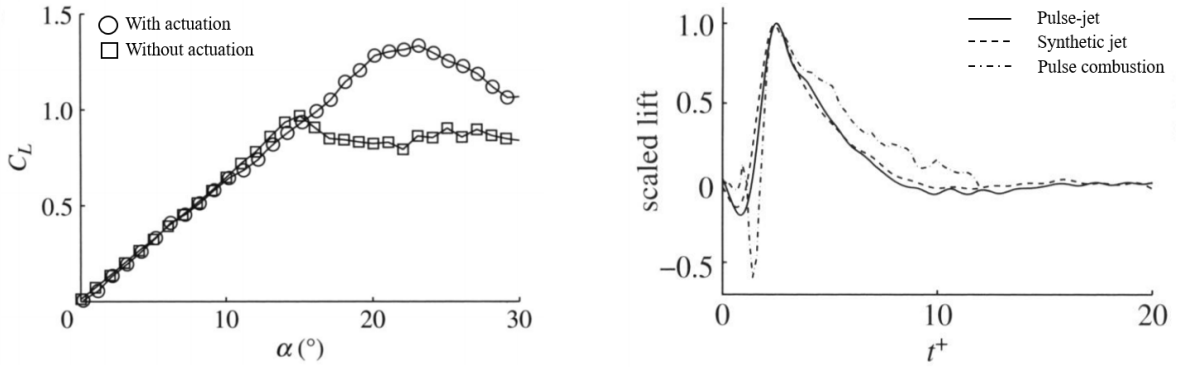

(a) (b)

Figure 1.8: (a) Lift versus angle of attack with (open circles) and without (open squares) actuation at constant free stream and (b) transient lift response to the actuator pulse, scaled by its maximum value. Pulsed jet effectively increases steady aerodynamic performance in (a), but the transient aerodynamics in (b) undergoes a negative lift spike before increasing to its peak lift after — convective time. Figures from Colonius and Williams [42]

range of flight conditions [43]. The specific control surface mechanism considered in this work is a large, high deflection-rate trailing edge flap for the intended situational use of an aggressive flight maneuver or effectively nullifying a gust encounter. Sanders et al. [49] addresses several advancements that must be accomplished for variable-geometry concepts to become practical, including the development of high-energy-density actuators, efficient integration of these actuation concepts into the structure, and understanding the aerodynamic performance of these adaptive structures. The present work aims to address and provide significant insight in the latter of these concepts.

Presently in the literature there is a considerable amount of work reported on the

use of trailing edge flaps as a form of active flutter suppression [44], small perturbation gust alleviation, [44, 45] and steady aerodynamic performance enhancement. There are many positive attributes of implementing a trailing edge flap, but it is deeply situationally dependent when it comes to flap design, construction, and actuation. In the aforementioned studies, the size of the flaps are typically a small fraction of the chord length $(4-27\%)$ [45, 46]. The actuation rates are in the quasi-steady range when used as a variable-camber device in steady flight and around $2.5-75$ Hz [47, 48] in the highly dynamic, periodic case of rotor blades. One novelty of the present work lies in its exploration of flaps with actuation rates shorter than one convective length that are capable providing nearly instantaneous, yet transient, lift enhancement for the purposes of rapid maneuvering or gust alleviation.

Recent studies on trailing edge flaps have made the leap from the high Reynolds number ($Re = \mathcal{O}(10^6)$) regime of large aircraft and entered the low Reynolds number regime ($Re = \mathcal{O}(10^4)$), applying them to micro air vehicle scale flapping wings [50, 51]. Xu et al. showed that in flapping wing flight, understanding the impact of flap deflection can significantly improve lift production on the vehicle. Their study provides an optimization technique that shows (via simulations) how using a simple hinged trailing edge flap can enhance overall lift by augmenting circulation production during the maneuver. Li et al. [51] came to a similar conclusion with their immersed boundary method, illustrating how the unsteady aerodynamic performance of the "deformable" (hinged) flapping plate is strongly dependent on the deflection phase of the trailing edge flap. They obtained a maximum lift enhancement of 26% by tailoring their time-dependent deflection amplitude and phase throughout the wing stroke. This evidence suggests that

dynamic trailing edge flaps have the potential to significantly improve lift production for rapidly maneuvering wings.

Sterenborg at al. attempted to calculate lift on a wing with a dynamic flap using velocity fields from particle image velocimetry [52]. Using a $0.2c$ flap at deflection angles $\Delta\delta = 6°$ they only calculated the theoretical steady lift, matching experimental measurements relatively well. However, the velocity fields were not obtained or presented as a time-resolved history and the motions were small at moderate deflection rates. Their aim was to apply Noca's method [53] for lift and drag calculation using velocity fields from PIV on a non-stationary body, i.e. the pitching trailing edge flap. Their results did match force measurements relatively well, but the motions were likely not generating much unsteady lift as they also matched forces using the steady form of Kutta-Joukowski's theorem.

There is a clear lack of experimental investigations of simplified trailing edge flap kinematics with the aim of isolating the flap and understanding the effect it has on lift. Often times in experiment, as is the case in Lee and Su [55], the trailing-edge flap is deployed as a subset of a greater airfoil motion to augment general aerodynamic performance, rendering its aerodynamic signature coupled. The most similar study to the present work was performed by Rennie et al. on a 27%-chord trailing edge flap undergoing pitch-and-hold maneuvers with a reduced frequency of $k = 0.14$. In that range of flap deflection amplitudes and rates, they concluded that during the transient pitch down (or up) motion of the flap, the airfoil achieves an "inviscid efficiency," where the lift history can be accurately predicted using unsteady thin airfoil theory. The present work will expand on Rennie's study by employing a larger (50%-chord) flap at

higher deflection rates and introducing experimental particle image velocimetry (PIV) measurements. Additionally, the more aggressive maneuvers presented in this work introduce the dominance of non-circulatory forces on both the trailing edge flap itself, as well as the stationary leading edge element, which to the authors' knowledge has not yet been addressed in the literature.

1.3.5 Low Order Modeling of Unsteady Lift

Capabilities of aerodynamic modeling range from highly-resolved CFD [56] to simplified linear analytical solutions [57]. Computationally expensive, yet potentially rich in physical accuracy, CFD and non-linear numerical solvers [58, 59] provide fundamental insight into the physical nature of unsteady flows. However, these methods are time-intensive in their setup and execution may contain a number of numerical instability issues [60]. Thus, low-order modeling fits well into the realm of optimization, sensitivity analysis, and dynamics and control. Figure 1.9 provides a taxonomy of hovering and forward flight regimes, outlining the applicable regions for several specific low-order modeling techniques. Figure 1.9 also indicates the scope of the present work and highlights the current gap in the literature this study aims to fill. Specifically, this work considers the application of solutions from Theodorsen and Wagner to predict lift production.

1.3.6 Classical Theories: Theodorsen and Wagner

Theodorsen's theory was originally derived with the intention of modeling unsteady loads due to aeroelastic effects that led to aerodynamic instabilities for fixed-wing aircraft

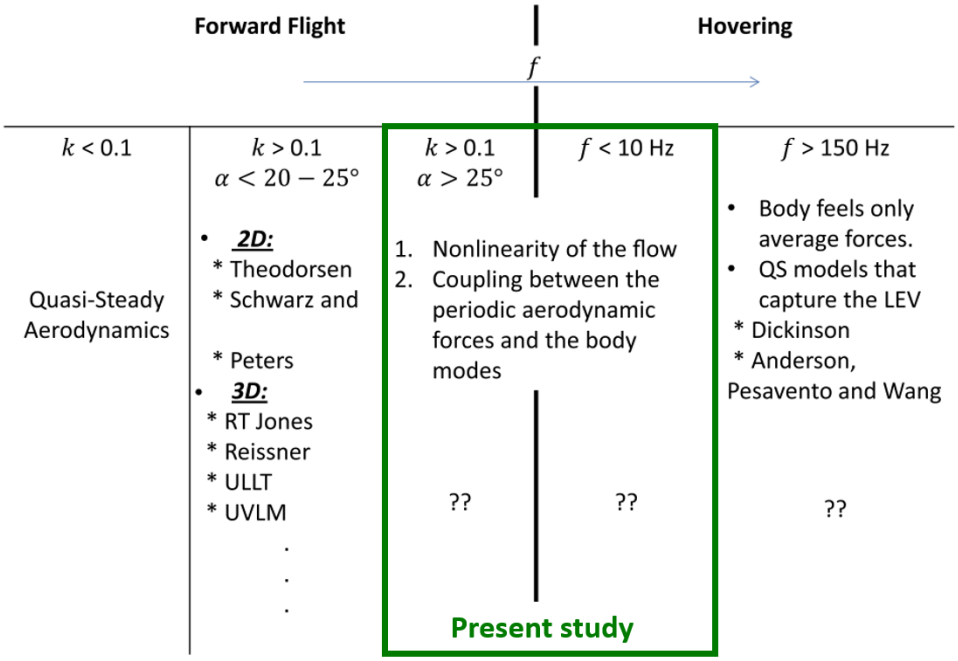

Figure 1.9: Table adapted from Taha [60] describing the various flight regimes of forward and hovering flight in terms of reduced frequency, k. Each region has an applicable set of aerodynamic models, except those of the present study as indicated on the table for $0.1 \leq k \leq 10$.

[61]. Theodorsen provides a general analytical solution for lift on a pitching and plunging wing with a trailing edge flap. The potential flow solution solves for unsteady forces on a 2-D harmonically oscillating plate under the assumptions of inviscid, incompressible flow and subject to small disturbances. In this work, Theodorsen discloses the basic nature of the mechanism of flutter and leaves "modifications of the primary results by secondary effects for future investigation. Such secondary effects are: The effects of section shape, finite span, and deviations from potential flow" [61]. The latter two are directly investigated in the present study. The novelty of Theodorsen's solution is its

convenient parsing of the lift history into its constituent parts. The equation consists of a linear superposition of terms proportional to motion history, each describing a specific mechanism by which lift is produced. For a purely pitching wing in harmonic motion with reduced frequency, k, the solution is given by

$$L = \pi\rho b^2\Big[U\dot{\alpha} - ba\ddot{\alpha}\Big] + 2\pi\rho UbC(k)\Big[U\alpha + b(\frac{1}{2} - a)\dot{\alpha}\Big]. \tag{1.3}$$

All terms within the brackets are directly proportional to angle of attack, α, and its time derivatives: angular velocity, $\dot{\alpha}$, and angular acceleration, $\ddot{\alpha}$. The coefficients consist of geometric, kinematic, and free stream conditions that are typically prescribed. The first term in Equation 1.3 contains inertial effects due to the physical body moving through the fluid. They are non-circulatory in nature and contain what is termed the "added mass" force. The second term is due to unsteady circulation [61–63]. Theodorsen's function, $C(k)$, introduces an amplitude reduction and phase lag on the circulatory lift response due to the presence of vorticity in the trailing edge wake. Setting $C(k) = 1$, as will be done in the present work, recovers the quasi steady-state assumption. This assumption neglects the effect of periodicity and influence of wake vortices on the airfoil. Thus, what the present work will call "Theodorsen's solution" is simply an unsteady potential flow solution satisfying the boundary conditions of no through-flow on the wing surface and trailing edge Kutta condition, both of which will be discussed in later chapters. This analytical solution accounts for unsteady, rate-dependent effects proportional to velocity and acceleration that will prove to be dominant sources of force production during rapid maneuvers. Theodorsen's solution presents an extremely valuable tool for the use of predictive modeling and control applications. However, with

distinct assumptions of attached flow, small amplitude oscillations, and a planar wake, it seems dubious that this solution would accurately predict forces on wing motions that generate large leading edge vortices and non-linear trailing edge wakes.

The results of Ramesh et al. [64] indicate that lift production in high reduced frequency, large amplitude motions appears to be heavily dependent on non-circulatory rate-dependent lift forces (i.e., the first set of brackets in Equation 1.3) that are strictly concerned with the motion of the wing itself and less on contributions from circulatory forces. McGowan et al. [65] and Ol et al. [15] performed experiments on aggressive pitch-plunge maneuvers and demonstrated a considerable resilience of Theodorsen's lift prediction for cases that largely violate the assumption of attached flow (see Figure 1.10). The middle case in Figure 1.10 shows a high reduced frequency, small amplitude motion that matches Theodorsen's solution well. The left and right cases of Figure 1.10 describe cases with moderate reduced frequencies but large plunge amplitudes, which are intentionally performed to violate the small amplitude and attached flow assumptions. Although the results clearly show a discrepancy between Theodorsen and experimental measurements, this work demonstrated for certain cases a relative insensitivity to flow separation and viscous sources of circulation production that are not modeled by Theodorsen. It was concluded that Theodorsen's model works for cases that, despite substantial leading edge vortex formation, still satisfy the trailing edge Kutta condition and for cases dominated by pitch rate effects due to rapid acceleration (i.e., high reduced frequency). However, the issue remains to fully understand the aerodynamic response for conditions in which classical linear predictive models are not valid. The present work aims to quantify vorticity production for cases that invalidate Theodorsen's solution and

assess which sources of force production accurately describe the physical flow and can be linearly superimposed.

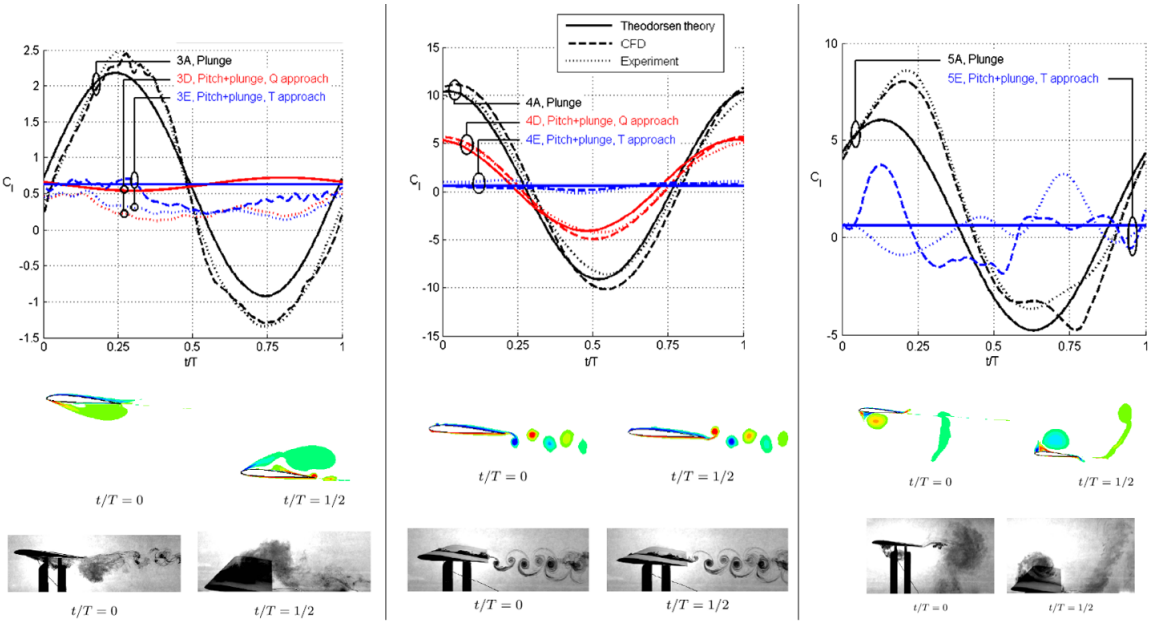

Figure 1.10: Pure plunge cases (black lines, labeled 3A, 4A, 5A) with reduced frequency and plunge amplitudes (left) $k = 0.393$, $h/c = 0.5$; (middle) $k = 7.86$, $h/c = 0.025$; (right) $k = 1.179$, $h/c = 0.5$. Also shown are (middle row) corresponding vorticity fields from CFD and (bottom row) dye flow visualization, illustrating the flow topology for each case and its deviation from Theodorsen's assumptions of attached flow and planar wake. Figure adapted from McGowan et al. [65].

Surging wing kinematics do not have rotational velocity from which to calculate reduced frequency and are better described using the classical solution of Wagner [13]. Theodorsen's theory is a representation of Wagner's theory in the frequency domain

(i.e. solution is a function of k) [66]. Wagner derived the growth of circulation about an airfoil starting impulsively from rest at a small fixed angle of attack and describes the lift coefficient as a function of chords traveled for a two dimensional airfoil given by

$$C_L = (2\pi \sin \alpha)\phi(s), \tag{1.4}$$

where $\phi(s)$ is the Wagner function. Wagner's classical 2D attached-flow solution [13] for impulsive-start (equivalently impulsive change in free-stream speed, after subtracting buoyancy or inertial effects [67], or impulsive change in angle-of attack), must of course be modified for experimentally-realizable acceleration rates. Exploration into the accuracy of Wagner's solution for cases containing leading edge vortices was done for a wing at 15 degrees incidence by Pitt-Ford and Babinsky [68], who argued that while bound circulation on the plate was essentially zero, vorticity ascribed to the leading-edge vortex is responsible for producing circulation not unlike that given by Wagner's theory. Further, Pitt-Ford and Babinsky, following Brennan [69] and Lamb [54], obtained a solution for the apparent-mass contribution during the acceleration-phase of the plate's motion. In Wagner's treatment this would have been a delta-function. Instantaneous acceleration is not physically possible, so it is important to obtain theoretical solutions that represent the correct wing kinematics.

1.4 Summary

Small-scale vehicles operate at low Reynolds number in a regime where conventional airfoil performance degrades due to flow separation and loss of attached flow pressure forces. Based on observation of natural fliers and replication of their wing strokes,

flat plates supersede airfoils in aerodynamic performance for $Re \leq 10^5$. Characteristic flight kinematics in this regime include high reduced frequency and large amplitude wing motion. Natural fliers and MAVs overcome limitations of flow separation by generating lift-enhancing leading edge vortices that lead to large transient unsteady lift production. Present low-order modeling techniques struggle to accurately predict the effect of vortex formation, which limits their applicability to use in flight control or predictive modeling. Steady modeling techniques simply do not capture time-dependent lift production, which motivates an assessment of classical *unsteady* models such as Wagner and Theodorsen to determine how accurately real-world unsteady lift production can be predicted by classical theory. These models theoretically pertain only to low amplitude motions containing attached flow and planar wakes. The high incidence angle, large amplitude motions of rapidly maneuvering aircraft, however, largely violate these assumptions. It is of immediate interest to assess the extent to which these classical models are capable of providing accurate results for lift on airfoil and airfoil-aileron systems and amend the theoretical equations to better describe the physical flow.

1.5 Research Objectives

Review of prior work on wings operating at high incidence angle and low Reynolds number motivates the need for a deeper understanding of the exact force-producing mechanisms involved during aggressive wing maneuvers. In particular, the study of unsteady aerodynamic phenomena surrounding leading edge flow separation and relative magnitude of vortex lift to motion-induced lift has been carried out via several water

tunnel experiments. The present work considers two wing motions fundamental to low Reynolds number flight: translational surge and pitch (Figure 1.1). The objectives of the present work are as follows:

1. Measure time-resolved circulation production and unsteady force histories over a range of incidence angles and motion rates for two canonical flat plate wing kinematics: 1) impulsively started translation and 2) pitch in a free stream from $\alpha = 0°$ to $\alpha = 45°$.

2. Relate unsteady force histories of pitching and surging flat plates to their respective flow topologies and analytical force predictions.

3. Characterize the aerodynamic behavior in terms of circulation and force production of a large rapidly-deflecting trailing edge flap for a wide parameter space of deflection rates, incidence angles, and initial flow conditions.

4. Propose modified semi-empirical and analytical aerodynamic models capable of successfully predicting lift history on a hinged flat plate undergoing rapid deflection.

5. Apply existing analytical and numerical low-order modeling techniques to the present set of kinematics to identify each of the physical mechanisms responsible for lift production (e.g. added mass, virtual camber).

It should be noted that actual biological fliers typically do not have rigid rectangular wings. However, due to its inherent simplicity, the rigid thin flat plate has been the subject of many research efforts in the fluid dynamics community, and it serves as a

universal wing geometry upon which complex fluid phenomena can be studied without concern of dissimilar planform and aeroelastic effects. Data from the present work will contribute to the literature by providing a vast amount of experimental results that not only covers the immediate force transient due to motion onset but also the relaxation period over long convective times. The results of this work will improve the physical understanding of force production during rapid wing maneuvers at low Reynolds number and aim to provide several techniques from which to confidently predict lift.

Chapter 2

Methodology: Experimental Setup and Analysis

2.1 Facilities

This work is the result of a multi-year collaborative effort between the University of Maryland (UMD) and the Air Force Research Laboratory (AFRL). This collaboration capitalized on the capabilities of each facility to provide a vast library of experimental data in the form of direct force measurements, particle image velocimetry (PIV), and fluorescent dye flow visualization.

2.1.1 Air Force Research Lab (AFRL), Wright Patterson AFB

Recirculating Water Tunnel

A significant portion of the experimental campaign was performed at Wright Patterson Air Force Base in the Horizontal Free-Surface Water Tunnel (Figure 2.1), detailed extensively by Ol [70]. All force measurements and flow visualization, as well as particle image velocimetry for the single-element wing, were performed in this tunnel. The water tunnel has a 4:1 contraction ratio, a test section 46 cm wide by 61 cm high,

and a speed range of 3 to 60 cm/s. A three-degree-of-freedom motion rig is fitted to the tunnel and consists of a triplet of H2W linear motors, driven by AMC DigiFlex servo-drives controlled by a Galil DMC 4040 4-channel card. Each channel is carefully configured with user-selected proportional/integral/derivative (PID) constants. Each motor is programmed independently so that the desired angle of attack and horizontal position time-history of the model are converted to position commands for each linear motor. This allows for single degree-of-freedom motions such as pure pitch and pure translation, which will be the extent of motion complexity in this work

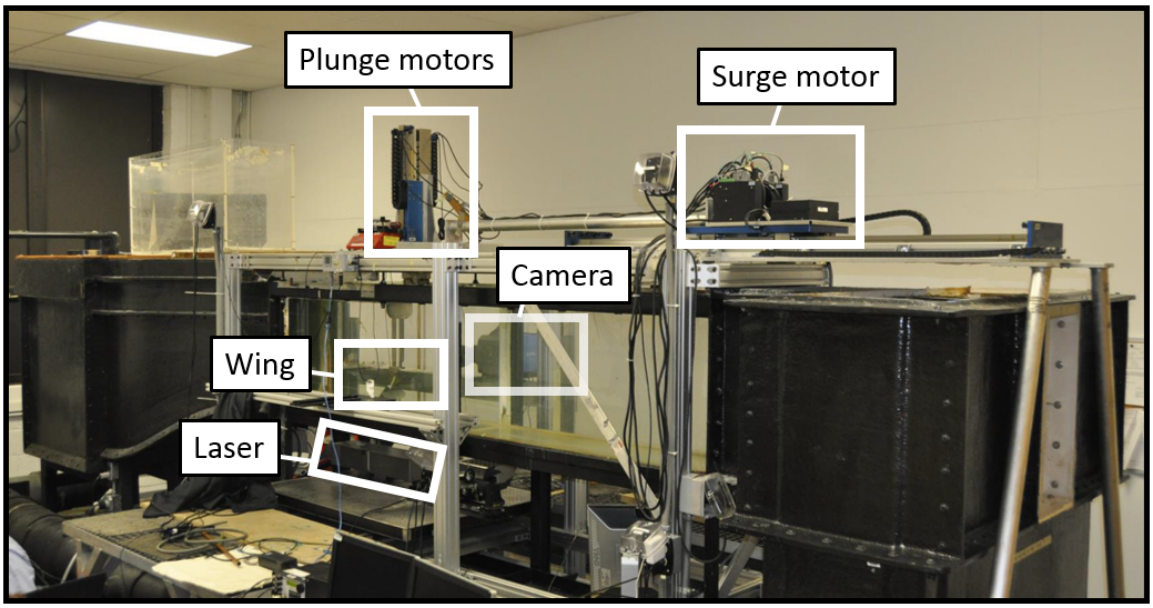

Figure 2.1: AFRL recirculating water tunnel.

2.1.2 University of Maryland

UMD Towing Tank

Contributions to the experimental dataset from the University of Maryland were in the form of particle image velocimetry on the hinged wing experiments in its 7 ×

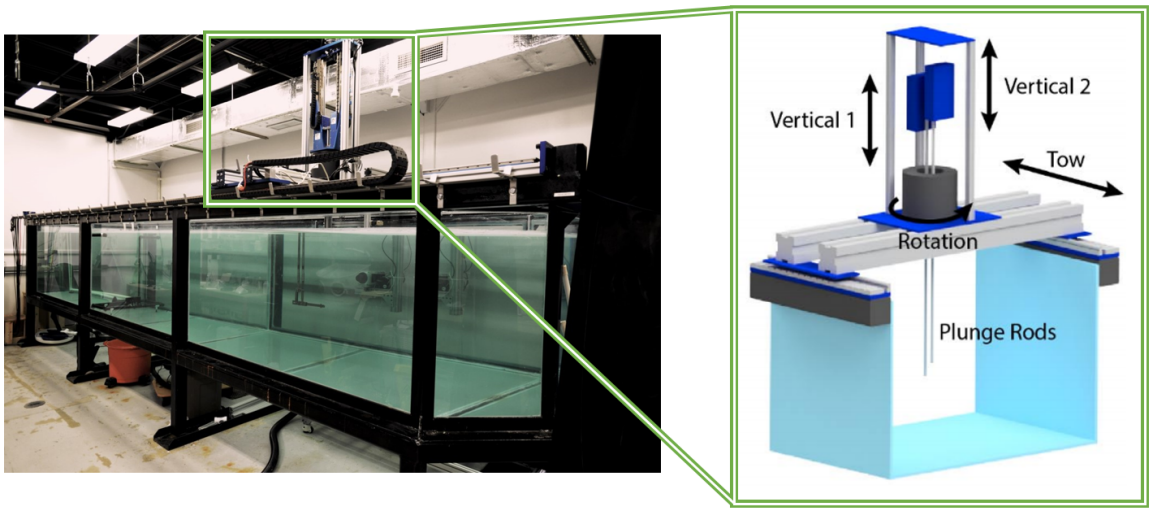

Figure 2.2: UMD free-surface water tank. CAD model of motor system from Manar and Jones [71].

1.5 × 1 m towing tank, equipped with a four-axis motion control system capable of independent pitch, plunge, surge, and rotational motion. The motor assembly, shown in Figure 2.2, sits fixed atop an 80/20-constructed carriage fitted with a pair of H2W BLDC-08 brushless linear motors that drive the assembly down the length of the 7 m tank along a track of magnetic encoders that reports motor positions to within 0.001 mm. The motor assembly itself (inset in Figure 2.2) consists of two independently-controlled H2W BLDC-04 brushless linear motors for pitch/plunge control of the vertical plunge rods and a direct-drive H2W TMS7C brushless rotary stage with a slip ring to allow for continuous rotation. Note that the rotary stage will not be used in this study. Motor positions were controlled using a multiaxis Galil DMC 4153 motion controller, producing a motor position accuracy within 0.250 mm for the tow axis and 0.010 mm in the plunge rods.

2.2 Experimental Parameter Space

When it comes to obtaining a full understanding of unsteady aerodynamic phenomena and physical principles, rapidly maneuvering wings provide a challenging engineering problem that gets increasingly more difficult with complex motions. The comprehensive library of experimental data obtained in this study focuses on acquiring a physical understanding of the transient lift response and flow field development of two unique but similar sets of simple canonical wing geometries and kinematics. The two major experimental investigations include: 1) single element flat plates undergoing rapid pitch and startup surge kinematics and 2) hinged wings with large, rapidly deflecting trailing edge flaps.

The experimental campaign on single-element flat plates studies two very simple motion types: **linear translation from startup** in the streamwise direction and a **pitch-and-hold** maneuver on a wing traveling at constant free stream. The hinged wing experiments explore pitch-and-hold maneuvers of the trailing edge flap for various deflection rates, deflection angles, and fixed fore element positions. The following sections detail the kinematic and geometric parameter spaces explored in these experiments.

2.2.1 Wing Models

In an effort to minimize geometric complexity, the wing shapes for both single-element and hinged wing studies were kept as simple as possible. The single-element wing, shown in Figure 2.3, is of aspect ratio (AR) 4 with chord length $c = 76.2$ mm, 5% thickness ($t = 0.05c$), and rounded leading and trailing edges, where aspect ratio is

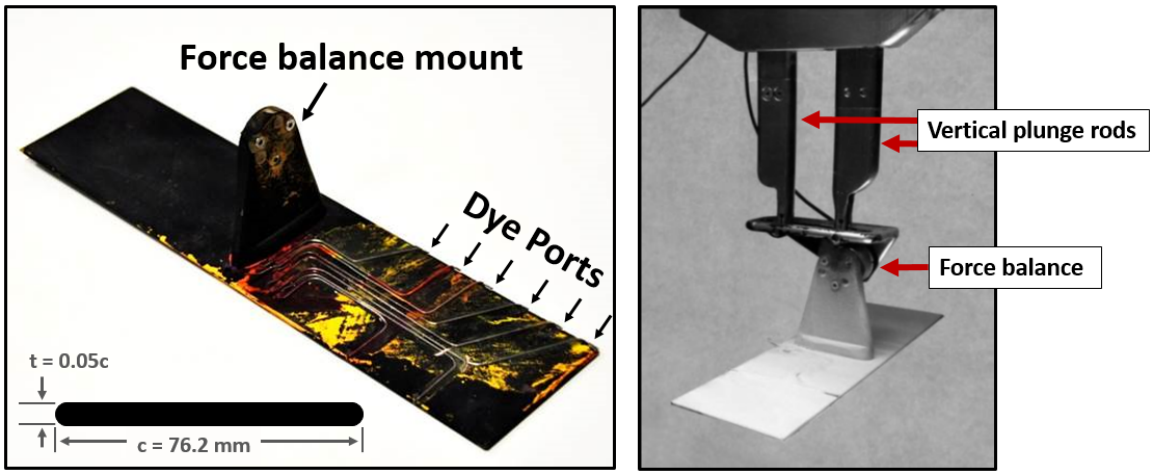

Figure 2.3: Aspect ratio (AR) 4 flat plate used in translational surge and pitch studies. The plate is fitted with six dye ports along the span for dye visualization and a force balance mount for time-resolved direct force measurements.

defined as $AR = \frac{b^2}{S}$, S is planform area, and b is wingspan. This wing was used for both pitch and surge experiments.

Extending the analysis of aerodynamic behavior on single-element wings and slightly increasing complexity, a subsequent study was performed on a hinged wing pinned at the mid chord, shown in Figure 2.4. A plastic 3D printed NACA-0006 of 200 mm chord, strengthened by carbon-fiber rods, spanned the test section as shown in Figure 2.4a. This wing, manufactured and instrumented at AFRL, was sliced at the mid chord and fitted with a connecting mechanism that allows for the instrumentation of two independent force balances: one for the fore-element and one for the aft-element [72]. The gap was approximately 0.5 mm and was bridged with flexible rubber tape of 0.2 mm thickness.

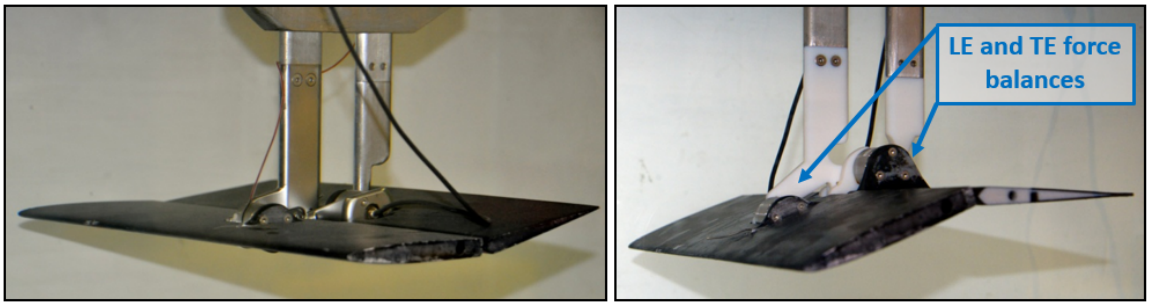

(a)

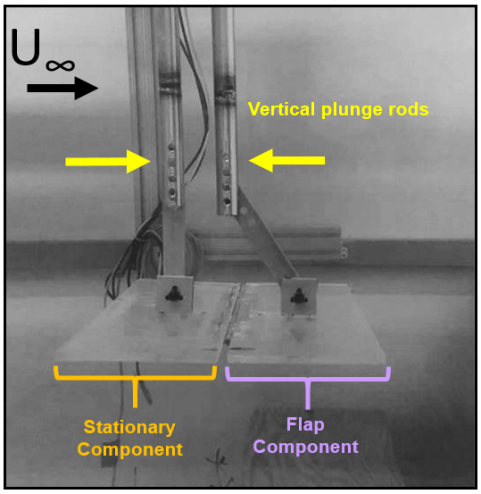

(b)

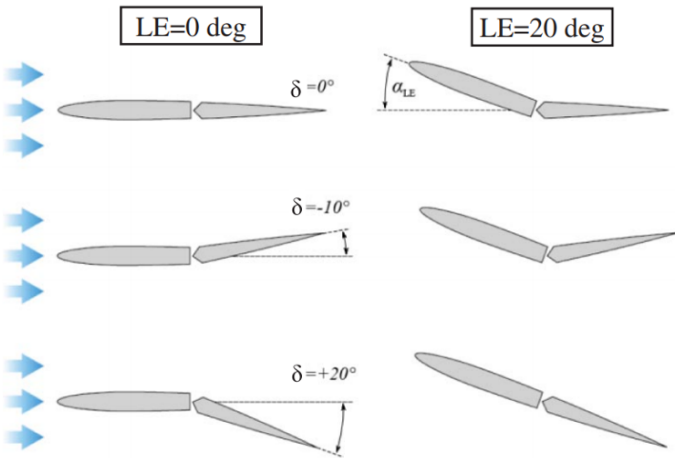

(c)

Figure 2.4: (a) 3-D printed hinged wing fitted with front and rear component force balances. (b) Glass hinged wing mechanism at UMD. (c) Illustration of trailing edge flap kinematics for leading edge fixed at $\alpha_{LE} = 0°$ and $\alpha_{LE} = 20°$.

The hinged wing mechanism used exclusively for particle image velocimetry at UMD was constructed using two rectangular sections (2.5 in. $\times$ 20 in. $\times$ 0.125 in.) of standard glass connected with a metallic piano hinge, as shown in Figure 2.4b. The use of thin glass as the wing material allowed for the laser sheet in PIV experiments to pass through undistorted, illuminating both the pressure and suction sides of the wing. Gaps between the two plate sections were covered with a clear flexible adhesive. The two wings used in this study (NACA-0006 at AFRL and flat plate at UMD) differed in cross-sectional thickness; however, because both wings have symmetric profiles and flow attachment, or lack thereof, was determined to be independent of thickness for the present kinematics, the difference in wing sections was considered negligible, allowing for direct comparisons between the experimental measurements.

2.2.2 Translational Surge

Figure 2.5 shows the velocity profiles describing the wing kinematics pertaining to the surging AR 4 flat plate (see Figure 2.3). The velocity profile describes a wing to beginning at rest and increasing velocity linearly (i.e. with constant acceleration) to a finite final velocity at which it will translate for the remainder of the motion. Because that ideal profile would require infinite acceleration at time $t = 0^+$ resulting in serious rig vibrations, velocity profiles were generated using the infinitely differentiable Eldredge function [73], which provides a nearly trapezoidal profile with respect to time but also includes a smoothing parameter to round the corners of the profile, which minimizes jerk-induced rig vibrations. Velocity profiles (as shown in Figure 2.5) are computed

using

$$U(t) = \frac{k}{a} \ln \left[\frac{\cosh(a\frac{U_\infty}{c}(t - t_1))}{\cosh(a\frac{U_\infty}{c}(t - t_2))} \right] + \frac{U_\infty - U_0}{2}, \tag{2.1}$$

where $k = \dot{U}c/2U_\infty$ is the nominal acceleration rate, a is the smoothing parameter, and t_1 and t_2 are the start and end times of the constant acceleration region, respectively. Purely surging motions did not require significant corner smoothing and the velocity profiles were made as nearly trapezoidal as the motors would allow, setting $a = 21$. During all of the experiments presented here (with the exception of static measurements) the tunnel was not running and was used as a towing tank. The wing was driven in pure rectilinear translation at a fixed angle of attack, α. The final free stream velocity was set to $U_\infty = 0.26$m/s, corresponding to a Reynolds number of Re = 20,000.

All velocity profiles were linear with respect to time, accelerating to a target velocity and carrying out the rest of the motion at this terminal speed. The distance over which the wing accelerated, s_a, is normalized by its chord length, c, and determines the travel distance over which there is non-zero acceleration. Figure 2.5 illustrates the parameter space of the investigation into the effects of wing acceleration, ranging from a slowly accelerating case over 6 chord-lengths of wing travel to a fast case accelerating over 0.125 chords. Additionally, an angle of attack study was performed on the $s_a/c = 1$ case for $\alpha = 5°$, $7°$, $8°$, $10°$, $15°$, $20°$, $30°$, $35°$, and $45°$. Because this study was solely focused on the effect of the startup transient and subsequent constant-speed translation, the deceleration region is not of interest to the present study. The following figures will

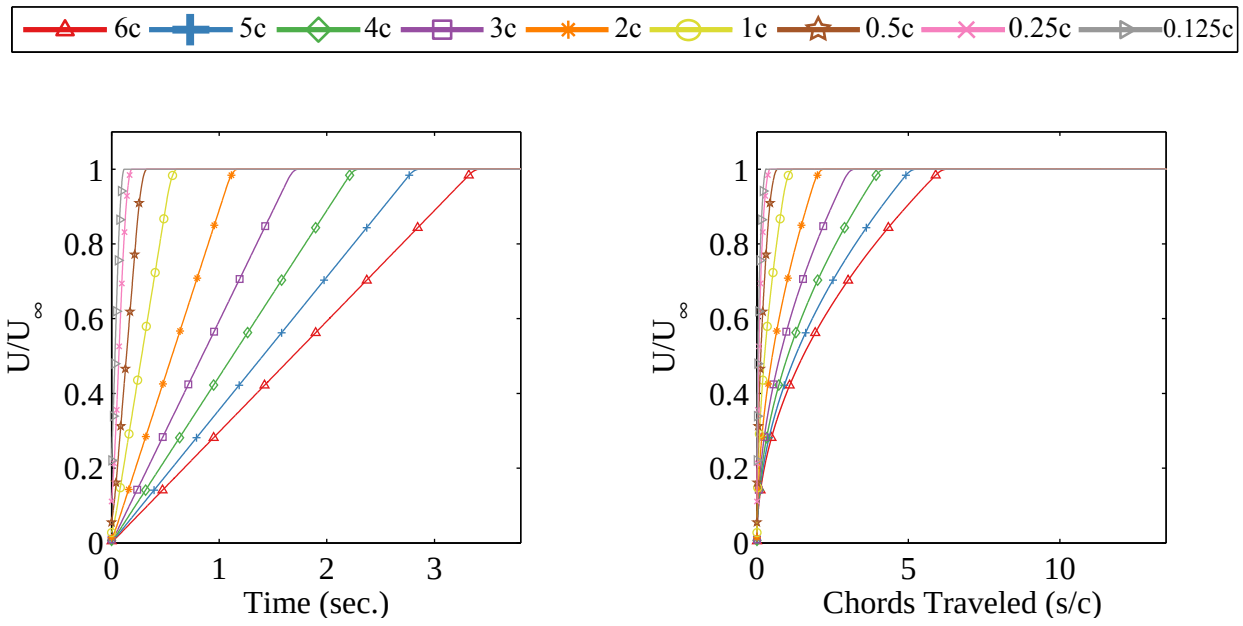

(a) Velocity profile with respect to time.

(b) Velocity profile with respect to distance traveled.

Figure 2.5: Velocity profiles for $0.125 \leq s_a/c \leq 6,\ \alpha = 45°$.

therefore be truncated at $s/c = 14$, the point at which the wing reaches the physical constraint of the test section and deceleration begins.

2.2.3 Translational Pitch

The second simple maneuver studied here is a pitch-and-hold motion on a wing traveling at constant speed. This motion is characteristic of perch maneuvers in fixed wing aircraft [74] and large birds [75], as well as during stroke reversal in flapping fliers [76,77]. Granlund et al. [22] cover a very wide and dense parameter space in terms of pitch rate and pivot axis and provide detailed force histories and flow visualization. The current study focuses on a smaller subset of the kinematic space, but additionally applies novel analysis techniques on leading edge vortex dynamics, force histories, and

circulation production.

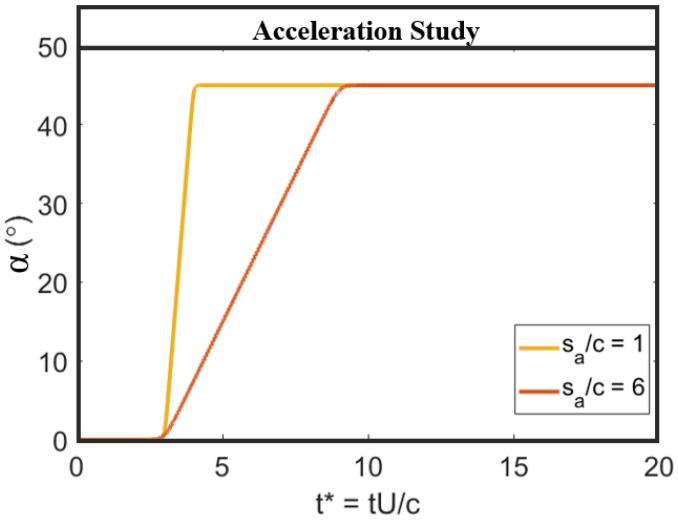

Figure 2.6: Angle of attack time history for acceleration study. The two accelerations are representative of a "slow" and a "fast" case pitching to a final angle of $\alpha = 45°$.

Figure 2.6 illustrates the experimental parameter space for the pitching flat plate experiments. This includes an abridged study on pitch rate, Figure 2.6. Pitch motions were run with the tunnel on at constant free stream corresponding to a Reynolds number of Re = 20,000 and begin with an initial incidence angle of $\alpha = 0°$. Since the goal of this study was to observe and quantify the development of fully separated flow and the formation of leading edge vortices, a final deflection angle of $\alpha = 45°$ was chosen to assure leading edge separation and make for an intentionally aggressive maneuver. Much like the translational surge kinematics, pitch motions were generated using Eq. 2.1 by replacing all velocity terms $(\dot{U}, U_\infty, U_0)$ with angle of attack terms $(\dot{\alpha}, \alpha_{\text{final}}, \alpha_0)$. Smoothing transients are required for the accurate observation of non-circulatory, pitch-

rate dependent forces. The upper limit on attainable pitch rate is dependent on the excitation of the test rig natural frequency, which causes oscillations that distort the observable non-circulatory effects during acceleration phases [22]. The smoothing parameter, a, was selected to be 4 for the slow case and 15 for the fast case, which provided smooth transitions to the linear profiles shown in Figure 2.6 without inducing undesired motor jerk and wing oscillations.

2.2.4 Hinged Wing with Large Trailing Edge Flap

Much like the single-element wing experiments, the wing kinematics of the hinged wing were kept simple to isolate the aerodynamic effect due to deploying the trailing edge flap. The onset of trailing edge flap motion begins after the wing traveling at constant velocity with front and back elements at fixed incidence angles reaches steady state. Free stream was set to 200 mm/s, which, with a 200 mm chord, gave a nominal chord-based Reynolds number of approximately 40,000. The flap is then deployed, as given by the deflection history in Figure 2.8. The motion profile is half of a sine wave of the form $\delta(t) = \delta_0 + 0.5A(1 - \cos(2\pi f t))$, where δ_0 is the initial flap angle, A is the amplitude of the sine wave, and f is the dimensional frequency in Hz. However, to ensure a smooth acceleration transient, we again use Eq. 2.1 with the form

$$\delta(t) = \frac{k}{a} \ln \left[\frac{\cosh(a\frac{U_\infty}{c}(t - t_1))}{\cosh(a\frac{U_\infty}{c}(t - t_2))} \right] + \frac{\delta_F + \delta_0}{2}, \tag{2.2}$$

where $k = \dot{\delta}_{max} c/2U_\infty$ is the reduced frequency, $a = \pi^2 k/(2|\delta_F - \delta_0|(1 - \sigma))$, and σ is a fitting parameter. σ is chosen such that Eq. 2.2 replicates the half-sinusoid, see Figure

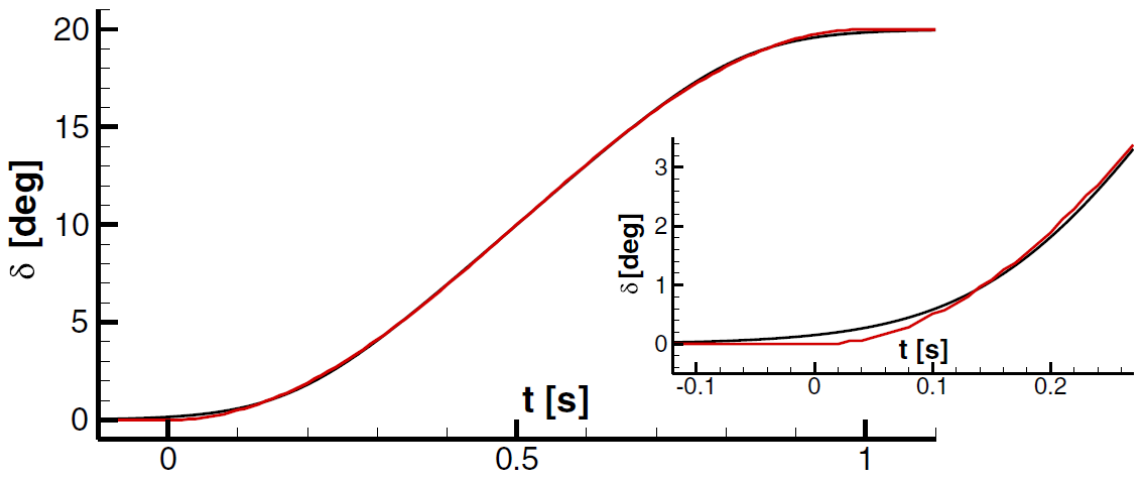

Figure 2.7: Typical history of flap deflection angle versus time for a motion occurring over 1 second. (black) Motor flap deflection using Eq. 2.2, (red) half sinusoid. [72]

2.7.

2.3 Force Measurements

One of the primary methods of data acquisition in the current study was time-resolved force measurement. Forces and moments were obtained via ATI NANO-25 IP68 six-component force balances. The manufacturer's quoted uncertainty bounds for the NANO-25 load cell are $\leq$ 0.28 N, which is commensurate with the highest 95% confidence interval for dimensional forces in this study. Measurements were sampled at 1 kHz and filtered in hardware at f = 18 Hz. Results were again filtered in post-processing with a Chebychev II low-pass filter at 12 Hz with -20 dB attenuation. To offset the time-shift applied to the data in the passband, a forwardbackward filtering

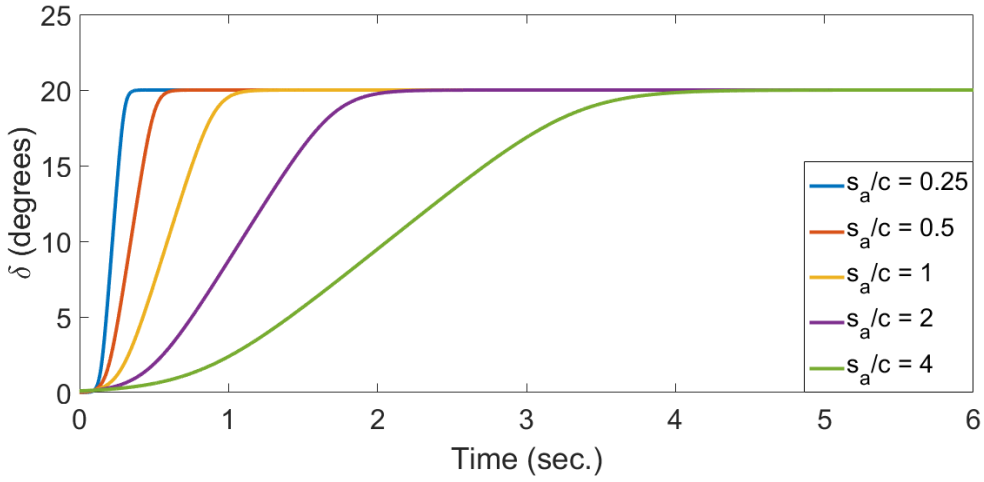

Figure 2.8: Motion history of the trailing edge flap for several flap frequencies.

technique is applied using the MATLAB command `filtfilt`, eliminating any phase shifts in the filtering process. Each measurement is the result of an ensemble average of five consecutive runs. Figure 2.9 provides representative examples of surge and pitch cases, providing the raw, unfiltered result as well as the final result. To determine at which frequency to apply the low-pass filter, fast Fourier transforms (FFT), using the MATLAB function `fft`, were plotted to identify significant spikes corresponding to the mechanical ringing seen in the raw force measurements. In both pitch and surge cases, the largest peak in the FFT occurs at 12 Hz, thus dictating the frequency for the low-pass filter. It should be noted that not all motions in this study contain large, undesired mechanical vibrations. Less aggressive cases, e.g. slow pitch over 6 chords (red line in Figure 2.9b), contained very little vibration throughout the prescribed motion.

Force measurements on the hinged wing were obtained in an identical fashion via two NANO-25 force balances: one on the fore element and one on the rear element (see Figure 2.4a).

2.4 Particle Image Velocimetry (PIV)

Time-resolved, planar (two dimensional) PIV was performed at both AFRL and UMD to quantify velocity fields around the single-element and hinged wings. Results were used quantitatively to measure circulation production and track the trajectories of leading edge vortices as well as qualitatively to visually assess the nature of the flow field and comment on its behavior.

AFRL: Single-element pitching and surging plate

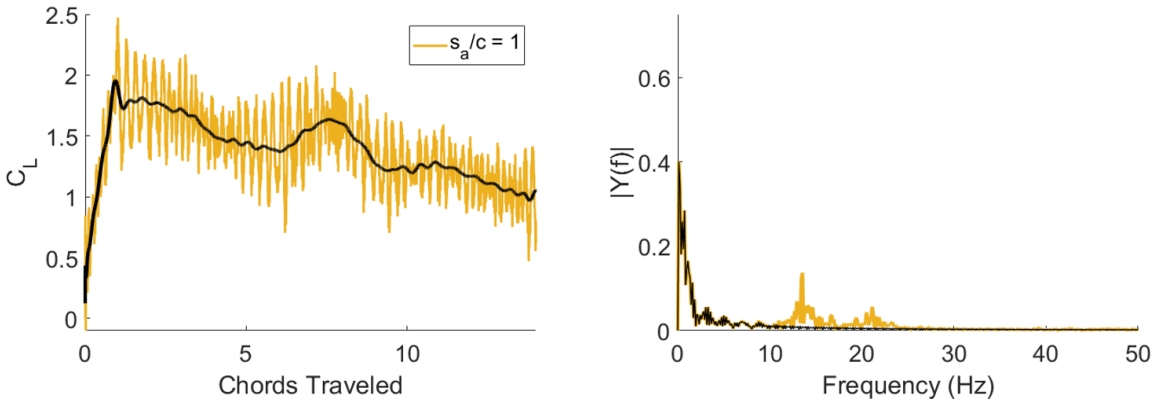

(a) Lift coefficient (left) and its fast Fourier transform (right) for the $s_a/c = 1$ at $\alpha = 45°$ surge case described in Figure 2.5. Raw data is in yellow, 12 Hz low-pass filtered data is in black.

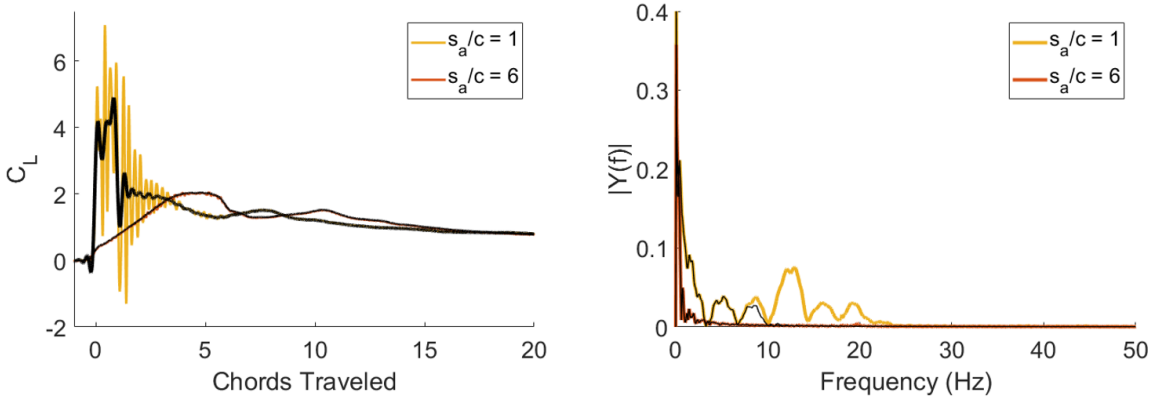

(b) Lift coefficient (left) and its fast Fourier transform (right) for the $s_a/c = 1$ and $s_a/c = 6$, $\alpha = 0 - 45°$ pitch case described in Figure 2.6. Raw data is in yellow, 12 Hz low-pass filtered data is in black.

Figure 2.9: Representative cases for surge and pitch motions demonstrating the low-pass filtering process.

Shown schematically and as a lab snapshot in Figure 2.10, PIV experiments on single-element surging and pitching flat plates at AFRL used an Nd:YLF 527nm pulsed laser sheet of 2 mm thickness at 50 Hz to illuminate the 5 μm Vestosint seeding particles.

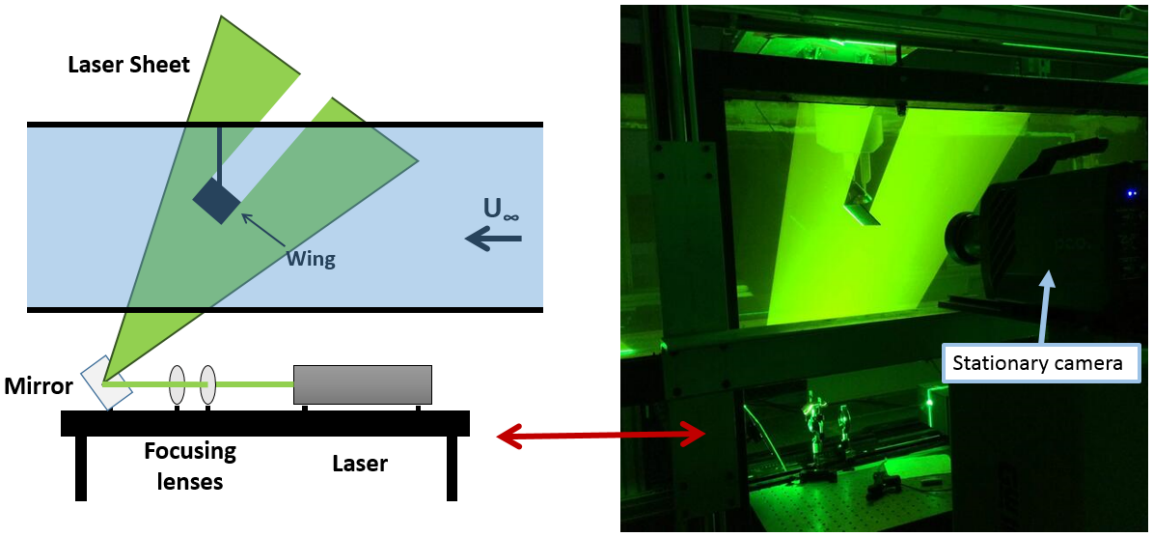

Figure 2.10: Particle image velocimetry (PIV) setup at AFRL.

Figure 2.11 provides snapshot images of the PIV experiment, showing the aforementioned 2 mm laser sheet (seen as illuminated line on suction side) aligned with the three-quarter span and streaklines of seed particles. Images were recorded with a lab-fixed PCO DiMax high-speed camera at a rate of 667 Hz, i.e. dt = 1.5ms. This image pair time step was selected based on the desired particle displacement between frames of 6-10 pixels. The camera and laser operation were externally synchronized to the wing motion via a Quantum Composer timing box. PIV processing was performed on Lavison's DaVis 8.1 software. A multipass, variable window-size processing method was implemented. The first pass used a 48×48 pixel window with 1:1 square weighting and 50% overlap. The next two passes used 32×32 pixel windows with 1:1 circular weighting and 75% overlap. Vector post-processing was kept to a minimum by only utilizing a remove-and-replace median filter of 2 standard deviations.

UMD: Hinged plate

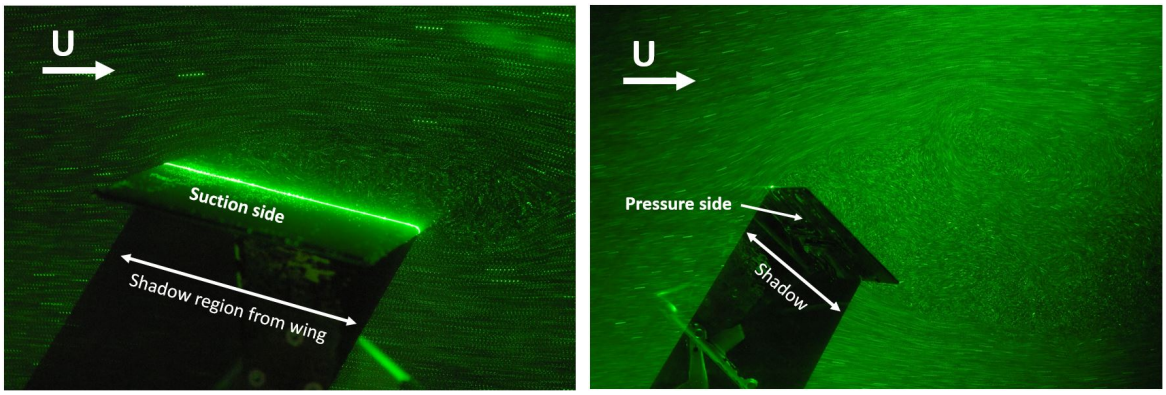

(a) (b)

Figure 2.11: Snapshots of the particle image velocimetry experiment taken with a standard SLR camera. These images provide visuals of the shadow region beneath wing due to the opaque wing material, streaklines of particles convecting over the wing, visualization of spanwise location of the laser plane (indicated by bright line on suction surface).

Wing-fixed PIV on the hinged flat plate was conducted at the University of Maryland in the 7 m $\times$ 1.5 m $\times$ 1 m towing tank equipped with an Nd:YLF 527 nm pulsed laser sheet to illuminate the $\sim$ 32 μm seeding particles. To create the laser sheet, a series of mirrors and focusing optics directed the beam down the length of the tank to hit the carriage-fixed optics that allowed the sheet to travel with the wing. As shown in Figure 2.12, the beam, once directed vertically downward towards the wing, hits a Powell lens to turn the beam into a triangular planar laser sheet. The width and brightness of the laser sheet can be adjusted by switching out Powell lenses of various angles (top right image of Figure 2.12). A steeper Powell lens roof angle results in a wider but less bright laser sheet. The laser plane was aligned with the three-quarter span location on the wing, intended to provide two-dimensional flow fields (minimal out-of-plane flow) while also being close enough to the camera to make use of the entire field of view. Images were recorded at a rate of 100 Hz with a 1 MPx high-speed camera that was fixed to the motor carriage and translated with the wing allowing for wing-fixed PIV measurements (see Figure 2.13). The sampling rate was selected based on the desired particle displacement between frames of, on average, 6-10 pixels. The camera and laser operation were externally synchronized to the wing motion. PIV processing was performed on Lavison's DaVis 8.1 software. A multipass, variable window-size processing method was implemented. The first pass used a 48 $\times$ 48 pixel window with 1:1 square weighting and 50% overlap. The next two passes used 16 $\times$ 16 pixel windows with 1:1 circular weighting and 50% overlap. Vector post-processing was kept to a minimum by only utilizing a remove-and-replace median filter of 1 standard deviation.

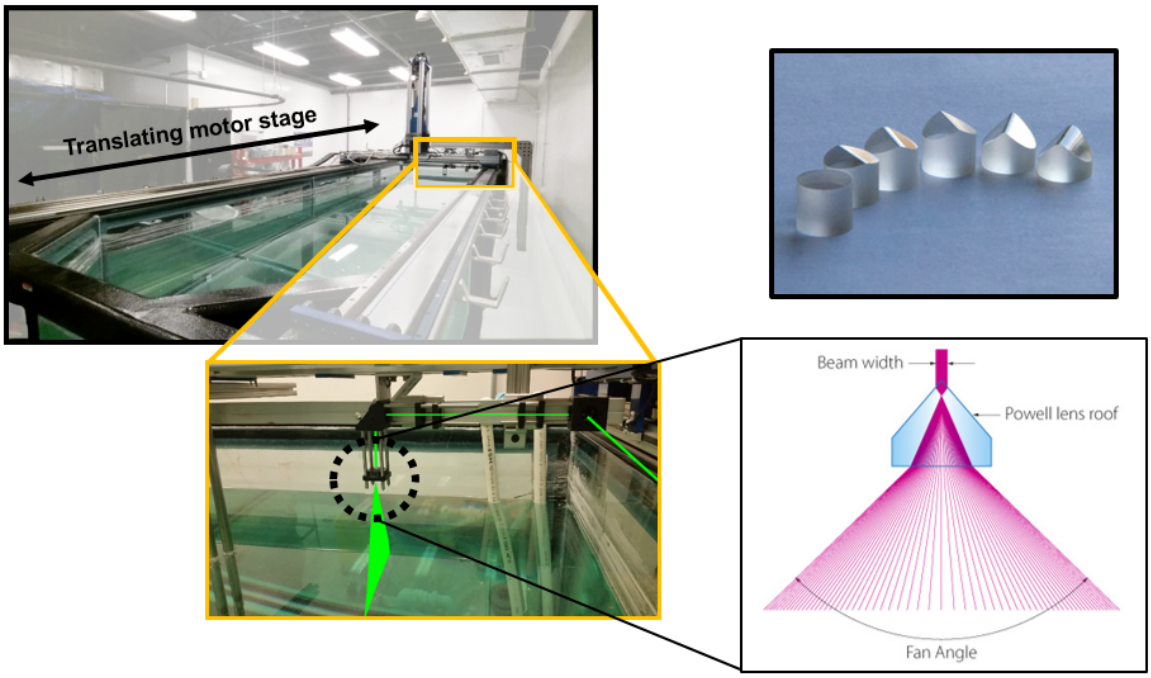

Figure 2.12: Snapshot of UMD tank and laser beam path. Before interacting with the wing, the beam enters a Powell lens (shown on right) to expand itself into a thin sheet. (Lens image and schematic provided by http://www.altechna.com)

2.5 Flow Visualization

Qualitative flow visualization was performed at AFRL using fluorescent dye and planar laser fluorescence. A high concentration of Rhodamine 6G in water was injected at the leading and trailing edges at the 3/4 semispan location by a positive-displacement pump with a prescribed volumetric infusion rate. The dye was injected via a set of 0.5 mm internal-diameter rigid lines glued to the surface of the plate (shown in Figure 2.3). Dye was illuminated by the Nd:YLF 527 nm pulsed laser sheet of 2 mm thick-

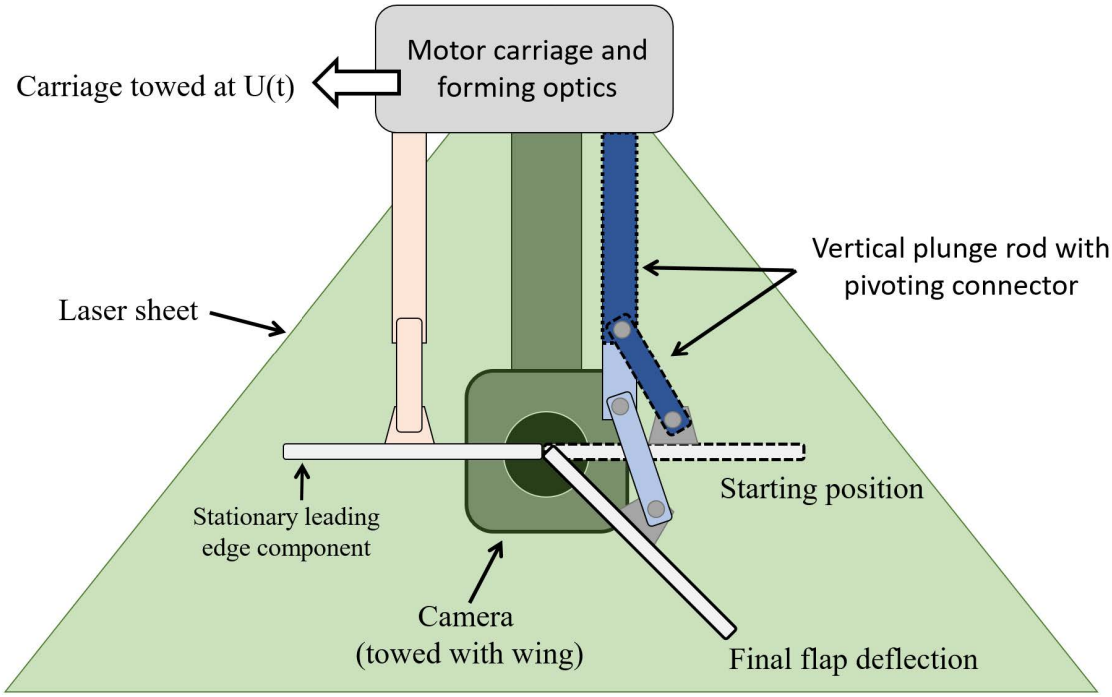

Figure 2.13: Schematic of UMD's wing-fixed PIV setup. The wing-laser-camera system travels together down the length of the tank as the hinged wing, centered in the camera frame, undergoes its trailing edge flap deflections.

ness at 50 Hz. Images were recorded with a PCO DiMax high-speed camera through a Nikon PC-E 45 mm Micro lens. A Tiffen orange #21 filter was used to remove the reflected 527 nm laser light. Since the dye fluorescence wavelength was 566 nm, the resulting image contained only the flow structures formed by the dye. To supplement the quantitative force measurements, flow visualization provides images of clearly defined flow structures that qualitatively show the flowfield throughout the wing's motion. Force measurements and PIV were acquired at a chord-based Reynolds number of Re = 20,000 to assure sufficient signal-to-noise ratio. However, all flow visualization experiments were performed at a Reynolds number of 2,500 to avoid immediate diffusion and dissipation

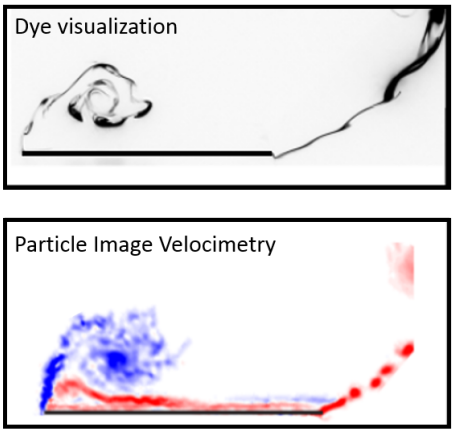

(a) Dye visualization (top) and PIV vorticity field (bottom) of surging $s_a/c = 1$ $\alpha = 45°$ case

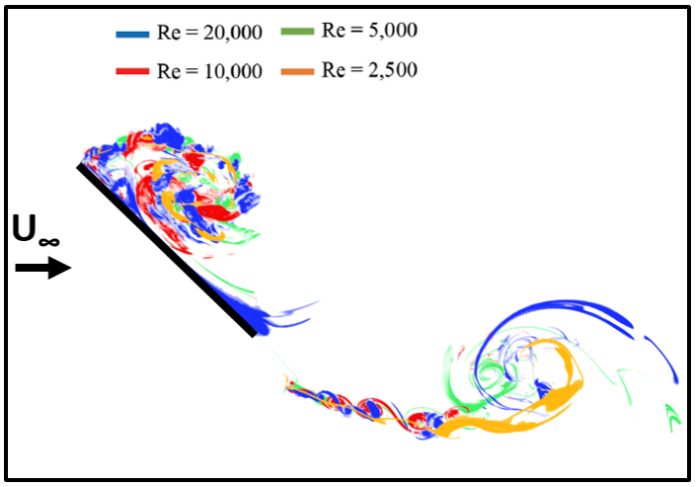

(b) Dye visualization for several Reynolds numbers, showing nearly identical flow structures developing independent of Re.

Figure 2.14: Although PIV and dye visualization are performed at different Re (Re = 20,000 and 2,500, respectively), the flow structures are very similar.

of the dye. Figure 2.14 provides a comparison between 1) dye experiment and PIV for the fast surging plate at $\alpha = 45°$ (images rotated to place chord on the horizontal) and 2) Reynolds numbers for the same case ranging from Re = 2,500 - 20,000, all of which provide nearly identical flow structures.

2.6 Analysis Techniques

Section 2.4 detailed the instrumentation and acquisition of time-resolved velocity fields via particle image velocimetry. Beyond the straightforward acquisition of velocity fields, additional analysis techniques were performed on PIV measurements to quantify the strength and trajectory of vorticity production. Specifically for the hinged plate,

vorticity measurements were used in a semi-empirical low order lift prediction model based on the principles behind Lamb's vortex impulse analysis [54]. The lift calculated from the following vortex impulse method was compared to direct force measurements, shedding light on the sources of lift production during highly unsteady kinematics and illustrating the equivalence between force production and vorticity production.

2.6.1 Vortex Impulse

One major goal of this work is to illustrate the direct relationship between force production and vorticity (or circulation) production on wings undergoing rapid maneuvers. Section 2.3 described the acquisition of direct force measurements via installing a submersible force balance on the wing. The theoretical concept of vortex impulse, as popularly derived by Lamb [54], introduces the idea of obtaining force production solely via the time-resolved magnitude and trajectory of generated vorticity. Thus, we are able to use PIV measurements to obtain a non-intrusive time-resolved force calculation for lift production, which can be a useful tool for experiments incapable of instrumenting a force balance.

An analytical depiction of this concept, detailed in Lamb [54], describes the fluid impulse, $\mathbf{J}$, resulting from the relative motion and growth/decay of two equal, opposite-strength vortices as

$$\mathbf{J} = \rho \Gamma s \hat{\mathbf{e}}_{\mathbf{n}}, \tag{2.3}$$

where s is the distance between the vortices of strength Γ and $\hat{\mathbf{e}}_\mathbf{n}$ is the unit normal vector to the line of length s connecting the vortex centers. Eq. 2.3 can be broken down into horizontal, $\mathbf{P}$, and vertical, $\mathbf{Q}$, components as

$$\mathbf{J} = \mathbf{P} + i\mathbf{Q} = \rho\Gamma[(z_+ - z_-) + i(x_- - x_+)], \tag{2.4}$$

where the subscript "+" corresponds to the vortex with positive vorticity and "-" corresponds to its opposite-signed companion vortex with negative vorticity.

von Karman and Sears [78] extended upon this work and explained that the lift force is equal to the time rate of change of vertical momentum. Differentiating Eq. 2.4 and applying the chain rule results in a lift force given by

$$L' = -\rho[(u_- - u_+)\Gamma + (x_- - x_+)\dot{\Gamma}], \tag{2.5}$$

where $u(t)$ is a horizontal velocity given by the time derivative of $x(t)$. Non-dimensionalizing Eq. 2.5 by the freestream dynamic pressure and chord length, we obtain an equation for the lift coefficient,

$$C_L = -\frac{2}{U^2 c}[(u_+ - u_-)\Gamma + (x_+ - x_-)\dot{\Gamma}] \tag{2.6}$$

According to Eq. 2.6, the only quantities required to compute lift (using only flowfield information) are vortex strength, $\Gamma(t)$; relative position between the vortices, $x(t)$; and each of their time derivatives, $\dot{\Gamma}(t)$ and $u(t)$. Section 2.4 covered particle

image velocimetry, which provides time-resolved velocity fields and, via mathematical manipulation, vorticity fields. The following section will discuss the methodology by which to obtain the vortex strength and position values required in Eq. 2.6.

2.6.2 Vortex Tracking: γ_1 Criterion

The practice of identifying vortex structures is quite common in low Reynolds number flow investigations [79–81]. There are several methods for doing so, but one of the most common and robust methods for identifying a vortex center is to use the γ_1 equation proposed by Graftieaux, et al. [82]. This function, applied to fluid velocity fields, characterizes the extent to which the fluid motion is circular around a point, P, and is given by

$$\gamma_1(P) = \frac{1}{S}\int_S \sin(\theta)\mathrm{d}S, \tag{2.7}$$

where S is the area of integration and θ is the angle between point P and the velocity vector at $\mathrm{d}S$. A γ_1 value of 1 indicates purely tangential flow and one that is highly rotational about a single point P. As explained by Manar et al. [80], a benefit of implementing this method is that it incorporates spatial averaging that attenuates measurement noise, resulting in smooth, contiguous regions that ease the vortex identification process. As will be shown, this method very effectively captures the location of a single coherent, circular vortex, but it does not have the capability to identify non-circular, asymmetric regions of vorticity, such as the feeding shear layer to the leading and trailing edge vortices or the bound circulation along a wing experiencing attached flow.

2.6.3 Vortex Tracking: Centroid of Vorticity

Calculating vortex impulse lift via Eq. 2.6 requires the position and convection speed of two opposite-signed ideal vortices. However, because we are dealing with real flows that generate vorticity via viscous phenomena (boundary layer development, shear layer and vortex formation at the leading edge) there is more to the vorticity field than purely two clearly defined vortices. Thus, we now seek to apply the principles of the vortex impulse method to cases in which the flow field is more complex than the ideal case. This section explains the method of tracking the position and relative motion of a *region of vorticity* rather than any single coherent vortex.

Figure 2.15 provides representative vorticity measurements for the flat plate and hinged wings during their motion transients. During the flapping motion, the hinged wing (Figure 2.15b) experiences considerable periods of attached flow followed by gradual development into separated flow, during both of which there is no clearly identifiable vortex. Thus, common vortex identification methods such as γ_1 will not yield an accurate representation of the flow configuration and cannot provide the necessary values for Eq. 2.6. This motivated the implementation of a robust method that accurately defines a representative location for the center of vorticity corresponding to the wake or to the bound circulation on (or above) the wing.

Tracking the centroid of vorticity is an easy to implement, robust method, which is necessary when the flow field contains more than coherent circular vortices. Centroid coordinates $[x_{cent}, y_{cent}]$ are determined based on the equations

$$x_{cent} = \frac{\sum_{j=1}^{M}\sum_{i=1}^{N} x_{ij} w_{ij}}{\sum_{j=1}^{M}\sum_{i=1}^{N} w_{ij}} \tag{2.8}$$

$$y_{cent} = \frac{\sum_{j=1}^{M}\sum_{i=1}^{N} y_{ij} w_{ij}}{\sum_{j=1}^{M}\sum_{i=1}^{N} w_{ij}}, \tag{2.9}$$

where w_{ij} is the vorticity ($w = \nabla \times V$) at point x_{ij}. To capture the vorticity corresponding to only bound circulation or trailing edge wake circulation, masks were applied to the flowfield to isolate the areas of interest (see solid and dashed boxes in Figure 2.15). Within the solid contour (bound circulation) there contains both positive and negative vorticity, highlighting another shortcoming of using γ_1. The location of the resulting "vortex" is calculated as the average of both positive and negative vorticity centroids.

$$\bar{x}_{bound} = \frac{x^{+}_{cent} + x^{-}_{cent}}{2} \tag{2.10}$$

$$\bar{y}_{bound} = \frac{y^{+}_{cent} + y^{-}_{cent}}{2} \tag{2.11}$$

Figure 2.15 contains the locations of bound and wake centroids corresponding to $(x_{\text{cent}}, y_{\text{cent}})$ of Eq. 2.8 - 2.9 for positive, negative, and total (Eq. 2.10 - 2.11) vorticity, indicated by red, blue, and black outlined circles, respectively. Notice that the γ_1 method, shown in Figure 2.15 as a star, accurately captures vortex centers for the surging plate's LEV and TEV and the hinged wing's TEV; however, it could not accurately identify

a location for the bound circulation on the hinged wing. The centroid of vorticity is insensitive to the shape of the resulting flow field and will provide a time-resolved trajectory of the motion of all the vorticity in the flowfield rather than of one single vortical structure. For this reason, the vorticity centroid will be used to compute vortex location for the hinged plate, whereas γ_1 will be used for the surging and pitching single-element plates.

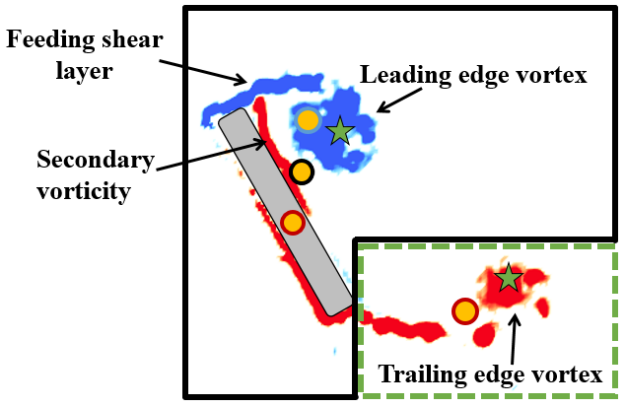

(a) Surging wing at $\alpha = 60°$. Both γ_1 and centroid method locate leading edge vortex.

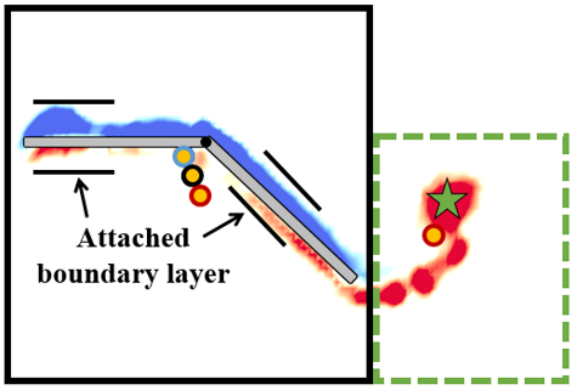

(b) Hinged wing at deflection angle $\delta = 40°$. Without a discernible leading edge vortex, γ_1 (star) struggles to find a location for the LEV as required by Eq. 2.6.

Figure 2.15: Two PIV snapshots for (a) surging plate and (b) hinged wing experiments. Note that when there is a clear leading and trailing edge vortex, as in (a), the γ_1 criteria (star) successfully locates the vortex center. However, when there is no coherent circular structure, as in (b), the γ_1 method struggles to accurately find a center. The centroid method (circles), however, robustly quantifies the center of vorticity, regardless of coherent structures or circular flow.

2.7 Chapter Summary

The experimental portion of this work aimed to quantifying the lift production and vorticity generation during motion transients of rapidly maneuvering wings and its subsequent relaxation to steady state. This experimental study is the result of a multi-year collaborative effort between the Air Force Research Laboratory and the University of Maryland, containing results of two major experimental campaigns. The first study focuses on the force histories and separated flow development of surging and pitching single-element flat plates at $2,500 \leq \mathrm{Re} \leq 20,000$, all of which were performed at AFRL. The second study explores the lift history and flow field development of a hinged wing with a rapidly deflecting trailing edge flap. For the hinged wing study, force measurements and flow visualization were acquired at AFRL whereas PIV was acquired at UMD. Both sets of experiments were measured by the methods of direct force measurements via 6-component force balance, particle image velocimetry, and fluorescent dye flow visualization. Velocity fields acquired from PIV were used to track and quantify regions of vorticity and, using a vortex impulse method, to predict lift production. This method serves as both an insightful tool to examine the sources of force production as well as a powerful non-intrusive technique for semi-empirically modeling force histories.

Chapter 3

Methodology: Analytical and Numerical Models

The previous chapter contained a detailed description of the experimental campaign regarding flat plates undergoing various combinations of surge and pitch. This chapter aims to describe the various analytical and numerical aerodynamic force prediction models that will be applied in Chapter 5 to predict force histories on the rapidly deflecting trailing edge flap. This chapter also describes the theoretical sources of steady and unsteady lift production that will be discussed throughout this work for each of the experimental investigations. The main benefit of the low-order models used in this work are their relative simplicity, which allows us to identify specifically which physical mechanisms are being modeled and further analyze which mechanisms are dominant for each motion. The *analytical* models, based in classical aerodynamic theory, require only inputs of wing kinematics, making them suitable tools for controller applications. The *numerical* model is an unsteady discrete vortex panel method that provides accurate aerodynamic force histories and chord-wise pressure distributions at relatively low computational cost. The following sections provide descriptions and limitations of each

model, delving into the physical mechanisms modeled in each.

3.1 Theodorsen

In the late 1930's, Theodore Theodorsen and I.E. Garrick [14,61,66] published their revolutionary work on the problem of aerodynamic flutter. This work eventually led to the widely used unsteady aerodynamic lift model commonly attributed to Theodorsen. Theodorsen's unsteady flow model provides explicit parsing of the lift history into constituent parts - not only inertial and circulatory loads, but also the contribution from the resulting trailing edge wake. This provides physical insight typically unavailable in CFD or panel methods. The assumptions in the formulation of this model include: inviscid, attached flow; small angular deflections, i.e. $\sin(\alpha) \approx \alpha$; planar trailing edge wake; and satisfaction of the Kutta condition at the trailing edge. Thus, Theodorsen's solution ignores viscous and non-ideal flow phenomena such as wake roll-up, large vortex formation and convection over the airfoil, laminar separation bubbles, and so on. However, as discovered by many researchers to date, Theodorsen's theoretical lift model is able to predict with reasonable accuracy the lift due to wing kinematics that wildly disobey these assumptions [15, 83], as is the case in the present work.

A comprehensive derivation and discussion of Theodorsen's lift solution is provided in Appendix A. Theodorsen's model provides a general solution for an airfoil-aileron system under arbitrary pitch kinematics in a constant horizontal freestream, as shown in Figure 3.1. The airfoil system can be simplified to a single-element airfoil by setting the aileron hinge location to $c = 1$. Both the single-element airfoil and airfoil-aileron

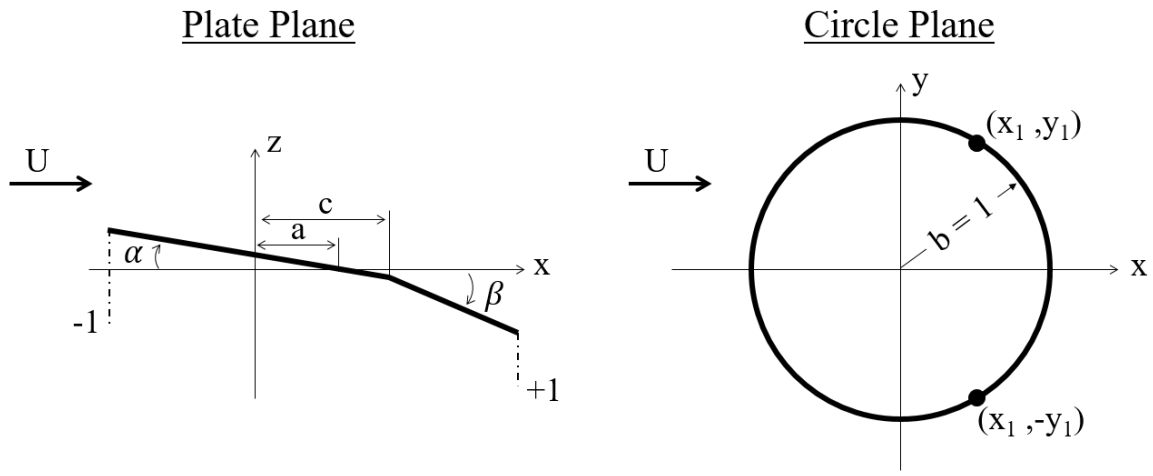

Figure 3.1: Airfoil-aileron system in the xz-plate plane (left) and its conformal representation in the xy circle plane (right)

will be studied here. To more easily enforce boundary conditions using potential flow singularities, the airfoil-aileron system is typically represented in the circle frame via Joukowski's conformal transformation, shown in the right image of Figure 3.1. The following sections contain a recount of Theodorsen's solution along with an explanation of its terms. From this mathematical abstraction of the physical flow, two primary categories of forces arise: **non-circulatory** and **circulatory forces**.

To represent the physical flow, Theodorsen introduces potential flow singularities whose strengths are assigned to satisfy the necessary boundary conditions (i.e. the Kutta condition and no flow through the wing). The category of **non-circulatory** forces arises from enforcing the no through-flow boundary condition as the wing moves through the surrounding fluid. This boundary condition is enforced by placing point sources and sinks along the surface of the airfoil and assigning their strengths such that the normal velocity at the plate surface is zero. There is no constraint placed on flow behavior other

than the fact that it cannot physically penetrate the airfoil. Because no circulation is introduced to satisfy this condition, these are considered **non-circulatory forces**.

Circulatory forces arise from the creation of circulation about the airfoil, which is modeled by enforcing the Kutta condition at the trailing edge. This requires that no infinite velocities can exist at the trailing edge, leading to a unique solution for vorticity distribution along the airfoil and thus a unique lift force.

3.1.1 Non-Circulatory Flow

In order to solve the potential flow solution for flow over an airfoil undergoing arbitrary kinematics, some key approximations and simplifications must first be made. By observation that airfoil thicknesses typically have slopes much less than unity ($\frac{\partial z_a}{\partial x} << 1$, where $z_a(x)$ are the coordinates of the airfoil surface in the xz-plane) and that the resultant fluid velocity vector differs only slightly in direction and magnitude from the horizontal free stream velocity, $U = U_\infty$, we can introduce a disturbance velocity potential, ϕ', which is obtained by parsing the total velocity potential into the uniform flow and a perturbation potential as

$$\phi = \phi' + Ux \tag{3.1}$$

The disturbance velocity components are thus

$$u - U = u' = \frac{\partial \phi'}{\partial x}, \qquad w' = \frac{\partial \phi'}{\partial z}, \tag{3.2}$$

which are assumed to satisfy the order-of-magnitude requirement of small disturbance theory of $u', w' << U$.

For incompressible flows, it can be shown that the problem simplifies to Laplace's

equation

$$\nabla^2\phi' = 0, \tag{3.3}$$

subject to two-dimensional boundary conditions at the surface. The condition at the boundary, covered in detail in Lamb [54], states that the component of fluid velocity normal to the body, $\frac{\partial\phi}{\partial n}$, is fixed by the body motion.

As previously stated, we are assuming small disturbance theory, which requires $u', w' << U$. Thus, neglecting the terms u'^2 and w'^2 due to order of magnitude insignificance, we obtain a linearized solution. For details of the derivation and use of the unsteady Bernoulli equation, the reader is instructed to reference Appendix A.1. The resulting expression for pressure via the linearized unsteady Bernoulli equation is given by

$$p - p_\infty = -\rho(U\frac{\partial\phi}{\partial x} + \frac{\partial\phi}{\partial t}) \tag{3.4}$$

Due to antisymmetry between sources on the upper surface and sinks on the lower surface, the pressure difference between upper and lower surfaces is

$$p_L - p_U = \Delta p = -2\rho(U\frac{\partial\phi}{\partial x} + \frac{\partial\phi}{\partial t}). \tag{3.5}$$

Finally, the total non-circulatory contribution to the lift force on the wing can be calculated by integrating the pressure difference over the entire airfoil:

$$\begin{aligned} L_{NC} &= 2\rho b\int_{-1}^{1} U\frac{\partial\phi}{\partial x}\mathrm{d}x + 2\rho b\int_{-1}^{1}\frac{\partial\phi}{\partial t}\mathrm{d}x \\ &= 2\rho b\int_{-1}^{1}\frac{\partial\phi}{\partial t}\mathrm{d}x \end{aligned} \tag{3.6}$$

Applying Eq. 3.6 to the velocity potentials given in Eq. A.14-A.17 results in the familiar

form of Theodorsen's non-circulatory lift

$$L_{NC} = -\rho b^2[U\pi\dot{\alpha} - b\pi a\ddot{\alpha} - UT_4\dot{\beta} - bT_1\ddot{\beta}], \tag{3.7}$$

where

$$T_4 = -\cos^{-1} c + c\sqrt{1-c^2} \tag{3.8}$$

$$T_1 = -\frac{1}{3}\sqrt{1-c^2}(2+c^2) + c\cos^{-1} c \tag{3.9}$$

Rotational Acceleration Force: Added Mass

Eq. 3.7 describes the *total* non-circulatory lift force on the airfoil-aileron system. Considering now only the terms dependent on acceleration ($\ddot{\alpha}$ and $\ddot{\beta}$) we can identify the contribution of what is typically termed the "added mass force." Added mass describes the inertia added to a system due to the acceleration of the fluid surrounding a submerged body, which in the present case is a pitching wing in water or air. This motion causes a reaction force from the fluid normal to the plate surface and is proportional to the acceleration of the body. In terms of Theodorsen's derivation, this term arises due to the satisfaction of the no penetration boundary condition specifically due to the wing moving through the fluid. An additional velocity potential has to be placed in the system to assure that the fluid velocity always remains tangent to the wing along the surface as it moves through the fluid. This additional velocity potential is given by Eqs. A.15 and A.17.

Non-circulatory forces due to acceleration are of considerable importance for the present kinematics, as the reduced frequencies ($k = \frac{\dot{\beta}c}{2U_\infty}$) of the trailing edge flap range from $0.044 \leq k \leq 0.70$, which fall well into the range of what is considered "unsteady" and where pitch rate effects become significant contributors to force production [63].

Figure 3.2 provides lift histories (Eq. 3.7) and chordwise non-circulatory pressure distributions (integrand of Eq. 3.6) for the *non-circulatory* lift components for several different wing geometries and pitch axis locations.

Figure 3.2(a,b) shows the results for a single-element wing pitching about its leading edge from $\alpha = 0 - 20°$ at reduced frequency $k = 0.35$. It is clear that for this case the majority of non-circulatory force production is manifested in the angular acceleration $\ddot{\alpha}$ term, which is antisymmetric across the x-axis following the shape of the acceleration profile. We also notice that the pressure distribution is not symmetric over the airfoil, but biased towards the rear half of the wing. For the case in Figure 3.2(a,b), most of the lift is generated towards the rear of the wing due to the larger normal velocities farther from the axis of rotation.

Similar to the single-element case, Figure 3.2(c,d) shows the effect of a large trailing edge flap ($c = 0$) on a wing with a stationary leading edge component, ($\alpha(t) = 0$). Looking only at the rear half of the airfoil containing the pitching flap, we notice a very similar pressure distribution to that of Figure 3.2(a): biased lift production farther from the pivot axis and antisymmetric lift proportional to the flap acceleration (points/distributions A and C). Looking at the forward half of the wing, one should note that the motion of the trailing edge flap appears to induce a *non-circulatory* lift component on the *stationary* leading edge element. Mathematically, this occurs because of the influence each point singularity on the airfoil surface has on each other. Otherwise stated, the lift-producing point sources and sinks on the trailing edge flap element induce a velocity potential on the leading edge element that creates a net pressure distribution, despite its zero angle to the free stream ($\alpha = 0$). To understand this effect

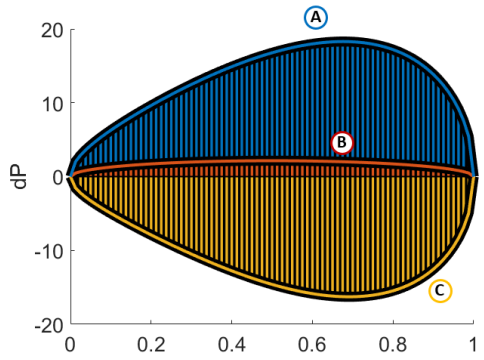

(a) $\alpha = 0 - 20°$, $a = -1$

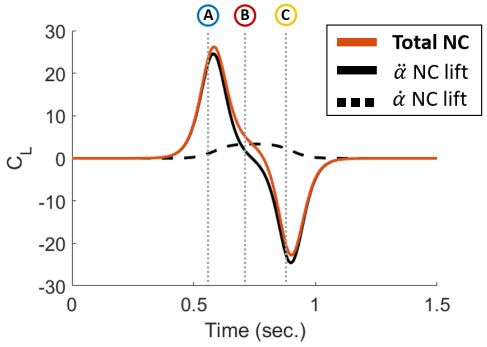

(b) $\alpha = 0 - 20°$, $a = -1$

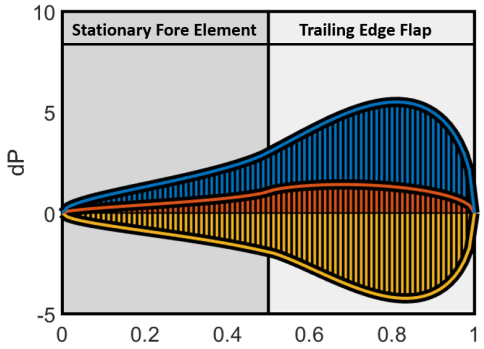

(c) $\beta = 0 - 20°$, $c = 0$, $\alpha = 0°$

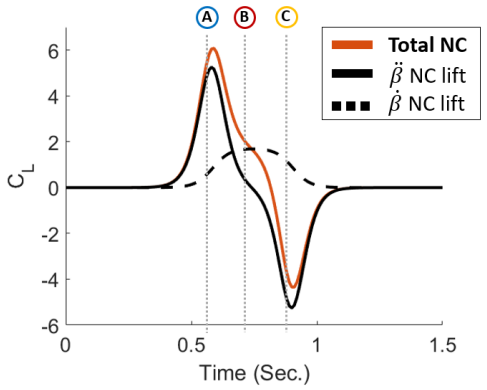

(d) $\beta = 0 - 20°$, $c = 0$, $\alpha = 0°$

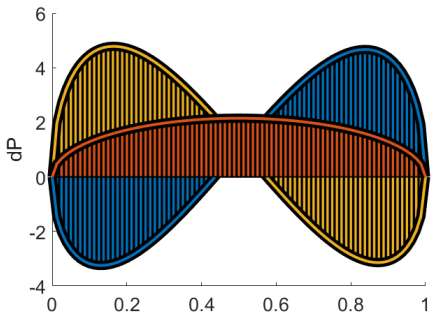

(e) $\alpha = 0 - 20°$, $a = 0$

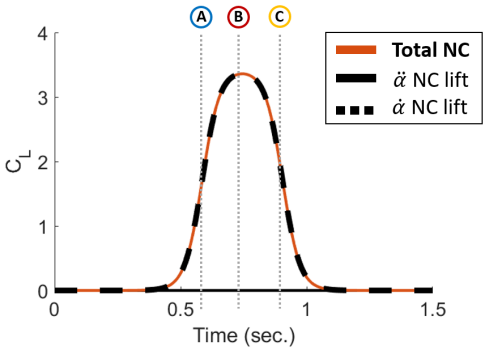

(f) $\alpha = 0 - 20°$, $a = 0$

Figure 3.2: Chordwise pressure distributions (left) and non-circulatory lift contributions (right) of Theodorsen's quasi-steady solution for an (a,b) aileron pitching about its leading edge, (c,d) airfoil-aileron system with $c = 0$, and (e,f) airfoil pitching about its mid-chord. All pitch motions are for α (or β) $= 0 - 20°$ at reduced frequency $k = 0.35$.

from a physical standpoint, we must first examine the underlying assumptions in the model. The assumption of inviscid flow ignores any viscous effects (e.g. flow separation, skin friction, etc.) which all require a diffusion time scale over which to develop. We can then conclude that any disturbance introduced by the wing will take the form of a pressure force, as viscous forces are neglected. Further, by assuming incompressible flow we approximate the speed of sound as approaching infinity, and thus propagation of pressure disturbances becomes instantaneous. Therefore, the physical disturbance of the deflecting trailing edge flap will have an effect on the streamlines over both the forward and aft portions of the wing simultaneously, resulting in a non-zero pressure distribution over the stationary leading edge component.

For the cases presented in this work, all of which have reduced frequencies that characterize the motion as "unsteady", the acceleration-dependent non-circulatory lift component will be a driving factor in much of the lift production. This is because the wing (or trailing edge flap) will be pitching about its leading edge, maximizing its potential for force production. However, to show the minimizing case, Figure 3.2(e,f) provides the case of a single-element wing pitching about its mid-chord, $a = 0$. Here we see the acceleration term identically zero throughout the motion due to the antisymmetric pressure distribution shown in Figure 3.2e. The antisymmetry arises because the front half of the wing is accelerating in a "pitch-down" motion whereas the back half is accelerating in a "pitch-up" motion, causing an equal and opposite pressure distribution.

Rotation-Induced Plate-Normal Acceleration Force

Non-circulatory pitch rate terms (those containing $\dot{\alpha}$ and $\dot{\beta}$) arise from the time

derivative of the velocity potential due to instantaneous angular deflections α and β. When the wing is deflected with incidence to the free stream, point sources and sinks are added to the system in order to enforce the no penetration condition solely due to the fact that the velocity at the wing surface must now be inclined at some angle so as to follow the shape of the wing. Eqs. A.14 and A.16 provide the velocity potential equations for deflections α and β.

Let us now think about the effect of this deflection on velocity components in the wing frame. Figure 3.3 provides a schematic showing the plate normal, $V_{\perp}$, and plate parallel, $V_{||}$, velocities due to a wing in constant free stream. For each instantaneous incidence angle, there is a trade-off between plate parallel and plate-normal velocities according to $V_{||} = U\cos(\alpha)$ and $V_{\perp} = U\sin(\alpha)$. Therefore, as the wing pitches over time there is a corresponding change in plate normal velocity. A time rate of change of the normal velocity can be viewed as an acceleration, and as discussed in the previous section, that acceleration leads to force production on the wing. The time rate of change of plate normal velocity can be described as

$$\dot{V}_{\perp} = \frac{\partial}{\partial t}V_{\perp} = \frac{\partial V_{\perp}}{\partial \alpha}\frac{\partial \alpha}{\partial t} = U\cos(\alpha)\dot{\alpha}, \tag{3.10}$$

but with the small angle assumption, $\cos(\alpha) \approx 1$, and Eq. 3.10 simplifies to

$$\dot{V}_{\perp} \approx U\dot{\alpha} \tag{3.11}$$

Figure 3.4 shows the time histories of Eq. 3.10 and Eq. 3.11 for the $\alpha = 0 - 20°$ and $\alpha = 0 - 40°$ cases at $k = 1$. The results of Eq. 3.10 are provided simply to show the relative effect of applying the small angle assumption. It is evident that the assumption, although wildly violated by the $\alpha = 0 - 40°$ case, only slightly alters the time history

of plate normal velocity. Theodorsen does use the small angle assumption, however, and for the present case (sinusoidal pitch) it results in a symmetric profile. Note that the acceleration term provided by Eq. 3.11 is equivalent to that given in the first term of Theodorsen's non-circulatory lift, Eq. 3.7. This force can be considered a *rotation-induced plate normal acceleration force.*

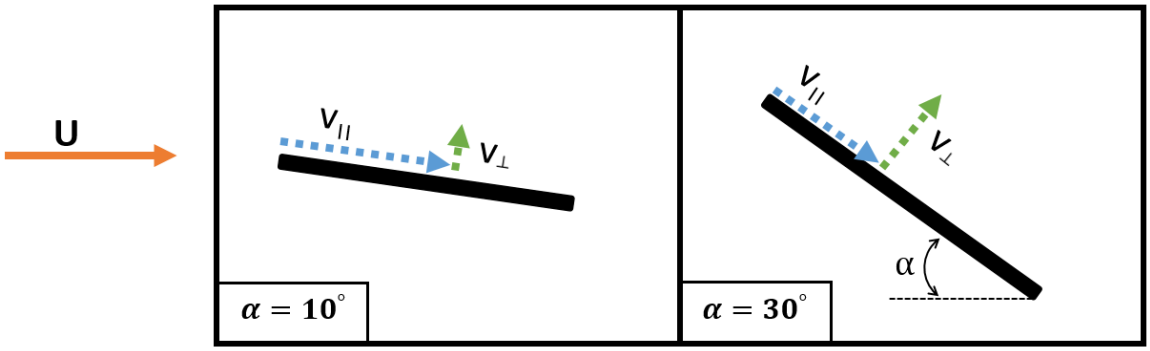

Figure 3.3: Plate tangential and normal velocities due to the free stream at two different angles of attack, illustrating the increase in plate normal force with an increase in angle of attack.

It is important to recognize that this acceleration term is *independent* of pitch axis location. Unlike the non-circulatory rotational acceleration force discussed in the previous section, Eq. 3.11 does not depend on pitch axis as it is simply an instantaneous change in the direction and magnitude of the plate normal velocity component, which also means that this effect is uniform along the chord. Recalling the non-circulatory force histories of Figure 3.2, Point B on each plot represents the point at which the force due to rotational acceleration is zero and lift is solely due to the pitch rate term. From the pressure distributions for the single-element pitch cases (Figure 3.2 a,e), symmetry about the mid-chord confirms that the plate-normal acceleration due to pitch rate is

uniform along the chord. Thus, it can be stated that the resultant force from this term acts at the mid-chord. To further investigate the nature of this force, observe the single-element force histories given in Figure 3.2(b, f). Although they differ in pitch axis location, by which the rotational acceleration term is significantly affected, the pitch rate term remains the same between the two cases.

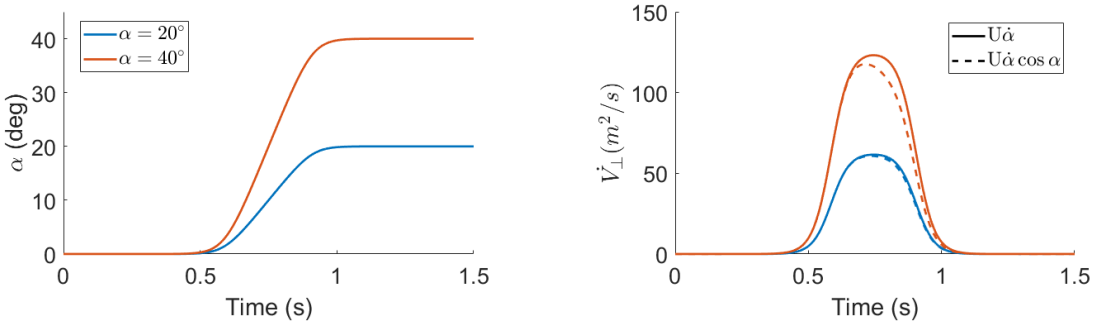

(a) Pitch kinematics

(b) Time derivative of plate-normal velocity component.

Figure 3.4: (a) Angle of attack history and (b) normal velocity component on a single-element pitching plate, illustrating the change in plate normal velocity due to pitch. It should be noted that this effect is independent of pivot axis location.

3.1.2 Circulatory Flow

Theodorsen derived the present formulation in consideration of a harmonically oscillating airfoil with a fully developed planar wake extending from the trailing edge to infinity. The present work concerns only a flap-and-hold motion of the trailing edge flap (as opposed to reciprocating flap motions), which does not produce an oscillating fully developed wake, especially in the time during and immediately following the transient

flap. Although there is yet much insight to be gained from understanding the effect wake vorticity has on the airfoil, that is not of immediate interest in the present study and we are going to ignore the wake in our own formulation. That said, it is still important to cover, although in a slightly abridged fashion, the underlying physics modeled in the circulatory lift term of Theodorsen's model. As with the non-circulatory material, a comprehensive derivation and discussion of Theodorsen's circulatory lift solution is provided in Appendix A.2.

The magnitude of bound circulation on the wing is determined by satisfying the Kutta condition, which states that circulation must be chosen such that the fluid velocity is finite at the sharp (trailing) edge. Leaving the mathematical derivation for the reader to examine in the Appendix, the final expression for *circulatory* lift in Theodorsen's model [61] is

$$L_C = -2\pi\rho U b\Big(U\alpha + b(\frac{1}{2} - a)\dot{\alpha} + \frac{T_{10}}{\pi}U\beta + b\frac{T_{11}}{2\pi}\dot{\beta}\Big)C, \tag{3.12}$$

where

$$T_{10} = \sqrt{1-c^2} + \cos^{-1} c \tag{3.13}$$

$$T_{11} = \cos^{-1} c\,(1-2c) + \sqrt{1-c^2}\,(2-c) \tag{3.14}$$

and C is the Theodorsen function,

$$C = \frac{\int_1^\infty \frac{x_0}{\sqrt{{x_0}^2-1}}\gamma(x_0)\mathrm{d}x_0}{\int_1^\infty \frac{\sqrt{x_0+1}}{\sqrt{x_0-1}}\gamma(x_0,t)\mathrm{d}x_0}. \tag{3.15}$$

As Bisplinghoff [62] comments, there are two ways researchers typically simplify the lift

expression when dealing with low-reduced-frequency unsteady motions. The most basic simplification is to assume that all aerodynamic loads can be calculated from steady-state formulas (i.e. $\frac{\partial}{\partial t}() = 0$), which for the present case means only those terms dependent on instantaneous angle of attack, α, resulting in

$$L \approx 2\pi\rho U b\,[U\alpha]. \tag{3.16}$$

The other common simplification, and the method employed in this work, is the "quasi steady-state" assumption, which neglects the effect of the wake vortices on the flow and on the airfoil. This is equivalent to setting $C = 1$, which technically signifies the reduced frequency of a harmonically oscillating airfoil approaching zero. This can be physically interpreted as a case where the wake is determined to have negligible influence on the wing. The validity and accuracy of this assumption for the present cases will be addressed in later sections.

Finally, combining the contributions from non-circulatory lift (Eq. 3.7) and circulatory lift (Eq. 3.12) we now have the full quasi steady Theodorsen model for aerodynamic lift on a wing in arbitrary motion:

$$\begin{aligned} L = &-\rho b^2(U\pi\dot{\alpha} - b\pi a\ddot{\alpha} - UT_4\dot{\beta} - bT_1\ddot{\beta}) \\ &+ 2\pi\rho U b(U\alpha + b(\frac{1}{2} - a)\dot{\alpha} + \frac{T_{10}}{\pi}U\beta + b\frac{T_{11}}{2\pi}\dot{\beta}) \end{aligned} \tag{3.17}$$

Circulatory Pitch Rate Force

It was previously stated that the *non-circulatory* force components arise by means of satisfying the no penetration boundary condition on the wing surface. That is a

Table 3.1: Breakdown of total lift production into its constituent forces according to Theodorsen's solution, Eq. 3.17.

Breakdown of Lift Contributions	
Added mass	$\rho b^2(b\pi a\ddot{\alpha} + bT_1\ddot{\beta})$
Rotation-induced plate normal acceleration	$-\rho b^2(U\pi\dot{\alpha} - UT_4\dot{\beta})$
Virtual camber	$2\pi\rho U b^2((\frac{1}{2} - a)\dot{\alpha} + \frac{T_{11}}{2\pi}\dot{\beta})$
Steady lift	$2\pi\rho U b(U\alpha + \frac{T_{10}}{\pi}U\beta)$
$T_1 = -\frac{1}{3}\sqrt{1-c^2}(2+c^2) + c\cos^{-1}c$	$T_4 = -\cos^{-1}c + c\sqrt{1-c^2}$
$T_{10} = \sqrt{1-c^2} + \cos^{-1}c$	$T_{11} = \cos^{-1}c\,(1-2c) + \sqrt{1-c^2}\,(2-c)$

verifiable physical boundary condition due to the fact that the fluid cannot physically pass through the wing itself. The *circulatory* terms, however, take their form due to the implementation of Kutta's hypothesis. In an effort to sidestep the mathematical result of infinite velocities at the trailing edge, Kutta's hypothesis suggests that there is smooth flow off the sharp trailing edge if there is no pressure discontinuity when passing rearward of the airfoil. The Kutta condition therefore enforces a finite velocity at the trailing edge ($x = 1$), leading to a unique solution for the bound circulation. This appears ostensibly to be a strong-arm method for removing a mathematical discontinuity, but in fact this result was originally observed in experiments on airfoils in steady flow at low angle of attack, and the analytical result matches experimental force data accurately within the confines of the original flow assumptions (i.e. steady, low angle of attack, thin airfoil).

Turning now specifically to the circulatory *pitch rate* components of lift ($\dot{\alpha}$ and $\dot{\beta}$ terms in the second term of Eq. 3.17), we find what is typically called the "virtual

camber" term. A pitch rate about an axis ab from the mid-chord produces a linear variation in normal perturbation velocity that results in a flow in which a fluid particle experiences an induced camber, as shown in Figure 3.5. The distribution of normal velocity along the chord is analogous to a shape change in the airfoil. A flat plate pitching about point ab at rotation rate $\dot{\alpha}$ generates a normal perturbation velocity, $w_{\dot{\alpha}}$, of the form

$$w_{\dot{\alpha}} = \dot{\alpha}(x - ab). \tag{3.18}$$

This pitch rate-induced velocity can be considered the addition of an effective camber, $z_{eff}(x)$, of the form

$$w_{\dot{\alpha}} = U\frac{\partial z_{eff}}{\partial x}. \tag{3.19}$$

Substituting Eq. 3.18 into Eq. 3.19 and integrating with respect to x,

$$z_{eff}(x) = \int \frac{w_{\dot{\alpha}}}{U}\mathrm{d}x \tag{3.20}$$

one can obtain the effective wing camber due to a pitch rate $\dot{\alpha}$ as follows

$$z_{eff}(x) = \dot{\alpha}x(\frac{x}{2} - ab). \tag{3.21}$$

Contrary to the non-circulatory pitch rate term (Eq. 3.7), this term *does* depend on pitch axis location.

Figure 3.6 provides time histories of the individual lift components in Eq. 3.17, illustrating their relative magnitudes as the pitch rate varies from a fast motion ($k = 1$) to a slower motion ($k = 0.16$). Much like the non-circulatory pitch rate term, virtual camber (dashed blue line in Figure 3.6) follows the shape of $\dot{\alpha}$ but is consistently of

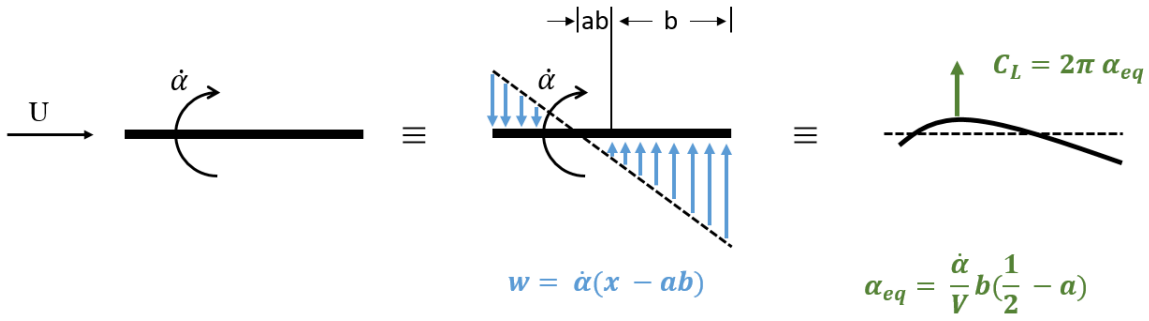

Figure 3.5: Virtual camber effect caused by wing pitching about pivot axis *ab*. Recreated from Leishman [63].

much larger magnitude than its non-circulatory counterpart. This relative magnitude will differ, however, for variable pitch axis locations.

Circulatory Steady Force

The final term in Theodorsen's lift solution is the *steady* circulatory lift force. Only dependent on instantaneous angle of attack, steady lift is, mathematically, a result of enforcing the Kutta condition and solving for a bound circulation about the wing that satisfies the geometric boundary conditions (no penetration, attached flow, finite velocity at trailing edge). In the limit of all time-dependent kinematics approaching zero (i.e. $\frac{\partial}{\partial t}() = 0$) we are left with the steady state lift of Eq. 3.16. Physically, to maintain attached flow the fluid must accelerate around the inclined leading edge over the top surface (termed the "suction side") leading to a lower pressure than what is experienced on the bottom surface (the "pressure side"). The pressure imbalance leads to a resulting steady lift force.

Now that we have an understanding of each term's origin and physical significance,

we turn once again to Figure 3.6 to observe the relative magnitude of each term in Theodorsen's solution for several reduced frequencies. It is clear from the figure that non-circulatory acceleration force (solid black line) is very sensitive to reduced frequency. Its magnitude relative to the other terms should be acknowledged when understanding the driving forces in a particular set of kinematics, as it could either be the main driving force ($k = 0.35$) or a small component of force ($k = 0.058$). Notice the steady state lift force remains unchanged for every reduced frequency. Thus, it is clear that when all of the rate terms approach zero for very slow motions, the only remaining non-zero lift component will be the steady circulatory lift.

3.1.3 Concluding Remarks on Theodorsen

Section 3.1 explored the application of Theodorsen's solution to the current problem of a pitch-and-hold airfoil-aileron system, addressing the model's utility as well as its limitations. Each constituent term in Theodorsen's final lift equation was explained in detail and categorized as either a non-circulatory or circulatory contribution. It was shown that there is a coupling between the fore and aft elements when the flap deflects, due to the nature of the incompressible and inviscid flow assumptions. As will be shown at the end of Chapter 5, for a large trailing edge flap deflecting at high pitch rates to angles beyond the range of the small angle assumption, Theodorsen's model largely over-predicts lift production compared to experimental results. The following section seeks to develop a modified version of Theodorsen's model to more appropriately predict physical lift production.

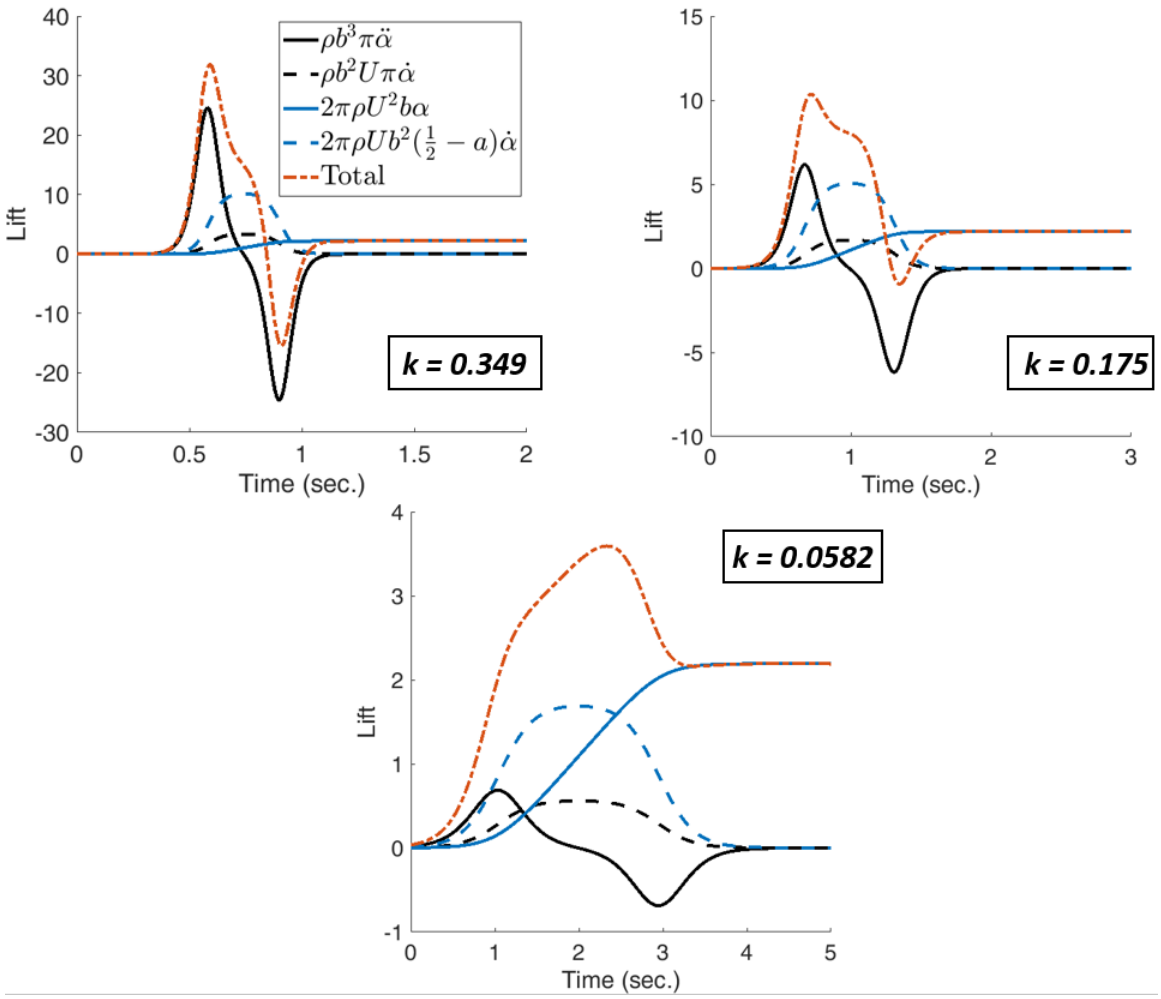

Figure 3.6: Lift histories for several reduced frequencies ($k = 0.35$, $k = 0.18$, and $k = 0.058$) for a pitching single-element flat plate from $\alpha = 0 - 20°$ to illustrate the contributions from the various non-circulatory and circulatory components of lift. Notice the various changes in magnitude of each rate-dependent term as the flap rates vary from fast to slow pitching.

3.2 Modified Aerodynamic Model

Among the discussion of Theodorsen's solution and its physical interpretation, Section 3.1 showed that, theoretically, there is a non-circulatory force imposed on the

stationary fore element when a dynamically deflecting trailing edge flap is deployed. Theodorsen's theory was derived from potential flow theory under the assumptions of inviscid and fully attached flow, which might not be entirely accurate in the case of a real world physical flow. As will be shown in the experimental results of Chapter 5, although the flow is largely attached during the flap transient, there also exists development of a boundary layer and small scale structures over the leading edge element. Such developments may cause the flow to deviate from strictly adhering to potential flow assumptions and alter the accuracy of Theodorsen's prediction. Thus, a modified model is presented here to provide an analytical solution for lift on a dynamic airfoil-aileron system that does not account for the synergistic effect the wing elements have on each other in the ideal flow case. This model aims to capture the lift-producing mechanisms of each separate wing element and assess, based on comparisons with experiment, at what point the aerodynamic coupling between the connected bodies becomes significant.

In the present model description, each wing element is treated as its own isolated wing with no knowledge of a connected body to itself. Thus, contrary to Theodorsen, this model will contain zero non-circulatory forcing on the leading edge element, because it is stationary throughout the motion.

Figure 3.7 illustrates the decomposition of the hinged wing into two isolated wing elements. The fore element (shown in green) is stationary at all times at constant angle of attack $\dot{\alpha} = 0$. One might hypothesize, therefore, that the total lift due to attached flow on the fore element in the present geometry would be zero. Had the stationary element been at a nonzero angle of attack, however, its lift contribution would be the steady state circulatory lift from Theodorsen's solution in the previous section as given

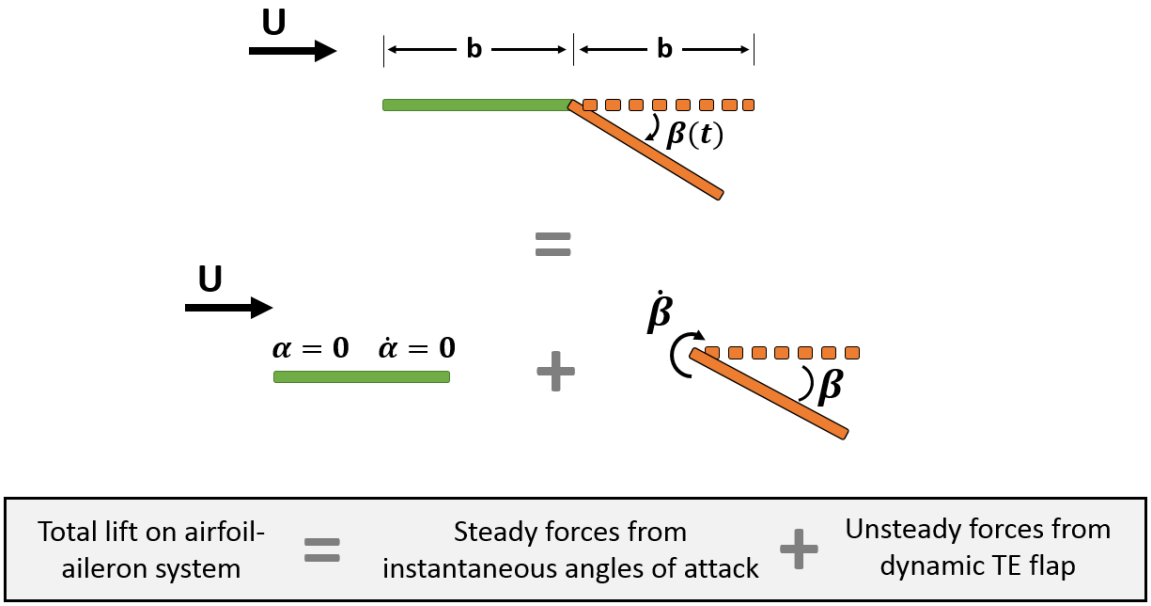

Figure 3.7: Illustration of lift contributions as expressed in the modified aerodynamic model.

by

$$L_{C,fore} = 2\pi\rho U\frac{b}{2}(U\alpha), \tag{3.22}$$

where b, the semi-chord of the entire airfoil-aileron system, is the whole chord length of each wing component. Thus, the semi-chord for each of the isolated wing elements is $b/2$. Applying Theodorsen's model to the dynamically pitching rear element results in non-circulatory and circulatory lift given by

$$L_{NC,flap} = -\frac{\rho\pi b^2}{4}(U\dot{\beta} - \frac{b}{2}a\ddot{\beta}) \tag{3.23}$$

$$L_{C,flap} = -2\pi\rho U\frac{b}{2}(U\beta + \frac{b}{2}(\frac{1}{2} - a)\dot{\beta}), \tag{3.24}$$

where $a = -1$ because the wing is pitching about its leading edge. Total lift on the

aileron-airfoil system can be computed by adding the contributions from Eq. 3.22 - 3.24, resulting in

$$L_{total} = \frac{\rho\pi b^2}{4}(U\dot{\beta} + \frac{b}{2}\ddot{\beta}) + 2\pi\rho U\frac{b}{2}(U\beta + \frac{3b}{4}\dot{\beta})$$

$$L_{total} = \pi\rho b[\frac{b^2}{8}\ddot{\beta} + Ub\dot{\beta} + U^2\beta]. \tag{3.25}$$

We are now left with a very simple model for lift production that only requires *a priori* knowledge of the wing kinematics. Although similar to Theodorsen's solution, this modified lift model differentiates itself by ignoring the effect of each element on the other. In contrast, recall from Figure 3.2 that deflecting the trailing edge flap in Theodorsen's formulation induces a non-circulatory load on the stationary fore element. The idea behind the modified model of Eq. 3.25 is to decouple the predicted lift on each element with the hope of a) gaining a more complete understanding of the physical mechanisms responsible for lift production and b) creating a robust model that more closely predicts lift even when deflection angles exceed those approximated as "small angles."

3.3 Panel Method

Sections 3.1 and 3.2 covered analytical solutions for calculating aerodynamic lift on pitching airfoils. These solutions made some major geometric simplifications, i.e. wing was approximated as a flat, zero-thickness surface and boundary conditions were applied at that surface. However, for more complicated wing geometries and kinematics, where

those geometric assumptions become increasingly unrealistic, numerical solvers are commonly introduced to loosen the geometric restrictions on the wing and wake, applying boundary conditions on the true wing surface and allowing the wake to convect appropriately throughout the spatial domain based on instantaneous local velocities. The numerical solver presented here, and what is commonly used in aerodynamics research due to its practicality and low computational costs [84] [85], is an **unsteady panel method**. Discretizing the wing and wake lends the problem to be solved numerically, which avoids the elaborate mathematical exercise required of the wake influence integral discussed in Appendix A.2. The unsteady discrete vortex panel method, as detailed in Katz and Plotkin [86] and described here in Appendix B, provides a model that does not restrict the geometry or wake structure of the problem. The *numerical* solution from the panel method will be compared to the *analytical* result of Theodorsen to assess the utility and applicability of both methods and to experimental results to compare force production on each of the discrete wing elements.

A panel method, among other descriptions, is a type of *collocation method*, which discretizes a finite-dimensional space to numerically solve ODEs, PDEs, and integral equations by means of satisfying the governing equations at selected points in the domain, called *collocation points*. In the present work, the boundary condition of zero normal flow on the solid surface of the airfoil is solved and satisfied using a discrete vortex panel method at such collocation points, illustrated in Figure 3.8.

We discussed in Section 3.1 an analytical approach to solving the vorticity distribution along the airfoil and in the wake. A panel method, as outlined here, presents a numerical approach to solving the same problem. The utility of a discrete vortex

method lies in its use of singular vortices in place of a continuous vorticity distribution $\gamma(x)$. This is called a *lumped vortex method*, and it represents the chord-wise distribution of vorticity along a panel as one vortex, $\Gamma = \int_0^c \gamma(x)\mathrm{d}x$, shown as a "panel vortex" in Figure 3.8. In lieu of requiring an exact analytical solution, this method allows us to numerically solve a system of equations that satisfies the appropriate boundary conditions by calculating the induced velocities from each of these discrete vortices. For further description of the implementation process, the reader is directed to Appendix B.

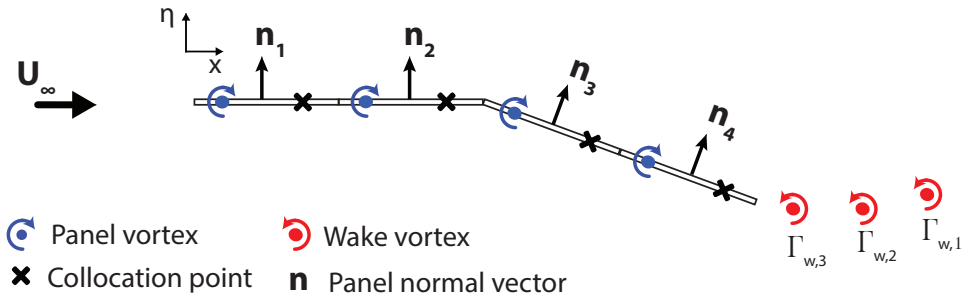

Figure 3.8: Schematic of the panel method implementation for flow about an airfoil with a trailing edge flap. Panel vortices are placed at the quarter-chord and collocation points are placed at the three-quarter chord of each panel.

Using the unsteady Bernoulli equation, a chord-wise pressure distribution can be computed as

$$\Delta p_j = \rho(U_\infty \frac{\Gamma_j}{\Delta l_j} + \frac{\partial}{\partial t}\sum_{k=1}^{j}\Gamma_k), \tag{3.26}$$

where Γ_j is the discrete vortex strength at the j-th panel of length Δl_j. Notice that the unsteady term in the pressure calculation is simply the time rate of change of the bound

circulation on the wing, whereas the first term is essentially the Kutta-Joukowski form of steady circulatory lift.

Finally, total lift is calculated by integrating pressure along the chord:

$$L = \sum_{j=1}^{N} \Delta p_j \Delta l_j \cos \alpha_j \tag{3.27}$$

where α_j is the incidence angle of the j-th panel. The current work will present lift in the non-dimensional form of lift coefficient, which is normalized by the freestream dynamic pressure:

$$C_L = \frac{L}{\frac{1}{2}\rho {U_\infty}^2 c} \tag{3.28}$$

3.4 Chapter Summary

Several modeling efforts have been implemented in this work to complement the experimental results and elucidate some of the flow physics and lift producing mechanisms during rapid maneuvers. This chapter described the mathematical details of those modeling efforts as well as the physical mechanisms they represent. Section 3.1 covered the derivation of Theodorsen's solution for analytically solving aerodynamic lift on a pitching airfoil-aileron system. Each of the non-circulatory and circulatory components were discussed in terms of the mathematical result and physical meaning. The modified model of Section 3.2 has been developed to decouple the interaction between the fore and aft elements. By comparison with Theodorsen's solution, we can determine the extent

to which real flows, as demonstrated through experiments, behave within (or deviate from) the ideal assumptions made by Theodorsen. Finally, an unsteady panel method is introduced to remove geometric and wake shape restrictions, providing a low computational cost numerical solution to be compared with the theoretical result of Theodorsen as well as experimental results.

Chapter 4

Experimental Results: Surging and Pitching Single-Element Flat Plates

The experimental results in this chapter aim to expand the extant literature on rapidly maneuvering wings [21–25] by providing a comprehensive parameter sweep of surge and pitch motions characteristic of low Reynolds number flight. The goal is to impart new insights into the fundamental physical mechanisms responsible for force production and flow field development from highly unsteady wing kinematics. Partially due to the complex flow physics taking place over the wing, where nearly every assumption in classical aerodynamic modeling is wildly violated (e.g. attached, inviscid flow; Kutta condition at trailing edge) there lacks a low order modeling technique that accurately predicts unsteady forces and moments on fully separated, rapidly maneuvering wings. In order to arrive at such a model it is imperative to first grasp an understanding of the underlying flow physics and force-generating mechanisms. This chapter experimentally examines the unsteady aerodynamics and flow field development of single-element wings undergoing rectilinear motions in pitch and surge at $Re = 20,000$ and aims to ascertain

the physical mechanisms responsible for lift production.

The single-element surge campaign studies the problem of a flat plate at fixed incidence starting from rest over several angles of attack ($5° \leq \alpha \leq 45°$) and acceleration rates ($0.125 \leq s_a/c \leq 6$). The pitch study addresses the problem of a wing at zero angle of attack in constant free stream pitching up to 45°, focusing on two pitch rates representative of a "fast" motion ($k = 0.39$) and a "slow" motion ($k = 0.065$).

4.1 Streamwise Surge: Force and Moment Histories

In this section, we compare particle image velocimetry and qualitative flow visualization with direct measurement of lift and pitching moment for a range of smoothed rectilinear acceleration profiles, where the acceleration (apart from endpoint smoothing) is constant with wall-clock time for early time and then goes to zero. The goal is to segregate circulatory from noncirculatory contributions by tracking leading edge and trailing edge vortex trajectories, and to attempt to collapse lift coefficient variations for a range of acceleration rates. The philosophical goal is to distill the flow physics to their simplest form towards a closed-form or reduced-order model purely derived from kinematics.

4.1.1 Variations in Angle of Attack

The effect of angle of attack on force coefficients was investigated to ascertain the existence of high lift on translating wings, pinpoint the range of incidence angles over which vortex lift becomes important, and evaluate the time scales over which it persists.

Time histories of lift and pitching moment were measured and normalized with respect to the wing's terminal velocity.

The flat plate wing was set at a fixed angle of attack and accelerated to its terminal velocity over 1 chord-length of travel. Angles of attack ranged from 5 to 45 degrees. The resulting lift force histories, obtained at AFRL, are given in Figure 4.1. At low angles of attack, $\alpha = 5°$-$10°$, the lift coefficient curves agree well with Wagner's prediction (shown in the figure as Jones' approximation [87]) and experiments from Beckwith and Babinsky [88]. At these low angles of attack, the flow appears largely attached and adheres to the trailing edge Kutta condition (see Figure 4.2), as is assumed in Wagner's analysis. Bound circulation gradually builds, monotonically increasing lift until it eventually converges to its final steady state lift value. In an attached flow, no leading edge vortex forms and thus there is no vortex lift.

At higher angles of attack ($\alpha \geq 15°$), however, the flow separates at the leading edge, a leading edge vortex forms on the suction side of the wing (Figures 4.2-4.3), and the lift coefficient experiences a significant increase (Figure 4.1). The favorable impact on lift from a leading edge vortex has been demonstrated by Lind [89] and Panah [31] using chordwise pressure taps on harmonically oscillating airfoils. Once the flow becomes largely separated as in the present case, use of classical aerodynamic theory becomes less valid as the assumptions of attached, inviscid flow and trailing edge Kutta condition less accurately depict the flow. Although the assumptions held within the classical models are quite stringent, their use to help solve real world problems is rather widespread, likely because there does not presently exist a more accurate analytical model that more reasonably models real flow conditions.

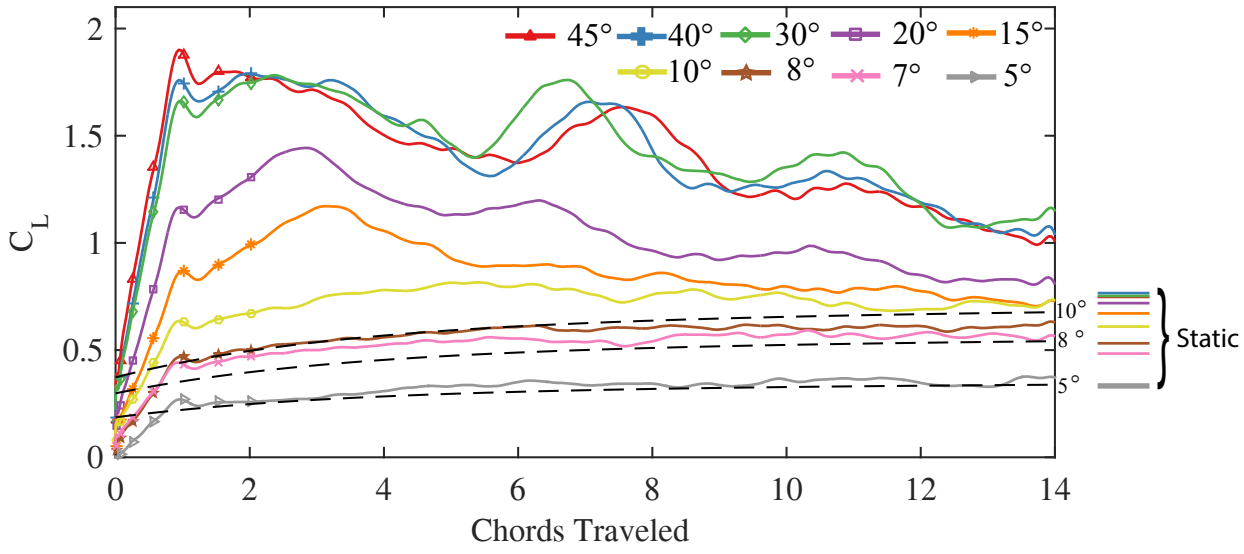

Figure 4.1: Unsteady force histories for $5° \leq \alpha \leq 45°$ and $s_a/c = 1$, as well as each angle's corresponding static lift value.

With regards to sources of lift production, several noteworthy phenomena occur over the course of the wing translation. As the wing accelerates from rest, lift increases steeply until reaching a maximum at exactly 1 chord-length of travel (i.e., when the wing stops accelerating). While the wing is accelerating, both inertial and circulatory effects contribute to lift production, i.e. the total lift measured is the sum of that due to added mass as well as the growth of circulation around the wing and/or that of the leading edge vortex. Past this point, the leading edge vortex that began forming at the start of the wing motion continues to grow, but the added mass force (due to wing acceleration) goes to zero. The continued growth leads to a local maximum around s/c = 2-3. As the wing continues to translate, lift decreases as the LEV becomes less coherent and convects down the wing towards the trailing edge, and the trailing edge shear layer curls

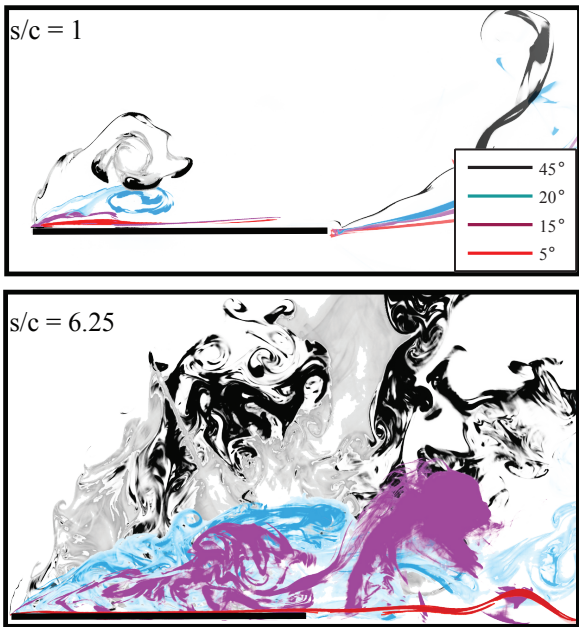

Figure 4.2: Flow visualization at (top) $s/c = 1$ and (bottom) $s/c = 6.25$ for for [$s_a/c = 1$, $\alpha = 5°$, $15°$, $20°$, and $45°$]. Images have been rotated by their corresponding incidence angles.

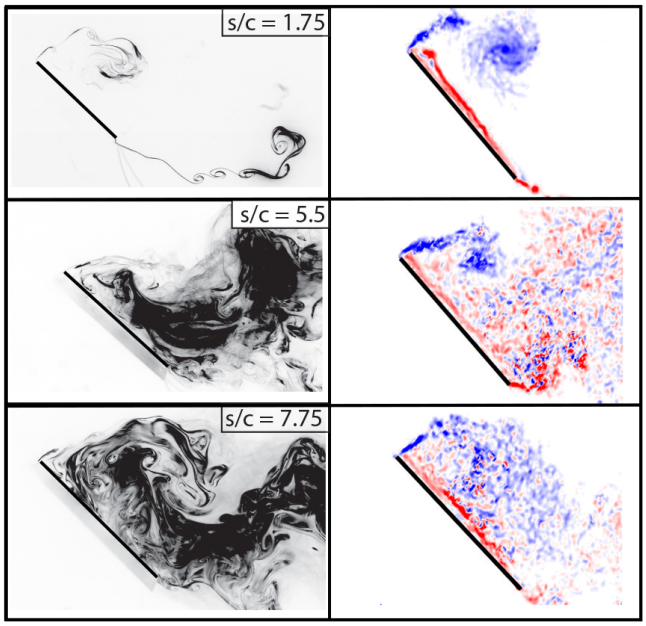

Figure 4.3: Dye flow visualization (left) and PIV (right) showing the flowfield at for $s_a/c = 1$, $\alpha = 45°$ at three different values of s/c.

around and into the wake of the wing (see Figure 4.3, $s/c = 5.5$). At this stage, flow over the upper surface of the wing is arguably more a region of recirculating flow than a coherent vortex. Note that although the described flowfield is clearly shown in the PIV image in Figure 4.3, the corresponding dye visualization does not at first glance provide a similar result. Remember, dye is only injected at the 3/4 span, aligned with a thin laser sheet as the interrogation plane. As long as the flow is sufficiently two-dimensional (as is the case early in the wing motion), laser-fluorescent dye visualization provides an accurate representation of the flow structures, making it an excellent heuristic tool for PIV. However, upon the onset of three-dimensionality (e.g. spanwise flow), dye is occasionally pulled out of the interrogation plane and is not present in the resulting image. Thus, the presence (or absence) of dye in the flowfield images indicate possible locations of spanwise flow.

At high angles of attack, the flow is largely separated over the entire upper surface of the wing (see Figure 4.2), leading to unsteady flow structures shedding and reforming throughout the wing motion. Following the local lift minima around $s/c = 5.5$ for the high angle of attack cases, clockwise circulation about the leading edge regains dominance over the wing surface (see Figure 4.3, $s/c = 7.75$), resulting in a second lift peak. These periodic flowfield oscillations continue while the force histories gradually decline towards their respective steady state values. It appears that once the high angle of attack cases reach peak lift at the end of their motion transient ($s/c = 1$), there exists a similar relaxation shape among the cases, barring humps due to LEV formation. This downward relaxation to steady state for high angle of attack cases ($\alpha \geq 20°$) is due to the gradual flow development toward their steady fully separated condition. The time

scale over which this occurs appears to mirror that of the lower angle of attack cases ($\alpha \leq 15°$) that gradually *increase* in lift toward their steady condition due to circulation growth towards their final attached flow state, as predicted by Wagner.

It is clear from the results presented here that local flow structures such as leading edge vortices caused by leading edge flow separation favorably augment lift by providing a low pressure region on the suction surface. However, vortex-induced lift enhancement comes at the cost of simultaneously increasing drag coefficient. Figure 4.4a provides drag histories for the angle of attack study and shows a relatively linear drag increase for $5° \leq \alpha \leq 20°$ with increasing incidence angle, yet in the fully stalled cases ($\alpha \geq 30°$) there is a large non-linear jump in drag coefficient. Drag increases monotonically with incidence angle as the plate-normal force vector tilts more toward the horizontal drag direction. Lift coefficient (Figure 4.1), however, reaches a saturation point around $\alpha = 30°$, after which an increase in angle of attack does not result in an increase in lift. At high angles where the flow is fully stalled (i.e. full separation at the leading edge), the resulting force vector points in the plate-normal direction. Figure 4.4b shows the lift-to-drag ratio (C_L/C_D) for the angle of attack study and confirms the transition to plate-normal force, as easily evidenced by $C_L/C_D = 1$ for $\alpha = 45°$. Insect flight, an observable example of accelerating wings at high incidence, typically operate at a lift-to-drag ratio around unity [90] whereas avian fliers fly around $C_L/C_D \approx 4 - 10$ [91].

Static force measurements were acquired using a stationary wing at fixed angle of attack with the tunnel operating at a speed corresponding to $Re = 20{,}000$. Measurements were obtained for $-45° \leq \alpha \leq 45°$ in increments of 2° as shown in Figure 4.5a. Force measurements at each angle of attack were averaged over 26 chords traveled before

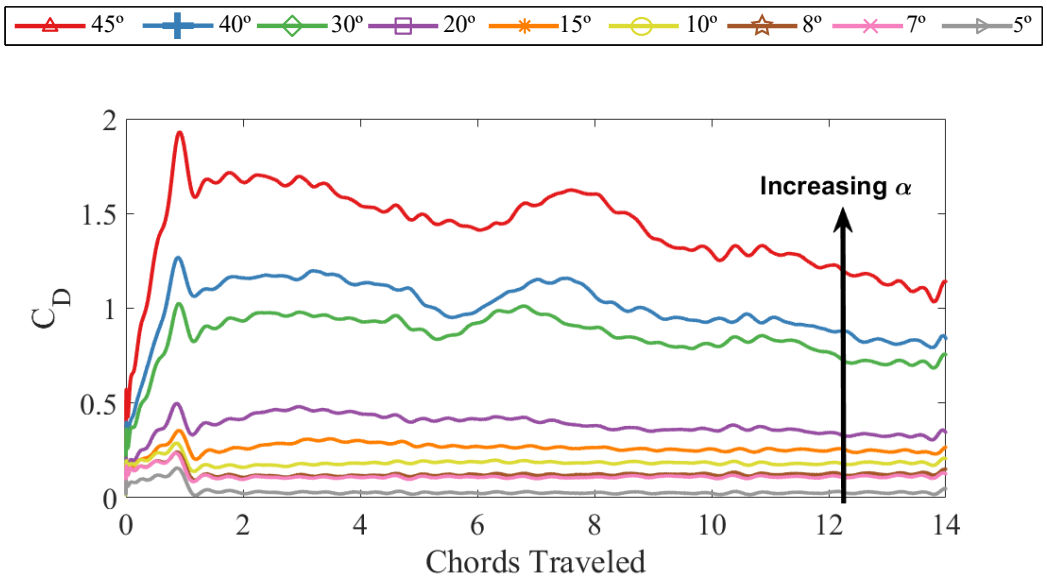

(a) Drag coefficient

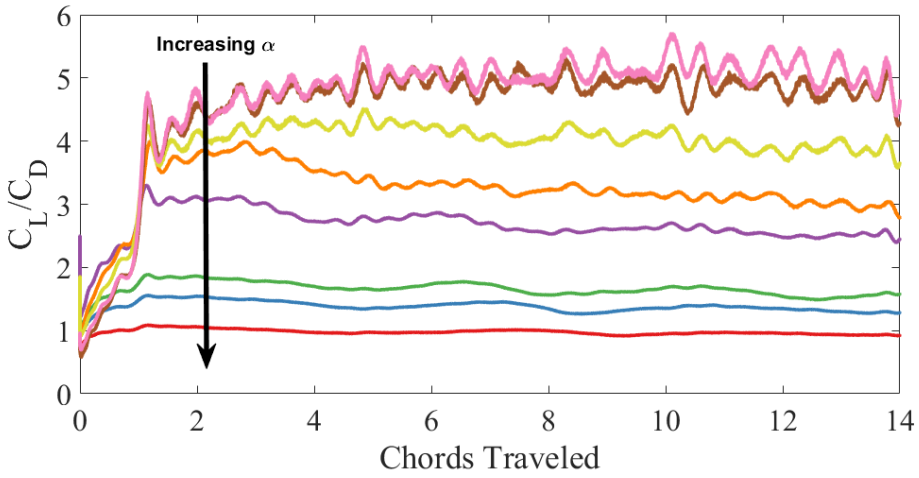

(b) Lift-to-Drag ratio

Figure 4.4: Plots of drag coefficient (C_D) and lift-to-drag ratio (C_L/C_D) for surging wings with acceleration $s_a/c = 1$ showing the tradeoff between increased lift (see Figure 4.1) and drag.

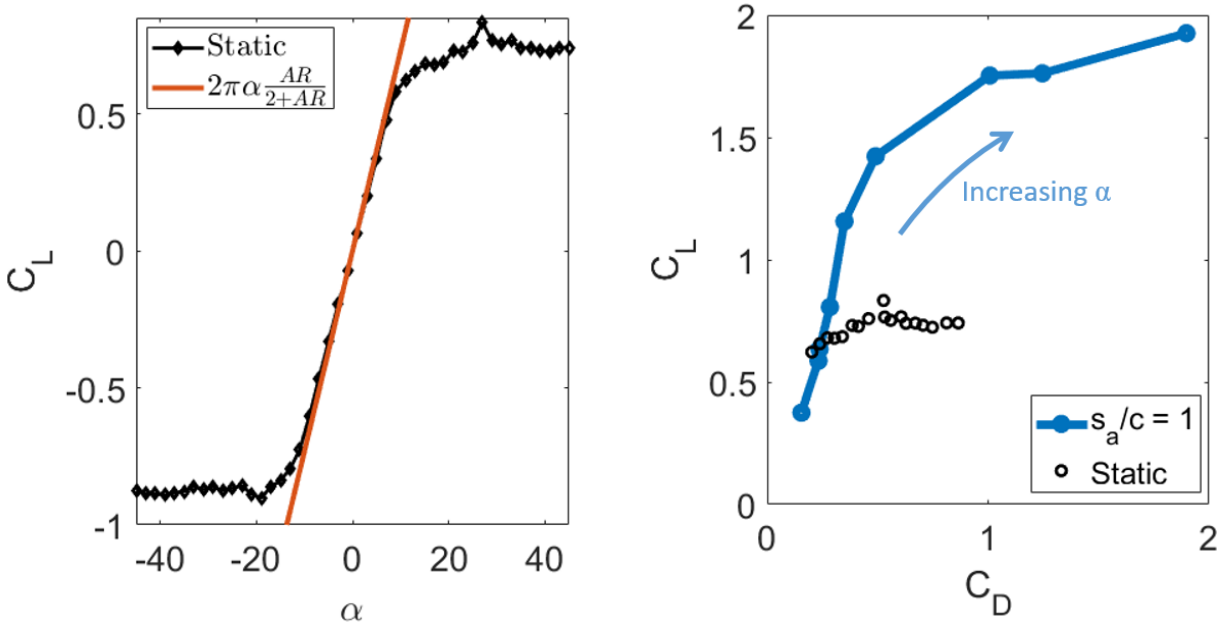

(a) (b)

Figure 4.5: (a) Static lift curve for flat plate with theoretical prediction adjusted for aspect ratio effects. (b) Drag polar of maximum lift coefficient for $s_a/c = 1$ surge and static measurements.

slowly incrementing by 2° to the next angle. The measured static lift for $\alpha = \pm 10°$ was in good agreement with Prandtl's lifting line theory, $C_L = 2\pi\alpha\frac{AR}{AR+2}$. Since lifting line theory only accounts for bound circulation, it makes sense that there is good agreement for cases in which the flow is attached and there is little to no leading edge vortex formation. This is also the region in which Wagner's effect matched well with the unsteady lift after long convective time in Figure 4.1. As a result, we can now compare the dynamic and static drag polars for the surging wing angle of attack study. Figure 4.5b shows the drag polar for both the static case and at the point of maximum lift achieved by each $s_a/c = 1$ case. The static polar is in agreement with flate plate results from Wang et al. [92]. From the dynamic drag polar it is clear that around $\alpha = 20°$ any further increase in angle of attack leads to a much higher drag penalty with diminishing gains in lift coefficient. Since high angle of attack cases experience fully separated flow and a resultant plate-normal force vector, by inclining the plate further it essentially turns the force vector more in the drag direction.

The purpose of extending the travel distance out to many chord-lengths was to assess the short-term and long-term effects of transient disturbances, e.g. wing acceleration and gusts, on force coefficients. Comparing the lift produced at the end of the 14 chord-length surge motion to that of its corresponding steady state value provides an assessment of convergence. Although the unsteady lift forces in Figure 4.1 appear to be converging in the direction of the static measurements, Figure 4.1 shows that at $s/c = 14$ the unsteady forces are still 20-50% larger than static values for $\alpha > 20°$. For cases with largely separated flow ($\alpha > 15°$), the effect of a transient disturbance has a lasting effect on force coefficients. Low angle of attack cases experience less of a long

term effect from the transient disturbance, as they converge more closely to their steady values at the end of the 14 chords.

4.1.2 Variations in Acceleration

The discussion of variations in angle of attack addressed the concepts of circulation growth and formation and convection of leading edge vortices. This study, too, will address those concepts, but now the area of interest lies within the startup transient and the relationship between acceleration-dependent (non-circulatory) forces and circulatory forces. To gain insight into the effect of transient disturbances on the flowfield and force histories, experiments were run at fixed angle of attack of $\alpha = 45°$ with widely varying acceleration profiles.

Figure 4.6a shows the time history of lift coefficient for a wing at angle of attack $\alpha = 45°$ and acceleration distances $s_a/c = \{0.125, 0.25, 0.5, 1, 2, 3, 4, 5, 6\}$. Focusing on the acceleration phase, the measured C_L for each case appears to increase proportionally to (or maintain the same shape as) its prescribed motion profile (refer to Figure 2.5), illustrating a partial dependence on acceleration profile for lift production. It was mentioned in the previous section that although these aggressive maneuvers are capable of producing large lift spikes, it comes at the penalty of increased drag. This acceleration study addresses a wing at $\alpha = 45°$, where the flow is fully separated and the resultant force is plate-normal. Figure 4.4 showed that the $s_a/c = 1$ case has a constant lift-to-drag ratio of $C_L/C_D = 1$, but Figure 4.7 shows that is the case at long times

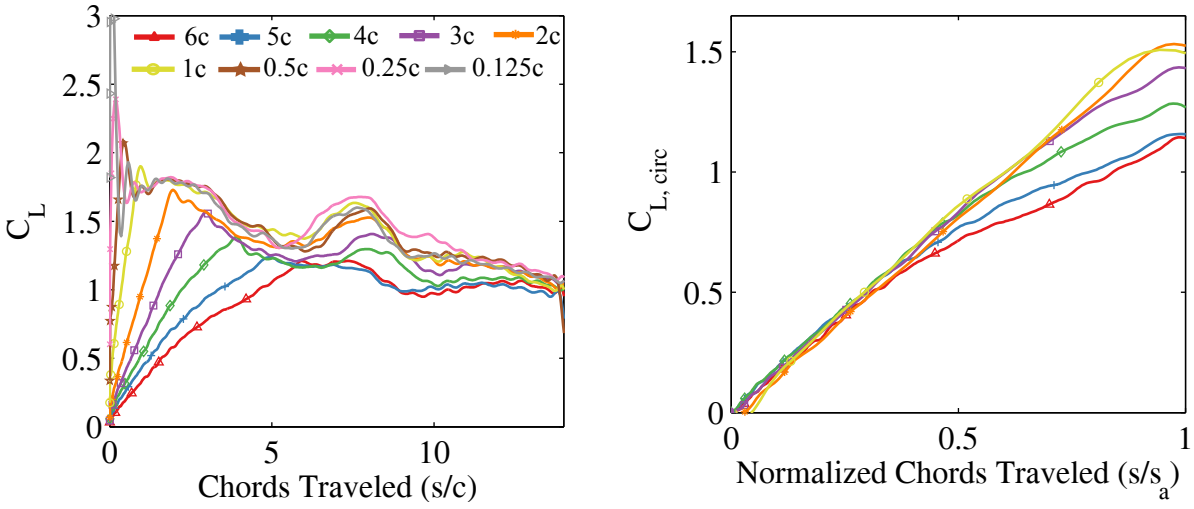

(a) (b)

Figure 4.6: Acceleration study at $\alpha = 45°$ for $0.125 \leq s_a/c \leq 6$. (a) Lift coefficient histories. (b) Circulatory component of lift history during each acceleration phase. Convective time, s/c, is scaled by acceleration distance, s_a/c.

for any acceleration rate. With the exception of minor differences due to varying LEV strengths for the different acceleration profiles, the lift-to-drag ratio for a surging plate accelerating from rest is independent of acceleration rate.

To further understand the physical sources of lift during the acceleration phase, force measurements will be broken down into two components: circulatory and non-circulatory. When a body accelerates through a fluid, it experiences an inertial force often referred to as an "added-mass" effect. This non-circulatory force can be thought of as the reaction force by the mass of the fluid being accelerated by the wing. Pitt Ford [68] provides a complex potential analysis for an accelerating rigid flat plate in pure translation and derives the lift coefficient contribution from added-mass as

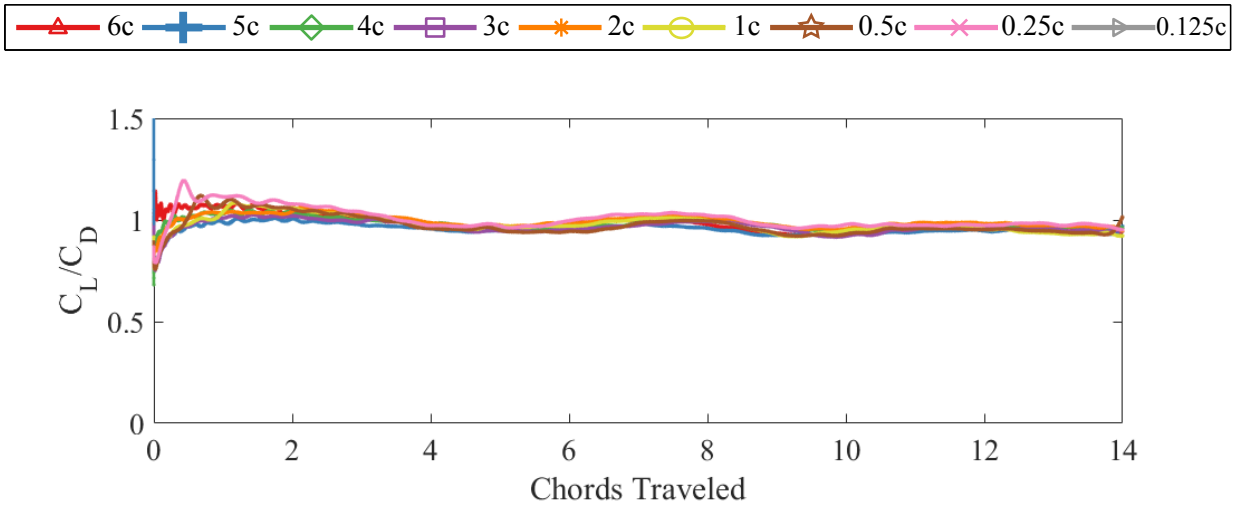

Figure 4.7: Lift-to-drag ratio for acceleration study at $\alpha = 45°$

$$C_L = \frac{\pi}{4}\frac{(\frac{dU}{dt}c)}{U^2}\sin(2\alpha) \tag{4.1}$$

where α is the plate's angle of incidence and U is the plate's instantaneous velocity. For the case of constant acceleration, this can be simplified to

$$C_L = \frac{\pi c}{8a}\sin(2\alpha) \tag{4.2}$$

where a is the number of chord-lengths traveled during acceleration. From Eq. 4.2, it is evident that the effect of added mass increases with angle of attack and with decreasing acceleration distance (i.e. faster acceleration rate). When the wing ceases acceleration, however, the added-mass term goes to zero. The remaining "circulatory" lift may consist of contributions from both bound circulation and leading edge vortices. However, Pitt Ford [68] concluded that at early time in the trajectory of a flat plate at large angle of attack surging from rest, the bound circulation is negligibly small and, therefore, the lift must be caused only by external vortices and non-circulatory effects. Thus, the focus on physical sources of lift for the surging plate will remain with the non-circulatory added mass term and the formation of leading and trailing edge vortices as the flow field develops.

Focusing now solely on the acceleration phase, Figure 4.6b suggests a rescaling of the x-axis of Figure 4.6a by each respective acceleration distance, s_a/c, to collapse the lift curves during their acceleration transients. Due to rig vibrations in cases where $s_a/c < 1$, accelerations faster than $s_a/c = 1$ have been omitted from the figure. Applying the new scaling, each acceleration phase occurs within $0 \leq s/s_a \leq 1$. Additionally, the added

mass term from Eq. 4.2 is subtracted from the measured lift to isolate the growth of only the circulatory force component. Understand that this "circulatory force", $C_{L,circ}$, is simply theoretical added mass subtracted from measured lift, i.e. $C_{L,circ} = C_{L,meas.} - C_{L,noncirc}$, and thus may contain lift contributions from the classical understanding of circulatory lift in addition to that from any auxiliary lift-augmenting flow structures, such as leading edge vortices. Figure 4.6b shows that the circulatory lift curves collapse nicely when $s/s_a \leq 0.4$, indicating a region where circulatory lift is independent of acceleration profile. After this collapsed region, the curves diverge and peak at $s/s_a = 1$. This result suggests that a main factor corresponding to the difference in lift production between the cases (at least during the acceleration phase) is an increased circulatory force component after $s/s_a \leq 0.4$.

Once the wing ceases acceleration, the added mass contribution goes away, leaving only circulatory forces responsible for lift production. (The minor oscillations in the beginning of the faster motions are due to physical vibrations of the rig.) Following the peak at the end of acceleration, all curves show a decrease in lift, reaching a minimum around $s/c = 5.5-6$, except for the $s_a/c = 5$ and 6 cases, which reach minimums around $s/c = 9.5 - 10$. For $s_a/c \leq 4$, the lift once again increases to a second local maximum around $s/c = 7.5-8$. After the second lift peak, all acceleration cases gradually decrease in lift until the end of the motion. The motion ceases at $s/c = 14$ due to the physical limitations of the tunnel.

Looking further into the dynamics and force contribution of the leading edge vortex, the moment coefficient was also examined. Figure 4.8 shows the pitching moment about the mid-chord for the same range of acceleration distances. Dye flow and PIV im-

ages in Figure 4.8 correspond to the local maxima and minima of the moment coefficient. Since all acceleration profiles with considerable lift oscillations appear to have the same trend, flowfield images are given only for $s_a/c = 1$. Positive vorticity, shown in blue, can be attributed to the leading edge vortex and clockwise rotation from the leading edge shear layer. Negative vorticity, shown in red, typically manifests from the trailing edge and contributes counter-clockwise vorticity to the flow field. Figure 4.8 conveys how the formation, shedding, and reformation of the leading edge vortex shifts the location of the dominant low pressure region chordwise along the wing. Consequently, this moves the location of the center of pressure, affecting the moment coefficient. A similar effect from the convecting leading edge vortex was noted in our discussion of lift coefficient. Figure 4.8 also provides lift coefficient for the $s_a/c = 1$ case to show the similarity in trends.

The mid-chord pitching moment reaches a maximum around $1c$, when the wing ceases acceleration and the leading edge vortex is strong, coherent, and attached to the leading edge of the wing. The clockwise circulation from this LEV is located forward of the mid-chord (observed in both dye flow and vorticity in Figure 4.8), thus producing a clockwise pitching moment (plotted as positive). This maximum, however, is short-lived. The LEV subsequently convects off the wing surface and downstream, during which counter-clockwise circulation from the trailing edge appears and interacts with the leading edge vortex. This effect is clearly illustrated in the vorticity field at $s/c = 5$ in Figure 4.8. This phenomenon is not, however, observable in the corresponding dye flow visualization, and thus presents a limitation in relying solely on dye injection to visualize flow fields. The competition between the leading and trailing edge vortices leads

to a lower resultant force and one that is located closer to the mid-chord, explaining the minimum in moment coefficient. The LEV formation and convection repeats once more as the clockwise vorticity from the leading edge regains dominance over the wing surface (see Figure 4.8, $s/c = 7$) and moves the resulting low pressure region (and resultant force) farther forward of the mid-chord, leading to a second local maximum. It is of interest to note that as the center of pressure moves chordwise along the wing, the pitching moment coefficient does not change sign, contrary to classical dynamic stall [63] during which there is a sharp change in sign of the pitching moment [9,94]. In the case presented here, there are dips in lift and moment coefficients corresponding to shedding LEVs, but not to the extent one typically sees in dynamic stall.

4.2 Streamwise Surge: Fast versus Slow Comparison

Looking more closely at two cases, a "fast case" ($s_a/c = 1$) and a "slow case" ($s_a/c = 6$), we consider the force contributions from circulatory and non-circulatory effects during the acceleration of the wing. These two cases have been selected for comparison because they differ greatly in motion aggressiveness and allow for some insightful comparisons into the nature of force production on accelerating plates. The fast case accelerates to its final velocity six times faster than the slow case and, thus, will have a theoretical added mass contribution six times greater as well (see Equation 4.2). The added mass force in the slow case is small in comparison to total lift production, comprising only 5% of total lift by the end of the acceleration transient.

To isolate the effect of the circulatory forces on lift in the acceleration region,

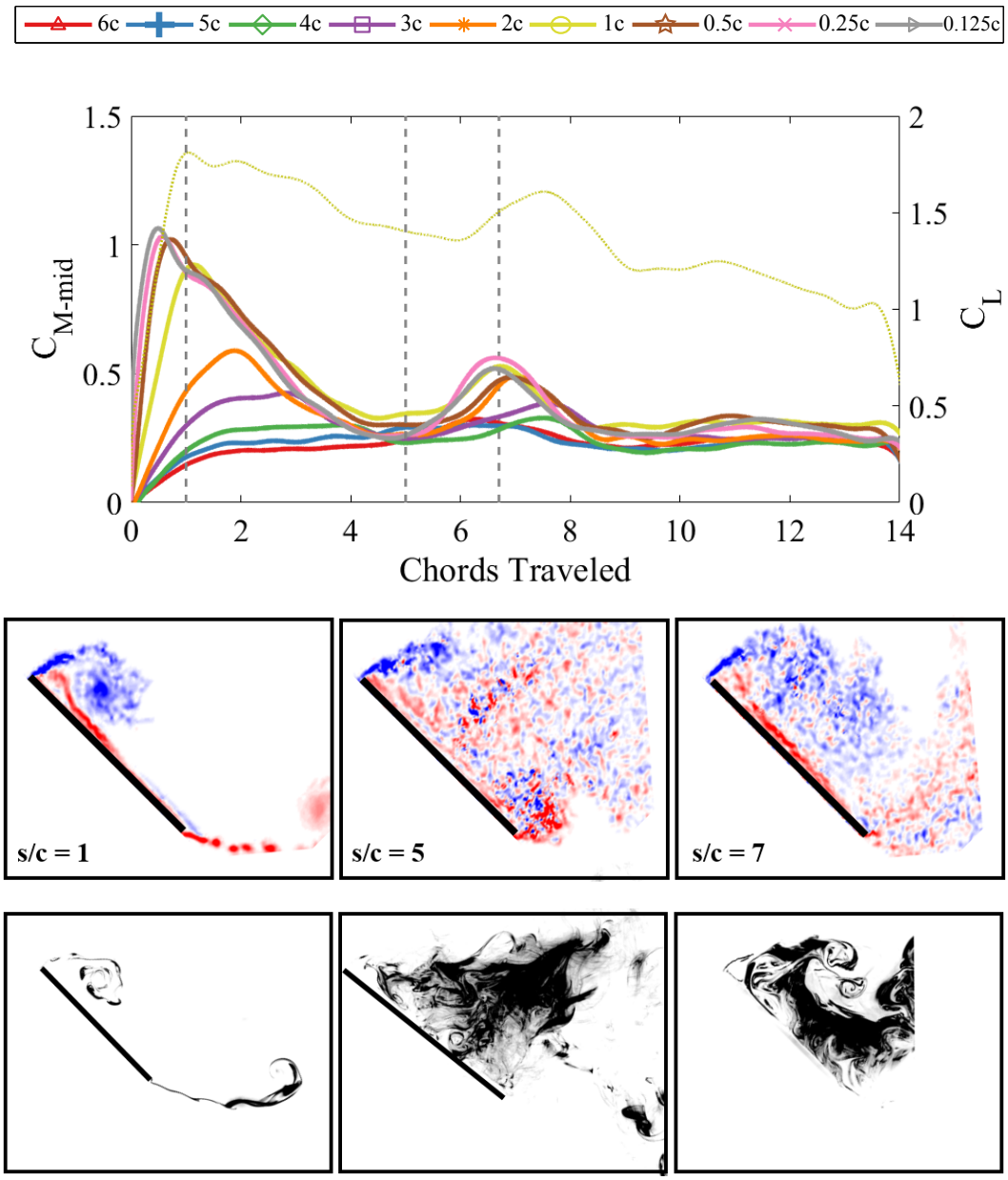

Figure 4.8: (Top) Pitching moment coefficient about the mid-chord (solid lines) for the entire acceleration study. Lift coefficient for the $s_a/c = 1$ case (dotted) is provided to show similarity in trends between lift and moment coefficients. Vorticity plots (middle) and flow visualization (bottom) correspond to maxima and minima locations in mid-chord pitching moment for the $s_a/c = 1$ case, indicated by vertical lines in the plot.

the non-circulatory added-mass force from Eq. 4.2 was removed from the measured force data, as shown in Figure 4.9. Even after removing the theoretical added-mass force from the two lift curves, there is still a ΔC_L between the cases, implying that the difference in lift during the transient phase of each acceleration profile is not completely due to inertial forces, but that circulatory forces provide a significant portion of the measured lift, even during wing acceleration. In both of these cases, wing acceleration is high enough that the added mass force is significantly large (- - line in Figure 4.9), but circulatory forces (-.- line in Figure 4.9) quickly become larger in magnitude than added mass forces early after motion onset. Recall that what is called "circulatory force" here is theoretical added mass subtracted from measured lift, $C_{L,circ} = C_{L,meas.} - C_{L,noncirc}$. It is thus gratifying that following the acceleration transient the resulting "circulatory" lift directly aligns with measured lift at a point after which there is theoretically no added mass contribution. This result further motivates the possibility of a linear superposition of force contributions in the form of a low order prediction model. It is evident by the results here that the added mass contribution is well understood. It now behooves us to search for a physical understanding and quantification of the circulatory force contribution.

The circulation in the flow field can be measured by summing up all of the vorticity located above the wing within the image frame at each time step. Because the field of view is small enough such that the image only contains approximately a $1c \times 1c$ box above the suction side, it was deemed that all circulation in the field of view was "relevant" to lift production. Presently, there is not a standard convention for measuring "relevant" circulation or even a definition of such, unless it takes the form of an identifiable coherent

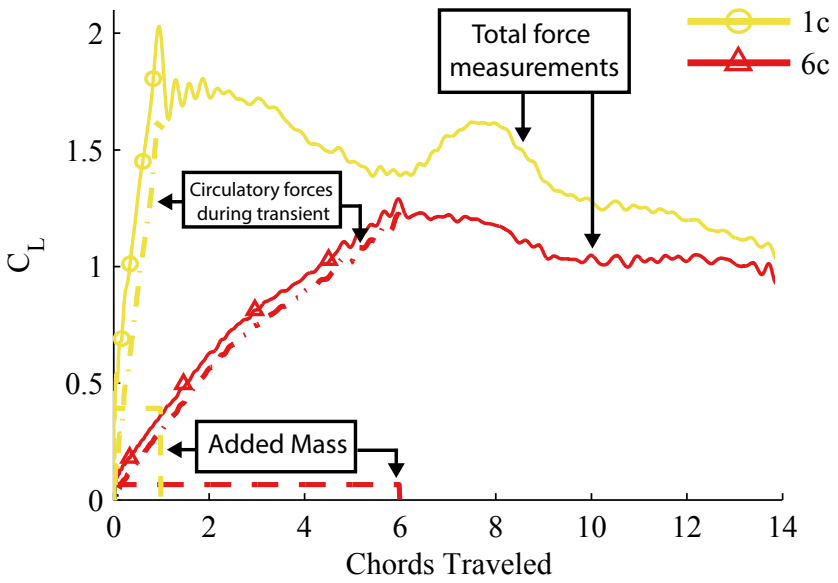

Figure 4.9: Force histories of the fast ($s_a/c = 1$) and slow ($s_a/c = 6$) cases showing the contributions of circulatory and non-circulatory effects.

vortex. Thus, this study limits itself to the primitive, yet robust and insightful, method of summing up all vorticity production local to the wing within approximately a $1c$ radius of the wing surface. Figure 4.10 provides time histories of measured circulation for the fast and slow surge cases. As predicted, the fast case produces higher leading edge vortex circulation (solid lines) during the acceleration transient, which the results of Figure 4.9 suggested. Following the rise in circulation several chords after acceleration ceases, the fast case experiences a significant dip in total circulation (dotted lines), reaching a local minimum at $s/c = 5.5$. Although this is partially due to vorticity leaving the field of view, the PIV image in Figure 4.3 at $s/c = 5.5$ corroborates this result showing opposite sign vorticity from the trailing edge making its way onto the suction surface, decreasing

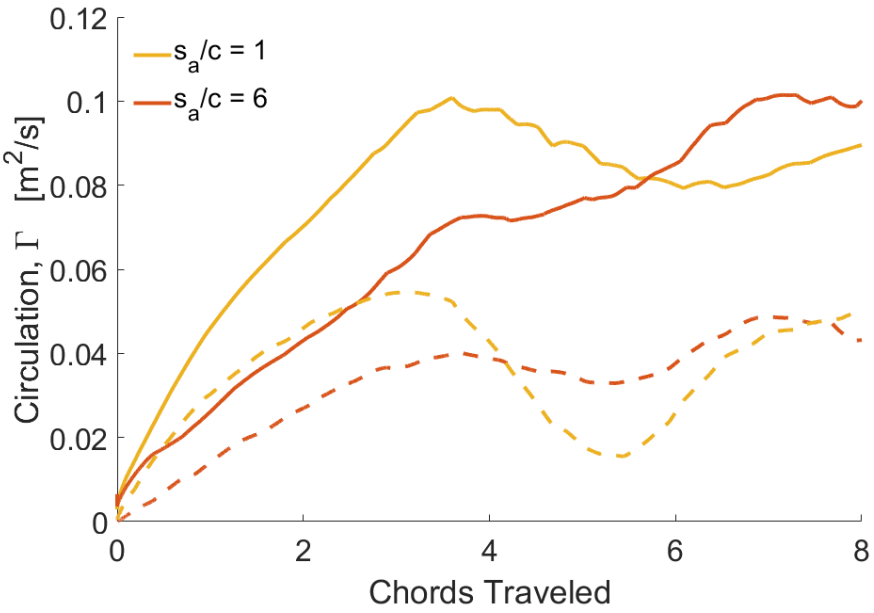

Figure 4.10: (-) LEV circulation, i.e. summation of blue clockwise vorticity, and (- -) total (positive + negative) circulation for fast and slow surge cases.

the circulation within the interrogation window. These events line up precisely with the local minimum in lift coefficient shown in Figure 4.6. Subsequently, the rise in circulation peaking around $s/c = 8$ in Figure 4.10 lies directly in phase with the local maximum in lift coefficient in Figure 4.6.

4.3 Streamwise Surge: Vortex Tracking

The vortex tracking algorithm described earlier, which identifies local extrema in the γ_1 function to locate vortex centers, was used to identify the leading edge vortex trajectory throughout the wing motion. Because the real flow is in a viscous fluid, at some point in the motion, the vortex breaks down and loses its coherent structure.

Following vortex dissipation, the tracking algorithm can no longer accurately locate the correct vortex center. Thus, the tracking method presented here is only carried out until the first LEV can no longer be detected.

Figure 4.11 plots vortex trajectories in the lab-fixed and wing-fixed reference frames for the fast and slow cases. It was previously hypothesized that, because the two cases have vastly different force histories, their vortex trajectories would also show notable differences. However, Figure 4.11a shows that the fast and slow surging cases actually produce nearly identical vortex trajectories with respect to convective time. The leading edge vortex forms immediately upon startup and translates linearly and nearly aligned with the freestream over the first chord of travel. At $s/c \approx 1.25$, both LEVs take an immediate departure normal to the wing surface, illustrated by Figure 4.11c, remaining at a relatively constant X' location (Figure 4.11b).

Vortex trajectory provides the instantaneous position of the vortex, but it does not contain information about its size or strength. Figure 4.12 provides visualization of the vortex in the form of vorticity plots, showing a clear difference between the two cases. The fast surge case forms a tight, coherent vortex upon startup, and the vortex remains this way through $s/c = 1.5$. The slow case, however, forms a much weaker leading edge vortex that quickly dissipates as it convects from the wing surface. This point is reiterated quantitatively by Figure 4.10. As expected from the larger vortex with stronger vorticity (as seen in Figure 4.12a-b), the fast case produces consistently higher circulation throughout the motion. As stated previously, force production during these particular wing kinematics is largely driven by circulatory forces, which manifest themselves largely in the strength of the leading edge vortex. This analysis shows that

despite having nearly identical LEV trajectories, the fast and slow surging cases produce vortices of different strengths at early times, explaining the large difference in force histories.

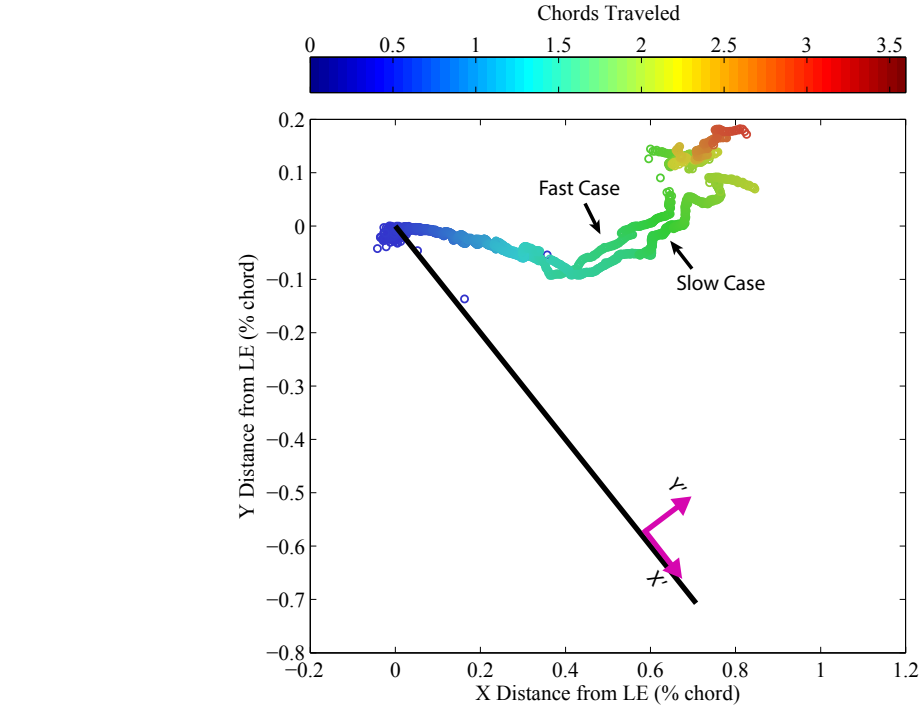

(a)

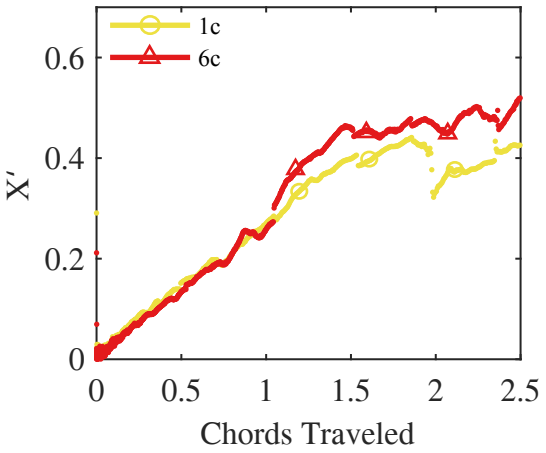

(b)

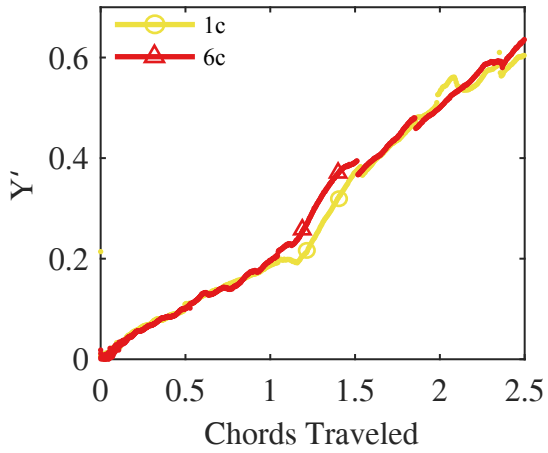

(c)

Figure 4.11: (a) Vortex trajectories in a lab-fixed reference frame for $s_a/c = 1$ (fast) and $s_a/c = 6$ (slow) cases. Trajectories in the wing-fixed reference frame are separated into (b) wing-parallel and (c) wing-normal directions.

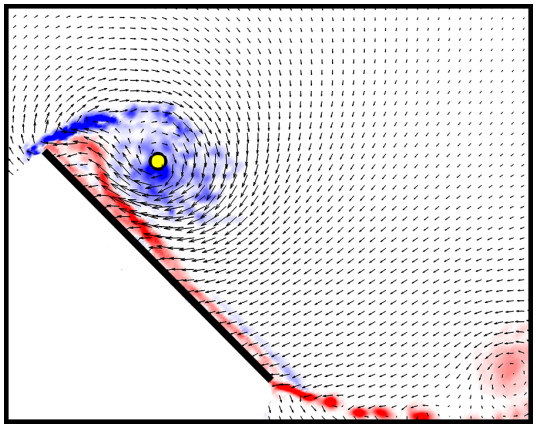

(a) Fast Surge: $s/c = 1$.

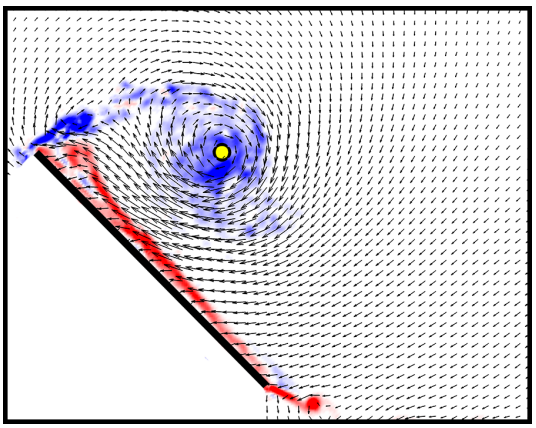

(b) Fast Surge: $s/c = 1.5$.

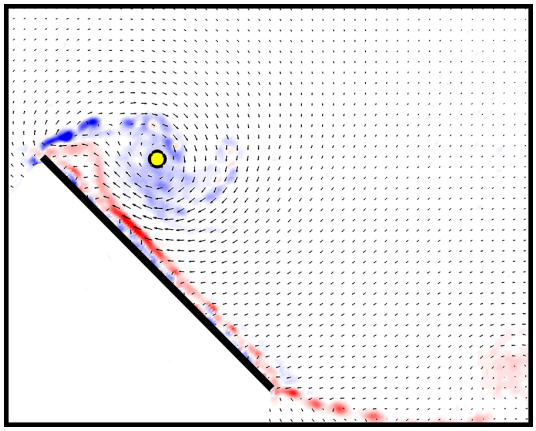

(c) Slow Surge: $s/c = 1$.

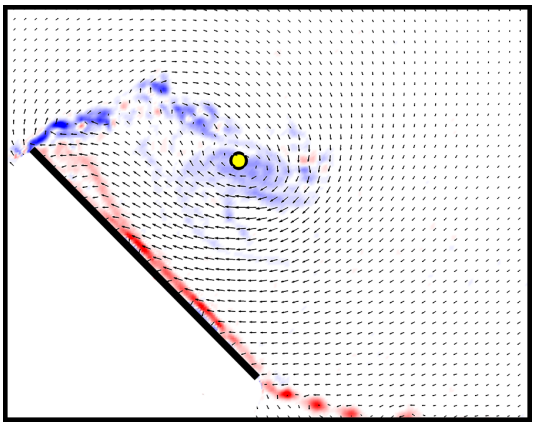

(d) Slow Surge: $s/c = 1.5$.

Figure 4.12: Contours of vorticity and velocity vector fields illustrating leading edge vortices on fast and slow surging wings. The yellow dot indicates the vortex location as given by the centroid of γ_1. Only every fifth velocity vector is shown here.

4.4 Translational Pitch: Force and Moment Histories

Pitch plays a pivotal role in rapidly maneuvering aerial vehicles, having prevalence in perching MAVs or tactically evasive aircraft [95, 96] and during stroke reversal in reciprocating wings [97, 98]. The present study aims to build on the large body of research surrounding pitching wings at low Reynolds number and offers a comparison to the surging wing regarding vortex trajectory, circulation production, and relaxation to steady state.

4.4.1 Lift Coefficient and Lift-to-Drag Ratio

In similar fashion to the surging wing experiments of Section 4.1, an acceleration study was performed on the pitching wing to quantify force and circulation production. The focus remains on the idea of a "fast" and "slow" motion, in which the motion occurs over $1c$ and $6c$, respectively. As defined in Figure 2.6, these correspond to reduced frequencies $k = 0.39$ and $k = 0.065$.

Figure 4.13 provides lift histories for both fast and slow cases in which the wing pitches about the leading edge and the corresponding surging cases from the previous section. As discussed in Chapter 3, much of the force produced during the motion transient of rapidly pitching wings is due to non-circulatory and circulatory pitch rate contributions, i.e. added mass, rotation-induced plate-normal acceleration, and virtual camber. Referring back to the force component breakdown of Theodorsen's equation in Figure 3.6, not only does the pitching wing have an acceleration-proportional lift term (as does the surging wing) but also two angular velocity-proportional lift terms. The

largest of these terms is virtual camber, which aids in turning the flow in the direction of flow attachment and leads to a significantly larger circulatory lift force than achieved on the surging wing. It is important to remember these additional lift sources when observing the vastly different force histories between surge and pitch.

Figure 4.13b zooms in on the time during and immediately following the pitch-and-hold maneuver. For the $s_a/c = 1$ ($k = 0.39$) motion, peak lift is achieved at a value nearly five times that of its steady state lift. The slow pitch case, $s_a/c = 6$ ($k = 0.065$), also experiences an unsteady lift increase, but only to a maximum value roughly twice that of its steady state. Due to the rotational acceleration and angular velocity terms during the motion transient, unsteady lift production exists only until $t^* = 1$ and $t^* = 6$ for fast and slow motions, respectively, after which all motion-dependent lift sources go to zero and lift production slowly relaxes to its steady state. A similar trend, although of lower magnitude, was observed in the aforementioned surging cases. As annotated in Figure 4.13b, after $t^* = 1$ the fast surging and pitching cases are kinematically equivalent; both wings are translating at constant free stream at fixed angle of attack $\alpha = 45°$. Notice that once the motion transients complete, both lift histories converge and follow the same trends at the same magnitude for the duration of translation. The repeatability of these results is further verified by Figure 4.14, which provides a comparison of force measurements between the two facilities used in the present study: UMD and AFRL. UMD force measurements on an $AR = 2$ wing were provided by Manar et al. [80]. Figure 4.14 includes the acceleration transient and several subsequent convective lengths, during which differences in lift history due to aspect ratio effects have yet to manifest, and shows that measurements between the two facilities are very similar.

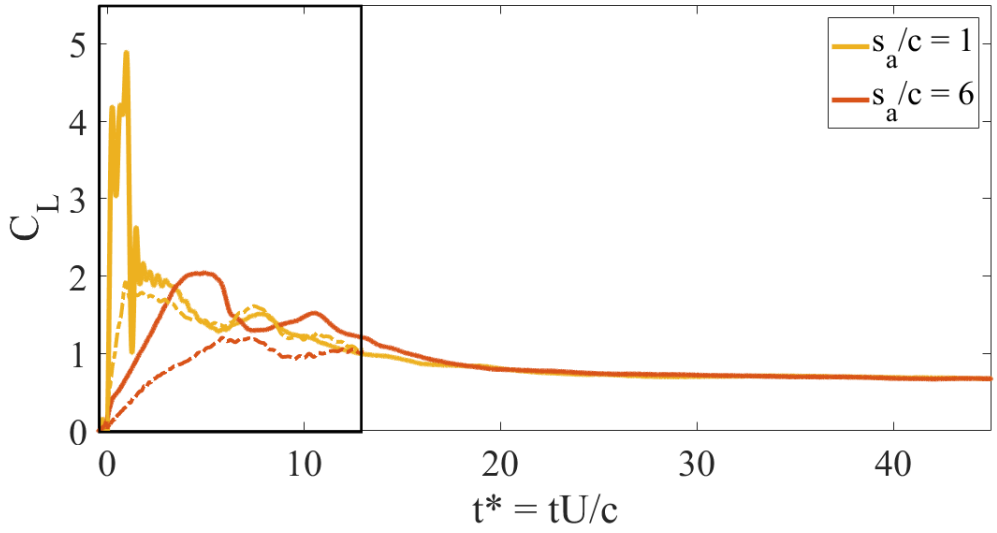

(a) Time history of lift coefficient for pitching (solid) and surging (dashed) wings. Regardless of initial transient motion, all cases converge to the same final steady lift.

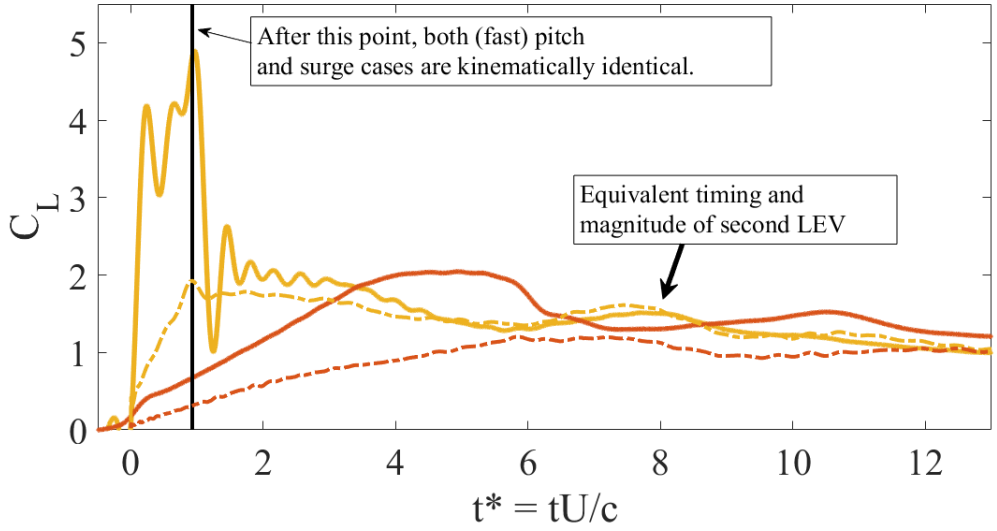

(b) Contents of box in (a) showing a more detailed plot of lift coefficient for the four cases. Note that after the initial motion transient, the fast pitch and surge show extremely similar unsteady force histories.

Figure 4.13: Lift histories for fast and slow pitching and surging cases.

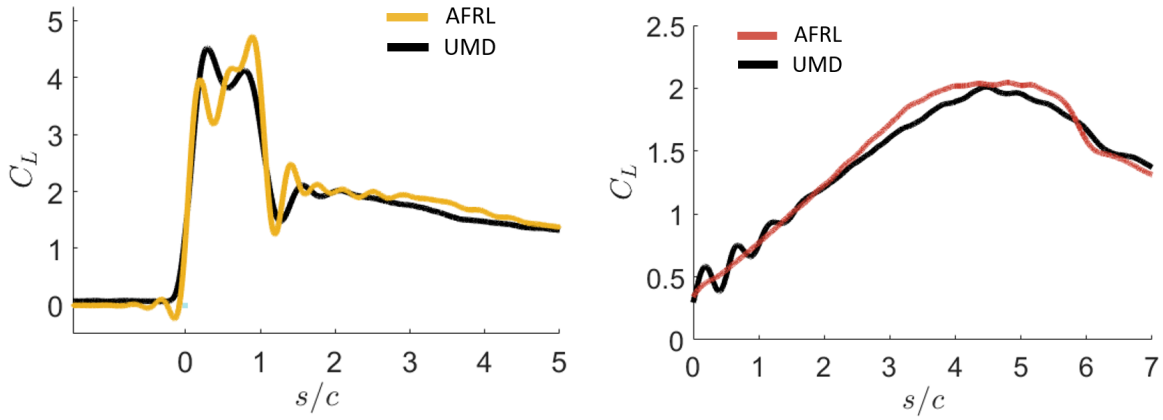

(a) $s_a/c = 1$ (Fast pitch).

(b) $s_a/c = 6$ (Slow pitch).

Figure 4.14: Comparison of lift histories for (a) fast and (b) slow pitching cases from each of the facilities used in this study. The two facilities produce largely equivalent force histories, despite some discrepancies due to different installation/mounting techniques. UMD forces provided by Manar et al. [80]

Figure 4.15 provides circulation measurements for the fast and slow pitch and surge cases. Circulation is measured by summing up all vorticity in the frame, which admittedly neglects the pressure side and causes a nonzero circulation at time $t = 0+$ for pitch measurements. Observing the total circulation for *fast* pitch and surge kinematics of Figure 4.15, the two cases experience identical trends: increasing circulation from the onset of motion through $s/c = 3$, undergoing a dip in total circulation reaching a minimum at $s/c = 5.5$, and subsequently increasing circulation to a second local maximum at $s/c = 8$ due to reformation of leading edge circulation. The peaks and troughs in the circulation time history for fast pitch and surge are cataloged via PIV snapshots of the vorticity field in Figure 4.16.

Circulation for the slow cases is provided in Figure 4.15b and PIV snapshots in Figure 4.17. The slow cases, however, do not show as similar a trend to one another. One explanation for this lies in recognizing the significant differences in their kinematics. Both wings complete their motions over six chords of travel, a relatively long time in terms of convective distance and duration of flow field development. The surging case does so fixed at high incidence angle, $\alpha = 45°$, from motion onset. Thus, immediately, a leading edge vortex will form and separated flow phenomena begins, see Figure 4.17. The pitching wing, however, experiences over one chord of travel under attached flow at low angle of attack (Figure 4.17a,b) before flow develops into a feeding shear layer at the leading edge eventually developing into a large region of circulation akin to an LEV. Hence, the pitch vortex lasts longer than that of the surging wing. The dissimilarity in flow development for the slow cases is reflected in dissimilar force histories (Figure 4.13). The fast cases, however, show nearly homologous flow development and identical force histories beyond the initial acceleration phase.

The existence of a coherent LEV has little impact on lift-to-drag ratio, as was shown for the surging plate in Figure 4.7. A comparison of C_L/C_D for the pitch study is given in Figure 4.18 and shows ratios well above unity for both fast and slow pitch. This, of course, is partially due to the very low drag experienced by the pitching wings near the onset of motion when the wing is deflecting from $\alpha = 0°$. Throughout each of the pitch cases, the resulting C_L/C_D is always well above that of the surging case, likely due to the dominance of virtual camber. This highlights the importance of understanding the aerodynamics of pitching wings and the possibility for practical use in rapidly maneuvering vehicles, as was the intent for a majority of research efforts on

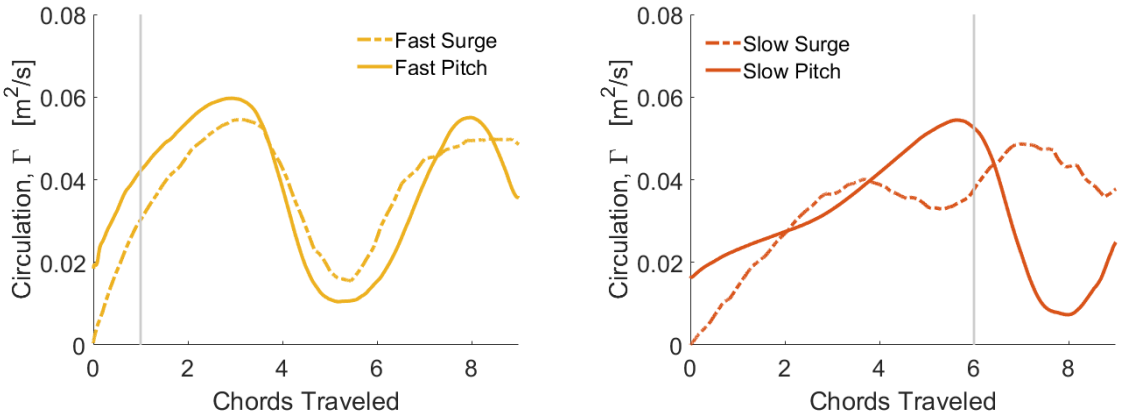

(a) $s_a/c = 1$, $k = 0.39$

(b) $s_a/c = 6$, $k = 0.065$

Figure 4.15: Circulation histories for fast and slow pitching and surging cases. Vertical lines correspond to the end of each acceleration phase.

reciprocating wings. The elevated lift-to-drag ratio evident at the start of the pitch motion is not permanent, however. Non-circulatory forces during pitch act normal to the plate; thus, throughout the pitch motion, as the plate-normal direction changes, there is a transfer of component forces from the lift direction to drag direction. This provides partial explanation for the steep decrease in C_L/C_D during motion transient as the plate-normal vector rotates from $\alpha = 0°$ to $45°$. The insets in Figure 4.18 show that the instant the pitch motion completes, C_L/C_D converges to the steady state condition of a flat plate at $\alpha = 45°$ translating at constant velocity, where all the resultant force is largely plate-normal resulting in $C_L/C_D \approx 1$.

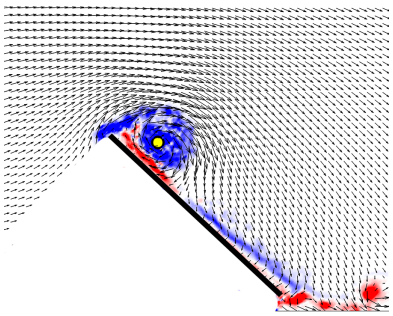

(a) **Fast Pitch**: $s/c = 1$.

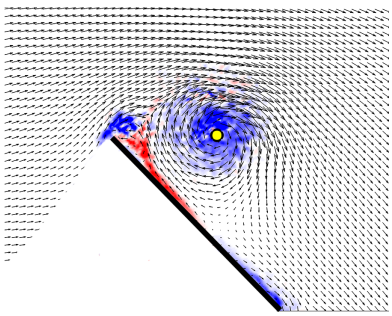

(b) **Fast Pitch**: $s/c = 1.5$.

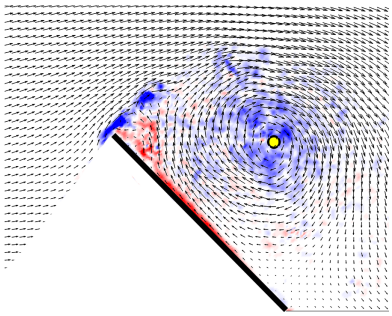

(c) **Fast Pitch**: $s/c = 2.5$.

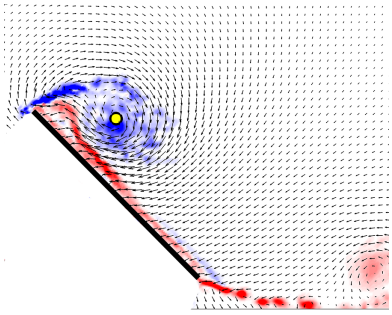

(d) **Fast Surge**: $s/c = 1$.

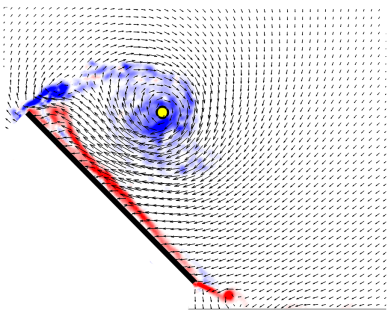

(e) **Fast Surge**: $s/c = 1.5$.

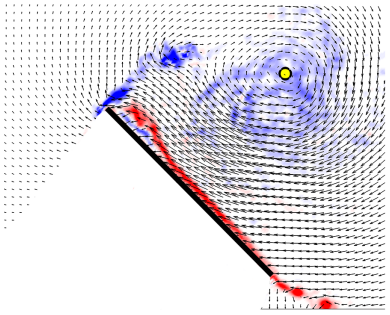

(f) **Fast Surge**: $s/c = 2.5$.

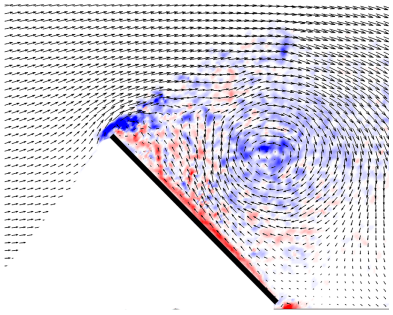

(g) **Fast Pitch**: $s/c = 3$.

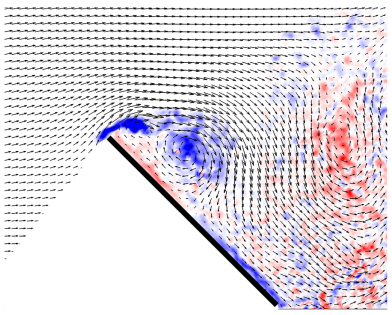

(h) **Fast Pitch**: $s/c = 5.5$.

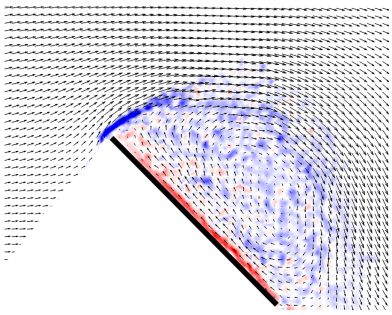

(i) **Fast Pitch**: $s/c = 8$.

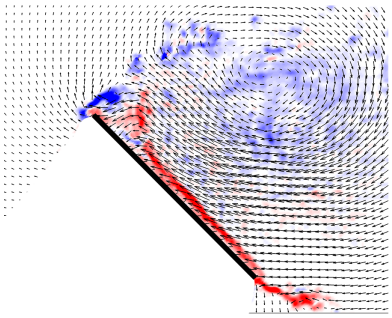

(j) **Fast Surge**: $s/c = 3$.

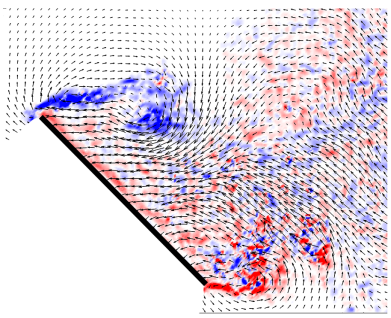

(k) **Fast Surge**: $s/c = 5.5$.

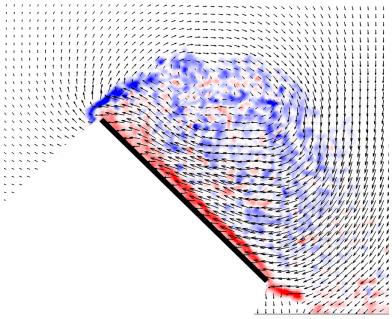

(l) **Fast Surge**: $s/c = 8$.

Figure 4.16: Vortex development on fast pitching and surging wings. The yellow dot indicates the vortex location as given by the local maximum of γ_1.

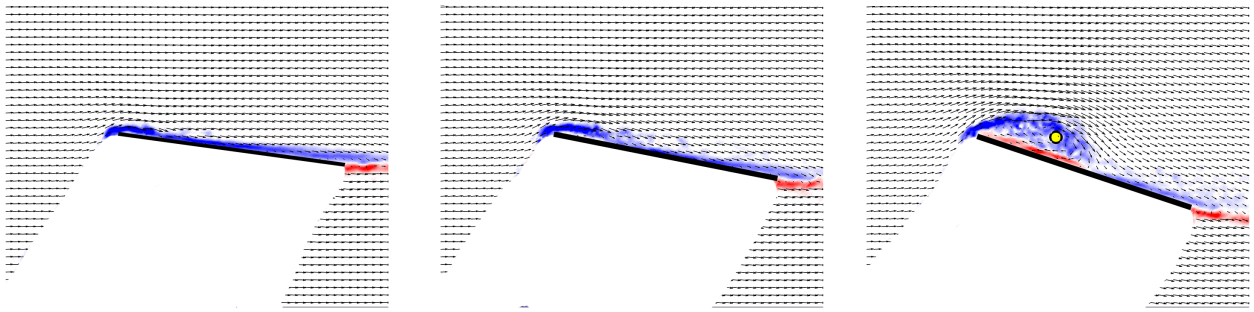

(a) **Slow Pitch**: $s/c = 1$. (b) **Slow Pitch**: $s/c = 1.5$. (c) **Slow Pitch**: $s/c = 2.5$.

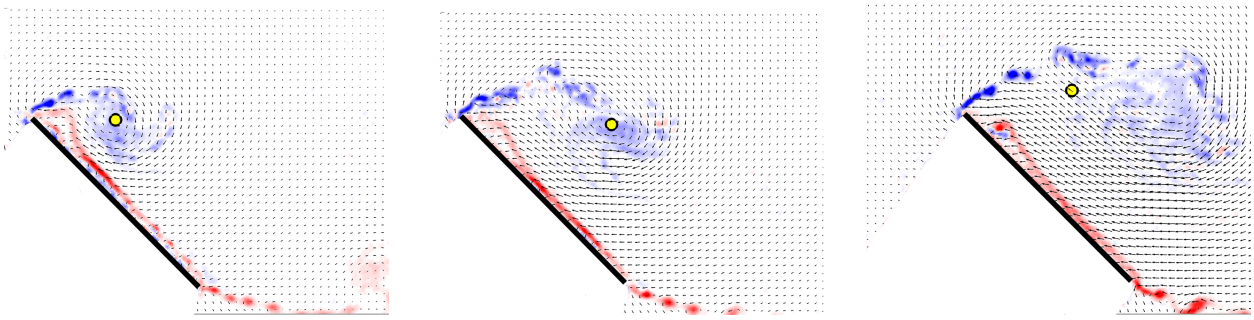

(d) **Slow Surge**: $s/c = 1$. (e) **Slow Surge**: $s/c = 1.5$. (f) **Slow Surge**: $s/c = 2.5$.

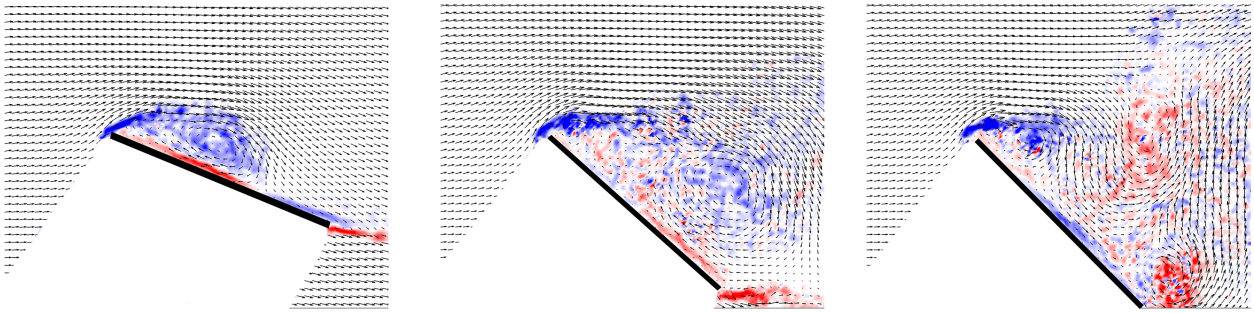

(g) **Slow Pitch**: $s/c = 3$. (h) **Slow Pitch**: $s/c = 5.5$. (i) **Slow Pitch**: $s/c = 7.25$.

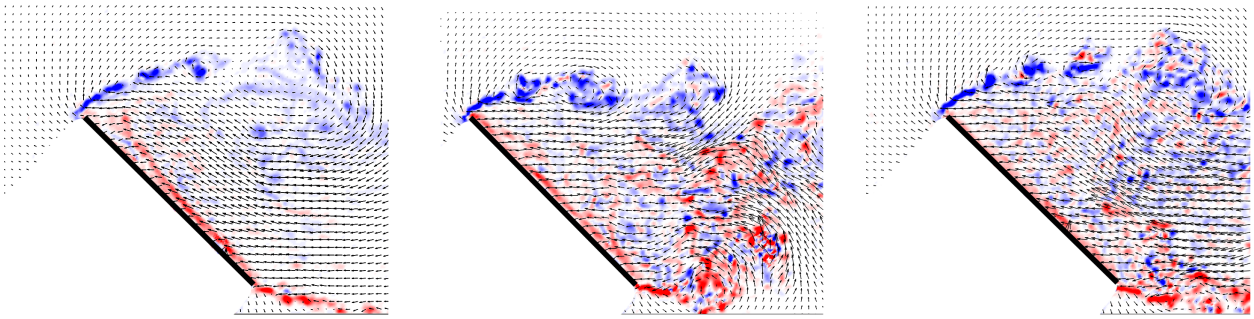

(j) **Slow Surge**: $s/c = 3$. (k) **Slow Surge**: $s/c = 5.5$. (l) **Slow Surge**: $s/c = 8$.

Figure 4.17: Vortex development on slow pitching and surging wings. The yellow dot indicates the vortex location as given by the local maximum of γ_1.

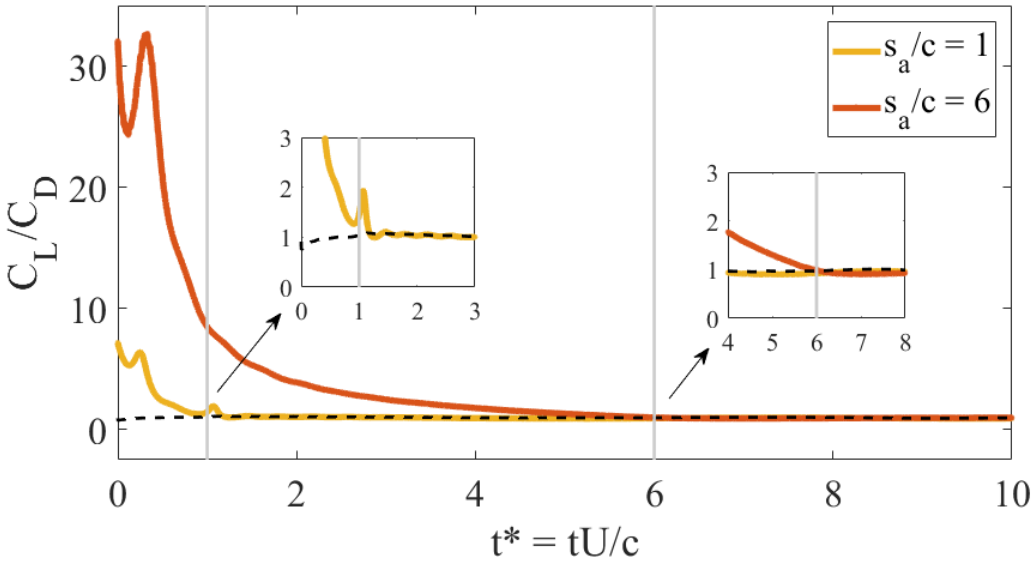

Figure 4.18: Lift-to-drag ratio for fast and slow pitch to $\alpha = 45°$ (solid) and fast surge $\alpha = 45°$ (dashed).

4.4.2 Moment Coefficient

Figure 4.19 contains moment coefficients about the mid-chord for the fast and slow pitch and surge studies. Focusing on the fast motions, both pitch and surge show increasing moment coefficient throughout the duration of the acceleration phase, peaking at $s/c = 1$. Flow visualization and PIV for the surging wing in the previous section suggested that this rise in moment coefficient was due to the growth of a leading edge vortex fixed forward of the mid-chord. The same flow development is observed for the fast pitch case, as shown in Figure 4.16. Yu et al. [94] provide dynamic and steady pitching moment coefficient for a flat plate pitching about its leading edge, and their results are direct agreement with the results presented here. Yu et al. concerned themselves

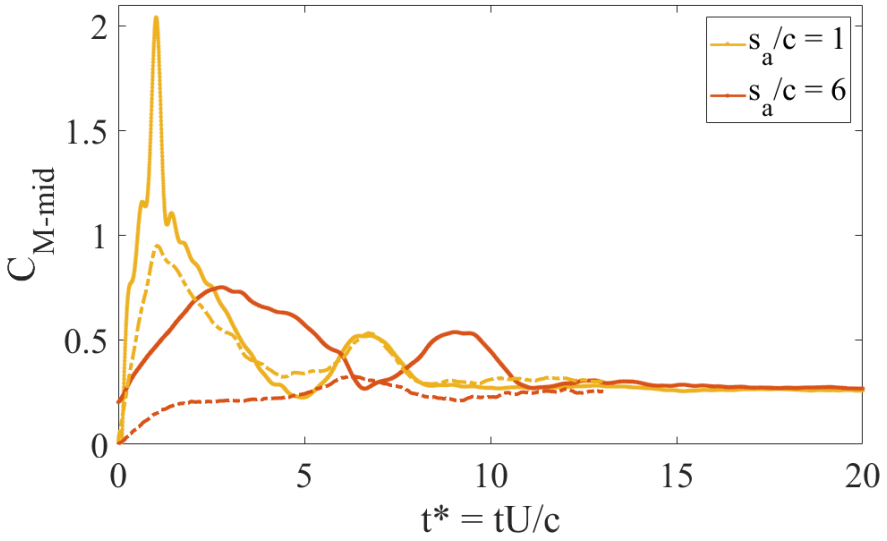

Figure 4.19: Moment coefficient about mid-chord for fast and slow pitch (solid) and surge at (dashed).

only with the motion transient and force histories therein. The present work provides extended time histories of pitching including the startup transient and its subsequent development into its steady state condition. Without chordwise pressure transducers (or similar measurement technique), it is not possible to identify the load distribution on the airfoil and conclusively describe the physical sources causing the particular shape of each moment curve. Illustrated by Figure 4.16-4.17, it is clear that flow separates immediately at the leading edge, removing all hopes of adopting physical flow features described by classical attached flow theory, which predicts zero moment about the quarter-chord for symmetric airfoils.

The exact aerodynamic contribution from the leading edge vortex on pitching moment has not been quantified here, but its position relative to the wing has been

measured, which allows for a discussion of its trajectory and relevance to the directly measured force and moment quantities. Figure 4.20 presents LEV trajectory in both the lab-fixed (X, Y) and wing-normal (X', Y') reference frames. Keep in mind that (X', Y') is wing-fixed with the leading edge at $(0, 0)$ and the coordinate system rotates with the wing. Looking first at vortex tracking in the lab-fixed reference frame, Figure 4.20a, notice that every case, regardless of acceleration or motion type, has relatively similar trajectories pointed in the horizontal free stream direction during early motion. However, observing the results in the wing-fixed reference frame, accounting for the time-varying wing position for pitching cases, Figure 4.20d represents vortex dynamics as seen by the surface of the wing.

Ultimately, it is proximity to the wing surface that determines the LEV's effect on force and moment histories. There are many factors that contribute to the moment coefficient, the details of which are beyond the scope of this work, but one observable factor is the LEV's X' position relative to the mid-chord and Y' distance off the wing surface. Figure 4.20b-c provide time histories of vortex trajectories in the wing-fixed frame. Regarding fast cases, the pitching wing generates a LEV that remains closer to the leading edge ($X'_{\text{pitch}} < X'_{\text{surge}}$) and closer to the wing surface ($Y'_{\text{pitch}} < Y'_{\text{surge}}$), both of which will contribute to a larger pitching moment about the mid-chord. However, vortex trajectories during the first 2.5 chords traveled are not so different as to result in the drastically larger moment coefficient in Figure 4.19.

As discussed in Chapter 3, during the acceleration phase the pitching wing experiences a linear variation of angular velocity along its chord, resulting in a non-uniform pressure distribution, which contributes to the moment about the mid-chord. The large

spike in moment coefficient in Figure 4.19 arises during the angular deceleration portion of the pitch that contributes a large downward force aft of the mid-chord. Differences in LEV trajectory and strength are potentially responsible for the slightly elevated pitching moment during the constant angular velocity/linear acceleration portion, while the non-circulatory force distribution at the end of the pitching motion is responsible for the large spike at $s/c \approx 1$. Since the acceleration profile is antisymmetric, one might expect to see a negative spike in moment coefficient upon motion onset. At present, this work cannot assuredly explain why that is not the case, but it is likely that the resultant circulatory force lies forward of the mid-chord such that it offsets the negative moment caused by plate acceleration. Whereas the large positive spike is enhanced by the location of circulatory lift as well as plate deceleration.

Beyond approximately $s/c = 2$, vortices for pitch and surge depart onto different paths: pitch remaining at constant Y' and traveling along the chord with increasing X' and surge convecting normal to the wing at constant chordwise position X'. With no more non-circulatory forces to account for, these vortex trajectories explain the elevated pitching moment for the pitch case. Vortex tracking ends when vortices dissipate and become unidentifiable by the γ_1 method and vortex tracking becomes no longer reliable. However, as shown in the PIV of Figure 4.16, following the dissipation and breakdown of the original leading edge vortices, the two fast motions produce identical flow fields and thus identical force and moment histories. This also exemplifies why it is difficult to rely on individual vortex tracking to help explain force histories. At the onset of motion, when the vortex is clearly defined and relatively circular, it can be tracked confidently without issue. However, at some point it will break down, dissipate, and/or

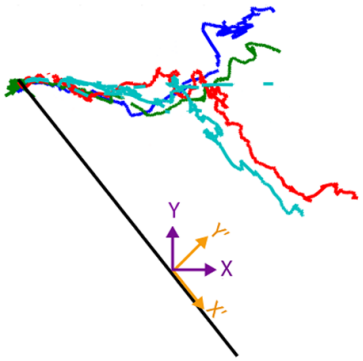

(a) Lab reference frame.

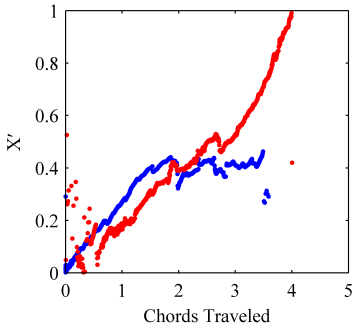

(b) Fast case vortex trajectories in the X' direction.

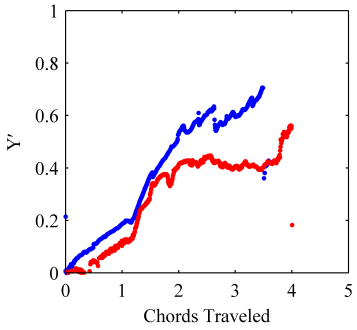

(c) Fast case vortex trajectories in the Y' direction.

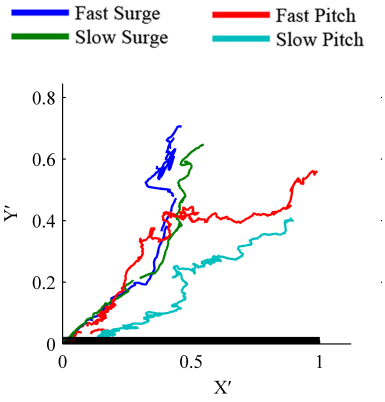

(d) Wing reference frame.

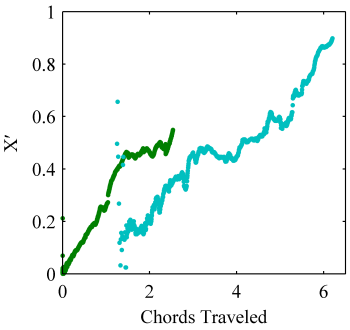

(e) Slow case vortex trajectories in the X' direction.

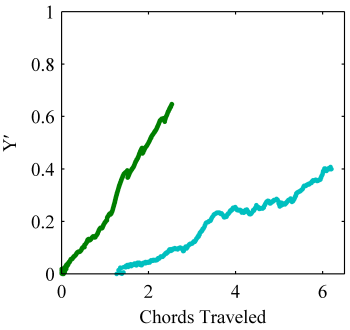

(f) Slow case vortex trajectories in the Y' direction.

Figure 4.20: Vortex trajectory based on the γ_1 tracking algorithm. Corresponding flow field images are shown in Figure 4.16-4.17(a-f).

leave the field of view. What then? At what point does a region of vorticity no longer have influence on the aerodynamic forces and moments? These questions motivated the departure from vortex tracking using the γ_1 criterion to the vorticity centroid method introduced in Section 2.6.3. The latter is especially useful if there is no circular vortex at all, but instead an amorphous region of vorticity within a selected proximity to the wing. This method will be covered in detail in the following chapter.

4.5 Chapter Summary

This chapter provided experimental analysis on unsteady aerodynamic characteristics of rapidly surging and pitching AR = 4 flat plates with the goal of specifically identifying physical mechanisms of lift production and their behavior at all times in the motion. Time-resolved particle image velocimetry and unsteady force measurements were used to describe force production on the wing as well as track and quantify the concurrently developing flow field, all evaluated at a Reynolds number of Re = 20,000. The surging wing investigation consisted of two separate studies of a plate at incidence starting from rest. The first study varied angle of attack from $\alpha = 5° - 45°$ for a single acceleration profile, $s_a/c = 1$. The second study varied acceleration from $s_a/c = 0.125 - 6$ at fixed incidence $\alpha = 45°$. The pitching wing study focused on one "fast" motion ($s_a/c = 1$) and one "slow" motion ($s_a/c = 6$) of a wing pitching from $\alpha = 0°$ to 45° with which to compare force histories and vortex dynamics with those of the surging wing.

It was shown that vortices form via shear layer at the leading edge in cases of leading edge pitch and translation from startup for $\alpha \geq 15°$, resulting in a sequence

of vortex detachment, convection, and new vortex reformation throughout the wing translation. At high angles of attack, each vortex contributes an additional source of circulatory lift that causes an oscillation in force history as lift histories converge downward to their steady state lift value. Formation of a leading edge vortex leads to temporary lift peaks, while LEV convection and subsequent encroachment of trailing edge vorticity above the wing leads to local lift troughs. It was shown that LEV *strength* is proportional to acceleration rate. Faster motions generate stronger, more coherent vortices that are easier to detect using tracking methods such as γ_1. However, the *trajectory* of LEVs in the lab-fixed reference frame are independent of motion rate.

Chapter 5

Experimental Results: Hinged Wing with Large Trailing Edge Flap

As shown in Chapter 4, dynamically pitching wings achieve immediate force production upon the onset of motion, and that force is proportional to frequency and amplitude. The ability to provide an instantaneous lift response from an actuated lifting surface is of extreme interest from a vehicle controls perspective and has use in the field of gust encounter mitigation and rapid vehicle maneuvering. The results of Chapter 4 illustrate the lift-producing capabilities of single-element wings, but the high lift was shown to come at a cost of significantly high drag signature. This chapter presents the use of a *hinged wing* that aims to utilize the lift-producing capability of a pitching flap without the need to mechanically move the entire wing.

The present hinged wing experiment extends upon the work of Rennie and Jumper [99–101] and more recently Phillips and Wygnanski [102] by 1) approximately doubling the size of the deflecting flap from ∼27%-chord to 50%-chord and 2) increasing the non-dimensional flap rate by an order of magnitude. As was the case with choosing aggressive

single-element pitch and surge kinematics in Chapter 4, the hinge location and flap kinematics of the hinged wing have been selected to exaggerate the aggressiveness of a flap deflection than may typically be used in conventional aircraft. The goal is to quantify its behavior and assess the extent to which it deviates from the present understanding of flow physics surrounding trailing edge flaps, which are typically only used to enhance steady lift coefficient. This study addresses a much more aggressive maneuver than has previously been investigated, widely expanding the parametric library of rapidly deflecting trailing edge flaps and generating insight into the physical mechanisms of lift production for this wing geometry. An additional focus has been placed on the entry into and departure from separated flow by varying initial flap deflection angle and stationary fore element incidence angle. This work demonstrates the notion that separated and attached flows follow many of the same physical principles addressed by classical airfoil theory regarding sources of unsteady force production. Whether the plate is experiencing fully attached or massively separated flow, the rate and magnitude of vorticity production are illustrative of the forces produced by the wing, as evidenced by the implementation of a vortex impulse method (Section 5.5) as well as low order analytical and numerical models based solely on flap kinematics (Section 5.6).

Experiments on the hinged wing were performed in collaboration with the Air Force Research Laboratory. All force measurements and flow visualization were acquired by colleagues Albert Medina and Michael Ol, whereas all PIV measurements and data analysis were performed at the University of Maryland. Results from this collaboration were published by Medina, Ol, Mancini, and Jones [72].

5.1 Kinematics

Three major parameters are represented in the experimental test matrix presented in Table 5.1: flap deflection **rate**, deflection **amplitude**, and initial **flow condition** (separated or attached). Deflection rates range from a very fast motion, completing the transient flap over $s_a/c = 0.25$ to a nearly steady pitch over $s_a/c = 4$, which for $\delta = 0 - 30°$ correspond to $k = 1.05$ and $k = 0.065$, respectively. Recall that reduced frequency is given by $k = \frac{\dot{\delta}c}{2U_\infty}$. The complete parameter space (shown in Table 5.1) was chosen to encompass a range of reduced frequencies and deflection angles that will highlight the dominant force producing mechanisms for large rapidly deflecting flaps under attached and separated flow initial conditions.

Table 5.1: Experimental parameter space explored in the fast flap study.

$\boldsymbol{\alpha_{LE}}$	$\boldsymbol{\Delta\delta}$	$\boldsymbol{s_a/c}$	**Forces**	**PIV**
0°	$0 - 20°$	$0.25, 0.5, 1, 2, 4$	All	$s_a/c = 0.5, 1$
	$0 - 30°$		All	-
	$0 - 40°$	$0.5, 1$	-	$s_a/c = 0.5, 1$
0°	$20 - 0°$	$0.25, 0.5, 1, 2, 4$	All	$s_a/c = 0.5, 1$
	$30 - 0°$		All	-
	$40 - 0°$	$0.5, 1$	-	$s_a/c = 0.5, 1$
20°	$0 - 20°$	$0.25, 0.5, 1, 2, 4$	All	-
	$20 - 0°$		All	-

Bound circulation produced on the wing and trailing edge wake circulation were calculated using interrogation windows as shown in Figure 2.15. At each time step, all vorticity within each window was integrated according to the definition of circulation, $\Gamma = \int\int_S \omega \cdot dS$, to obtain a time history of circulation. With regards to quantifying circulation, the present analysis makes no attempt to distinguish flow structures, and thus provides a "total circulation" in each of the regions provided in Figure 2.15. Circulation computed by integrating all vorticity within a box surrounding the wing will be called Γ_{bound} and that of the *wake* will be Γ_{wake}. This method was chosen based on its simplicity, robustness, and ease of implementation for any wing geometry and kinematics.

5.2 General Flow Development and Inviscid Efficiency

The purpose of this section is to demonstrate the *general* behavior of a large (50%-chord) rapidly deflecting trailing edge flap, providing a foundation from which to gain intuition for how the flow behaves under such kinematics and preparing the reader for the detailed measurements and analysis of the test cases in the following section.

The most prominent concept throughout this chapter will be the idea of an "inviscid effectiveness," as termed by Rennie et al. [99], which refers to the observation that during dynamic flap deflection, the wing produces lift as predicted by unsteady thin airfoil theory. As shown in the top left image of Figure 5.1, Rennie found via smoke visualization that the inviscid effectiveness could be explained by a temporary flow attachment during flap deflection. Flow eventually separates at long time (see bottom left

image), resulting in a reduction in lift production, eventually relaxing to its steady state value. The second and third columns of Figure 5.1 contain PIV snapshots of the present experiment for $\delta = 0° - 20°$ and $\delta = 0° - 40°$ with acceleration $s_a/c = 0.5$. The top row corresponds to the moment flap deflection completes at $s/c = 0.5$ and the bottom row corresponds to the steady state reached 4 chords of travel after flap deflection. Rennie performed his experiments on a 27%-chord flap at small deflection angles ($\approx 10°$) at reduced frequencies on the order of $k = 0.01 - 0.1$. The middle and right columns of Figure 5.1 correspond to a 50%-chord flap at reduced frequencies $k = 0.35$ and $k = 0.70$, respectively, an order of magnitude larger than previous studies. This illustrates the notion that rapid trailing edge flap deflection induces attached flow over a wide range of motion rates and final deflection angles. It is not intuitive to imagine a large flap at relatively high incidence, e.g. $\delta = 40°$, maintaining attached flow for a significant period of time. Chapter 4 showed that single-element pitching wings experience exclusively separated flow from motion onset. The hinged wing draws inspiration from the lift-producing capability of a leading edge pitching wing, but with the added benefit of having a stationary leading edge element to prevent immediate leading edge separation.

Figure 5.2 provides instantaneous vorticity fields and streamlines for the $\delta = 0° - 40°$, $s_a/c = 0.5$ case, demonstrating characteristic flow field development of a flap-down motion. Before the onset of flap deflection (Figure 5.2a), where both wing components are stationary at zero incidence, it is expected that the flow is attached. Upon onset of motion, streamline curvature suggests that the pitching flap induces a downward velocity on the surrounding fluid, turning the flow in accordance to the virtual camber term introduced by Theodorsen and discussed in Chapter 3. Even after the wing attains

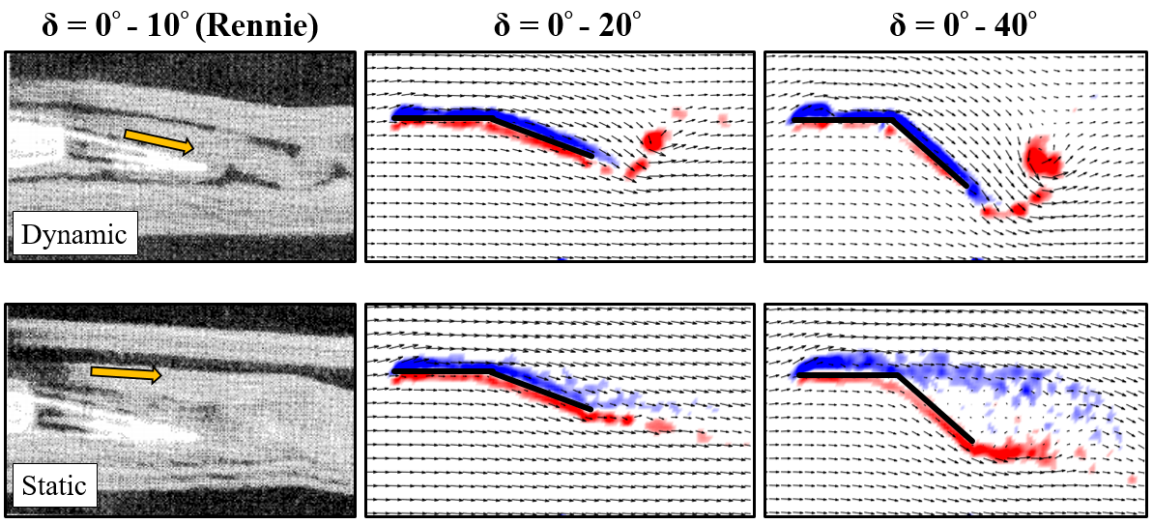

Figure 5.1: Smoke flow visualization and PIV of dynamic flap experiments showing attached flow during flap deployment (top) followed by eventual relaxation to separated steady state (bottom). Showing that the attached flow is a physically reproducible effect over a wide kinematic parameter space.

relatively large deflection angles ($\delta = 20°$ in Figure 5.2b and $\delta = 40°$ in Figure 5.2c) the flow does not immediately separate as seen previously on single-element pitching flat plates [15, 56]. Instead, flow follows the newly-acquired camber line of the deflected wing for the duration of the flap transient. Figure 5.3 provides a physical explanation for this flap-induced flow attachment. Chordwise surface pressure measurements given by Rennie et al. [100] in Figure 5.3a show the development of a favorable pressure gradient during the rapid flap deflection. This favorable pressure gradient allows the flow to remain attached, despite moderate to high deflection angles. A solution for the total pressure distribution along the wing of the present work via the unsteady panel method is shown in Figure 5.3b. The point-vortex panel method assumes a zero-thickness wing

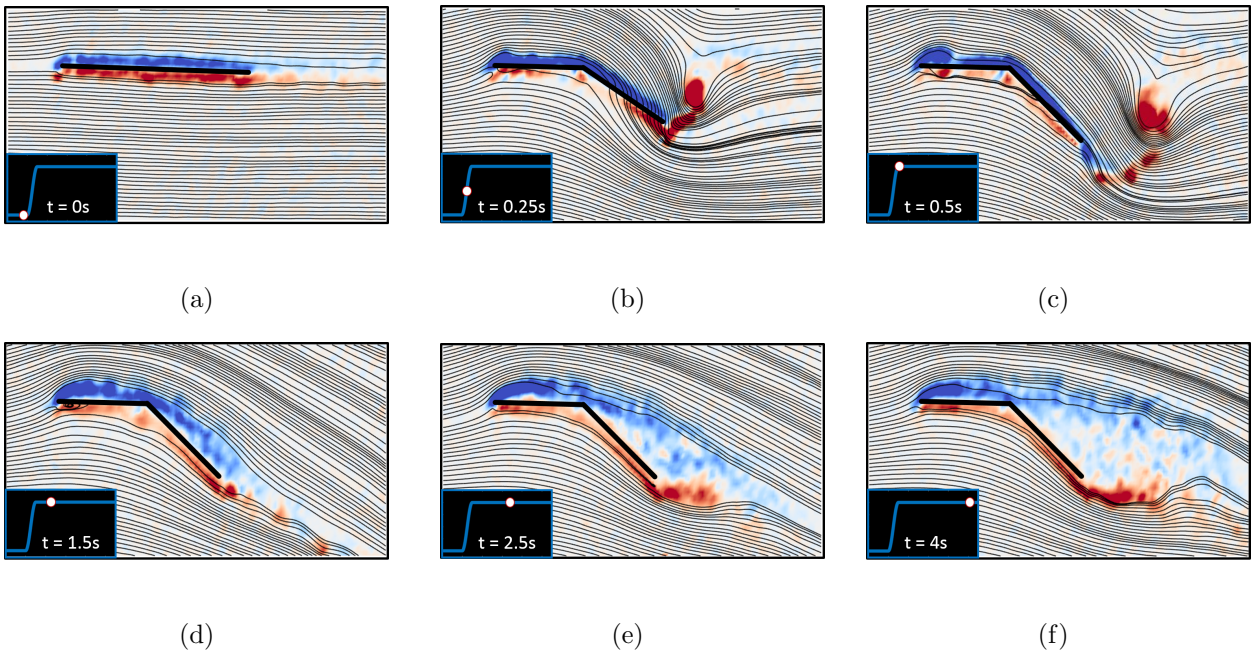

Figure 5.2: PIV vorticity fields and streamlines for the flap-down $\delta = 0° - 40°$, $s_a/c = 0.5$ case.

and does not provide separate surface pressure distributions, but instead provides total pressure, dP, which is equivalent to the difference between surface pressures in Figure 5.3a (see vertical red arrows in both figures). The foremost arrow corresponds to the middle of the stationary fore element and the aftmost arrow corresponds to the hinge location, which differ between the two studies. Thus, the two plots equivalently show a pressure decrease on the upper surface approaching the hinge location, where the attached flow experiences a sharp turn down the flap. This effect appears as an increase in $-C_p$ on the upper surface in Figure 5.3a and an increase in dP in Figure 5.3b. Based on observation of the streamlines, it appears that the strong counter-clockwise rotating trailing edge vortex also contributes to induced downward flow.

Following the completion of flap deflection, there remains a period of attached flow

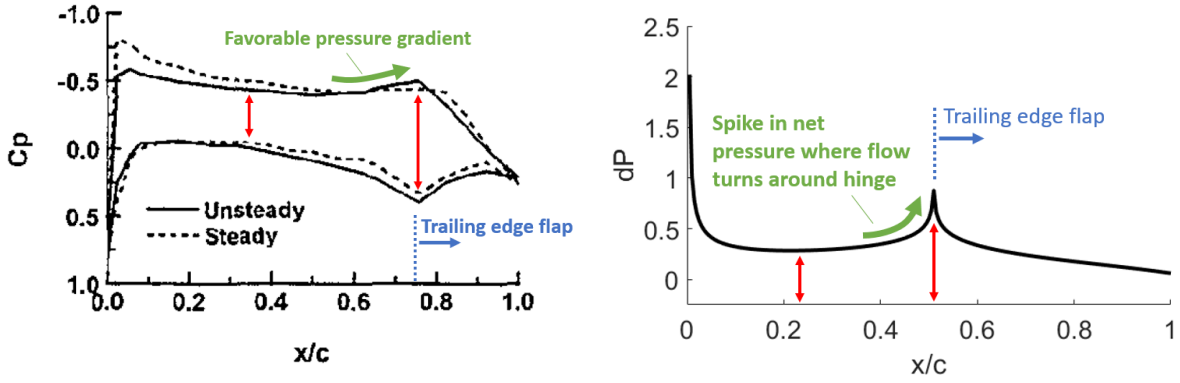

(a) Measured pressure with hinge at three-quarter-chord [100]

(b) Panel method solution with hinge at mid-chord.

Figure 5.3: Pressure distributions for $\delta = 0 - 10°$ using (a) measurements from chord-wise pressure taps, given by Rennie et al. [100], and (b) an unsteady point vortex panel method. Red arrows located in the middle of the stationary front element and at the hinge location illustrate the increase in total pressure as flow travels aft toward the hinge.

before it begins to slowly lift off the deflected rear wing component (see Figure 5.2d - 5.2f), gradually lifting off the surface as the wing travels at fixed incidence at constant velocity for the remainder of the test. The converse of the flap-down motion in Figure 5.2 is the flap-up motion shown in Figure 5.4, where the flow transitions from a fully separated state to fully attached flow at $\delta = 0°$. As opposed to the strong trailing edge starting vortex formed during flap-down kinematics, flap-up motions experience instead more of a severance of the trailing edge wake (Figure 5.4b). The discarded wake obstructs the path of the now-forming clockwise rotating trailing edge vortex attempting to form during flap-up. The result is a smooth transition into attached flow at its final

state (Figure 5.4d-f)

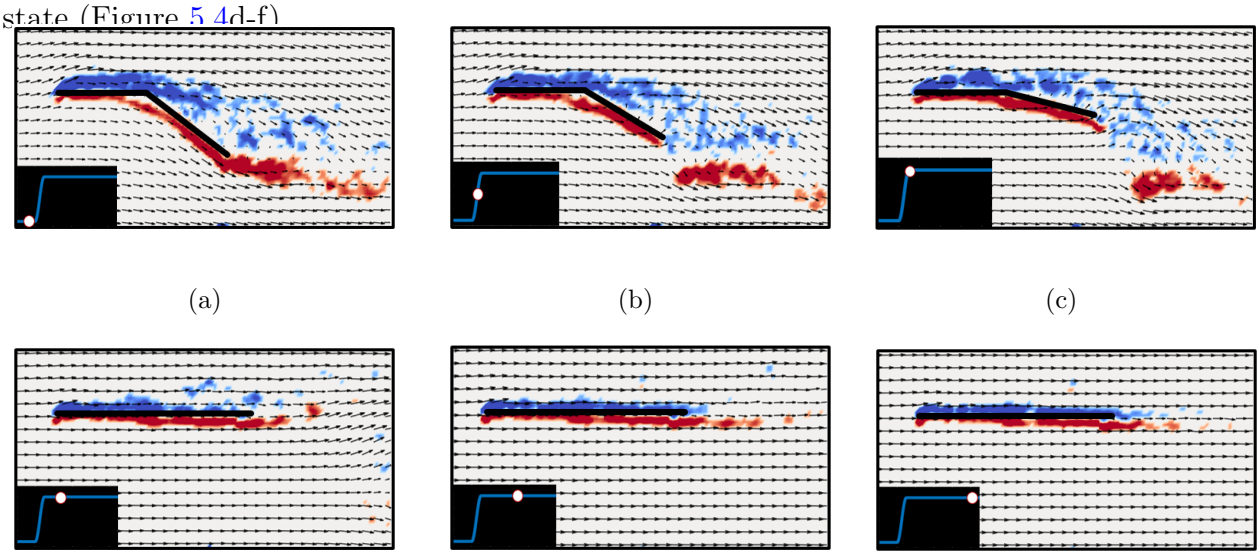

(a) (b) (c)

(d) (e) (f)

Figure 5.4: PIV vorticity and velocity fields for the flap-up $\delta = 40° - 0°$, $s_a/c = 0.5$ case.

Time-resolved bound circulation measurements for the two cases described above are provided in Figure 5.5a with yellow circles denoting the times corresponding to PIV images in Figures 5.2 and 5.4. Also provided in the figure are equivalent cases for $\delta = 0° - 20°$ and $\delta = 20° - 0°$. The general trend of circulation production for the flap-down kinematics is a nearly linear rise in circulation throughout the duration of the pitch transient, reaching a maximum upon motion cessation. Immediately following flap deflection there is a gradual departure from attached flow into separated flow with no external flow structures forming over the wing, e.g. an LEV. This relatively tame flow behavior results in a gradual decline in bound circulation until settling at its fully developed state after approximately four seconds, which also conveniently corresponds to a convective time of four chords traveled. The flap-up cases follow a similar, albeit

reverse, trend in which the initial state is fully separated and circulation decreases nearly linearly before settling to its final state, which is attached flow at zero degrees incidence and zero net circulation. However, as shown in the PIV, there is a complex interaction between the detached trailing edge wake and newly forming trailing edge vortex. This interaction leads to more counter-clockwise circulation production and a slight overshoot past the steady state value. This effect was not observed in the flap-down motion.

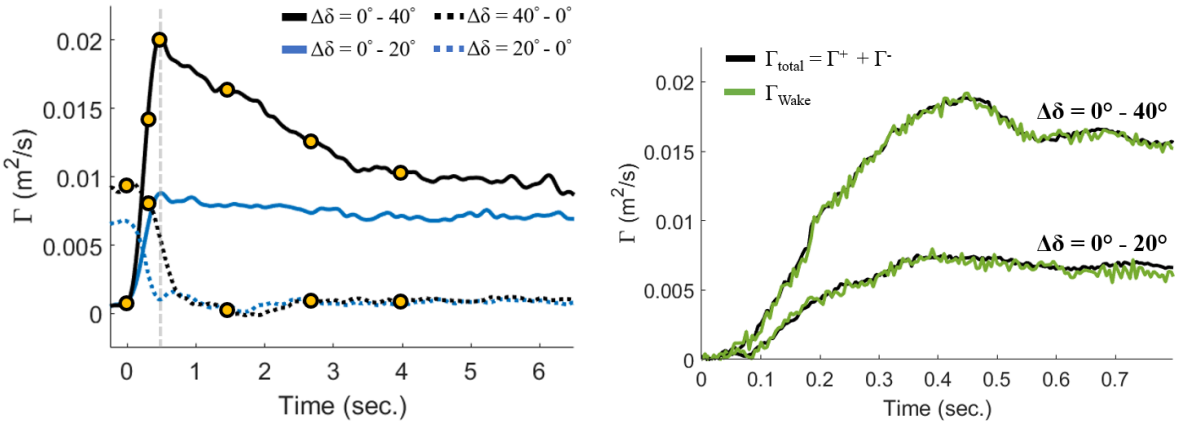

(a) (b)

Figure 5.5: (a) Circulation history for various hinged wing cases and (b) comparison between bound (black) and trailing edge wake circulation (green). Yellow circles in (a) correspond to PIV snapshots in Figure 5.2 and 5.4.

It should be noted that the intention of this work is not only to expand the documented body of experimental results, but also to use modeling to provide low order methods of predicting lift histories on the kinematics presented here and elsewhere within the parameter space. Potential flow theory, the basis for the panel method and analytical models in this work, assumes two-dimensional flow and a conservation of circulation

given by Kelvin's circulation theorem, which states that the time rate of change of circulation around a closed curve consisting of the same fluid elements is zero, typically expressed as $\frac{D\Gamma}{Dt} = 0$. Unfortunately, the present literature does not extensively overlap with the kinematics of the present study, and although it would be convenient to extrapolate the results of others to justify the assumptions in this work, it would be best to ensure the accuracy of our claims based on our own experimental results. The use of a transparent glass wing in the PIV experiments allows for a clear, unobstructed view of the entire flow field, providing the opportunity to check if circulation in the two regions is, in fact, equal. As shown in Figure 2.15, the wake boundary of integration is all encompassing of the flow field aft of the trailing edge, interfacing vertically with the bound circulation boundary. The results are presented in Figure 5.5b for the $s_a/c = 0.5$ $0 - 20°$ and $0 - 40°$ flap cases. The absolute values of bound circulation (black) and wake circulation (green) are nearly identical over the duration of the flap maneuver and continue to be so over the next half chord of travel. The fact that no vorticity suddenly leaves the PIV image frame indicates that all fluid motion is nominally two-dimensional within the imaging slice. Additionally, this indicates that vorticity did not diffuse or dissipate due to viscous effects in the wake over this time scale. Due to finite resolution of the camera and possible reflections off the surface of the glass wing, it is not possible to achieve complete resolution of the boundary layer near the wing surface. The near-wing velocity field measurements are almost certainly under-resolved. However, this effect is mediated by the fact that both the suction side and pressure side of the wing contain under-resolved sections of opposite sign. It will be assumed for the present study that these under-resolved regions essentially cancel out, leading to minimal inaccuracies in

the measured bound circulation production. This assumption is supported by the fact that the measured values of bound circulation and wake circulation are nearly identical.

Having addressed the assumptions of two-dimensional, inviscid, and attached flow, it is now suitable to move forward in the analysis and apply concepts from thin airfoil theory to compute lift on the wing. In a steady flow, one can calculate lift using bound circulation via the Kutta-Joukowski theorem, $L = \rho U \Gamma$. Having high deflection rates ($0.018 \leq k \leq 0.70$) and large flap amplitudes ($\delta \geq 20°$), the rapidly pitching trailing edge flap in the present study is far from what is typically considered "steady" motion. Thus, when applying the Kutta-Joukowski theorem to the PIV measurements and circulation calculations from Figure 5.5, one should not expect to accurately predict the *total* force production, as that contains time-dependent unsteady lift contributions not captured in steady theory. Rennie et al. [100] concluded that during rapid trailing edge flap deflection, the wing acts with an "inviscid effectiveness," during which the wing produces lift analogous to the potential flow solution. However, Rennie's study used a flap of only 27% of the chord and much smaller deflection rates ($k \leq 0.1$), which elicited negligible rate-dependent forces, e.g. added mass, and focused solely on the inviscid nature of the resulting circulatory force. Therefore, it is instructive to attempt to reach the same conclusion with the present setup and more aggressive motions with the hopes of drawing similarities between our conclusions and effectively increase the present literature's knowledge of the parameter space. Figure 5.6 presents a comparison of the measured steady circulatory lift (Kutta-Joukowski theorem applied to PIV data), non-dimensionalized by free stream dynamic pressure $q = 0.5\rho U_\infty^2$ and chord length, in addition to results from direct force measurements. It is clear that the calculated lift

from PIV does not directly match the measured lift during the motion transient, which, as stated previously, is expected. However, there is excellent agreement between the calculated steady lift and measured lift after the motion transient. This result coincides with Rennie's conclusions about the wing acting as though in ideal flow conditions in that after the flap transient, when there are zero rate-dependent force contributions, the force history aligns with Kutta-Joukowski theorem. Based on the results of Figure 5.6, two major attributes of trailing edge flaps become evident: 1) There is a nearly instantaneous lift response at the onset of motion and 2) unsteady pitch rate effects (due to $\dot{\delta}$ and $\ddot{\delta}$) are dominant in this kinematic regime and responsible for over 50% of force production. Achieving a deeper understanding of these unsteady forces and breaking down individual lift contributions of each wing component will be the focus of the following sections.

5.3 Test Matrix Results

5.3.1 Flap-Down

Flap-down experiments correspond to the topmost section of the test matrix (see Table 5.1). These motions have an initial condition of attached flow, as the front and rear elements are both at zero degrees incidence to the free stream before the trailing edge flap undergoes flap-and-hold kinematics down to its final deflection angle. Figures 5.7a and 5.7b provide the lift histories for several flap deflection rates for $\Delta\delta = 30°$ and $\Delta\delta = 20°$, respectively.

Recall that a key attribute of using trailing edge flaps as a control surface and

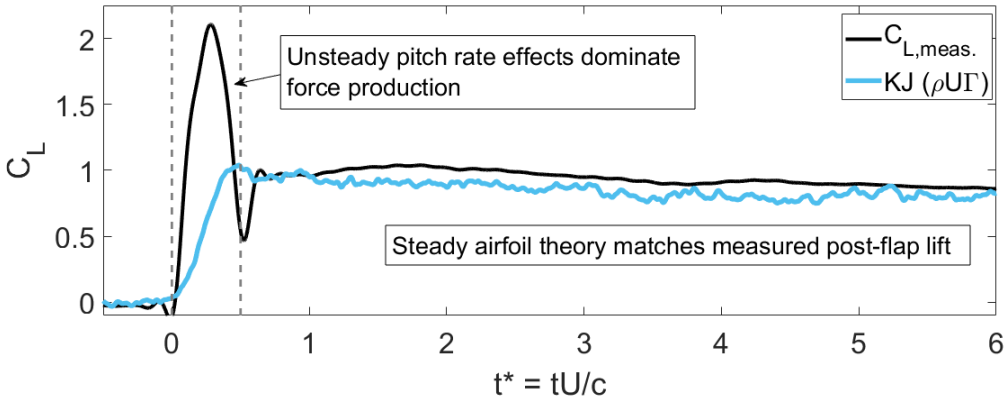

(a) Lift coefficient for $s_a/c = 0.5$, $\delta = 0° - 20°$ case.

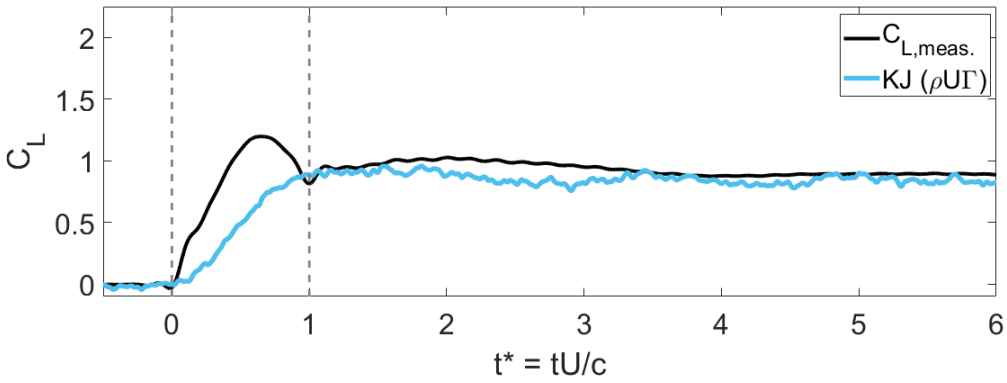

(b) Lift coefficient for $s_a/c = 1$, $\delta = 0° - 20°$ case.

Figure 5.6: Kutta-Joukowski lift calculated from measured circulation compared to directly measured lift from instrumented force balance. Duration of flap deflection lies within vertical dotted lines.

the motivation of this work to understand its aerodynamic lift response is their ability to generate instantaneous lift perturbations upon motion onset. It is clear from Figure 5.7 that flap deflection instantly generates a large lift spike over a very short convective time as a result of the added mass and pitch rate-dependent lift sources described in Chapter 3. The magnitude of the lift spike is directly proportional to motion flap frequency. The pitch-and-hold maneuvers in the present study vary in duration from a very aggressive case of $s_a/c = 0.25$, completing the motion over 0.25 chord-lengths, to a very slow motion of $s_a/c = 4$, nearing a condition of quasi-steadiness. Qualitatively, both figures show identical trends, the main difference being the 30 degree deflection case results in consistently higher forces. As the flap deflects more rapidly, additional lift is generated beyond the steady circulatory response and becomes exponentially larger with increasing flap frequency. Observe the non-linear increase in peak lift coefficient as deflection rate increases in Figure 5.7. Similarly, the drag histories experience a non-linear increase with increasing motion rate, as shown in Figure 5.8, although of much smaller magnitude than lift coefficient. More importantly, though, the pitching moment response, shown in Figure 5.9, follows the same shape as lift and drag and will likely lead to considerable vehicle control challenges if this flap device were to be directly implemented on a vehicle. The large force production from the trailing edge flap, concentrated near the rear portion of the wing, contributes to large peaks in pitching moment about the wing's quarter chord. It should be stated that the experiments in the present work are significantly rigid such that there is no aeroelastic effect during the flap motions.

Larger force production for faster deflection rates is coincident with larger cir-

culation production, shown in Figure 5.10a for $\delta = 0 - 20°$, $s_a/c = 0.5, 1$; which is in agreement with results of the previous chapter on pitching and surging wings. The faster pitch rate case generates a maximum circulation surpassing that of the slower case during the motion transient. However, both cases converge to the same value immediately following the end of flap deflection. Snapshots of PIV measurements in Figure 5.10b demonstrate the evolution of bound circulation and development of the trailing edge vortex wake. The top and middle rows correspond to $s/c = \frac{1}{2}(s_a/c)$ and $s/c = s_a/c$, respectively, showing that the flow field evolution in the two cases differs slightly during the flap transient, but 1 chord of travel after flap completion, i.e. $s/c = s_a/c + 1$, both cases converge to the same value of bound circulation and attain identical trailing edge wake trajectories.

Figure 5.11a more clearly illustrates the difference in circulation production by normalizing the horizontal axis by the duration over which the flap deflects, i.e. all motion transients occur over $s/s_a = 1$. Upon motion onset, both cases appear to produce identical circulation histories until $s/s_a = 0.3$, after which the two cases diverge and the faster flap produces additional circulation. A similar finding was presented for lift coefficient of the surging plate in Figure 4.5b, recreated here to show the similarities between the two sets of kinematics. In the case of linear surge acceleration, the difference in lift production shown in Figure 5.11b was said to be due to LEVs of increasing strength with increasing magnitude of acceleration. The present case of a hinged wing does not generate a LEV, as evidenced by PIV in Figure 5.10b, and therefore must be due to another source of additional circulation. Potential flow analysis suggests that the additional circulation is due to a "virtual camber" caused by the pitching flap that is a

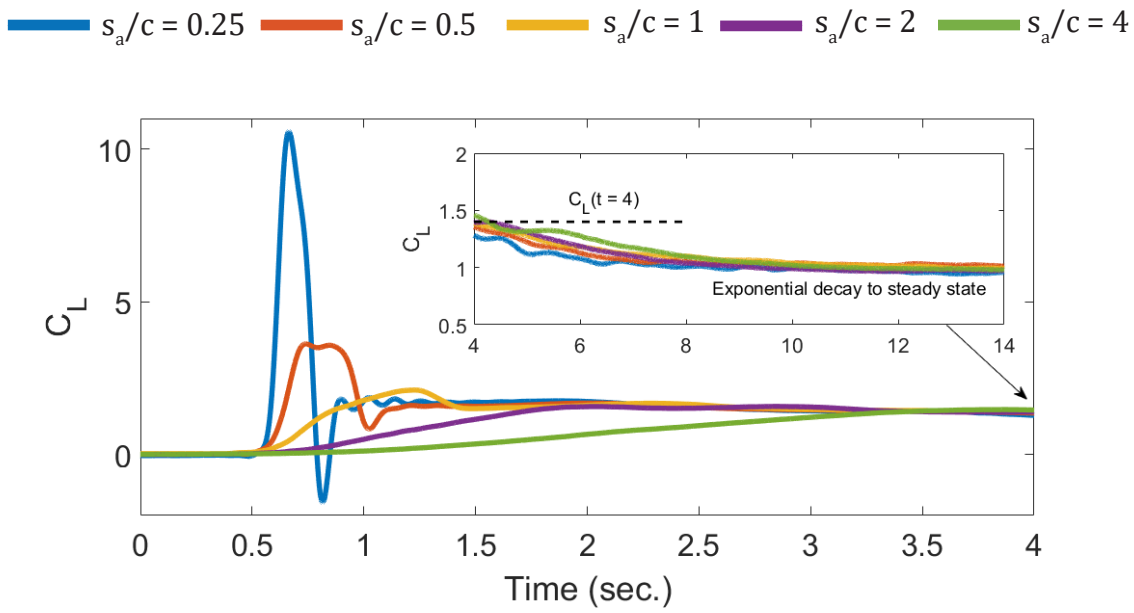

(a) Lift coefficient histories for deflection rate study of $\delta = 0° - 30°$ case.

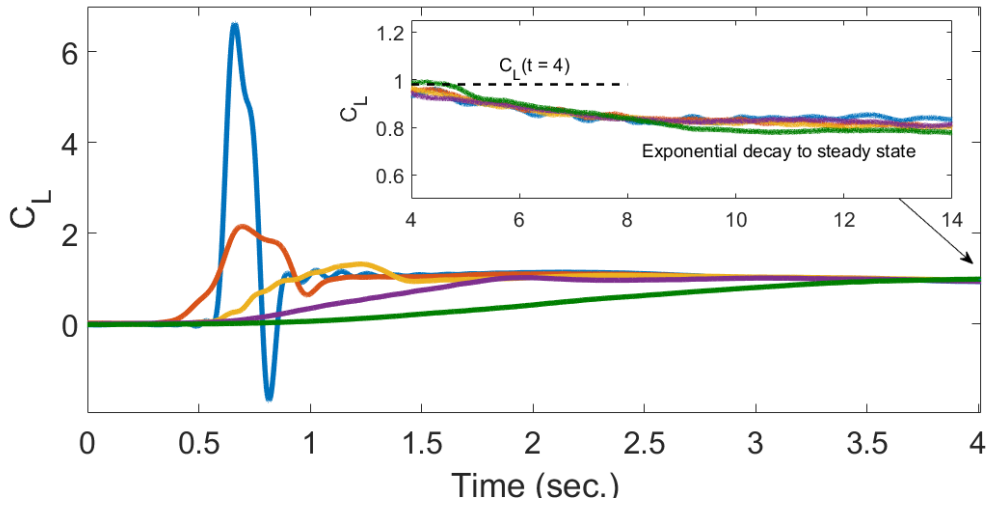

(b) Lift coefficient histories for deflection rate study of $\delta = 0° - 20°$ case.

Figure 5.7: Lift histories of deflection rate study for (a) $\delta = 0 - 30°$ and (b) $\delta = 0 - 20°$. Inset shows relaxation from elevated steady lift to fully developed steady state.

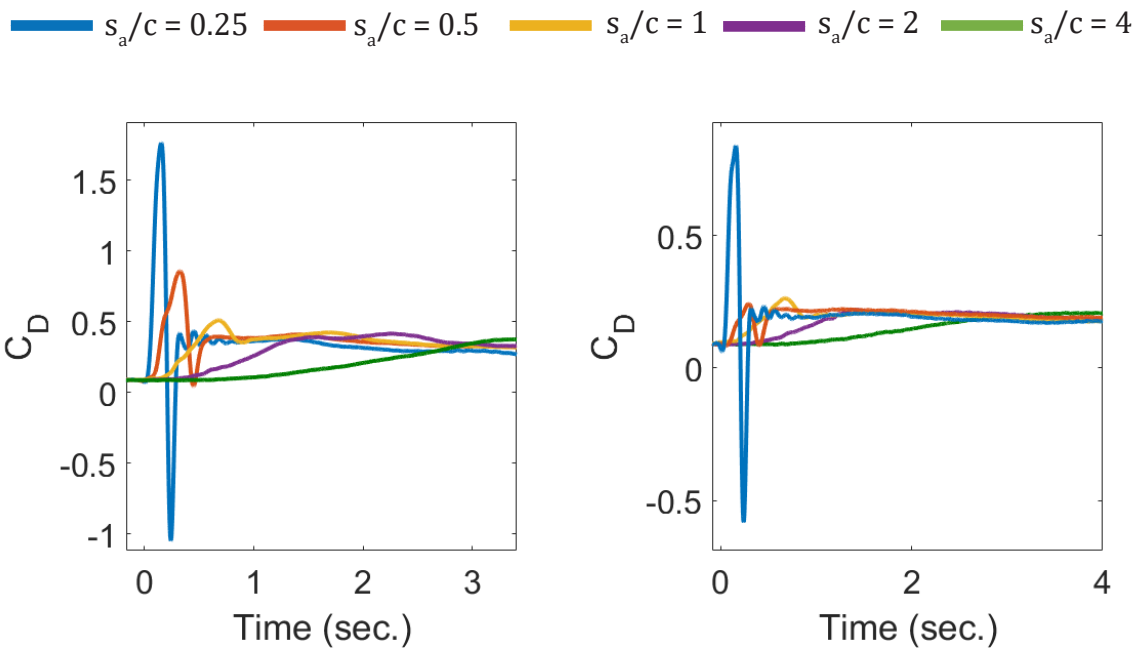

(a) $\delta = 0 - 30°$ (b) $\delta = 0 - 20°$

Figure 5.8: Drag histories for deflection rate study.

function of pitch rate, $\dot{\delta}$.

Despite the wildly different transient force responses for cases ranging from $0 < s_a/c < 4$, once the acceleration periods have completed and each case is kinematically identical, i.e. translating with fixed geometry at constant speed, all cases converge to the same lift value around $s/c = 4$ and subsequently exponentially decay to their steady state lift with identical slopes, see insets in Figure 5.7. This relaxation period corresponds to the loss of attached flow and "inviscid effectiveness" obtained in the flap transient that is maintained for several subsequent chords traveled. Rennie accounts for the loss of inviscid effectiveness in his model by switching from an inviscid lift prediction during the flap maneuver to empirical static lift data immediately following flap deflection. The present cases differ, however, because the results show a period of *prolonged*

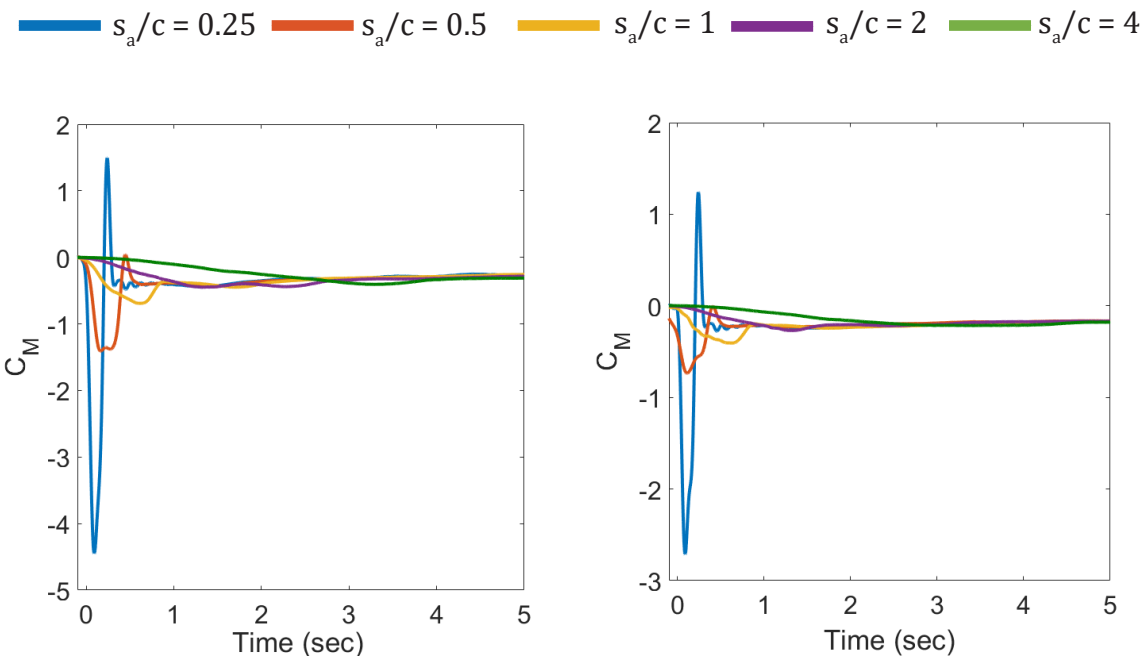

(a) $\delta = 0 - 30°$ (b) $\delta = 0 - 20°$

Figure 5.9: Pitching moment about the quarter-chord for (a) $\delta = 0 - 30°$ and (b) $\delta = 0 - 20°$.

inviscid effectiveness and attached flow that is obtained due to the more aggressive flap maneuvers, in comparison to Rennie's experiments.

Figure 5.12 illustrates the process of maintaining attached flow despite high angle of attack for rapid deflections and the eventual development into fully separated flow at long convective time. The extreme case of $\delta = 0 - 40°$ is shown here to more clearly highlight the transition process from attached to separated flow. Red and blue arrows are included to depict the gross motions of positive and negative vorticity in the flow field. During deflection, the suction surface maintains entirely attached flow and the trailing edge starting vortex curls up nearly perpendicular to the wing surface. After

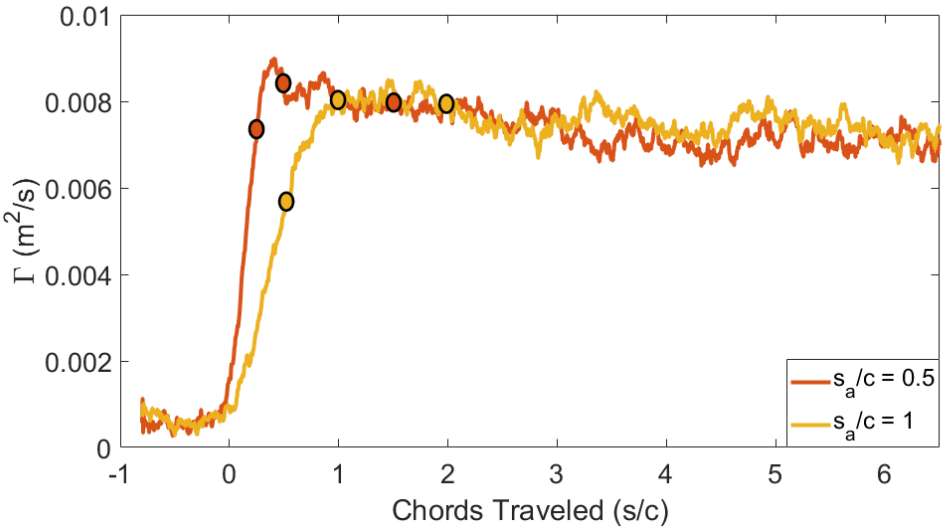

(a)

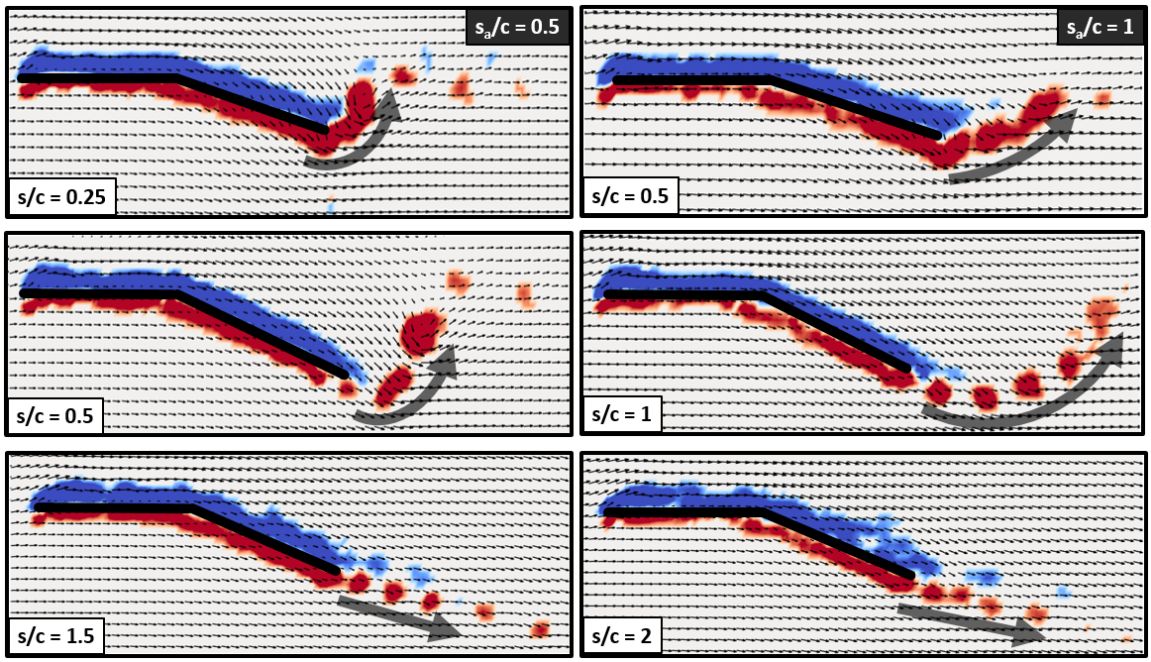

(b)

Figure 5.10: (a) Circulation histories for two deflection rates of $\delta = 0 - 20°$. (b) Velocity and vorticty fields from PIV measurements documenting circulation production for the cases presented in (a). (Top) $s/c = \frac{1}{2}(s_a/c)$, (middle) $s/c = s_a/c$, (bottom) $s/c = s_a/c + 1$. Circles in (a) correspond to PIV images in (b).

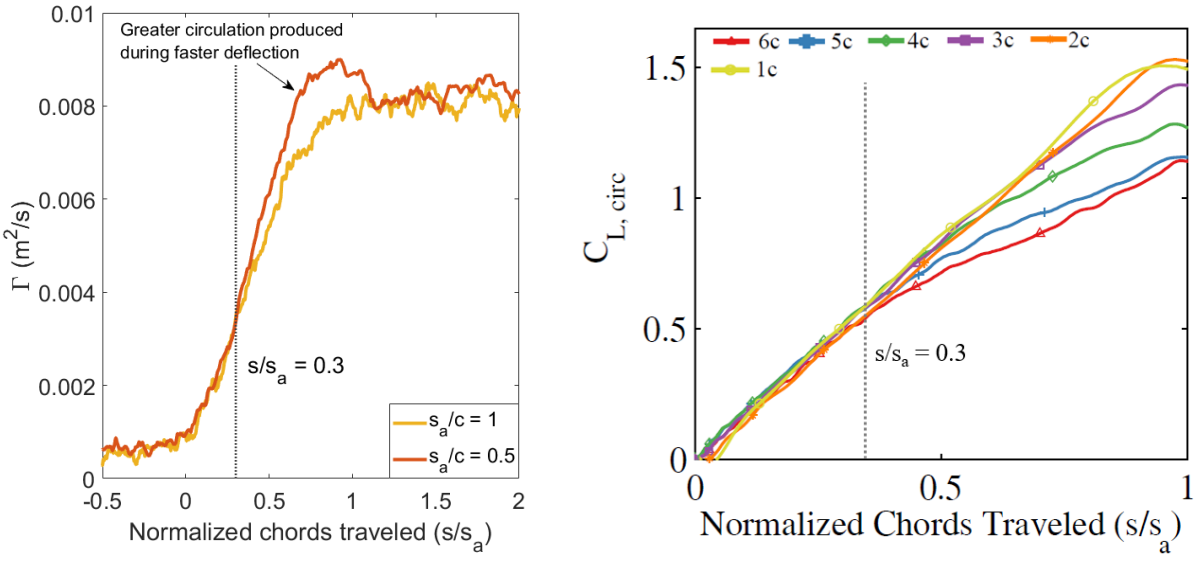

(a) (b)

Figure 5.11: (a) Circulation history of Figure 5.10 with convective time scaled by flap duration. (b) Circulatory lift component from surge acceleration study with identical scaling showing the similarities between the two sets of kinematics. Both cases contain identical circulation development until $s/s_a = 0.3$, after which cases diverge based on acceleration rate.

flap deflection is complete, vorticity produced on both the suction and pressure side of the wing flows off the trailing edge parallel to the flap (s/c = 1.5). As the wing translates at constant velocity at fixed angle of attack, attached flow along the deflected rear element begins to lift off, the free stream becomes less diverted down the path of the wing surface, and the flow relaxes to a final state where it remains largely uninhibited outside the regions of vorticity.

In contrast to the single-element pitch and surge cases of the previous chapter, this

particular geometry does not form any sort of leading edge vortex or external vortical structure following the acceleration phase of the motion, which for the single-element case led to a wide variation of relaxation slopes. Refer back to Figure 4.6 for $s/c > 6$, where all cases are kinematically identical but their lift histories vary greatly due to the reformation of LEVs, whose strengths depend on the acceleration profile during their motion transients several convective lengths prior. This pertains to the concept of a "memory" in the flow. The hinged wing does not produce any such leading edge vortices, and the result is that the flow has less "memory" with which to differentiate the relaxation response of each case.

Front and Rear Element Lift Contributions

It has been established that there are no LEVs forming over the hinged wing, which means all of the force production comes from wing camber and pitch rate effects. Chapter 3 detailed Theodorsen's potential flow solution and discussed each of the force-producing mechanisms. His model predicts that a hinged wing with deflecting trailing edge flap produces unsteady non-circulatory forces on the front element, despite it remaining stationary throughout the motion. Mathematically, this occurs because the distribution of sources and sinks placed on the wing to satisfy the no through-flow boundary condition affects the velocity field everywhere in the flow. Physically, the assumption of incompressibility mandates that any local disturbance to the flow (e.g. a physically deflecting flap) causes a pressure disturbance everywhere in the flow instantaneously. The model also assumes attached, inviscid flow at all times. These last two assumptions might be valid during the flap transient, but as shown in PIV images

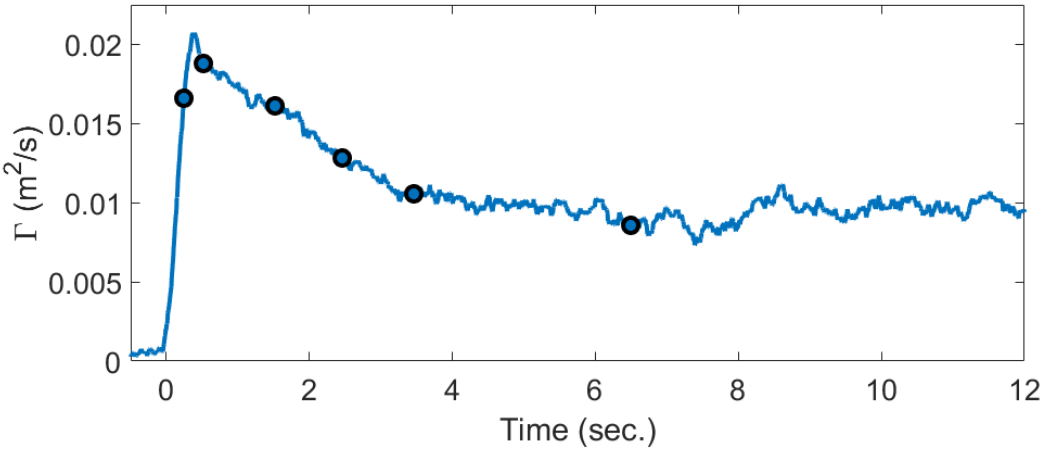

(a)

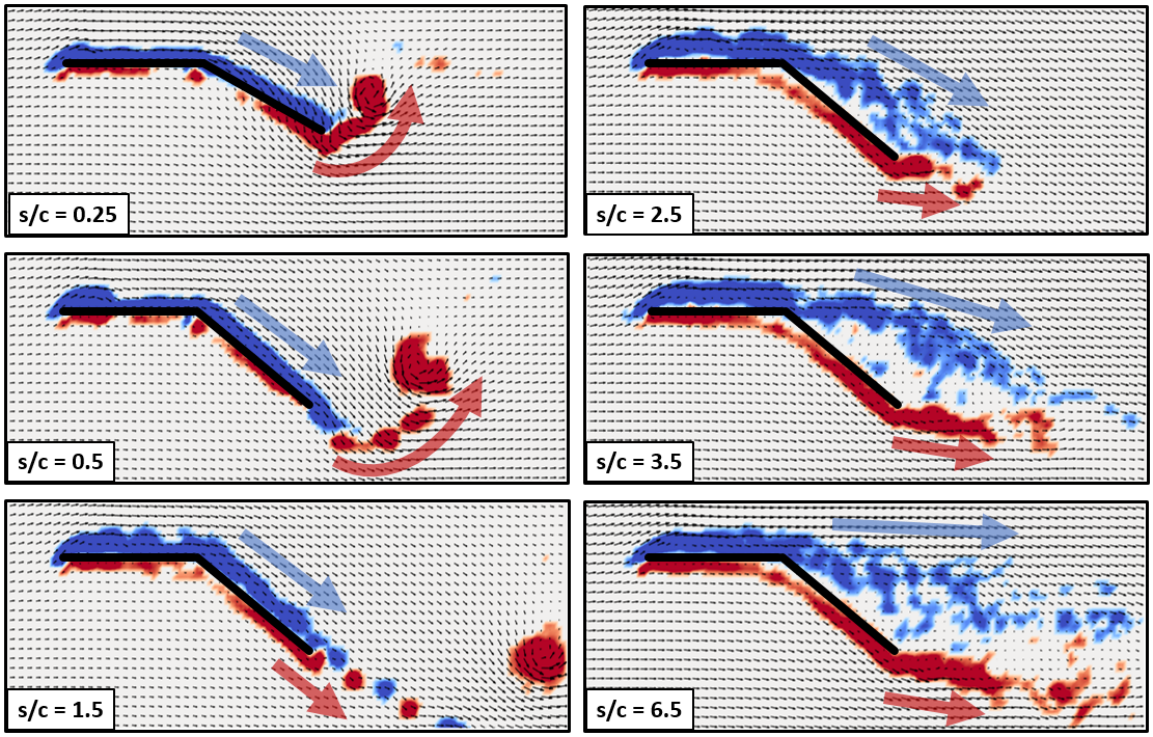

(b)

Figure 5.12: (a) Circulation history for $\delta = 0 - 40°$, $s_a/c = 0.5$. (b) Velocity and vorticty fields from PIV measurements. Circles in (a) correspond to PIV images in (b).

after long convective time the flow eventually separates from the wing surface into a fully developed separated state aft of the wing hinge. The duration of attached flow is directly related to the flap frequency and therefore one might hypothesize that for the slowest motions, $s_a/c \geq 2$, the strict potential flow assumptions may break down and not behave as predicted. This hypothesis has been examined by observing the force production on each of the fore and aft wing elements. Forces were measured using two force balances, one on the stationary front element and one on the trailing edge flap, allowing for the discretization of force contributions between the two wing elements. Figure 5.13 provides a breakdown of force histories for each pitch rate on each of the wing elements. Figure 5.13(a,c) show that the forces produced on the stationary leading edge element during slow flap cases appear to follow a quasi-steady force history with increasing angle of attack during motion transient without any sign of a lift spike or non-circulatory lift contribution. The fast cases ($s_a/c \geq 1$), however, experience a clear lift spike on the front element during flap transient very similar to, but of lesser magnitude than, that of its rear element, see Figure 5.13(a-b, c-d). It appears that a linear increase in flap deflection rate results in an exponential increase in lift produced by both the trailing edge flap and stationary front element.

To provide additional insight into each component's relative magnitude towards overall lift production, Figure 5.14 plots lift histories of both wing elements for $\delta = 0 - 20°$, $s_a/c = 0.25, 0.5, 1, 4$. Figure 5.14a contains results for the slowest case and it is shown that both elements provide relatively equal force contributions during the flap deflection. Post-flap they both relax to steady state conditions, of which the front element provides a majority of the circulatory lift. As deflection rate increases, notice

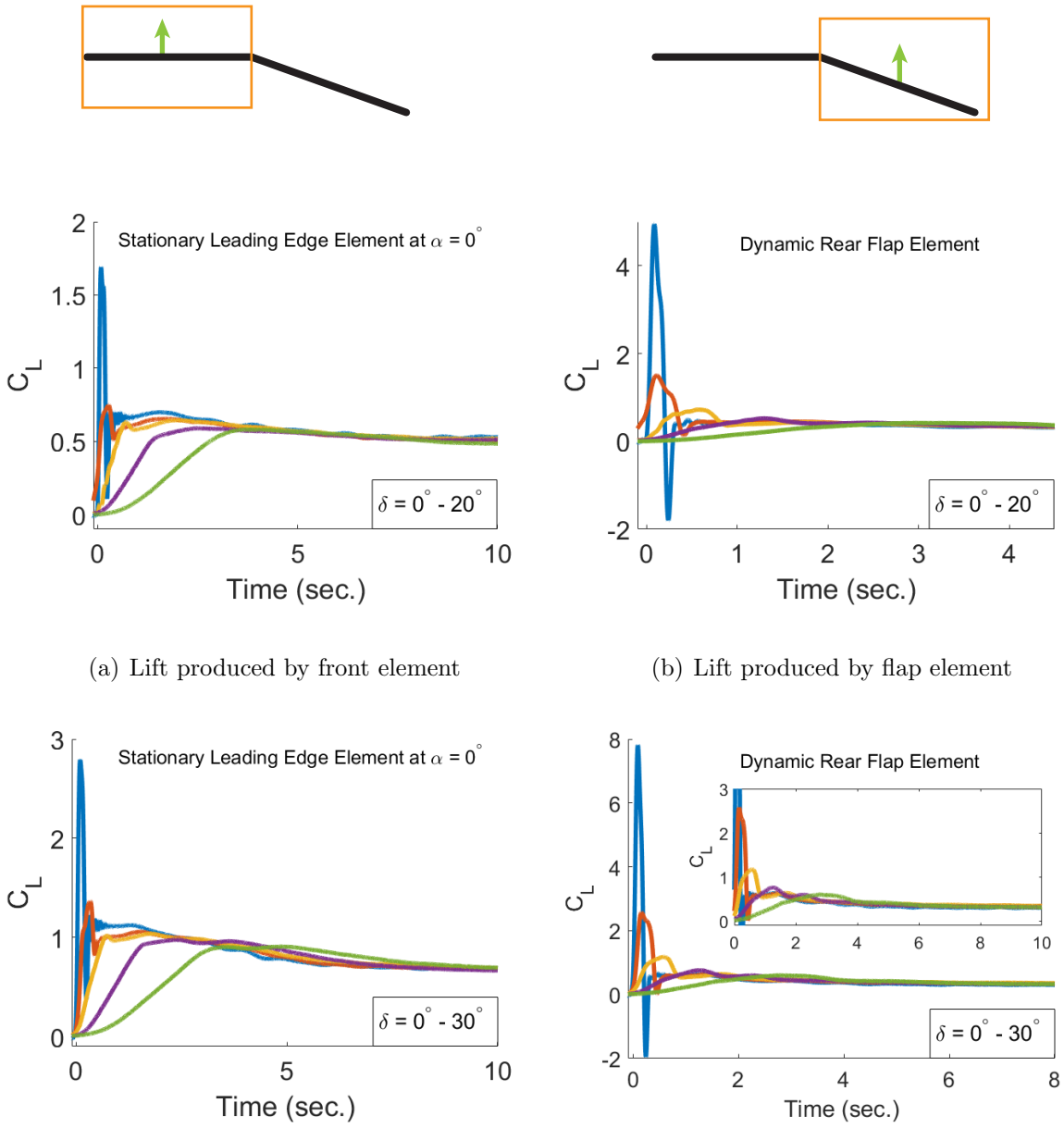

(a) Lift produced by front element

(b) Lift produced by flap element

(c) Lift produced by front element

(d) Lift produced by flap element

Figure 5.13: Measured lift coefficient on stationary front element (a,c) and rear flap element (b,d) for a range of deflection rates $0.25 \leq s_a/c \leq 4$.

that lift produced by the trailing edge flap quickly and drastically surpasses that of the leading edge element as force production becomes more dependent on pitch rate forces than steady circulatory force. It is not until $s_a/c = 0.5$ that the shape of the front element lift curve changes from resembling a quasi-steady lift slope to one containing additional pitch-dependent forces.

For extremely aggressive flap kinematics, it is evident that lift on the front element is significantly augmented by flap motion as predicted by theory, at least qualitatively. Slow to moderate flap deflections do not appear to have much of an effect on the front element. The modified aerodynamic model presented in Section 3.2 neglects any added mass or pitch rate-dependent forces produced by the fore element in an effort to simplify the problem and improve upon the consistently over-predicted result of Theodorsen's model, as will be shown at the end of this chapter. It is understood that aggressive motions will physically contain lift on the fore element, and the difference between force measurements and the modified model will allow for a realization of the fore element's unsteady lift contribution. Due to the modified model's simplicity (three separate clearly-defined terms), it should be feasible to identify the contribution from each of the theoretically identified lift sources and assess the accuracy to which the model predicts each individual contribution.

5.3.2 Flap-Up

Test cases for *flap-up* kinematics presented here are the exact reverse of the *flap-down* kinematics of the previous section. The wing's geometric initial condition is that of

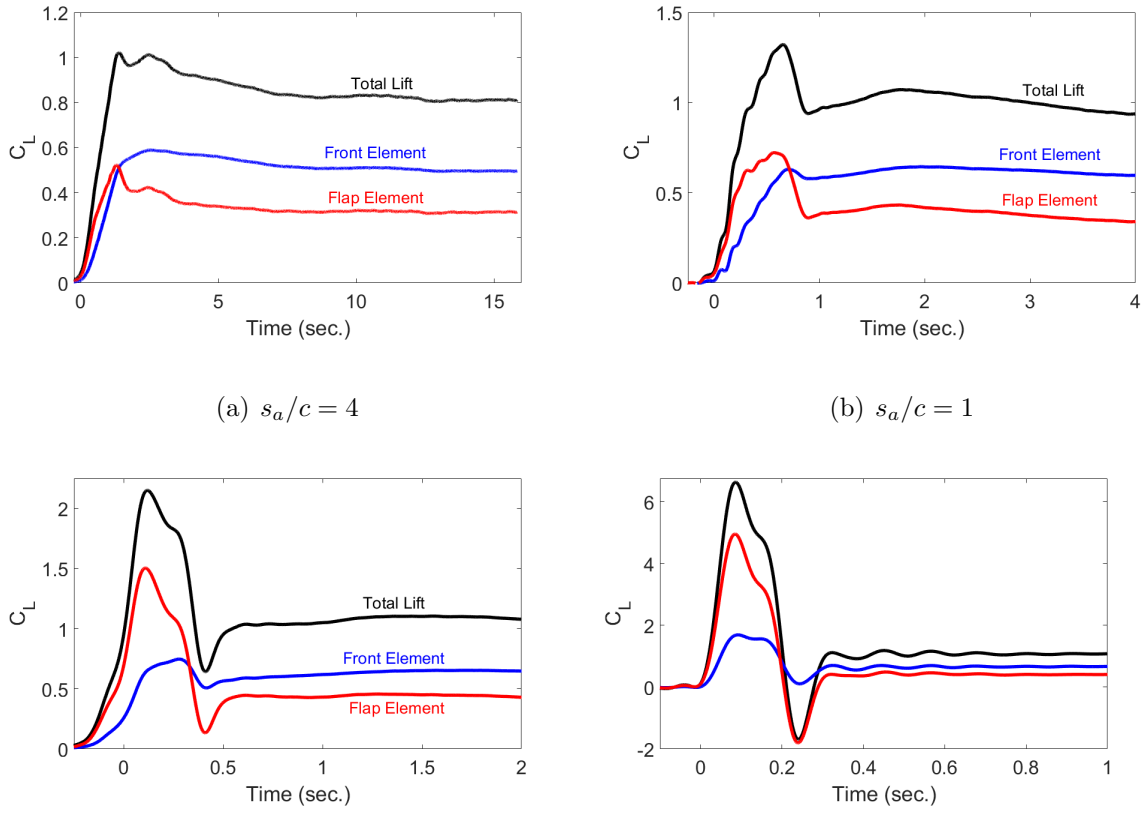

(a) $s_a/c = 4$

(b) $s_a/c = 1$

(c) $s_a/c = 0.5$

(d) $s_a/c = 0.25$

Figure 5.14: Measured lift coefficient produced by the front element (blue), rear flap element (red), and whole wing (black) for $\delta = 0 - 20°$.

a fixed-incidence trailing edge flap, where initial lift production is at its fully developed steady state value. The transient motion is an upward flap deflection to zero degrees incidence, resulting in an end condition of a wing at zero degrees angle of attack. It is important to note here that the initial condition of the flow field is fully developed flow with separation over the aft element. Therefore, this study is useful toward identifying whether the lift response of a flap in separated flow remains instantaneous and of the same magnitude (but in opposite direction) as for the flap-down cases.

Figure 5.15 provides lift histories for flap-up kinematics for several deflection rates. These rates are the same as those in Figure 5.7 but for reverse kinematics, i.e. flap pitches from 20° to 0° and 30° to 0°. The initial condition is that of a wing with deflected flap traveling at constant velocity, U_∞ and therefore has a non-zero lift coefficient for its initial value. Upon flap-up deflection at $t = 0$, there is indeed an instantaneous lift response without any lag or deadband as is occasionally observed in other lift-augmenting flow control mechanisms, e.g. pulsed actuators [103]. The inset in Figure 5.15b details the response time for the flap-up cases of $s_a/c = 0.25$ and $s_a/c = 1$. Plotted with lift coefficient is angular acceleration of the respective pitch-and-hold maneuver, acting as a representative quantity to show the timing of motion onset. Both plots show that acceleration and lift history are almost identically in phase with no lag in response time. Recall that the initial condition is not attached flow, yet there is still an instantaneous response as predicted by classical airfoil theory. The curves in Figure 5.15a and 5.15b are nearly indistinguishable in shape and only differ significantly in magnitude, as was concluded for the flap-down curves in Figure 5.7. This observation further encourages the notion that lift histories for the present geometry and flap kinematics, regardless of

attached or separated flow states, may prove to be predictable by some sort of low order model, two of which were discussed in Chapter 3.

Component forces for flap-up $\delta = 20° - 0°$ kinematics are provided in Figure 5.16 as blue and red lines for the $s_a/c = 0.25$ and $s_a/c = 0.5$ cases, respectively. Black lines in each plot correspond to each case's *flap-down* counterpart, i.e. both sets of lines should have opposite initial and final lift values. Finally, yellow lines are the result of flipping the flap-up lift about its initial value and shifting it to begin at zero to directly compare the magnitudes and shapes of flap-up and flap-down lift curves. Much like the flap-down case, flap-up kinematics are similarly driven by rate-dependent forces, which considerably surpass the contribution from quasi-steady circulatory lift and result in large lift spikes during the motion transient. Focusing first on the fast $s_a/c = 0.25$ case, comparing the yellow and black lines reveals a striking similarity in magnitude and shape of lift during the flap transient, $t < 0.25$. Classical aerodynamic theory using methods of linear superposition would predict a similar result. In fact, Theodorsen's model would predict the yellow and black lines to be exactly identical. We see here that this is not the case, and it is hypothesized that the disparity stems largely from the fact that the flap-up case begins its motion from a fully developed steady state whereas the flap-down case experiences a brief period of "inviscid effectiveness," where it reaches a maximum steady circulatory lift contribution akin to the theoretical value. This is evidenced by the large overshoot of the black curve in early times for the front element, after which it converges with the flap-up result around $t = 6$. Although the unpacking of individual force contributions is not possible with only a single force measurement, it is clear that rate-dependent forces dominate and are largely in accord between both

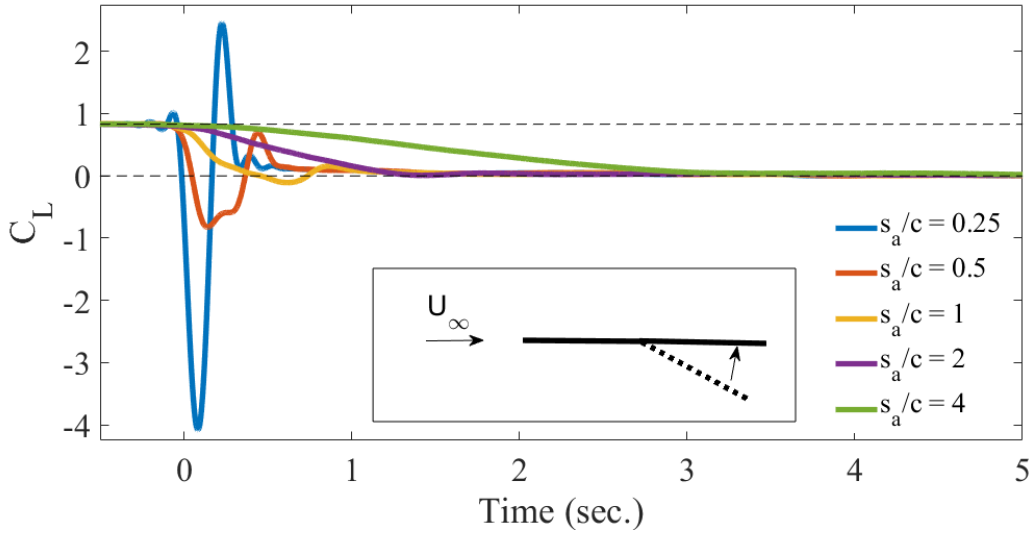

(a) $\delta = 20 - 0°$

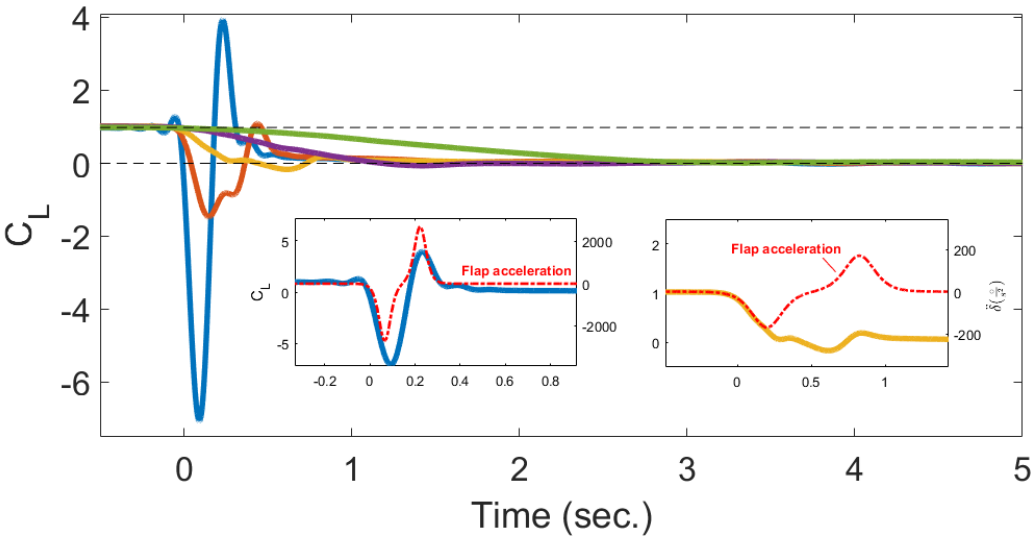

(b) $\delta = 30 - 0°$

Figure 5.15: Lift histories from deflection rate study for (a) $\delta = 20 - 0°$ and (b) $\delta = 30 - 0°$. Horizontal dotted lines indicate initial state and final steady state lift coefficient.

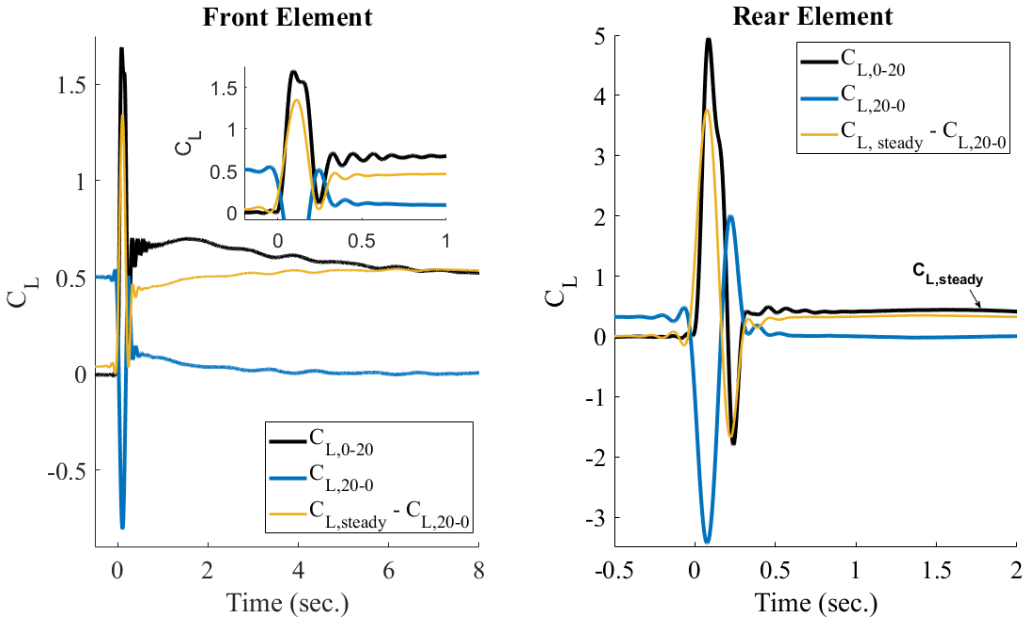

(a) $s_a/c = 0.25$ (b) $s_a/c = 0.25$

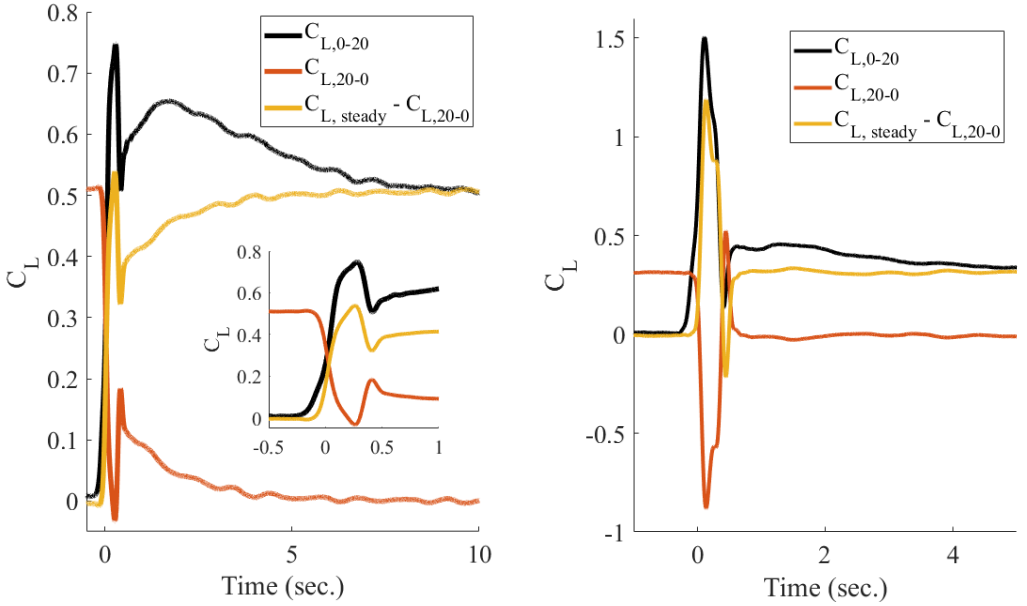

(c) $s_a/c = 0.5$ (d) $s_a/c = 0.5$

Figure 5.16: Component forces for $\delta = 20° - 0°$, $s_a/c = 0.25$ (blue) and $s_a/c = 0.5$ (red) kinematics. Black lines correspond to $\delta = 0° - 20°$ cases. Flap-up cases are also flipped and zeroed to show relative magnitude to flap-down motions.

sets of kinematics, suggesting that a successful low order model remains viable with the understanding that steady circulatory lift may have to be modified to account for varying initial flow conditions.

5.3.3 Flap in Full Leading Edge Stall

The experimental hinged wing survey concludes by addressing force production due to an actuating flap on a wing undergoing leading edge stall. The fore element of the hinged wing is fixed at incidence angle $\alpha_{LE} = 20°$, which at steady state results in fully separated flow about the leading edge. Figure 5.17 provides qualitative flow field images illustrating immediate separation at the leading edge for the entire motion. Flap-up and flap-down motions, corresponding to $\delta = 20° - 0°$ and $\delta = 0° - 20°$ cases, respectively, were tested. Flap deflection angle, δ, is measured exactly the same as it was for the $\alpha_{LE} = 0°$ cases, with $\delta = 0°$ corresponding to the flap aligned with the horizontal. The reader should compare the results of this section to their analogous $\alpha_{LE} = 0°$ cases of Figures 5.7 and 5.15.

Figure 5.18 provides experimental lift histories for flap-down and flap-up actuation with the fore element fixed at $\alpha_{LE} = 20°$. Focusing first on the motion transient portion of the force histories ($0 < s/c < s_a/c$), the immediate lift response in Figure 5.18 looks very similar in shape and magnitude to those from cases with the fore element at $\alpha_{LE} = 0°$. There is an immediate response without deadband (either positive or negative depending on flap direction) and maximum force production that far surpasses the static response. By now it should be clear that actuation of a large trailing flap at

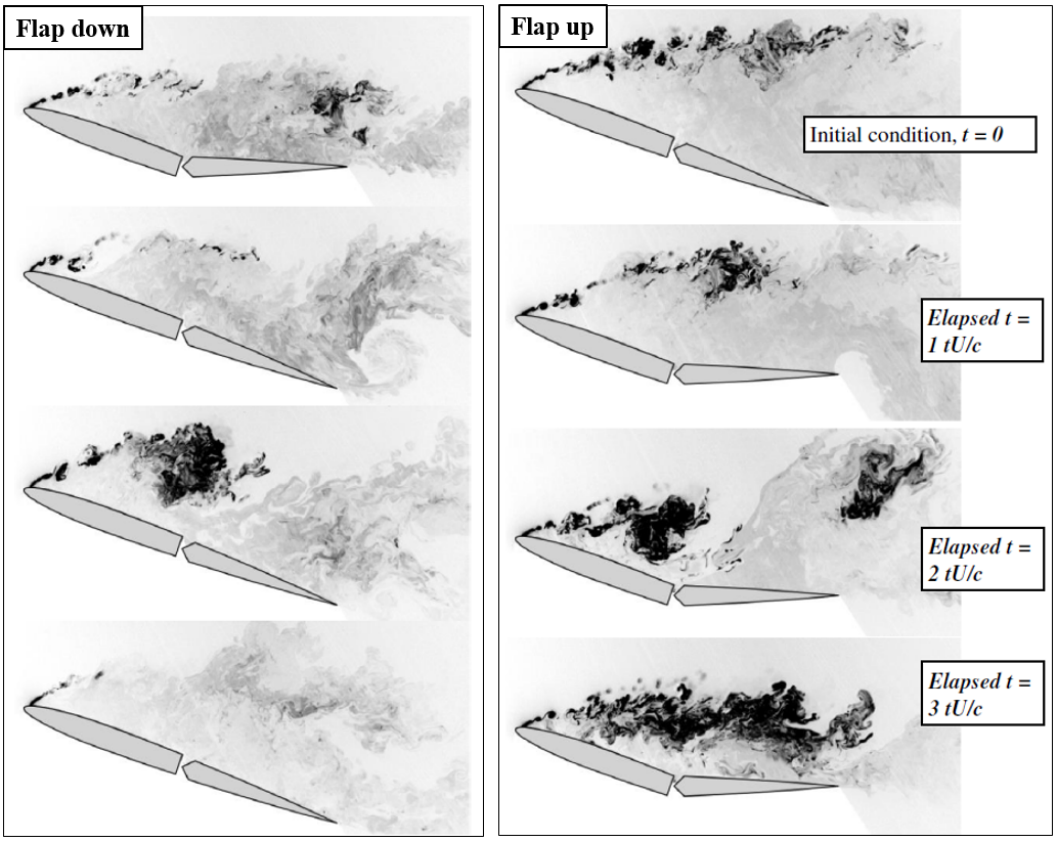

Figure 5.17: Flow visualization for $s_a/c = 0.5$ flap down (left) and flap up (right) kinematics with the leading edge element fixed at $\alpha = 20°$. Figure adapted from Medina, OL, Mancini, and Jones [72].

sufficiently high motion rate can provide significant force production independent of an attached flow state.

Upon completion of flap deflection for both flap-up and flap-down kinematics with $\alpha_{LE} = 20°$, a new vortical structure forms at the leading edge around $s/c \approx 2$, resulting in augmented circulatory forces. The flap-down case appears to generate a leading edge vortex akin to that formed during the single-element surging wing case in Chapter 4 that grows for several convective times and convects downstream, whereas the flap up case

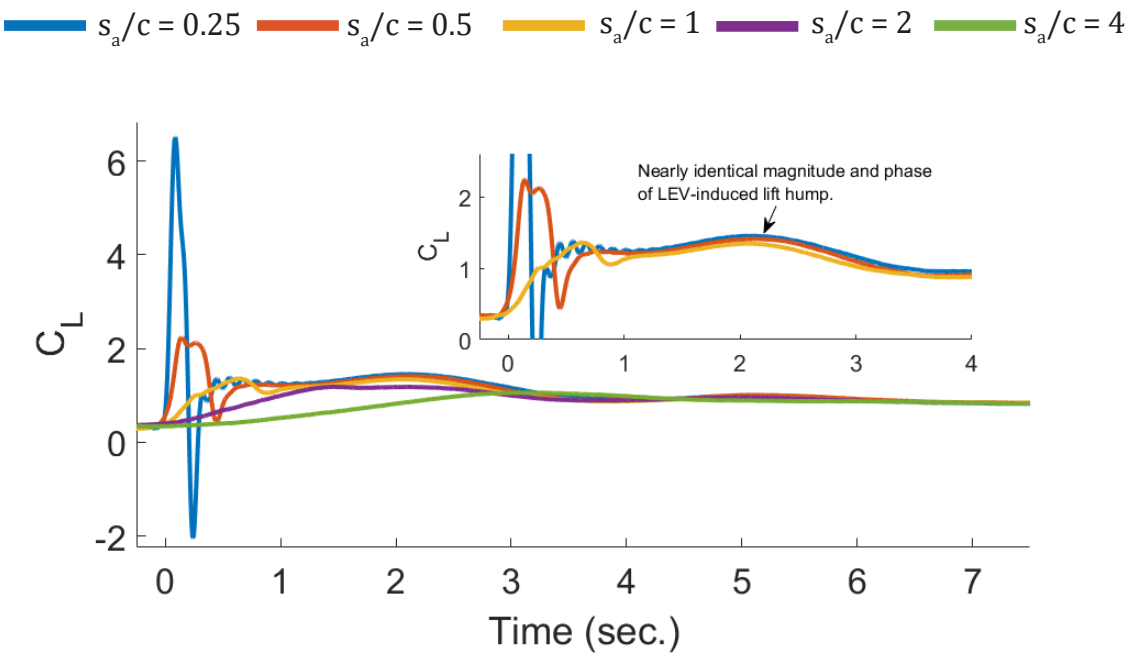

(a) $LE = 20°, \delta = 0 - 20°$

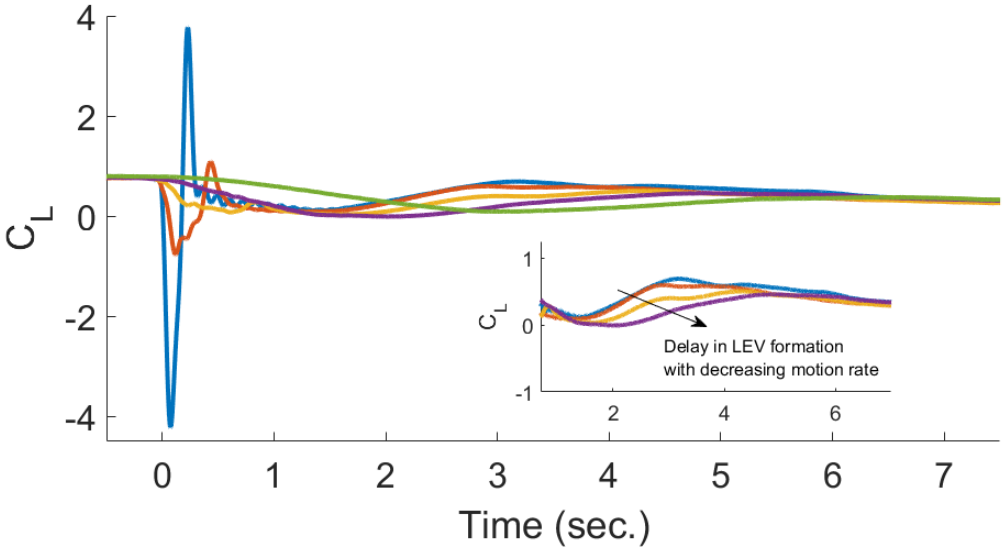

(b) $LE = 20°, \delta = 20 - 0°$

Figure 5.18: Lift histories from deflection rate study for (a) $\delta = 0 - 20°$ and (b) $\delta = 20 - 0°$ with LE element fixed at 20°.

develops more of a recirculation region than a coherent shedding LEV. These phenomena are documented via fluorescent dye flow visualization in Figure 5.17. The insets of Figure 5.18 highlight the effect of these LEVs on force production for flap-down and flap-up motions. The flap-down cases of Figure 5.18a result in nearly identical magnitudes and phases of the LEV-induced lift hump. The difference in magnitudes of the local lift coefficient maxima during LEV formation at $s/c = 2.2$ is approximately 0.1, which corresponds to 8% of the total lift, despite the motion profiles varying in acceleration by a factor of 4. Therefore, the subsequent LEV formation appears to be independent of deflection rate if the rate is sufficiently fast, i.e. in this case $s_a/c \leq 1$. Flap-up motions, however, do appear to be sensitive to deflection rate, as the subsequent lift increase due to formation of a recirculation region on the suction surface shows a delay in formation with decreasing deflection rate.

Comparison to Surging Wing

Drawing parallels between the leading edge vortex formation due to trailing edge flap actuation and that of an inclined plate surging from rest (described in Chapter 4), Figure 5.19 provides force histories from both flap and surge kinematics for non-dimensional acceleration rate $s_a/c = 1$. Recall that the for the hinged wing, the fore element is fixed at $\alpha_{LE} = 20°$ and the trailing edge flap reaches a final deflection angle of $\delta = 20°$; therefore, after $s/c = 1$, both cases are equivalently translating at constant free stream, U_∞, as an uncambered wing at angle of attack $\alpha = 20°$. It is not surprising that lift production during acceleration transients differ, as they have considerably different starting motions. However, the comparison in Figure 5.19 suggests that there might be a

sensitivity to the initial kinematics on subsequent flow field development and force production following the acceleration transient. Although both sets of of kinematics show

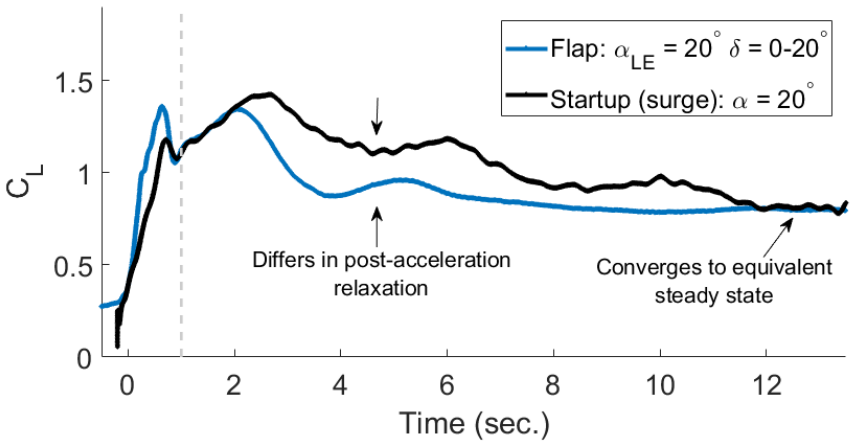

Figure 5.19: Comparison between surging flat plate at $\alpha = 20°$ and hinged plate with $\alpha_{LE} = 20°$, $\delta = 0° - 20°$. Both motion transients occur over $s_a/c = 1$.

formation, shedding, and reformation of leading edge vortices, causing an oscillatory relaxation to an equivalent steady state value, the single-element surging wing results in significantly larger lift during the development towards steady state. This is likely due to a stronger initial LEV for the single-element plate, which may lead to more aggressive shedding dynamics and subsequent reformation of stronger leading edge vortices. Ultimately gained from this analysis, and that of the previous chapter, is the insight and understanding that, depending on motion rate and type of transient kinematics, it is very important to have knowledge of the kinematic history if one is to attempt to predict a time history of force production on a moving wing.

Comparison to $\alpha_{LE} = 0°$ Case: Component Forces

We now compare component-specific force production between hinged wings undergoing rapid flap actuation in both *fully attached* and *fully separated* flow. Fore and aft component lift production for flap-down kinematics with stationary fore elements at $\alpha_{LE} = 0°$ (blue) and $\alpha_{LE} = 20°$ (red) are presented in Figures 5.20 and 5.21. Rear element actuation history is equivalent between the two cases. The only difference between the two geometries is the fixed incidence angle of the fore element.

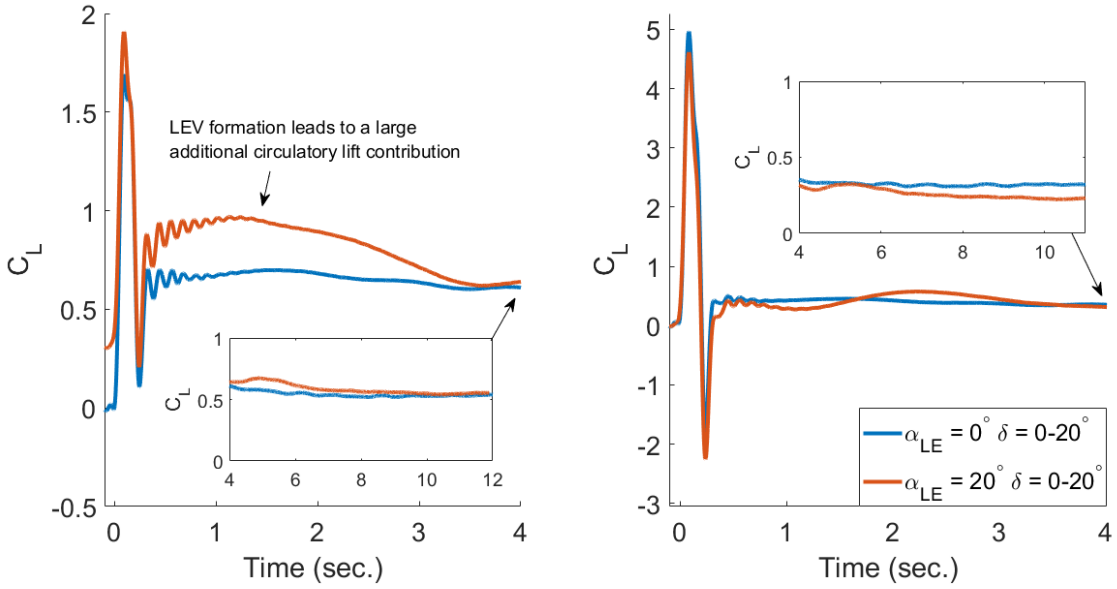

(a) **Front element**, $s_a/c = 0.25$ (b) **Rear element**, $s_a/c = 0.25$

Figure 5.20: Lift histories on (a) front element and (b) rear element for $\delta = 0{-}20°$ where the leading edge is fixed at $\alpha_{LE} = 0°$ (blue) and $\alpha_{LE} = 20°$ (red).

Static force production on the inclined front element naturally results in a non-zero steady state value, as shown in each of the left column figures at $t = 0$, thus resulting in an initial offset from the zero-incidence case. However, dynamic flap actuation results

in instantaneous force production on both stationary leading edge elements independent of inclination angle. Focusing solely on the acceleration phases, $0 \leq s/c \leq s_a/c$, if one was to tare the initial offset from the $\alpha_{LE} = 20°$ case, the transient lift responses would appear almost identical. Full leading edge separation does not cause a delay or deficiency in unsteady force production on the fore element during the motion transient, just merely a shift due to different initial conditions. Following flap actuation, the $\alpha_{LE} = 20°$ cases experience the formation of a LEV that results in large lift peaks on the fore element lasting approximately two convective lengths. LEV-induced lift enhancement occurring over the front element from $s_a/c \leq s/c \leq 3$ appears to be of similar magnitude between the three deflection rates, contributing a maximum additional lift coefficient increase of roughly 0.3. The primary difference between the curves is their transient response, but the post-acceleration lift history is rather similar. Note that curves may look dissimilar due to the difference in vertical axis scaling. The effect of the LEV is not limited to the front element. In fact, its convection is observable by a clear lift hump during $1.5 \leq s/c \leq 3.5$ on the rear element, capturing chordwise convection of the vortex and its effect on each wing element as it moves. As shown in the figure insets, both cases relax, perhaps coincidentally, to similar steady state values. Recall that one is in massively separated flow and the other is relatively attached.

Looking now at the dynamic rear element (right columns of Figures 5.20 and 5.21), both $\alpha_{LE} = 0°$ and $\alpha_{LE} = 20°$ cases begin at zero lift. As with the fore element, it appears that the rear wing element robustly produces similar force histories regardless of an attached flow state, with perhaps a slight decrease in circulatory component for the $\alpha_{LE} = 20°$ cases. However, that circulatory loss accounts for a difference of only

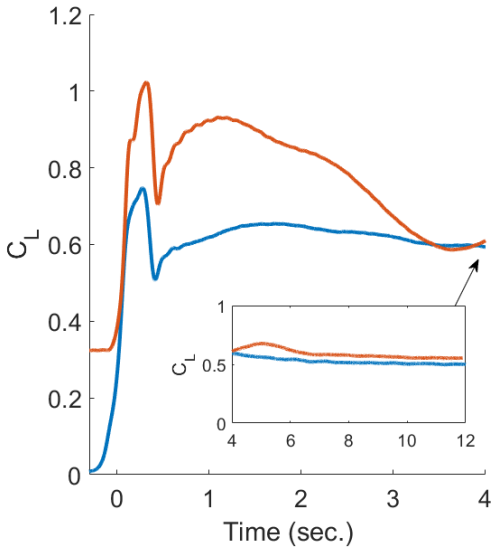

(a) **Front element**, $s_a/c = 0.5$

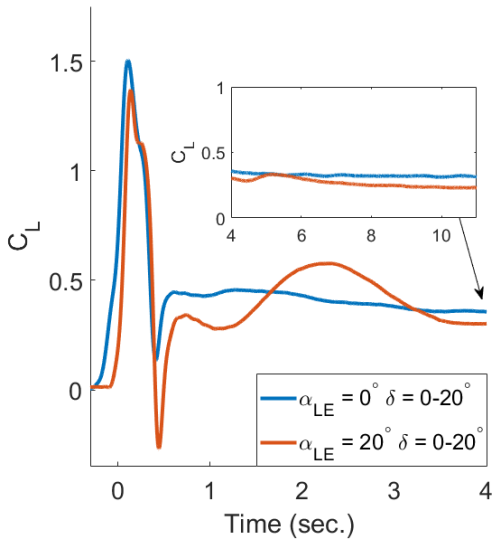

(b) **Rear element**, $s_a/c = 0.5$

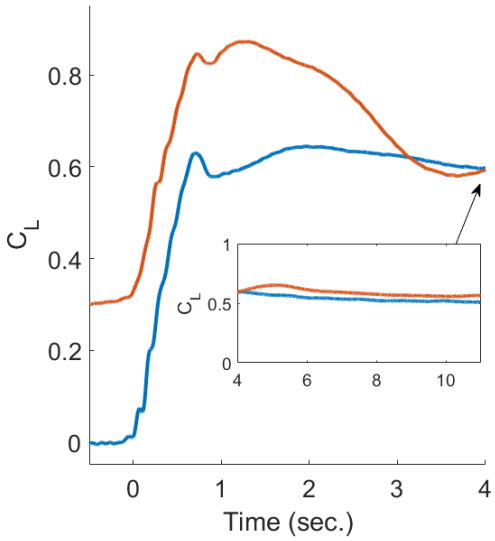

(c) **Front element**, $s_a/c = 1$

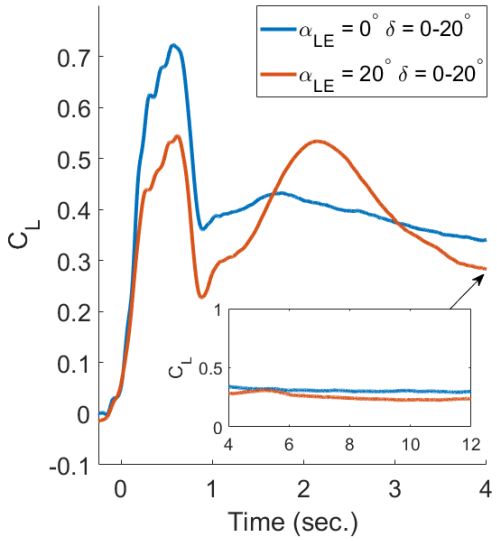

(d) **Rear element**, $s_a/c = 1$

Figure 5.21: Lift histories on (a,c) front element and (b,d) rear element for $\delta = 0 - 20°$ where the leading edge is fixed at $\alpha_{LE} = 0°$ (blue) and $\alpha_{LE} = 20°$ (red).

≈ 0.2 between attached and separated cases. Vertical axis scaling of the $s_a/c = 1$ case makes curves appear very different, but note that the difference is still only 0.2.

5.4 Concluding Remarks on Force Measurements

Insensitivity to the current flow state (attached or separated) of unsteady force production for the present wing kinematics motivates the hypothesis that the aerodynamic responses shown here have the potential to be accurately modeled analytically using classical attached flow theory, or some modification of such theory. This hypothesis will be tested in the final section of this chapter.

First, the following section will explore the application of a two dimensional semi-empirical model (vortex impulse method) to predict force production on the wing. This effort does not satisfy the ultimate goal of identifying an accurate model based solely on wing kinematics, as lift from vortex impulse currently requires empirical velocity field measurements. However, the results of the following section will be used to substantiate the use of the low order model presented in Chapter 3, providing support and explanation of each term's physical significance.

5.5 Force Prediction Using Vortex Impulse Method

In the early 1930's, Sir Horace Lamb published theoretical work outlining the concept of an impulsive fluid force generated from the growth and relative displacement of two equal, opposite-strength point vortices [54]. The crux of these efforts lies in the notion that aerodynamic lift can be determined by observable, quantifiable flow structures,

i.e. vortices, assuming their behavior falls in line with the assumptions on which the theory is based. The two main assumptions include: 1) two-dimensional, potential flow and 2) equal and opposite strength vortices created from a single event. This work was later expanded upon by von Karman and Sears and repackaged to present the result in terms of aerodynamic lift [78]. Dr. John Anderson shared this sentiment in a more general sense in his introductory aerodynamics textbook, stating "It is not quite proper to say that circulation 'causes' lift. Rather, lift is 'caused' by the net imbalance of the surface pressure distribution, and circulation is simply a defined quantity determined from the same pressures" [104]. It is the purpose of this section to reconcile the interchangeability of lift and circulation and understand that circulation production is a physical manifestation and visual representation of forces experienced by the lifting surface. Based on flow field analysis of the previous sections, it is clear that the present experiment does not contain two "vortices", but instead various forms of attached and separated shear layers. Thus, the present implementation will be an adaptation of Lamb's point vortex impulse model, redefining the *position* and *location* of each "vortex". It is therefore possible that some of the originally modeled physics may be lost. However, qualification for each adaptation will be provided and results of the model will be shown to agree very well with experimental measurements.

5.5.1 Vortex Dynamics: Application to Lamb's Model

Introduced in Chapter 2, non-dimensional lift coefficient normalized by the free stream speed as predicted by Lamb is given by

$$C_L = \frac{2}{U^2 c}[(u_+ - u_-)\Gamma + (x_+ - x_-)\dot{\Gamma}]. \tag{5.1}$$

Vortex convection speed, u, and vortex position, x, contain the subscripts "+" and "-" corresponding to positive and negative signed vortices, respectively. Γ and $\dot{\Gamma}$ are the strength and time rate of change of circulation. It is important to address the fact that Equation 5.1 is based on a potential flow model containing *point singularities*. Lamb's use of point vortices requires that all circulation is contained in an infinitesimally small point in an otherwise irrotational flow. Figure 5.22 illustrates Lamb's definition of a vortex pair.

We know that point singularities do not exist physically, as it is impossible to obtain infinite velocity at the vortex center. In order to apply Equation 5.1 to the PIV measurements of the current work, a few adaptations must be made to the definition of what Lamb considers a "vortex." It was shown in the previous sections that the present set of wing kinematics may or may not contain a coherent circular vortex, whose presence is highly dependent on flap deflection angle, pitch rate, and fore element incidence angle. To provide a robust method for determining "vortex strength" where an identifiable vortex is not present, the current work will use the integration bounds defined for circulation calculations, see Figure 2.15, as a fixed area in which all vorticity within those bounds will be amalgamated into a single "vortex" of circulation strength equal

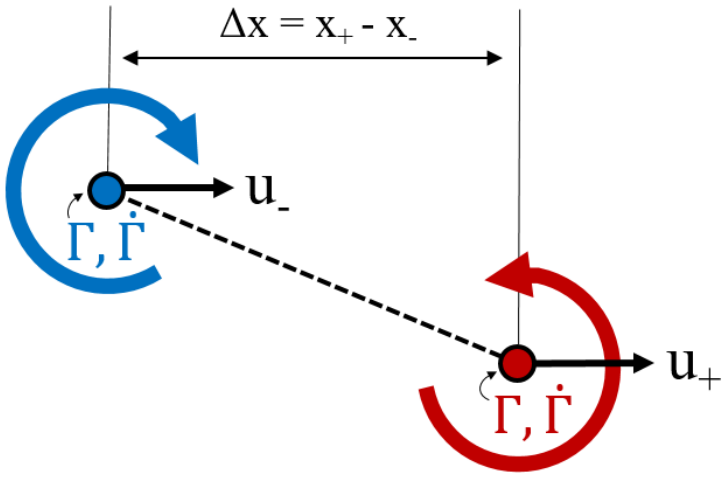

Figure 5.22: Schematic of equal and opposite strength point vortex pair as described by Lamb.

to the summation of that vorticity.

Vortex Strength, $\Gamma(t)$

Lamb assumes both vortices in his two-vortex system of Figure 5.22 to be of equal and opposite strength at all times. If Eq. 5.1 is to be applied to the present experiment it must first be proven that the two "vortices" in the PIV measurements are of equal and opposite strength. Figure 5.23 provides time histories of bound and wake circulation for several sets of flap kinematics. These comparisons can only be carried out for as long as the newly formed trailing edge vorticity remains in the PIV image frame, after which the *total* wake circulation can no longer be confidently measured. Additionally, since flap-up cases have an initial condition of separated flow, and because a complete time history of wake vorticity is not possible due to the fixed-size image window, wake vorticity mea-

surements were offset to begin in-line with bound circulation prior to motion onset at $t = 0$. This allows for the observation and comparison of their relative slopes and magnitudes over time. Ideally, any change in bound circulation should be equally reflected by opposite signed vorticity concurrently shed into the wake from the trailing edge. Since both bound and wake circulation are nearly identical for every case tested in this work, the result of Figure 5.23 provides evidence for the assumption that the current rapidly deflecting trailing edge flap motions generate two equal and opposite "vortices", checking off one requirement for the application of Lamb's vortex impulse model. Circulation strength and its time derivative will now be taken as that of measured bound circulation.

Relative Vortex Displacement and Velocity (Δx, Δu)

It is now necessary to discuss the spatial relation of these two "vortices" with respect to each other, as their relative displacement, Δx, and relative velocity, Δu, are directly proportional to lift production. Lamb's vortex impulse model requires the information from two distinct vortices. As evidenced by aforementioned figures and discussion, these results do not contain two distinct vortices. In order to implement this method to represent the shear layers both attached to the wing and freely convecting in the wake, it is necessary to redefine what is meant by each "vortex". This may result in a slight misrepresentation of the exact physics Lamb captures in his model, but the newly defined vortex strength and position aim to parallel as closely as possible with what is captured in Lamb's model.

Regarding the trailing edge wake, the present experiment contains a shear layer emanating from the trailing edge, and in order to apply a low order model, some ad-

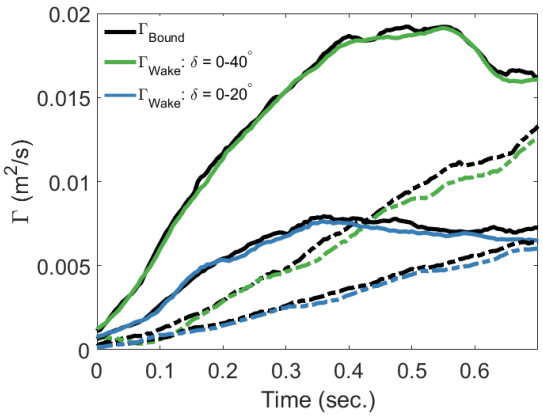

(a) Flap Down: (-) $s_a/c = 0.5$, (-.-) $s_a/c = 1$

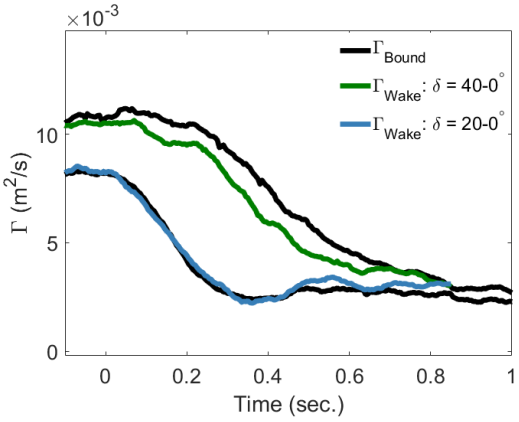

(b) Flap Up: $s_a/c = 0.5$

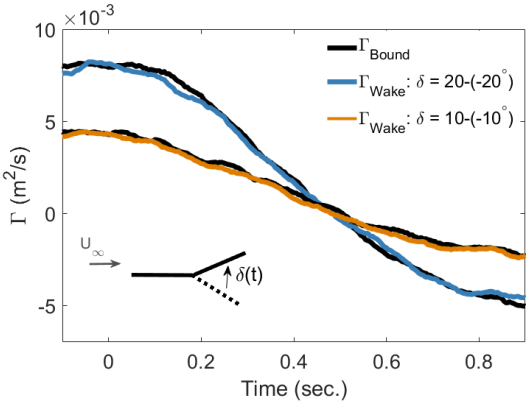

(c) Flap-Up: $s_a/c = 1$

Figure 5.23: Absolute values of bound and wake circulations during motion transients for flap-down and flap-up kinematics. Plot abscissas end around $t = 0.7 - 1$ depending on when the newly formed trailing edge vorticity exited the image frame.

ditional effort must be taken to characterize and simplify this spatially and temporally developing wake that contains structures other than coherent point vortices. Vortex wakes are typically categorized as either free wakes or prescribed (fixed) wakes [105]. Free wakes provide higher-fidelity solutions by accounting for mutual induction between

wake vortex elements, allowing the wake structure to deform with time. This comes at the expense of significantly higher computational costs. Fixed wakes, however prescribed, ignore time-stepping wake evolution altogether and enforce a specific wake trajectory. Classical airfoil theories, e.g. Theodorsen and Wagner's solutions, are typically developed under the assumption of a horizontally convecting wake extending into an undisturbed farfield. This allows for an analytical simplification and overall method robustness that has perpetuated its use for nearly a century. For the present work, the objective is to apply a low order model in a robust fashion to predict lift over a wide design space of deflection angles, pitch rates, and initial flow conditions. Thus, it is not practical to quantify wake shape development for *every* case in this work. Instead, a general assumption for relative vortex dynamics is explored to form a robust method of lift calculation applicable to any set of hinged wing kinematics.

Using time-resolved velocity fields from PIV measurements, two methods of vortex tracking have been implemented: 1) Centroid of vorticity and 2) vortex center identification via γ_1 criterion. The centroid of vorticity is calculated separately for both the bound and wake vortices using Equations 2.8 - 2.11 each within the their respective integration bounds. The γ_1 criterion, Equation 2.7, requires the existence of a coherent, circular vortex; thus, this method can only be applied to the trailing edge wake as the bound circulation does not contain a discernible circular vortex. Conversely, the centroid of vorticity method is the most robust of the two because it is insensitive to the existence of a vortex and simply computes the mathematical centroid of any vorticity in the interrogation region. For both methods, however, the duration over which the *entire* trailing edge wake can be tracked is limited to the time it takes for the shed trailing

edge vortex to leave the image. For the present field of view and free stream speed, that time corresponds to about 1 second (or one convective chord traveled). Although a short time relative to the entire duration of acquired PIV and force measurements, one convective chord of travel is sufficiently long to observe vortex dynamics during the flap deflection for $s_a/c = 0.5$ and a subsequent $s/c = 0.5$ at its fixed final deflection angle. Figure 5.24 illustrates the spatial evolution of bound and wake vortices using the centroid of vorticity and γ_1 methods. Note that the γ_1 method could not be applied to the bound circulation, as it does not contain a circular vortex for the γ_1 criterion to identify. Several instantaneous snapshots of the wake are included in the figure as well to show the nature of the wake shape over the course of flap deflection.

Focusing first, however, on the measured location of the *bound* vortex (green trajectory in Figure 5.24), notice that the centroid of vorticity remains relatively local to the mid-chord throughout the flap transient. Recall that this quantity is the spatial average between the centroids corresponding to both positive and negative vorticity on the wing itself (not shown in figure). The "vortex location" ascribed to the Lamb vortex from bound vorticity is well-described using the centroid method, because both the location of vorticity generation and the centroid itself are locally contained within a fixed region over all time. That is, opposed to the trailing edge wake whose interrogation region theoretically expands into the farfield along with the convecting wake vorticity. The invariability in bound vortex location supports the simplification of mathematically replacing the wing with a single vortex of strength Γ_{bound}.

As mentioned, the trailing edge wake is not locally constrained by a body and is free to convect with the free stream. Typical use for vortex tracking methods are

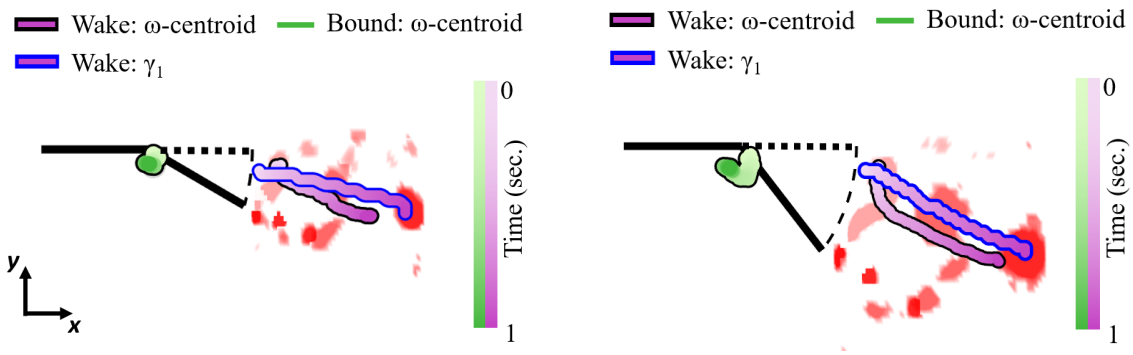

(a) Vorticity trajectories during time indicated by shaded box in Figure 5.25(a), $s_a/c = 0.5$, $\delta = 0 - 20°$

(b) Vorticity trajectories during time indicated by shaded box in Figure 5.25(b), $s_a/c = 0.5$, $\delta = 0 - 40°$

Figure 5.24: Wing-fixed time history of bound and wake vorticity trajectories.

to observe the motion of a particular flow structure identified as a "vortex". This definition may correspond to a particular threshold of the γ_1 criterion or it may simply refer to a bulk of vorticity traveling together in space. When simplifying this flowfield to apply Lamb's model, the trailing edge wake presents a unique problem in that its time-dependent and case-dependent wake shape makes it difficult to ascribe a single "location" of an entire wake. Typical vortex tracking methods are inherently weighted heavily by the strength of the initial trailing edge vortex, despite new (and potentially more relevant to lift production according to Biot-Savart) vorticity constantly being shed at the trailing edge. Observe the trailing edge wake trajectories calculated by both the vorticity centroid method and γ_1 method in Figure 5.24. The γ_1 method finds the maximum value of γ_1 in the flow field and follows the center of what is clearly the large starting vortex formed during the flap transient. This method gives a good indication of

the convection speed of a general element of wake vorticity and can be used to compute the relative velocity between the two Lamb "vortices". The vorticity centroid method is similarly dominated by the strong starting vortex but is slightly pulled back towards the wing as newly shed vorticity enters the wake. Although trajectories at long time are not able to be shown due to a fixed field of view, one can imagine that as the wing travels farther, the starting vortex, and subsequently the "vortex location" computed by the two methods, will continue to grow with time and move far downstream.

Figure 5.25 provides time histories of quantified bound and wake vortex x-locations for deflection rates $s_a/c = 0.5, 1$ and deflection angles $\delta = 0 - 20°, 0 - 40°$. The shaded area ($0 \leq s/c \leq 1$) corresponds to the duration of trajectory measurements covered in Figure 5.24. It was noted earlier that the objective of this effort is to develop a simplified model that can be applied to a wide range of flap kinematics without having to quantify the wake shape and vortex dynamics for each individual case. The results of Figure 5.25 provide evidence that a few parameters remain robust among cases. One of those parameters is the location of the bound vortex. It is rather clear from Figures 5.24 and 5.25 that the location of bound vorticity can be assumed to remain fixed to the mid-chord for all times. There are slight variations in its position over time, but for the purposes of a low order model it can be assumed as constant. Another similarity lies in the measured x-position history of the trailing edge wake when using either vorticity centroid or γ_1 methods. The γ_1 method could not be applied to the slower $s_a/c = 1$ cases because the tracking method could not identify one particular vortex to follow. Recall, it identifies the maximum value of γ_1 in the frame each time step, which typically resides within the strong starting vortex. However, as illustrated in Figure 5.10, the $s_a/c = 1$ wake

contains more of a streak of small relatively equal strength regions of vorticity, which causes the γ_1 method to inconsistently track the same piece of vorticity over time. This demonstrates the robustness of the centroid of vorticity method in that it will always provide a result no matter the shape or strength of the vorticity in a region of interest.

Since lift is expressed as the rate of change of vertical momentum [78], the only quantities required to calculate lift using Equation 5.1 are those in the horizontal direction. Thus, with the bound vortex fixed to the mid-chord ($u_- = \frac{dx_-}{dt} = 0$) and the wake vorticity convecting downstream at a velocity of $u_+ = \frac{dx_+}{dt} \approx U_\infty$ according to the slope measured in Figure 5.25, the relative velocity between the two Lamb "vortices" is $\Delta u = U_\infty$.

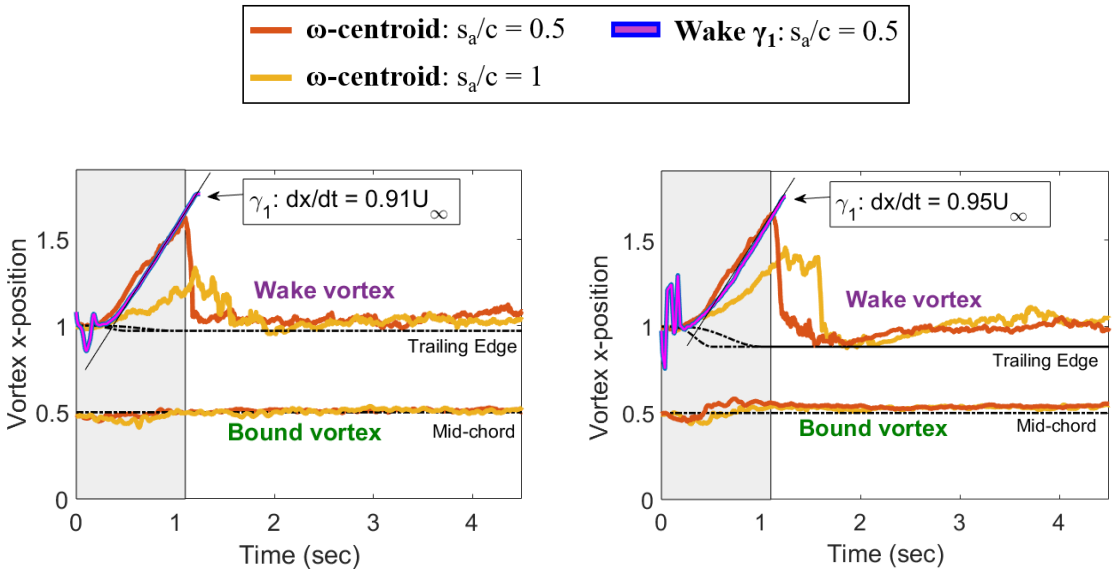

(a) $\delta = 0 - 20°$.

(b) $\delta = 0 - 40°$.

Figure 5.25: x-locations of centroid of vorticity and γ_1 for bound and wake circulations; $s_a/c = 0.5$ (red) and 1 (yellow).

Immediately following the shaded box in Figure 5.25 there is a sharp decrease in $x-$position of the tracked vortex for the $s_a/c = 0.5$ cases. That is because vorticity begins to leave the frame and the centroid is now shifting back towards the wing's trailing edge. That is, of course, a numerical artifact of the centroid method using only the information it has within the field of view. However, it does introduce the notion that theoretically, the trailing edge wake will eventually extend to the far field at long time as the wing translates away from it. Assuming we had an infinite field of view and computed the vorticity centroid, the relative distance between the wake centroid and the bound centroid, which is fixed to the wing, would go to infinity. Mathematically, that would be the case, but it is hard to say if that is physically correct in terms of the physics Lamb is modeling. Remember that we are modifying an ideal point vortex into a spatially expanding asymmetric convecting wake. The way the present work deals with the contrasting scenarios is to place the "vortex" *location* at the wing's trailing edge. At every instant, a small segment of vorticity is produced at the trailing edge. The assumption of inviscid flow eliminates the possibility of vortex dissipation downstream, so it will be assumed that once a segment of vorticity is created at the trailing edge it remains at that strength for all time. Thus, the *only* location in the wake where vorticity is allowed to change magnitude, i.e. $\dot{\Gamma} \neq 0$, is at the trailing edge.

Figure 5.27 summarizes the results of this section and the assumptions regarding vortex dynamics and their application to Lamb's vortex model. Applying the assumptions of $\Delta x = \frac{c}{2}\cos(\delta)$ and $\Delta u = U_\infty$ to Equation 5.1 results in a final equation for lift coefficient based only on circulation history and wing kinematics given by

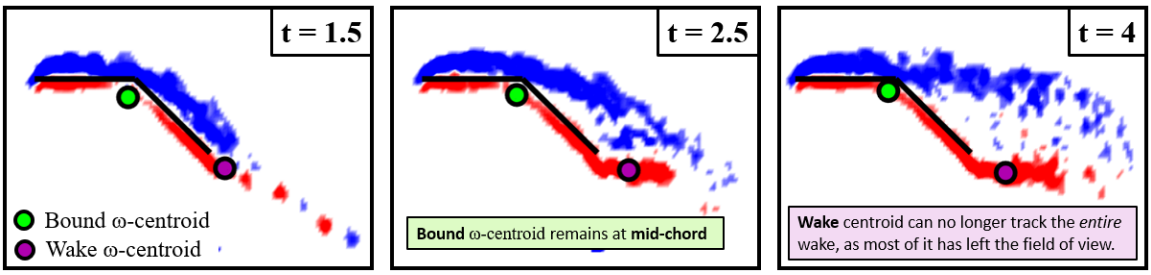

Figure 5.26: Bound and wake vorticity centroids at long time. Bound vorticity has converged to a constant location near the mid-chord. Trailing edge wake has long left the field of view and can thus no longer be accurately tracked

$$C_L = \frac{2\Gamma}{Uc} + \frac{\dot{\Gamma}}{U^2}\cos(\delta) \tag{5.2}$$

5.5.2 Vortex Impulse Model Results

Comparisons of experimental results to the semi-empirical low order vortex impulse model of Equation 5.2 are shown for flap-down cases in Figure 5.28 and for flap-up cases in Figure 5.29. Insets in Figure 5.28(a,b) are provided for a more detailed view of the comparison during the flap transient.

The initial lift spike during the flap transient is attributed to unsteady rate effects, both inertial and circulatory, as discussed via classical airfoil theory in Chapter 3. It appears, though, that all of the force production, regardless of its source has been captured by the simplified vortex impulse method of Equation 5.2. Flap-down cases in Figure 5.28 feature a large spike whose magnitude is dependent on deflection rate. The model appears to have no trouble accurately predicting the timing and magnitude

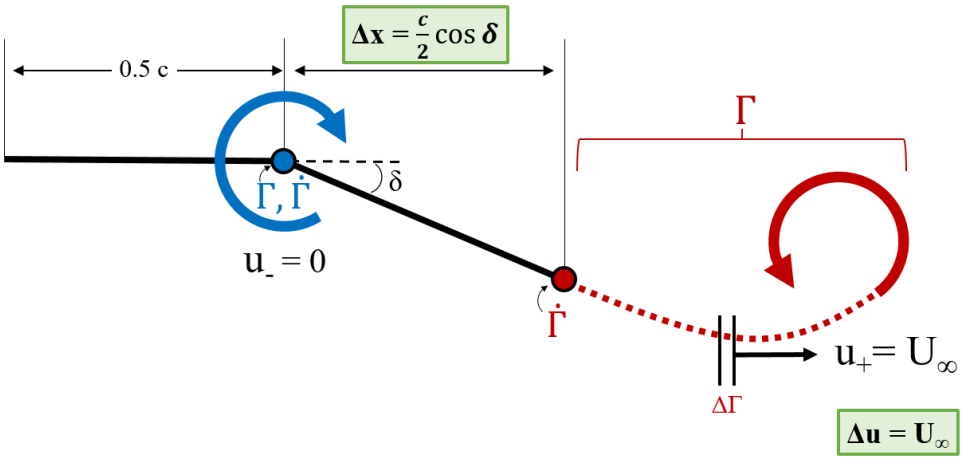

Figure 5.27: Schematic illustrating the extension of Lamb's vortex model to the present case of a hinged wing with rapidly deflecting flap. Relative displacement, Δx, and relative velocity, Δu, are indicated based on the aforementioned analysis and simplifications.

of that spike. The term in Equation 5.2 predominantly responsible for the lift spike is the term directly proportional to circulation growth, $\dot{\Gamma}$. It is interesting to observe what has been characterized by Theodorsen and others in the literature as a largely "non-circulatory" effect being modeled by an equation exclusively containing circulation terms. In line with what Dr. John Anderson and Sir Horace Lamb theorized, the circulation produced via the motion of a submerged body (under particular flow idealization) can be quantitatively reshaped to identically represent lift production. Not only does the vortex impulse model match experimental measurements during the high lift flap transient with remarkable accuracy given the approximations made to vortex location and convection speed, but it also predicts the relaxation to steady state. At long time, lift is largely dominated by the "steady" term in Equation 5.2, $\frac{2\Gamma(t)}{Uc}$, which

is dependent on instantaneous circulation. As shown back in Figure 5.5, circulation decreases as the flow field transitions from an attached to separated flow state following the aggressive transient flap, coinciding with a proportional lift reduction. This effect is accurately captured by the low order vortex model. Because the relaxation process involves a transition from attached flow to separated flow, it is further remarkable that this inviscid theory appears to hold even when flow over the rear half of the airfoil is entirely separated. With that known, maybe it is no longer surprising that the model and experiment are equally in agreement in Figure 5.29, where the initial condition at the start of the flap transient contains fully separated flow over the rear half of the wing.

The agreement between measurement and model becomes even more motivating when recalling that force measurements were obtained in a water tunnel facility with a NACA-0006 wall-to-wall airfoil whereas the PIV data used in the vortex impulse model was obtained in a water tank with a finite-span (AR 4) flat plate. Experiments were, of course, identically matched in terms of non-dimensional flap kinematics and free stream aspects, but the difference in physical test article still remained. The apparent independence of aspect ratio between the experimental facilities might be explained by the fact that the force measurements were designed to contain physically 2-D flow by using a wall-to-wall wing, and the vortex impulse method uses a 2-D plane to compute sectional lift near the mid-chord where the flow is known to be relatively two dimensional.

An objective of this work and especially this section, is to develop an understanding for the physical mechanisms responsible for lift production and the accuracy to which classical airfoil theory models these mechanisms. The vortex impulse model of Equation 5.2 can be characterized as a semi-empirical model, as it requires measured circulation

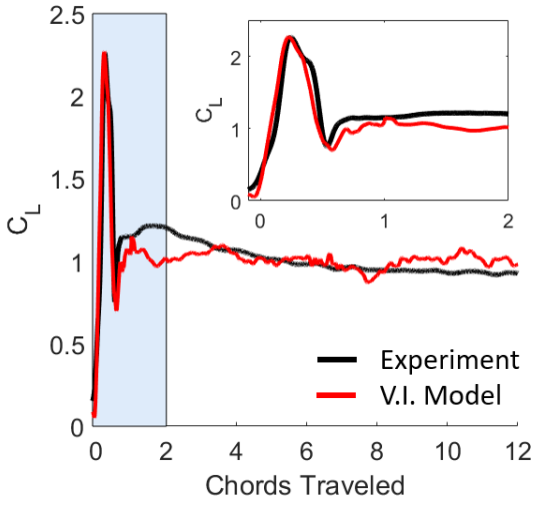

(a) $s_a/c = 0.5$, $\delta = 0 - 20°$

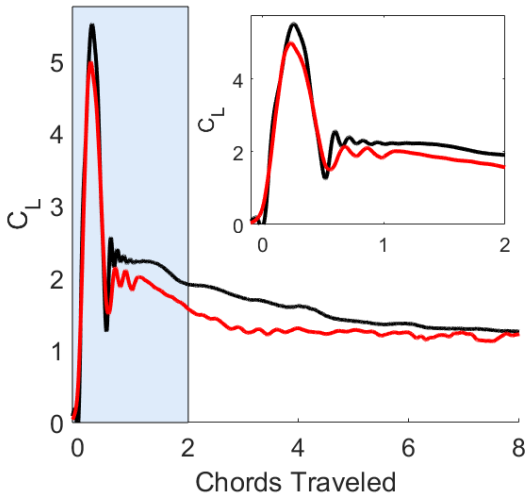

(b) $s_a/c = 0.5$, $\delta = 0 - 40°$

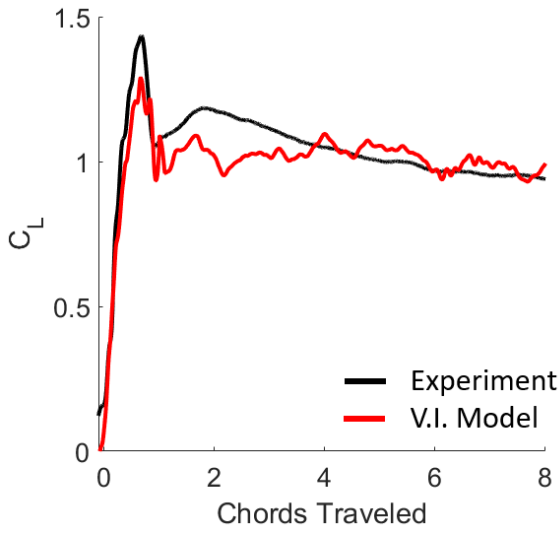

(c) $s_a/c = 1$, $\delta = 0 - 20°$

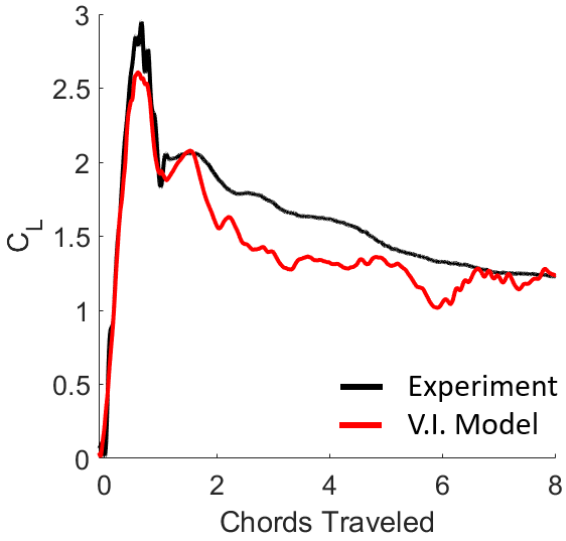

(d) $s_a/c = 1$, $\delta = 0 - 40°$

Figure 5.28: Vortex impulse model comparison to experiment for flap-down cases of various deflection rates and flap angles.

history as an input. From a practical application standpoint, it is not feasible to obtain a circulation history for every case one desires to model. This is the principal factor driving

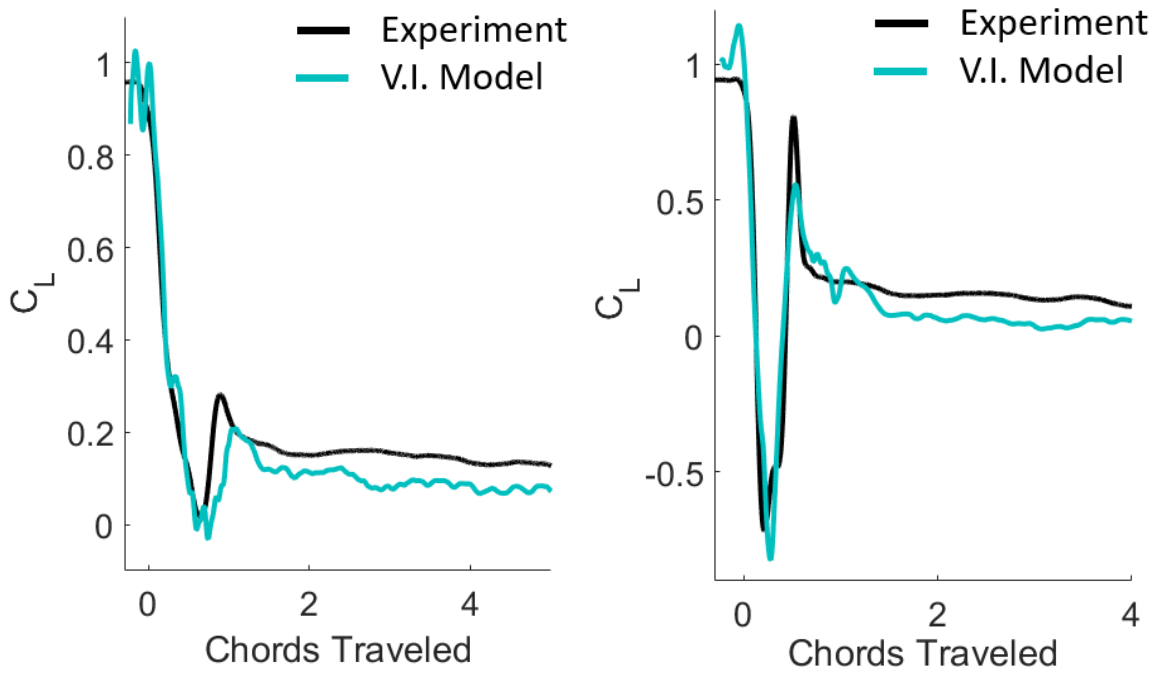

(a) $s_a/c = 0.5$, $\delta = 0 - 20°$

(b) $s_a/c = 0.5$, $\delta = 0 - 40°$

Figure 5.29: Vortex impulse model comparison to experiment for flap-down cases for $\delta = 0 - 20°$.

the use of classical analytical models, such as Theodorsen and Wagner's solutions, even for cases that do not strictly adhere to the assumptions on which the models were derived. Since these models are so widely used, it is now instructive to compare a classical model to a model based on accurately obtained physical data with the hopes of drawing parallels between the two.

Figure 5.30 presents the individual lift contributions from each term in the vortex impulse model to provide insight and general intuition for the relative magnitude of each term at every point during the motion. As hypothesized, the magnitude of the lift spike during flap deflection is largely dependent on deflection rate. Looking at the vortex

impulse results for $\delta = 0 - 20°$ cases of Figure 5.30(a,c), notice that although the term proportional to circulation remains of relatively equal magnitude between the cases, the term proportional to time rate of change of circulation is strikingly different. The slower case reaches peak circulation over a longer duration, resulting in over 50% reduction in the "unsteady" $(\frac{\partial \Gamma}{\partial t})$ lift term. The same trend is identified for the $\delta = 0 - 40°$ cases of Figure 5.30(b,d).

Figure 5.30 also contains a discretization of force contributions pertaining to the simplified classical model given by Equation 3.25, which provides an analytical lift model solely dependent on wing kinematics and free stream speed. Note that Equation 3.25 is now non-dimensionalized by the dynamic pressure, $\frac{1}{2}\rho U^2$, and chord length of the entire wing, $2b$, to produce lift coefficient. Most importantly, this is a purely analytical model and does not require empirical inputs or any flow field knowledge *a priori*. Figure 5.30 allows for the comparison of kinematic quantities $(\delta, \dot{\delta}, \ddot{\delta})$ to terms proportional to circulation behavior $(\Gamma, \dot{\Gamma})$. It has been reiterated throughout the results of this work that circulation production is proportional to motion rate. Figure 5.30 shows that the terms describing flap deflection rate in the analytical model are directly proportional to the circulation production term in the vortex impulse model. Likewise, the term describing instantaneous incidence angle is proportional to instantaneous circulation. Baik et al. [83] and Ol et al. [15] have demonstrated that classical airfoil theory provides reasonably accurate results when the motion rate is sufficiently high. Figure 5.30 reflects that conclusion as the faster cases result in closer agreement to the semi-empirical model than the slow cases, which experience an over-prediction of the analytical model. This is likely due to less stringent flow attachment for slower cases, resulting in a lower

aerodynamic efficiency compared to ideal airfoil theory.

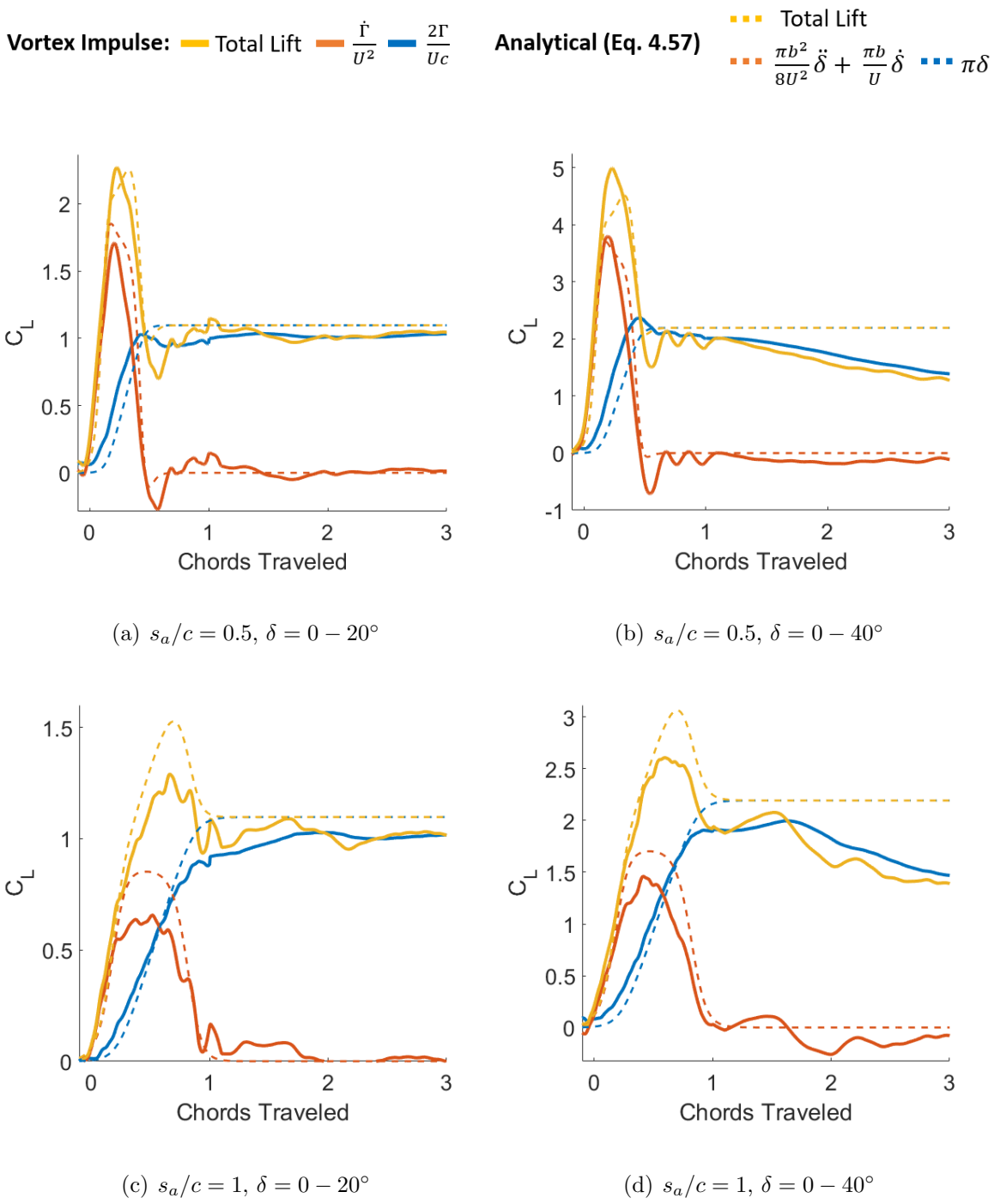

(a) $s_a/c = 0.5$, $\delta = 0 - 20°$

(b) $s_a/c = 0.5$, $\delta = 0 - 40°$

(c) $s_a/c = 1$, $\delta = 0 - 20°$

(d) $s_a/c = 1$, $\delta = 0 - 40°$

Figure 5.30: Vortex impulse method (Eq. 5.2) vs. simplified aerodynamic model (Eq. 3.25).

5.6 Force Prediction via Low-Order Analytical and Numerical Methods

The previous section presented a low-order model for unsteady lift prediction requiring experimental circulation data as input. For the purposes of optimization, sensitivity analysis, and control, low-order models cannot rely on the existence of experimental results, as they are typically used as prediction tools in the absence of physical data. This section aims to extend the discussion of theoretical lift prediction by applying classical aerodynamic concepts to accurately predict measured lift on a hinged wing with rapidly deflecting trailing edge flap. The two low-order quasi-steady models tested here include 1) Theodorsen's classical solution with $C(k) = 1$ as well as 2) the modified aerodynamic model of Equation 3.25 specifically introduced in the present work. Additionally, an unsteady panel method will provide a numerical solution to evince the accuracy and/or limitations of each low-order model.

This section will focus exclusively on the flap-down motions for $\delta = 0 - 20°$, $0 - 30°$ at deflection rates $s_a/c = 0.25, 0.5, 1, 2$. As shown in Section 5.3, during the flap-down motion transients ($0 \leq s/c \leq s_a/c$) flow is largely attached and produces lift in agreement with inviscid attached flow theory, making these kinematics excellent candidates with which to compare the theoretical models.

5.6.1 Theodorsen and Modified Model

Figure 5.31 shows the performance of the two low-order models compared to the measured lift history for (a-d) $\delta = 0 - 20°$ and (e-h) $\delta = 0 - 30°$ at deflection rates $s_a/c = 0.25, 0.5, 1, 2$. Theodorsen's solution captures the correct shape of the measured

force history, but clearly over-predicts lift for every case. Most notably, the steady state lift predicted by Theodorsen is considerably larger than the measured steady value. This suggests that one specific area in which to diagnose the discrepancy is the magnitude of its steady circulatory lift term. Inserting the present geometric and kinematic parameters into Equation 3.17, the resulting steady circulatory lift from Theodorsen's prediction is $C_L = (2 + \pi)\delta$. In comparison, the steady state lift predicted by the modified model is $C_L = \pi\delta$. The latter prediction agrees to a much higher degree with the measured data. Therefore, it is noted that one major source of the disparity in Theodorsen's prediction to measured lift is its treatment of the steady circulatory term. It should be reiterated that Theodorsen's solution was derived under the assumption of small angular deflections of the flap, which is clearly violated in the present case. The modified model, which treats the hinged wing as two decoupled single-element lifting surfaces, each producing lift according to Theodorsen's solution for single-element plates, very accurately predicts steady circulatory lift for all cases. To understand the accuracy of the steady circulatory term, consider the hinged wing as a cambered wing with an imaginary chord line connecting the leading and trailing edges. Because the hinge location is at the half chord, the angle of attack between the imaginary chord line and horizontal free stream, α, is $\alpha = \frac{1}{2}\delta$. Thus, the modified model predicts steady circulatory life to be $C_{L,steady} = \pi\delta = 2\pi\alpha$. The exceptions to this result are the slow, high deflection cases of Figure 5.31(g,h), in which flow is likely not very strongly attached and thus acts less efficiently than inviscid attached theory predicts.

At very early time after the onset of flap deflection, $t = 0^+$, the steady term for either model, which is proportional to deflection angle, is negligibly low and lift is

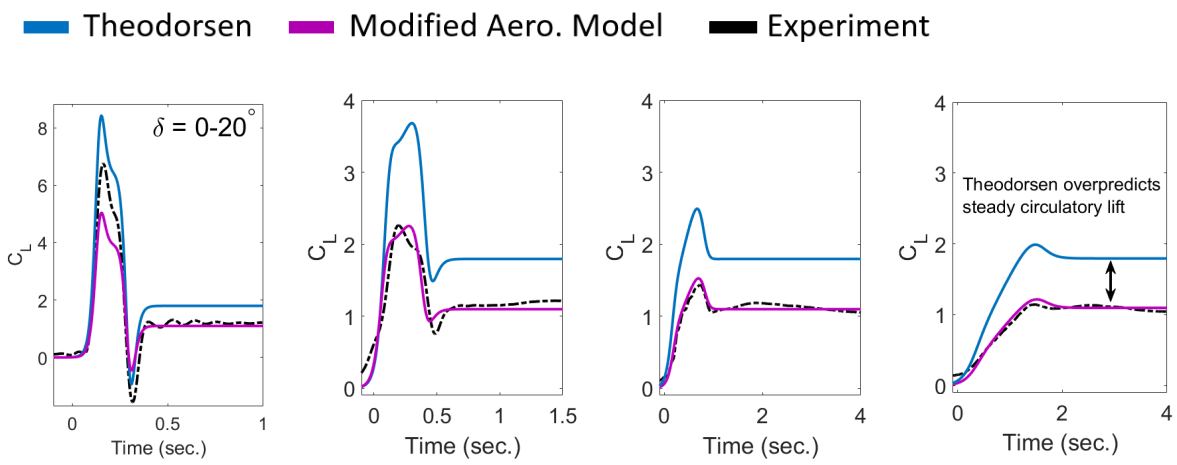

(a) $s_a/c = 0.25$ (b) $s_a/c = 0.5$ (c) $s_a/c = 1$ (d) $s_a/c = 2$

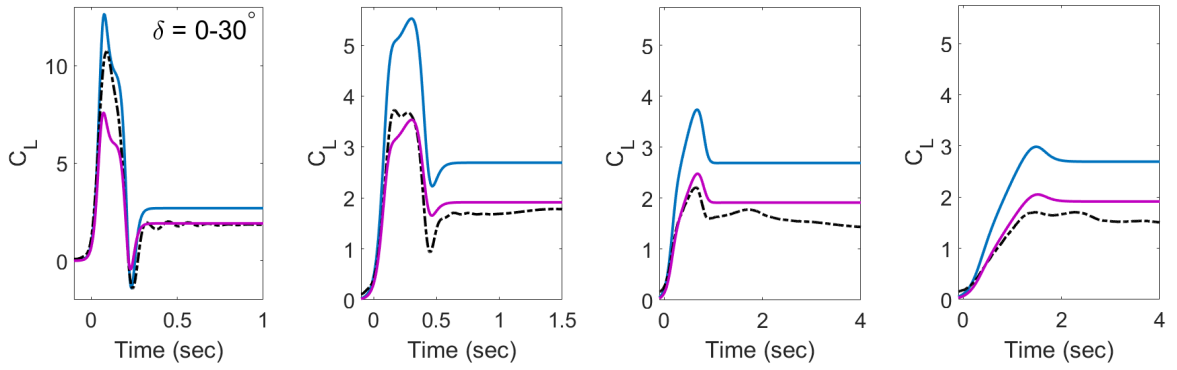

(e) $s_a/c = 0.25$ (f) $s_a/c = 0.5$ (g) $s_a/c = 1$ (h) $s_a/c = 2$

Figure 5.31: Experimental results compared to two analytical models: Theodorsen's solution and the modified aerodynamic model of Equation 3.25.

primarily driven by rate-dependent forces. This was also observed in Figure 5.30 via vortex impulse analysis, which showed that the term proportional to time rate of change of circulation is the overwhelming contributor to lift production during early stages of the flap transient. Recall the accuracy to which the vortex impulse method matched measured lift data. Now observe the congruence between the steady (Γ) and unsteady

($\dot{\Gamma}$) terms of the vortex model to the steady (δ) and rate-dependent ($\dot{\delta}$, $\ddot{\delta}$) terms of the modified model. This agreement forms a foundation for understanding the resounding accuracy with which the modified model predicts measured lift in Figure 5.31. As with the steady result, Theodorsen's model over-predicts lift during the flap transient but to a lesser degree for more aggressive flap deflections. As Theodorsen's rate-dependent terms (added mass, rotation-induced plate normal acceleration, and virtual camber) dominate force production relative to the steady circulatory force, Theodorsen becomes much closer to measured forces, though it still over-predicts for all time.

The modified model was designed to assume zero lift contribution from the stationary fore element by effectively decoupling any lift-augmenting effects of flap kinematics on the fore element. This causes an understood limitation to the model. The fact that there *exists* an unsteady force on the fore element is contained in Theodorsen's solution, but its accuracy to the physical problem remains unknown. The aforementioned limitation of the modified model is made evident by its considerable under-prediction of measured lift for the most aggressive flap cases in Figure 5.31. The inability of the modified model to predict measured lift is hypothesized to be a result of a significant physical unsteady lift force on the fore element. This hypothesis is addressed in Figure 5.32 and it is confirmed that although the rate-dependent terms of the model accurately depict forcing on the physical flap, there exists an additional unsteady lift force produced on the stationary fore element.

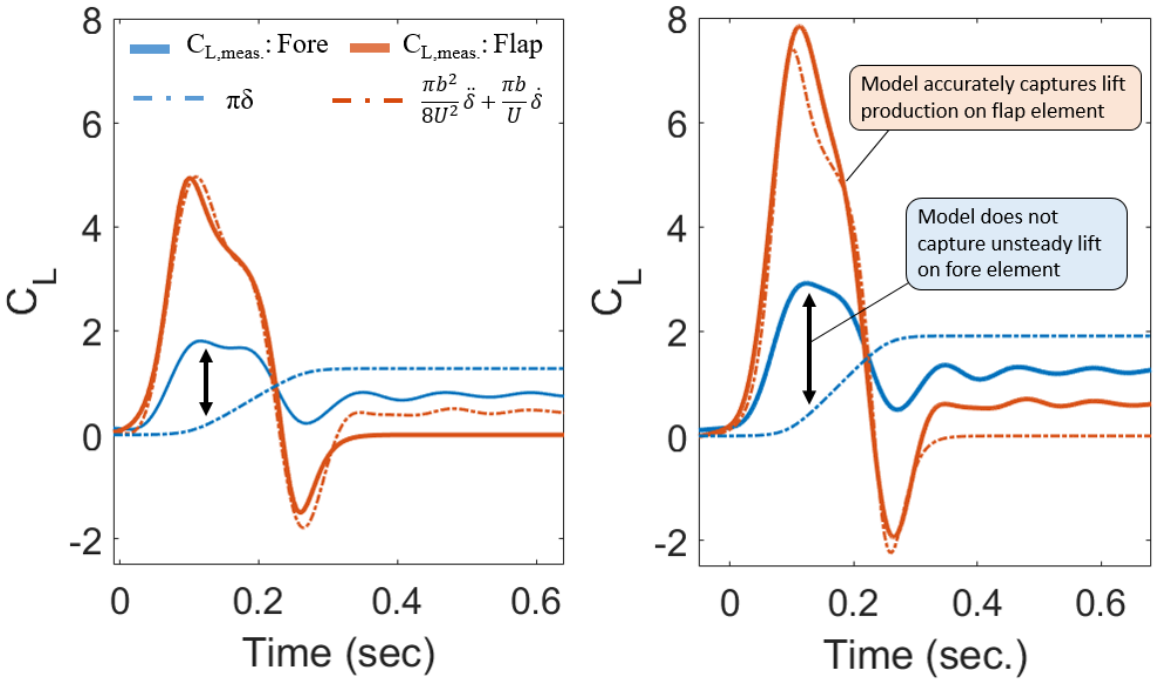

(a) $\delta = 0 - 20°$, $s_a/c = 0.25$

(b) $\delta = 0 - 30°$, $s_a/c = 0.25$

Figure 5.32: Measured lift on fore and flap elements compared to the two terms in the modified model.

5.6.2 Numerical Solution: Unsteady Panel Method

It was observed in Figure 5.32 that rapidly pitching the large trailing edge flap does physically produce an unsteady lift force on the *stationary* fore element. The plot shows that the modified model, although accurately capturing lift produced by the flap itself, is not capable of capturing the additional lift on the fore element. Thus, Theodorsen's solution, which predicts non-zero unsteady lift on the fore element, *over*-predicted measured lift, whereas the modified model *under*-predicted lift. This section presents the results of an unsteady panel method, a low computational cost numerical

solver, to address the discord between the analytical cases.

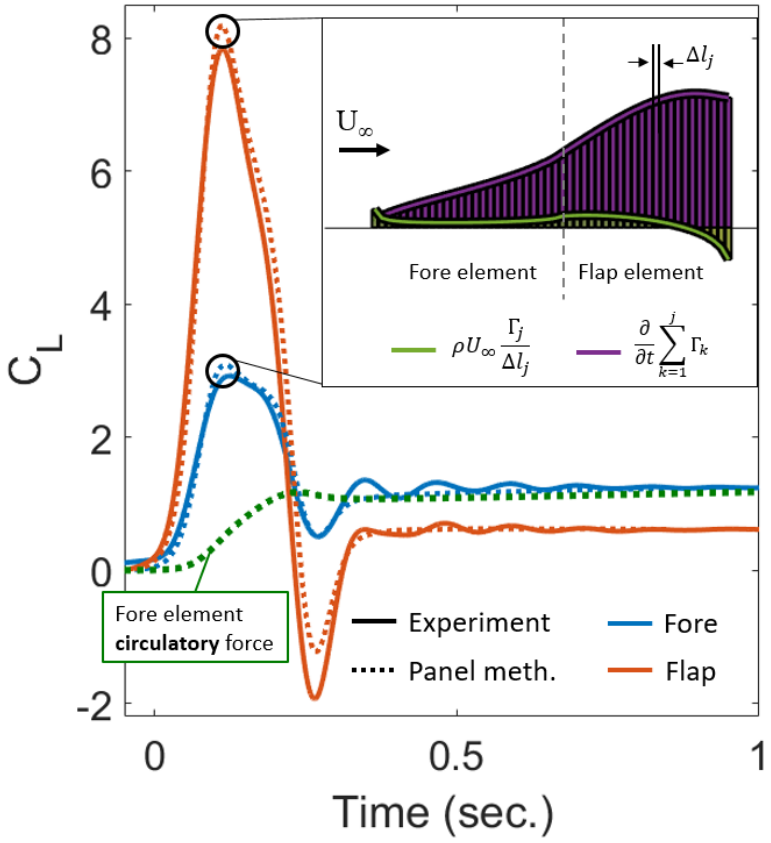

(a) $\delta = 0 - 30°$, $s_a/c = 0.25$

Figure 5.33: Comparison of panel method to experimental measurement with chord-wise pressure distribution at peak acceleration, showing large unsteady lift contribution from stationary fore element. (a) $s_a/c = 0.25$ (b) $s_a/c = 1$.

Detailed descriptions of the panel method and its implementation are covered in Chapter 3 as well as in Katz and Plotkin [86]. Figure 5.33 confirms that the panel method accurately models measured lift force for the $\delta = 0 - 30°$, $s_a/c = 0.25$ case that neither analytical model could properly capture. This result provides confidence that the resulting pressure distributions are equally representative of the physical case. Shown as an inset in Figure 5.33 is an instantaneous pressure distribution due to steady

and unsteady lift terms for the time corresponding to maximum flap acceleration.

We can now further break down fore element lift into its constituent steady (Γ) and unsteady ($\dot{\Gamma}$) values. Plotted in green, the Γ-proportional component of fore element lift follows the shape of the deflection history, much like the modified model's $\pi\delta$ term. In fact, a comparison of the blue and green lines in Figure 5.33 is nearly identical to the model vs. experiment result of Figure 5.32. Figure 5.33 clearly proves that the major discrepancy in the modified model lies in its inability to predict $\dot{\Gamma}$-proportional forces on the fore element. Recall that this discrepancy is not always critical in predicting lift with sufficient accuracy. Figure 5.31 shows that the modified model works very well for all but the most aggressive cases. Figure 5.34 provides panel method results for steady and unsteady pressure distributions as well as component-wise force histories for each of the examined deflection rates. Notice that pressures due to instantaneous circulation do not change as drastically with deflection rate as pressures due to circulation's time rate of change. The fact that "steady" lift varies with deflection rate at all, despite each case deflected to the same flap angle, is a result of the induced effect of the rapidly deflecting flap on the fore element. Satisfying the boundary condition of no penetration in steady flow ($\dot{\delta} = 0$) is exclusively dependent on instantaneous wing geometry. However, when the flap is in motion, induced flow on the fore element requires an additional circulation adjustment to the panel vortices in order to satisfy the boundary conditions.

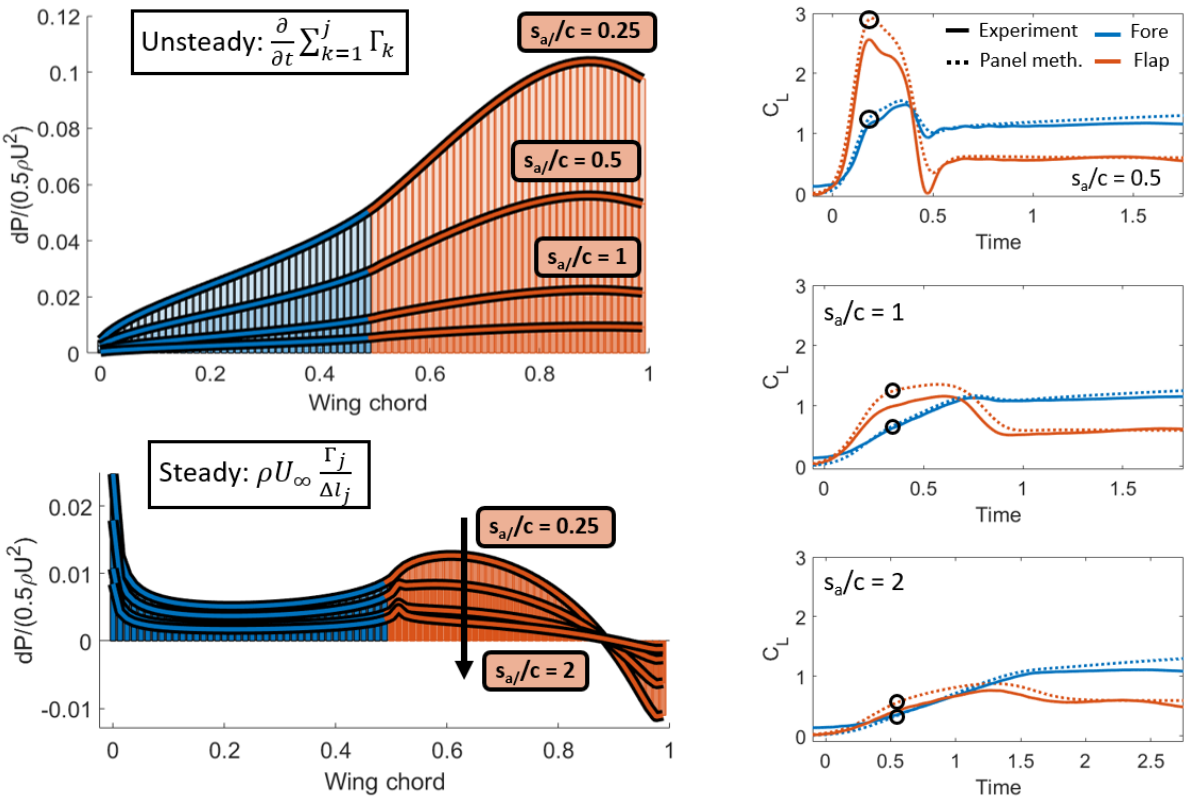

(a) Steady and unsteady sources of chord-wise pressure

(b) $\delta = 0 - 30°$, $s_a/c = 0.5,\ 1,\ 2$

Figure 5.34: (a) Panel method result of chord-wise pressure distributions due to unsteady lift term for several deflection rates of $\delta = 0 - 30°$ case, showing large unsteady lift contribution from stationary fore element. (b) Panel method compared to experimental force measurements on fore and flap elements.

5.7 Chapter Summary

This chapter provided an investigation into the force production, flow field development, and low order modeling of a hinged wing with rapidly deflecting trailing edge flap. A detailed parameter space was selected to measure the effects of a wide range of flap deflection angles, deflection rates, and initial flow conditions. Flap deflection rates

varied from $0.25 \leq s_a/c \leq 4$ with relative changes in deflection angle $\Delta\delta = 20°, 30°, 40°$. Both flap-down ($0° - \delta_f$) and flap-up ($\delta_f - 0°$) were examined. All cases were run at Re = 20,000 with the fore element stationary at fixed angle of attack $\alpha_{LE} = 0°$. Several additional experiments were performed with the fore element fixed at $\alpha_{LE} = 20°$ to assess the flap performance in a fully stalled flow.

A semi-empirical model was formulated to predict lift histories on the hinged wing based on the original work of Lamb's point vortex impulse model. A redefinition of the model's constituent terms allowed for an application of the potential flow model to be applied to the real flow of the present work. Semi-empirical model results matched experiment with remarkable accuracy, and an assessment of each term contributed to an understanding of lift sources during flap deflection and quantifying force production using only velocity fields.

Finally, several low-order models were implemented to assess whether force production of a large rapidly deflecting trailing edge flap could be predicted using simple low-order models. Theodorsen provides a classical solution that is widely used in the aerodynamics community, but results from this study show that it is unfit to predict lift on a wing with such a large flap (50% chord) deflecting at high amplitude. A modified aerodynamic model was developed to more accurately predict forces on the present kinematics. This model ignores any unsteady, non-circulatory effects on the stationary fore element and, as a result, leads to better agreement with measured lift history. Comparison of this modified model with Theodorsen's classical solution identifies a limitation of Theodorsen in its inability to accurately capture the steady circulatory lift contribution, leading to a significant over-prediction of total lift for every case in this study. The size

(50% chord) and deflection angle ($\delta > 20°$) both contribute to violating the small perturbation assumption integral to Theodorsen's analytical solution. The modified model presented in this work may be used to accurately predict forces on hinged wings undergoing flap kinematics ($s_a/c > 0.5$), for which the fore element produces negligible unsteady lift. The modified model begins to under-predict lift for the most aggressive motions, for which there is significant lift production on the fore element. An unsteady panel method provided a numerical solution that validated the modified model's ability to accurately predict rate-dependent forces produced by the deflecting flap but not for the fore element. Via chord-wise pressure distributions, the panel method confirmed that the modified model's under-prediction equates to the unsteady lift on the fore element.

Chapter 6

Conclusion

6.1 Summary of Research

This work contains experimental and low-order modeling efforts that have been performed on flat plate wings with the goal of providing a fundamental understanding of the underlying physical mechanisms by which lift is produced on rapidly accelerated wings. Experiments were performed in collaboration with the University of Maryland and Air Force Research Laboratory, capitalizing on the unique capabilities of each facility. Experimental methods included time-resolved unsteady force measurements, high-speed particle image velocimetry, and dye flow visualization. Test articles included single-element flat plates and a flat plate hinged at the mid-chord with dynamically deflecting trailing edge flap.

Chapter 4 explored force and moment production on surging and pitching single-element wings. Force histories were compared to time-resolved flow topology, drawing parallels between circulation production and lift force. Acceleration from rest cases were performed for an angle of attack sweep of $5^\circ \leq \alpha \leq 45^\circ$ over non-dimensional

acceleration distances $0.125 \leq s_a/c \leq 6$. Experiments investigating leading edge pitch were limited to only two sets of kinematics, $s_a/c = 1$ and $s_a/c = 6$ for $\alpha = 0 - 45°$, to represent a "fast" and "slow" case, respectively, and with which to compare to the surging cases of the same s_a/c. Results from this study concluded that for all motion rates at high incidence in which massive flow separation occurs over the leading edge there exists a stall delay and subsequent high lift transients due to motion-induced force production and auxiliary lift enhancement from leading edge vortex dynamics.

Chapter 5 studied a flat plate wing hinged at the mid-chord undergoing pitch-and-hold motions of the trailing edge flap. This study provided similar quantitative analysis as performed in Chapter 4 in addition to a series of low-order predictive modeling efforts including semi-empirical, numerical, and analytical approaches. Flap deflections ranged from $\Delta\delta = 20°, 30°$, and $40°$ at rates of $0.25 \leq s_a/c \leq 4$. Despite vastly different flow topologies and means of circulation production (attached vs. separated at the leading edge), both single-element wing and hinged wing experiments generated lift in the form of instantaneous force spikes upon motion onset and sustain high lift for the first few chords after the motion transient before developing into their respective fully developed states. Measured lift on the hinged wing has been shown to be accurately modeled by the present work's adaptation of a vortex impulse lift method and a modified aerodynamic model. The latter provided an avenue for discussion regarding the over-prediction of Theodorsen's steady circulatory term for the flapped wing and presents an alternative analytical model with which to predict lift.

6.2 Original Contributions

This work yields several important original contributions that will provide insight into lift production and modeling techniques for future studies on low Reynolds number rapidly maneuvering wings.

1. A comprehensive experimental investigation into the unsteady aerodynamic behavior of pitching and surging wings at low Reynolds number ($Re \sim 10^4$) using time-resolved force and velocity field measurements. Measurements were obtained over long convective time, allowing for detailed observation of the response to motion transient as well as relaxation to steady state.

2. A fundamental understanding of the individual sources of lift production on rapidly maneuvering wings over a wide range of motion rates and incidence angles, providing an assessment of each lift source's magnitude relative to total lift and dependence on motion rate.

3. An experimental campaign of a rapidly deflecting trailing edge flap, novel in its size for the tested pitch-and-hold deflection rates, cataloging lift production and flow field development for a range of flap angles and deflection rates.

4. Development of an analytical model that more accurately predicts time histories on a hinged wing with large trailing edge flap than Theodorsen's classical analytical solution.

6.3 Key Conclusions

6.3.1 Single-element flat plates

Surging from rest

1. *Angle of attack*

   - For $\alpha \geq 15°$, leading edge vortices form upon startup via the shear layer that forms at the leading edge, resulting in a sequence of vortex detachment, convection, and new vortex reformation throughout the wing translation.
   - Each vortex contributes an additional source of circulatory lift that causes an oscillation in force history as lift converges *downward* to its steady state value following the motion transient. Formation of a LEV leads to temporary lift peaks, while convection of the LEV and subsequent encroachment of trailing edge vorticity above the wing leads to local lift troughs.
   - Low angle of attack cases, $\alpha \leq 10°$, agree with Wagner's approximation, do not form vortices from leading edge flow separation, and trend *upward* towards their final steady lift value.
   - Drag, both transient and steady, increases monotonically with incidence angle but not entirely linearly. There is a relatively linear increase in drag for $\alpha \leq 20°$, beyond which there is a sharp increase in drag as flow transitions into a fully stalled state. The gains in lift achieved by increasing angle of attack are outweighed by the increase in drag for $\alpha > 20°$, as evidenced by the drag polar at the point of maximum lift as well as the time history of

lift-to-drag ratio.

2. *Acceleration rate*

   - Theoretical added mass, as given by Pitt Ford [68], appears to accurately model the non-circulatory force for a range of accelerations. This result suggests the linear superpositionality of this term for use in a low order modeling technique.
   - Lift-to-drag ratio for surging plates at $\alpha = 45°$ is independent of acceleration. The fully stalled flow results in an entirely plate-normal force and a $C_L/C_D \approx 1$ for every acceleration profile tested.
   - Plotting force histories versus a normalized convective time (s/s_a) revealed an independence of acceleration rate on lift production for $s/s_a < 0.4$, after which formation of LEVs proportional to acceleration rate caused a divergence in the curves in which the faster acceleration cases eventually produced higher lift.

Pitching in free stream

- Virtual camber aids in turning the flow in the direction parallel to the suction surface and retaining the LEV closer to the wing, leading to a significantly larger circulatory lift force than achieved on the surging wing.

General conclusions

- LEV strength is proportional to acceleration rate. Faster motions generate stronger, more coherent vortices that are easier to detect using tracking methods such as γ_1.

However, the trajectory of LEVs in the lab-fixed reference frame are independent of motion rate. From this analysis, it is shown that vortex *strength* is dependent on the *rate* of motion and vortex *trajectory* is dependent on the *type* of motion.

- The direct relationship between LEV trajectory and strength with lift force suggests a quantifiable link between observable vortex dynamics and force/moment coefficients. This motivates the work forward in the search for a quantitative relationship between circulation production and force production.

6.3.2 Hinged Wing

- Dynamically pitching a trailing edge flap generates instantaneous lift upon motion onset regardless of flow attachment. Lift production during motion transients of flap-down and flap-up motions were identical in shape and similar in magnitude, but the flap-up cases were consistently lower by roughly $C_L \approx 0.2$, presumably from a loss of circulatory lift due to initial flow separation over the flap element.

- Circulation and lift production due to rapid trailing edge flap deployment are proportional to motion rate.

- Bound circulation, measured as the summation of vorticity within a box encompassing the wing and its boundary layer, has been shown to be equal and opposite to wake circulation within the first chord of travel, after which vorticity leaves the field of view and is no longer detectable. This finding supports the assumption of two-dimensionality.

- Flap-down motions, containing deflection angles up to $\delta = 40°$, maintain an attached flow state during the motion transient and for several subsequent convective lengths before slowly transitioning to separated flow over the deflected element. Time-resolved circulation measurements reflect this transition with a gradual decrease in circulation of approximately 22% and 55% over 4 chords of travel for the $\delta = 0 - 20°$ and $\delta = 0 - 40°$ cases, respectively.

- Using an adaptation of Lamb's vortex impulse method, 2D PIV measurements were able to accurately predict measured force histories over the entire duration of the test. Bound vorticity was used as vortex strength and the locations of each vortex were selected as fixed to the mid-chord and trailing edge.

6.3.3 Low order modeling

- Theodorsen's solution with $C(k) = 1$ largely over-predicts lift for every flap-and-hold maneuver studied here. Specifically, the steady circulatory term contributes the largest discrepancy between model and measurement, over-predicting lift during and immediately following the motion transient by up to 61%

- The modified aerodynamic model, which decouples the two wing elements by treating each element as an isolated wing, predicts measured lift much better than Theodorsen both during and after the acceleration transient. For a wing hinged at the mid-chord, steady circulatory lift in the modified model is equal to $C_{L,steady} = \pi\delta$, opposed to $C_{L,steady} = (2 + \pi)\delta$ in Theodorsen's solution.

- Because the modified model predicts zero lift on the front element for all time

when $\alpha = 0°$, the modified model does not accurately predict total lift for the most aggressive flap cases $s_a/c \leq 0.25$, during which significant unsteady lift force is generated on the front element.

6.4 Future Work

The present work provided a detailed description of time-resolved force histories of rapidly accelerating plates and a fundamental analysis of the various sources of lift during those motions. This section offers suggestions for future experimental studies to further the work presented here and advance the knowledge of low Reynolds number unsteady aerodynamics.

1. The work presented here can be both validated and expanded upon through the use of chord-wise pressure taps instrumented on the wing. Pressure measurements with the flow field information shown here would combine to quantify the spatiotemporal response of lift enhancement due to the leading edge vortex along the chord. This will also provide further insight into the pitching moment beyond what is capable with measurements from a single force/moment transducer. Further, chord-wise pressure taps would allow for additional assessment of the accuracy of Theodorsen's predicted pressure distribution as well as that of the numerical panel method.

2. Varying the trailing edge flap hinge location would provide a wealth of information regarding validation for the modified model presented in this work as well as a bridge from the case of a very small trailing edge flap ($c \to +1$) to the single-element wing pitching about its leading edge ($c = -1$). Within that study,

there will be a drastic change in flow topology as the wing transitions from cases with temporarily attached flow post-acceleration as shown here, where $c = 0$, to cases with fully separated flow about the leading edge observed in single-element pitching wings. Questions that this study will likely answer: Holding pitch rate constant, do the unsteady force histories from the various hinge locations scale in a predictable fashion? At what hinge location, i.e. size of stationary front element, does flow separate about the leading edge as it does in the c = -1 case? Is there a hinge location, c, for which Theodorsen's solution more accurately predicts force measurements.

3. Introduce multiple hinge locations on the same wing to provide more degrees of freedom and geometric/kinematic permutations. Actuating multiple wing elements simultaneously leads down the path of designing continuously deformable wings capable of unique kinematics and tunable unsteady force production.

4. The present work provides a general understanding of the aerodynamic response of large trailing edge flaps. It is recommended for future work to explore using the flap as a control surface to mitigate the effect of a gust (streamwise or transverse), deflecting the flap such that the total gust force is negated. Preliminary experiments have been conducted, and the results suggest that gust mitigation with a large flap is feasible. It is suggested that future work first perform a hinge location study to completely characterize the effect of variably sized flaps in order to better understand the size and rate requirements pertaining to any desired lift response. The next step is to characterize the effect of a gust on the undeflected

wing to obtain the aerodynamic gust response of which the flap will aim to cancel out. Finally, implement a control algorithm to generate a set of wing kinematics to offset the known gust encounter. The simple analytical model presented in this work predicted lift production very well and would make an excellent candidate for use in a control algorithm.

Appendix A: Revisiting Theodorsen's Lift Derivation

The following sections provide a detailed derivation of Theodorsen's solution to supplement the discussion of its constituent terms in Chapter 3.

A.1 Non-Circulatory Flow: Velocity Potentials and Pressure Forces

Velocity Potential

We introduce a disturbance velocity potential, ϕ', which is obtained by parsing the total velocity potential into the uniform flow and a perturbation potential as

$$\phi = \phi' + Ux \tag{A.1}$$

The disturbance velocity components are thus

$$u - U = u' = \frac{\partial \phi'}{\partial x}, \qquad w' = \frac{\partial \phi'}{\partial z}, \tag{A.2}$$

which are assumed to satisfy the order-of-magnitude requirement of small disturbance theory of $u', w' << U$.

For incompressible flows, it can be shown that the problem simplifies to Laplace's equation

$$\nabla^2 \phi' = 0, \tag{A.3}$$

subject to two-dimensional boundary conditions at the surface. The condition at the boundary, covered in detail in Lamb [54], states that the component of fluid velocity normal to the body, $\frac{\partial \phi}{\partial n}$, is fixed by the body motion. Another critical assumption here is that the wing lies flat along the x-axis, despite having vertical displacement from the horizontal described by $z(x)$. Thus, the concern with satisfying $\frac{\partial \phi}{\partial n} = 0$ simplifies to $w = 0$ at the wing surface, where w is the vertical velocity perpendicular to the free stream. This simplification leads to the expression for vertical velocity:

$$w = \frac{\partial z_a}{\partial t} + U \frac{\partial z_a}{\partial x}, \tag{A.4}$$

To satisfy these conditions Theodorsen applies potential flow theory to assign a sheet of point sources and sinks along the wing surface in the circle plane to satisfy the physical boundary conditions of attached flow and no through-flow. A sheet of non-circulatory point sources and sinks on the upper and lower halves of the circle, respectively, are assigned their strengths such that they satisfy Eq. A.4. The velocity potential of a source with strength H placed at the origin is given by

$$\phi = \frac{H}{4\pi} \ln(x^2 + y^2) \tag{A.5}$$

and for a source placed at (x_1, y_1)

$$\phi = \frac{H}{4\pi} \ln\{(x - x_1)^2 + (y - y_1)^2\}. \tag{A.6}$$

To determine the necessary value of H, a close examination of the source/sink behavior at the wing surface $z = 0^+$ is required (presented in detail in Bisplinghoff [62]). Satisfying the spatial boundary condition of Eq. A.4 for $w(x, y, z)$

$$w(x, y, 0^+) = \frac{\partial \phi'(x, y, 0+)}{\partial z} \tag{A.7}$$

results in the strength of the source to be given by

$$H(x,t) = 2w(x,t) \tag{A.8}$$

or

$$H(x,t) = 2\frac{\partial z(x,t)}{\partial t} + 2U\frac{\partial z(x,t)}{\partial x} \tag{A.9}$$

The total potential due to the source and sink pairs can be expressed as

$$\phi = \frac{H}{4\pi}\ln\frac{(x-x_1)^2+(y-y_1)^2}{(x-x_1)^2+(y+y_1)^2} \tag{A.10}$$

Integrating Eq. A.10 along the chord, thus accounting for every source/sink pair's potential contribution at each location, provides an expression for the velocity potential of the entire source/sink pair sheet:

$$\phi = \frac{1}{4\pi}\int_{-1}^{1} H(x,t)\ln\frac{(x-x_1)^2+(y-y_1)^2}{(x-x_1)^2+(y+y_1)^2}\mathrm{d}x_1 \tag{A.11}$$

In lieu of the detailed integration provided by Theodorsen [61], we present the result of the necessary integral

$$\int_c^1 \ln\frac{(x-x_1)^2+(y-y_1)^2}{(x-x_1)^2+(y+y_1)^2}\mathrm{d}x_1 = 2(x-c)\ln N - 2\sqrt{1-x^2}\cos^{-1}c, \tag{A.12}$$

where

$$N = \frac{1-cx-\sqrt{1-x^2}\sqrt{1-c^2}}{x-c}. \tag{A.13}$$

and c is the hinge location of the trailing edge flap measured from the mid-chord.

Following Eq. A.11, computing the effect of an aileron bent down at deflection angle β results in a velocity potential, ϕ_β, found by substituting $H = 2U\frac{\partial z(x,t)}{\partial x} = -2U\beta b$:

$$\phi_\beta = \frac{U\beta b}{\pi}[\sqrt{1-x^2}\cos^{-1}c - (x-c)\ln N]. \tag{A.14}$$

Similarly, to obtain the effect of the aileron pitching down at an angular velocity $\dot{\beta}$, we set $H = -(x_1 - c)\dot{\beta}b^2$ and return

$$\phi_{\dot{\beta}} = \frac{\dot{\beta}b^2}{2\pi}[\sqrt{1-c^2}\sqrt{1-x^2} + \cos^{-1}c(x-2c)\sqrt{1-x^2} - (x-c)^2\ln N]. \tag{A.15}$$

To obtain the analogous effects of the angular displacement and motion of the entire airfoil, α and $\dot{\alpha}$, set c = -1 and get

$$\phi_\alpha = U\alpha b\sqrt{1-x^2} \tag{A.16}$$

$$\phi_{\dot{\alpha}} = \dot{\alpha}b^2(\frac{1}{2}x - a)\sqrt{1-x^2} \tag{A.17}$$

Table A.1 provides a summary of non-circulatory velocity potentials required to satisfy the no through flow boundary condition on a pitching airfoil-aileron system in a freestream.

Pressure and Forces

The ultimate goal of this derivation is to obtain the chord-wise pressure distributions and total force production of the airfoil-aileron system. Given the velocity poten-

Table A.1: Velocity potential contributions from instantaneous incidence angle and angular velocity for the airfoil-aileron system required to satisfy the no through flow boundary condition, as provided by Theodorsen [61].

Non-circulatory velocity potentials	
Angle of attack / Flap deflection	**Angular rotation rate**
$\phi_\alpha = U\alpha b\sqrt{1-x^2}$	$\phi_{\dot\alpha} = \dot\alpha b^2(\frac{1}{2}x - a)\sqrt{1-x^2}$
$\phi_\beta = \frac{U\beta b}{\pi}[\sqrt{1-x^2}\cos^{-1}c - (x-c)\ln N]$	$\phi_{\dot\beta} = \frac{\dot\beta b^2}{2\pi}[\sqrt{1-c^2}\sqrt{1-x^2} + \cos^{-1}c(x-2c)\sqrt{1-x^2} - (x-c)^2\ln N]$
$N = \frac{1-cx-\sqrt{1-x^2}\sqrt{1-c^2}}{x-c}$	

tials, we can now calculate pressure by employing the unsteady Bernoulli equation:

$$p_0 = p + \frac{1}{2}\rho V^2 + \rho\frac{\partial\phi}{\partial t}. \tag{A.18}$$

For the steady free stream ($V = U\hat{\mathbf{i}} + 0\hat{\mathbf{j}}$), the total pressure is

$$p_0 = p_\infty + \frac{1}{2}\rho U^2. \tag{A.19}$$

As stated previously, the present formulation maintains the assumption of small perturbations, which assumes the disturbance velocities in the x and y directions, u' and v', are small. The velocity on the wing surface can be expressed as

$$V = (U + u')\hat{\mathbf{i}} + w'\hat{\mathbf{j}} \tag{A.20}$$

where

$$V^2 = (U^2 + 2Uu' + u'^2)\hat{\mathbf{i}} + w'^2\hat{\mathbf{j}} \approx U^2 + 2Uu' \tag{A.21}$$

As previously stated, we are assuming small disturbance theory, which requires $u', w' << U$. Thus, neglecting the terms u'^2 and w'^2 due to order of magnitude insignificance, we obtain a linearized solution. Substituting Eq. A.21 into Eq. A.18 results in an expression for pressure via the linearized unsteady Bernoulli equation given by

$$p - p_\infty = -\rho(U\frac{\partial \phi}{\partial x} + \frac{\partial \phi}{\partial t}) \tag{A.22}$$

Due to antisymmetry between the sources on the upper surface and sinks on the lower surface, the pressure difference between the upper and lower surfaces is

$$p_L - p_U = \Delta p = -2\rho(U\frac{\partial \phi}{\partial x} + \frac{\partial \phi}{\partial t}). \tag{A.23}$$

Finally, the total non-circulatory contribution to the lift force on the wing can be calculated by integrating the pressure difference over the entire airfoil:

$$\begin{aligned} L_{NC} &= 2\rho b \int_{-1}^{1} U\frac{\partial \phi}{\partial x}\mathrm{d}x + 2\rho b \int_{-1}^{1} \frac{\partial \phi}{\partial t}\mathrm{d}x \\ &= 2\rho b \int_{-1}^{1} \frac{\partial \phi}{\partial t}\mathrm{d}x \end{aligned} \tag{A.24}$$

Applying Eq. A.24 to the velocity potentials given in Eq. A.14-A.17 results in the familiar form of Theodorsen's non-circulatory lift

$$L_{NC} = -\rho b^2[U\pi\dot{\alpha} - b\pi a\ddot{\alpha} - UT_4\dot{\beta} - bT_1\ddot{\beta}], \tag{A.25}$$

where

$$T_4 = -\cos^{-1} c + c\sqrt{1-c^2} \tag{A.26}$$

$$T_1 = -\frac{1}{3}\sqrt{1-c^2}(2+c^2) + c\cos^{-1} c \tag{A.27}$$

A.2 Circulatory Flow: Velocity Potentials and Forces

Theodorsen represents circulation by a sheet of vorticity along the wing and in the wake, which expands from the trailing edge to infinity. As in Section A.1, we will compute the induced velocity potential due to this newly introduced potential flow object, a vortex sheet. Each individual point vortex in the sheet has a velocity potential given by

$$\phi_{vortex} = \frac{\Gamma}{2\pi} \tan^{-1} \frac{Y - Y_1}{X - X_1}, \tag{A.28}$$

where Γ is the strength of the point vortex. To satisfy Kelvin's circulation theorem, which requires zero net circulation production in the system, each wake vortex is paired with a bound vortex of equal and opposite strength placed at the "image" location, $\frac{1}{X_0}$, shown in Figure A.1. The combined velocity potential due to a wake vortex at $(X_0, 0)$ and its image is

$$\phi_\Gamma = \frac{\Gamma}{2\pi} \left[\tan^{-1} \frac{Y}{X - X_0} - \tan^{-1} \frac{Y}{X - \frac{1}{X_0}} \right], \tag{A.29}$$

Defining $X_0 + \frac{1}{X_0} = 2x_0$ on the x-axis and $X = x$ on the circle, simplifies Eq. A.29 to

$$\phi_\Gamma = -\frac{\Gamma}{2\pi} \left[\tan^{-1} \frac{\sqrt{1 - x^2}\sqrt{{x_0}^2 - 1}}{1 - x x_0} \right] \tag{A.30}$$

Now that we have an equation for the velocity potential (although the vortex strength is still unknown), we can apply Eq. A.23 for the vorticity-induced pressure on the airfoil. Since each individual wake vortex element will be assumed to convect downstream

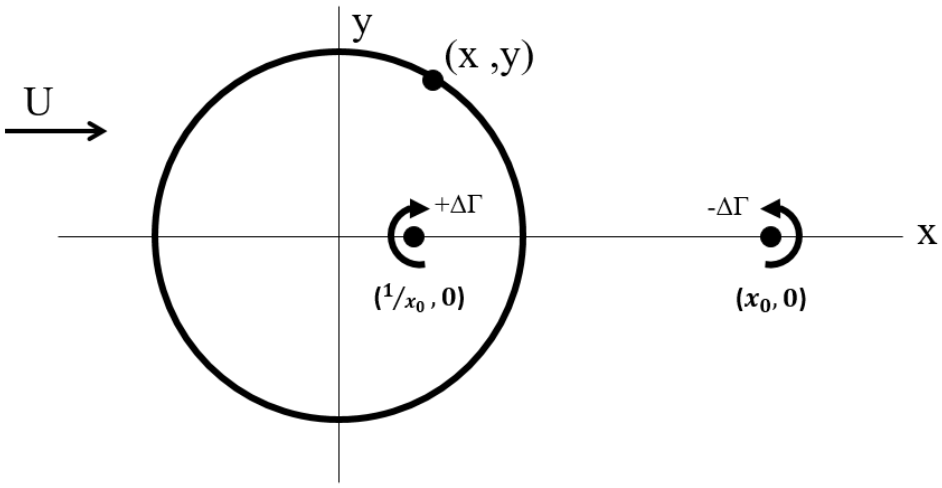

Figure A.1: Conformal representation of the wing profile illustrating vortex placement.

relative to the airfoil at velocity U,

$$\frac{\partial \phi}{\partial t} = \frac{\partial \phi}{\partial x_0} U \tag{A.31}$$

and thus

$$p = -2\rho U(\frac{\partial \phi}{\partial x} + \frac{\partial \phi}{\partial x_0}) \tag{A.32}$$

The partial derivatives can be simplified to

$$\frac{\partial \phi}{\partial x} = \frac{\Gamma}{2\pi} \frac{\sqrt{{x_0}^2 - 1}}{\sqrt{1 - x^2}} \frac{1}{(x_0 - x)} \tag{A.33}$$

$$\frac{\partial \phi}{\partial x_0} = \frac{\Gamma}{2\pi} \frac{\sqrt{1 - x^2}}{\sqrt{{x_0}^2 - 1}} \frac{1}{(x_0 - x)}. \tag{A.34}$$

Integrating Eq. A.32 from hinge location, c, to the trailing edge gives us the force contribution on the *aileron* from each individual vortex pair. This can be extended to the *whole* airfoil by setting $c = -1$. Thus, the circulatory aerodynamic load due to a wake vortex is given by

$$\Delta L = -2\rho U \int_c^1 \left(\frac{\partial \phi}{\partial x} + \frac{\partial \phi}{\partial x_0}\right) \mathrm{d}x$$

$$= -\rho U b \frac{\Gamma}{\pi}\left[\frac{x_0}{\sqrt{{x_0}^2 - 1}}(\cos^{-1} c - \sqrt{1-c^2}) + \sqrt{\frac{x_0+1}{x_0-1}}\sqrt{1-c^2}\right]. \tag{A.35}$$

At this point, vorticity, Γ, is still an unknown spatially-continuous quantity that spans the wake into infinity with the form

$$\Gamma = \gamma(x_0, t)\mathrm{d}x_0 \tag{A.36}$$

To obtain the total lift force on the *aileron* due to the continuous vortex wake, we substitute Eq. A.36 into Eq. A.35 and integrate over the entire wake.

$$L = -\frac{\rho U b}{\pi}\left[(\cos^{-1} c - \sqrt{1-c^2})\int_1^\infty \frac{x_0}{\sqrt{{x_0}^2-1}}\gamma(x_0)\mathrm{d}x_0 + \sqrt{1-c^2}\int_1^\infty \sqrt{\frac{x_0+1}{x_0-1}}\gamma(x_0)\mathrm{d}x_0\right] \tag{A.37}$$

For c = -1 we obtain the expression for lift on the *whole* airfoil.

$$L = -\rho U b \int_1^\infty \frac{x_0}{\sqrt{{x_0}^2-1}}\gamma(x_0)\mathrm{d}x_0 \tag{A.38}$$

Applying the Kutta Condition

Section A.2 covered how to calculate the lift on the airfoil given a continuous vortex wake. Here we discuss how to determine the magnitude of the vortex wake by satisfying the Kutta condition. The Kutta condition states that circulation must be chosen such that the fluid velocity is finite at the sharp (trailing) edge. Since the wing is assumed

to lie entirely along the x-axis, we restrict this requirement to the horizontal velocity (because the vertical component is zero due to the no through flow boundary condition), which takes the form

$$\begin{aligned} \left.\frac{\partial \phi_{total}}{\partial x}\right|_{x=1} &= \text{finite} \\ &= \frac{\partial}{\partial x}(\phi_\Gamma + \phi_\alpha + \phi_{\dot{\alpha}} + \phi_\beta + \phi_{\dot{beta}}) \end{aligned} \tag{A.39}$$

However, evaluating these derivatives at $x = 1$ leads to the denominator becoming zero, as shown using $\frac{\partial \phi_\alpha}{\partial x}$ as a representative example:

$$\frac{\partial \phi_\alpha}{\partial x} = -U\alpha b \frac{x}{1-x^2} \tag{A.40}$$

Since the denominator becomes zero at $x = 1$, the numerator must also become zero at $x = 1$ in order for the horizontal velocity to be finite at the trailing edge. Differentiating according to Eq. A.39 and setting the numerators equal to zero gives an expression relating the wake vorticity to the wing kinematics:

$$\frac{1}{2\pi}\int_1^\infty \frac{\sqrt{x_0+1}}{\sqrt{x_0-1}}\gamma(x_0,t)\mathrm{d}x_0 = U\alpha + b(\frac{1}{2}-a)\dot{\alpha} + \frac{T_{10}}{\pi}U\beta + b\frac{T_{11}}{2\pi}\dot{\beta} = Q, \tag{A.41}$$

where

$$T_{10} = \sqrt{1-c^2} + \cos^{-1} c \tag{A.42}$$

$$T_{11} = \cos^{-1} c\,(1-2c) + \sqrt{1-c^2}\,(2-c) \tag{A.43}$$

Multiplying and dividing Eq. A.38 by the right and left side of Eq. A.41, respectively, gives rise to the expression for circulatory lift in Theodorsen's model [61]:

$$L_C = -2\pi\rho U b Q C \tag{A.44}$$

where C is the Theodorsen function,

$$C = \frac{\int_1^\infty \frac{x_0}{\sqrt{{x_0}^2-1}}\gamma(x_0)\mathrm{d}x_0}{\int_1^\infty \frac{\sqrt{x_0+1}}{\sqrt{x_0-1}}\gamma(x_0,t)\mathrm{d}x_0}. \tag{A.45}$$

Finally, combining the contributions from non-circulatory lift (Eq. A.25) and circulatory lift (Eq. A.44) we now have the full quasi steady Theodorsen model for aerodynamic lift on a wing in arbitrary motion:

$$\begin{aligned} L = &-\rho b^2(U\pi\dot{\alpha} - b\pi a\ddot{\alpha} - UT_4\dot{\beta} - bT_1\ddot{\beta}) \\ &+ 2\pi\rho U b(U\alpha + b(\frac{1}{2} - a)\dot{\alpha} + \frac{T_{10}}{\pi}U\beta + b\frac{T_{11}}{2\pi}\dot{\beta}) \end{aligned} \tag{A.46}$$

Appendix B: Implementation of Unsteady Panel Method

The following is a detailed description of the unsteady panel method implemented in the present study. This discrete vortex panel method provides a numerical solution for the aerodynamic loads on a flat plate undergoing arbitrary motion.

The primary physical boundary condition on the plate is that of no through-flow on the wing surface. To satisfy this condition, the appropriate tangential and normal velocities, u and w, respectively, at each collocation point must be calculated every time step. For any vortex located at point (x_0, z_0), including panel vortices and wake vortices, the induced velocities at any point (x, z) are calculated by

$$\begin{pmatrix} u \\ w \end{pmatrix} = \frac{\Gamma}{2\pi r^2} \begin{pmatrix} 0 & 1 \\ 1 & 0 \end{pmatrix} \begin{pmatrix} x - x_0 \\ z - z_0 \end{pmatrix} \tag{B.1}$$

where

$$r^2 = (x - x_0)^2 + (z - z_0)^2 \tag{B.2}$$

To satisfy the zero normal flow boundary condition on the wing surface, the normal velocity component at each collocation point, which is comprised of an induced velocity

and a freestream velocity, can be expressed as

$$(u, w) \cdot \mathbf{n} + (U(t) + u_w, W(t) + w_w) \cdot \mathbf{n} = 0 \tag{B.3}$$

where the first term is the self-induced velocity from all bound vortices on the wing and the second term is a combination of kinematic velocity due to wing motion $[U(t), W(t)]$ and induced velocity from the wake vortices (u_w, w_w). The time varying shape of the airfoil in the wing-fixed frame is accounted for within the velocities $U(t)$ and $W(t)$. This is critical in capturing added mass forces on time-dependent airfoil geometries. Kinematic velocities are calculated as

$$\begin{pmatrix} U(t) \\ W(t) \end{pmatrix} = \begin{pmatrix} \cos\theta(t) & -\sin\theta(t) \\ \sin\theta(t) & \cos\theta(t) \end{pmatrix} \begin{pmatrix} -\dot{X}_0 \\ -\dot{Z}_0 \end{pmatrix} + \begin{pmatrix} -\dot{\theta}\eta \\ -\dot{\theta}x - \frac{\partial \eta}{\partial t} \end{pmatrix} \tag{B.4}$$

where θ is pitch angle of the entire wing, which for this study is fixed at zero, requiring all geometry deformations to be handled using the $\frac{\partial \eta}{\partial t}$ term.

At the beginning of each time step, the distribution of vorticity along the chord is unknown, but the freestream and wake-induced velocities are known. We must therefore solve for the magnitude of each panel's vortex strength at each time step using a variation of Equation B.3. The self-induced part can be represented by a combination of *influence coefficients*, which represent the velocity components due to a unit strength vortex element. Equation B.3 can be rewritten for collocation point 1 as

$$(a_{11}\Gamma_1 + a_{12}\Gamma_2 + a_{13}\Gamma_3 + ... + a_{1N}\Gamma_N) \cdot \mathbf{n} + (U(t) + u_w, W(t) + w_w) \cdot \mathbf{n} = 0 \qquad \text{(B.5)}$$

where N is the number of panels in the wing element. In order to solve the system of equations for every collocation point on the wing, we can turn Equation B.5 into a matrix equation of the form

$$\begin{pmatrix} a_{11} & a_{12} & ... & a_{1N} & a_{1W} \\ a_{21} & a_{22} & ... & a_{2N} & a_{2W} \\ \vdots & \vdots & \ddots & \vdots & \vdots \\ a_{N1} & a_{N2} & ... & a_{NN} & a_{NW} \\ 1 & 1 & ... & 1 & 1 \end{pmatrix} \begin{pmatrix} \Gamma_1 \\ \Gamma_2 \\ \vdots \\ \Gamma_N \\ \Gamma_W \end{pmatrix} = \begin{pmatrix} RHS_1 \\ RHS_2 \\ \vdots \\ RHS_N \\ \Gamma(t - \Delta t) \end{pmatrix} \qquad \text{(B.6)}$$

where

$$RHS_i = -[U(t) + u_w, W(t) + w_w]_i \cdot \mathbf{n}_i \qquad \text{(B.7)}$$

The last row in Equation B.6 represents Kelvin's circulation theorem:

$$\Gamma(t) - \Gamma(t - \Delta t) + \Gamma_{w_t} = 0 \qquad \text{(B.8)}$$

where Γ_{w_t} is the strength of the newly shed wake vortex at time t. This ensures that the total wake circulation is equal to the instantaneous airfoil circulation. Thus, each new shed wake vortex is equal to the change in airfoil circulation during that time step.

Additionally, since the vortex wake is force-free, each vortex must convect with the local flow velocity. This is handled in a similar manner to calculating induced velocities at panel collocation points. The local velocity at each wake vortex is the resulting induced velocity, $(u, w)_i$, from all other wake and panel vortices in the flow, in addition to the freestream. At each time step, wake vortex points are convected a distance of

$$(\Delta x, \Delta y)_i = (u, w)_i \Delta t. \tag{B.9}$$

Via the unsteady Bernoulli equation (see Katz and Plotkin [86] for details), a chord-wise pressure distribution can be computed as

$$\Delta p_j = \rho(U_\infty \frac{\Gamma_j}{\Delta l_j} + \frac{\partial}{\partial t} \sum_{k=1}^{j} \Gamma_k), \tag{B.10}$$

Notice that the unsteady term in the pressure calculation is simply the time rate of change of the bound circulation on the wing, whereas the first term is essentially the Kutta-Joukowski form of steady circulatory lift.

Finally, total lift is calculated by integrating pressure along the chord:

$$L = \sum_{j=1}^{N} \Delta p_j \Delta l_j \cos \alpha_j, \tag{B.11}$$

where Δl is the panel length and α_j is the incidence angle of the "j"th panel. The current work will present lift in the non-dimensional form of lift coefficient, which is normalized by the freestream dynamic pressure:

$$C_L = \frac{L}{\frac{1}{2}\rho {U_\infty}^2 c} \tag{B.12}$$

To review, the panel method, based on potential flow theory, has several key assumptions built into its derivation: 1) Flow remains attached. 2) Viscous effects are ignored, and thus wake vortices are of constant strength and do not dissipate with time. 3) Wake vortices are generated at the trailing edge only. 4) The Kutta condition at the trailing edge is satisfied. Panel methods remain powerful tools in analyzing flows over an airfoil, despite these simplifying assumptions. A major advantage of the unsteady panel method is its ability to provide information on wake evolution and dynamic effects in a distributed manner. This study aims to provide a deeper understanding of the individual contributions to lift on a wing with a large trailing edge flap, primarily in the domains of circulatory versus non-circulatory forces or steady versus unsteady forces. To ensure that we can accurately capture these forces, a case that should theoretically only produce an added mass force was explored: a single element flat plate at zero degrees incidence harmonically oscillating at a frequency of $f = 2$ Hz with a non-dimensional plunge amplitude of h/c=0.02 and a free stream of U= 0.2 chords/s. The intent here was to apply kinematics that would produce solely an added mass force for which we know the exact theoretical solution. Figure B.1(a) shows excellent agreement between the panel method result and the theoretical calculation based on quasi-steady potential flow theory given by Leishmann [63] as

$$C_L = \frac{\pi \ddot{h}}{2U^2}. \tag{B.13}$$

Since the panel method forces consist of both an unsteady and a steady term, we must be confident that the steady term is accurate as well. Figure B.1(b) shows the panel method result for an impulsively started single-element plate at 7 degrees angle of attack as well as the corresponding Wagner solution. The vortex panel method includes both circulatory and non-circulatory loads, whereas the Wagner function only includes the circulatory loads. An instantaneous change in bound circulation on the airfoil upon startup leads to large non-circulatory loads from the second term in Eq. B.10. Comparing the circulatory loads, however, it is clear that the panel method and Wagner's solution converge to the same value, confirming that the panel method provides accurate results for both non-circulatory (Figure B.1a) and circulatory (Figure B.1b) loads.

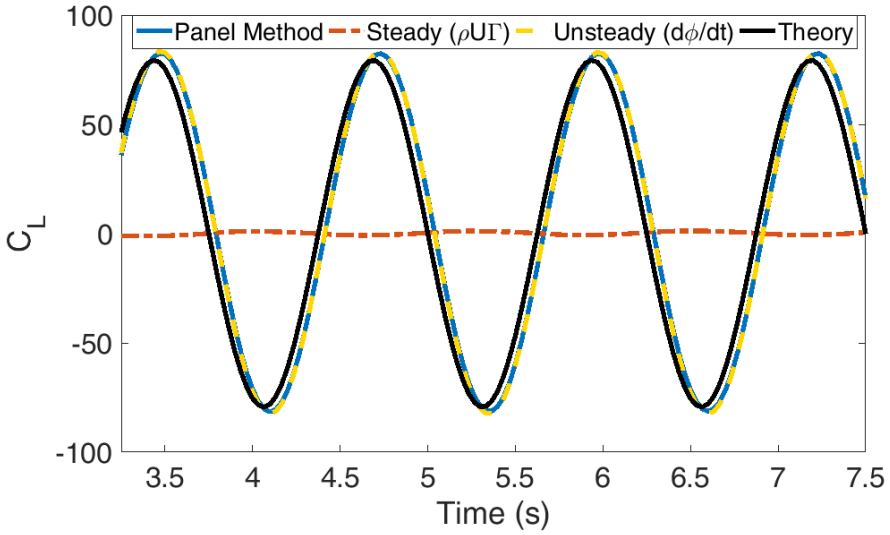

(a) Sinusoidal heaving at $h/c = 0.02$, $f = 2$Hz, $\alpha = 0°$

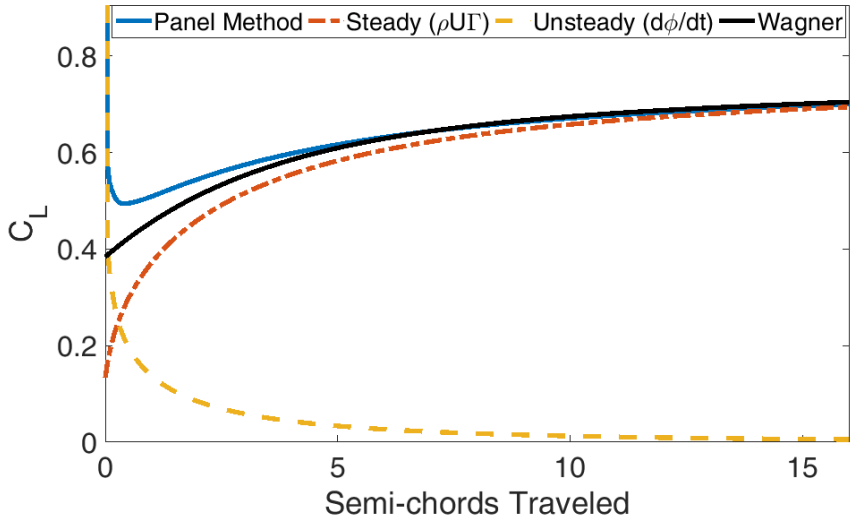

(b) Impulsively started plate at $\alpha = 7°$.

Figure B.1: Panel method result and theoretical prediction for (a) 2 Hz sinusoidal heaving motion at $\alpha = 0°$ and (b) an impulsively started flat plate at $\alpha = 7°$

Bibliography

[1] Pournazeri, S., Segre, P. S., Princevac, M., and Altshuler, D. L., "Hummingbirds Generate Bilateral Vortex Loops During Hovering: Evidence from Flow Visualization," *Experiments in Fluids*, Vol. 54, No. 1, Dec. 2012, pp. 1439.

[2] Fuchiwaki, M., Kuroki, T., Tanaka, K., and Tababa, T., "Dynamic Behavior of the Vortex Ring Formed on a Butterfly Wing," *Experiments in Fluids*, Vol. 54, No. 1, Jan. 2013, pp. 1450.

[3] Abdulrahim, M., Garcia, H., and Lind, R., "Flight characteristics of shaping the membrane wing of a micro air vehicle," *Journal of Aircraft*, Vol. 42, No. 1, 2005, pp. 131–137.

[4] Gerdes, J., Holness, A., Perez-Rosado, A., Roberts, L., Greisinger, A., Barnett, E., Kempny, J., Lingam, D., Yeh, C.-H., Bruck, H. A., et al., "Robo Raven: a flapping-wing air vehicle with highly compliant and independently controlled wings," *Soft Robotics*, Vol. 1, No. 4, 2014, pp. 275–288.

[5] Shyy, W., Berg, M., and Ljungqvist, D., "Flapping and flexible wings for biological and micro air vehicles," *Progress in Aerospace Sciences*, Vol. 35, No. 5, 1999, pp. 455–505.

[6] Doman, D., Oppenheimer, M., Bolender, M., and Sigthorsson, D., "Altitude Control of a Single Degree of Freedom Flapping Wing Micro Air Vehicle," *AIAA Paper 2009-6159*, 2009.

[7] Costes, M., Gravelle, A., Philippe, J., Vogel, S., and Triebstein, H., "Investigation of unsteady subsonic spoiler and flap aerodynamics," *Journal of Aircraft*, Vol. 24, No. 9, 1987, pp. 629–637.

[8] Garmann, D. J., Visbal, M. R., and Orkwis, P. D., "Three-dimensional flow structure and aerodynamic loading on a revolving wing," *Physics of Fluids*, Vol. 25, No. 3, 2013, pp. 034101.

[9] Garmann, D. J. and Visbal, M. R., "Numerical investigation of transitional flow over a rapidly pitching plate," *Physics of Fluids*, Vol. 23, No. 9, 2011, pp. 094106.

[10] Visbal, M. R., "High-fidelity simulation of transitional flows past a plunging airfoil," *AIAA journal*, Vol. 47, No. 11, 2009, pp. 2685.

[11] Wang, C. and Eldredge, J., "Low-order Phenomenological Modeling of Leading-Edge Vortex Formation," *Theoretical Computational Fluid Dynamics*, Aug. 2012.

[12] Xia, X. and Mohseni, K., "Lift evaluation of a two-dimensional pitching flat plate," *Physics of Fluids*, Vol. 25, No. 9, 2013, pp. 1–26.

[13] Wagner, H., "Uber die Enstehung des dynamischen Auftreibes von Tragflugeln," *A. angew. Math.*, 1925, pp. 17–35.

[14] Theodorsen, T. and Garrick, I., "Mechanism of flutter a theoretical and experimental investigation of the flutter problem," Tech. rep., NATIONAL AERONAUTICS AND SPACE ADMINISTRATION WASHINGTON DC, 1940.

[15] Ol, M., Bernal, L., Kang, C.-K., and Shyy, W., "Shallow and deep dynamic stall for flapping low Reynolds number airfoils," *Experiments in Fluids*, Vol. 46, No. 5, 2009, pp. 883–901.

[16] Anderson Jr, J. D., *A history of aerodynamics: and its impact on flying machines*, Vol. 8, Cambridge University Press, 1999.

[17] Cai, G., Dias, J., and Seneviratne, L., "A survey of small-scale unmanned aerial vehicles: Recent advances and future development trends," *Unmanned Systems*, Vol. 2, No. 02, 2014, pp. 175–199.

[18] Shyy, W., Aono, H., Kang, C.-k., and Liu, H., *An introduction to flapping wing aerodynamics*, Vol. 37, Cambridge University Press, 2013.

[19] Ellington, C. P., "The Aerodynamics of Hovering Insect Flight II. Morphological Parameters," *Philosophical Transactions of the Royal Society of London. Series B, Biological Sciences*, Vol. 305, No. 1122, 1984, pp. 17–40.

[20] Lehmann, F.-O., "When Wings Touch Wakes: Understanding Locomotor Force Control by Wake Wing Interference in Insect Wings," *Journal of Experimental Biology*, Vol. 211, No. 2, 2008, pp. 224–233.

[21] Lentink, D. and Dickinson, M. H., "Biofluiddynamic Scaling of Flapping, Spinning and Translating Fins and Wings." *The Journal of Experimental Biology*, Vol. 212, August 2009, pp. 2691–2704.

[22] Granlund, K. O., Ol, M. V., and Bernal, L. P., "Unsteady pitching flat plates," *J. Fluid Mech.*, Vol. 733, Oct 2013, pp. R51 – R513.

[23] Rival, D., Prangemeier, T., and Tropea, C., "The influence of airfoil kinematics on the formation of leading-edge vortices in bio-inspired flight," *Experiments in Fluids*, Vol. 46, No. 5, Nov. 2008, pp. 823–833.

[24] Kriegseis, J., Kinzel, M., and Rival, D., "A Langrangian Perspective on Vortex Formation for Unsteady Flat Plates," *AIAA 2013-0837*, 2013.

[25] Kriegseis, J. and Rival, D. E., "Vortex force decomposition in the tip region of impulsively-started flat plates," *Journal of Fluid Mechanics*, Vol. 756, 2014, pp. 758–770.

[26] Ansari, S., Żbikowski, R., and Knowles, K., "Aerodynamic modelling of insect-like flapping flight for micro air vehicles," *Progress in Aerospace Sciences*, Vol. 42, No. 2, 2006, pp. 129–172.

[27] Tennekes, H. and Lumley, J. L., *A first course in turbulence*, MIT press, 1972.

[28] Ames, A., Wong, O., and Komerath, N., *Fixed and Flapping Wing Aerodynamics for Micro Air Vehicle Applications*, Vol. 195 of *Progress in Astronautics and Aeronautics*, chap. 15, On the, American Institute of Aeronautics and Astronautics, 1801 Alexander Bell Drive, Reston, Virginia, 2001, pp. 287–306.

[29] Ramesh, K., Gopalarathnam, A., Edwards, J. R., Ol, M. V., and Granlund, K., "An unsteady airfoil theory applied to pitching motions validated against experiment and computation," *Theoretical and Computational Fluid Dynamics*, Vol. 27, No. 6, Jan. 2013, pp. 843–864.

[30] Ellington, C. P., Van Den Berg, C., Willmott, A. P., and Thomas, A. L., "Leading-edge vortices in insect flight," *Nature*, Vol. 384, No. 6610, 1996, pp. 626–630.

[31] Panah, A. E., Akkala, J. M., and Buchholz, J. H., "Vorticity transport and the leading-edge vortex of a plunging airfoil," *Experiments in Fluids*, Vol. 56, No. 8, 2015, pp. 160.

[32] Mueller, T. J., *Fixed and flapping wing aerodynamics for micro air vehicle applications*, Vol. 195, AIAA, 2001.

[33] Withers, P. C., "An aerodynamic analysis of bird wings as fixed aerofoils," *Journal of Experimental Biology*, Vol. 90, No. 1, 1981, pp. 143–162.

[34] Fry, S. N., Sayaman, R., and Dickinson, M. H., "The aerodynamics of free-flight maneuvrers in Drosophila," *Science*, Vol. 300, 2003, pp. 495–498.

[35] Altshuler, D. L., Quicazán-Rubio, E. M., Segre, P. S., and Middleton, K. M., "Wingbeat kinematics and motor control of yaw turns in Anna's hummingbirds (Calypte anna)," *Journal of experimental biology*, Vol. 215, No. 23, 2012, pp. 4070–4084.

[36] Dickinson, M. H. and Gotz, K. G., "Unsteady aerodynamic performance of model wings at low Reynolds numbers," *Journal of Experimental Biology*, Vol. 174, No. 1, 1993, pp. 45–64.

[37] Weis-Fogh, T., "Quick Estimates of Flight Fitness in Hovering Animals, Including Novel Mechanisms for Lift Production," *J Exp Biol*, Vol. 59, No. 1, 1973, pp. 169–230.

[38] Stevens, P. and Babinsky, H., "Experiments to investigate lift production mechanisms on pitching flat plates," *Experiments in Fluids*, Vol. 58, No. 1, 2017, pp. 7.

[39] Panah, A. E., Akkala, J. M., and Buchholz, J. H., "Vorticity transport and the leading-edge vortex of a plunging airfoil," *Experiments in Fluids*, Vol. 56, No. 8, 2015, pp. 160.

[40] Pitt Ford, C. W., *Unsteady aerodynamic forces on accelerating wings at low reynolds numbers*, Ph.D. thesis, University of Cambridge, 2013.

[41] Granlund, K. O., Ol, M. V., and Bernal, L. P., "Unsteady pitching flat plates," *J. Fluid Mech.*, Vol. 733, Oct 2013.

[42] Colonius, T. and Williams, D. R., "Control of vortex shedding on two-and three-dimensional aerofoils," *Philosophical Transactions of the Royal Society of London A: Mathematical, Physical and Engineering Sciences*, Vol. 369, No. 1940, 2011, pp. 1525–1539.

[43] Hernandez, G., Wood, R. M., and Covell, P. F., "Effect of leading-and trailing-edge flaps on clipped delta wings with and without wing camber at supersonic speeds," *NASA Technical Memorandum 4*, Vol. 4542, 1994.

[44] Karpel, M., "Design for active flutter suppression and gust alleviation using state-space aeroelastic modeling," *Journal of Aircraft*, Vol. 19, No. 3, 1982.

[45] Frederick, M., Kerrigan, E. C., and Graham, J. M. R., "Gust alleviation using rapidly deployed trailing-edge flaps," *Journal of Wind Engineering and Industrial Aerodynamics*, Vol. 98, 2010.

[46] Rennie, R. M. and J., J. E., " Experimental Measurements of Dynamic Control Surface Effectiveness ," *Journal of Aircraft*, Vol. 33, No. 5, 1996.

[47] Straub, F. K., Ngo, H. T., Anand, V. A., and Domzalski, D. B., " Development of a piezoelectric actuator for trailing edge flap control of full scale rotor blades ," *Smart Materials and Structures*, Vol. 10, 2001.

[48] Koratkar, N. and Chopra, I., " Analysis and Testing of Mach-Scaled Rotor with Trailing-Edge Flaps ," *AIAA Journal*, Vol. 38, No. 7, 2000.

[49] Sanders, B., Eastep, F. E., and Forster, E., "Aerodynamic and Aeroelastic Characteristics of Wings with Conformal Control Surfaces for Morphing Aircraft," *Journal of Aircraft*, Vol. 40, No. 1, 2003.

[50] Xu, M., Wei, M., Li, C., and Dong, H., " Adjoint-based optimization of flapping plates hinged with a trailing-edge flap ," *Theoretical and Applied Mechanics Letters*, Vol. 5, 2015.

[51] Li, C., Dong, H., and Geng, L., " Effects of aerodynamic trailing-edge flap on the aerodynamic performance and flow structures in hovering flight ," *Journal of Fluids and Structures*, Vol. 58, 2015.

[52] Sterenborg, J., Lindeboom, R., Ferreira, C. S., van Zuijlen, A., and Bijl, H., "Assessment of PIV-based unsteady load determination of an airfoil with actuated flap," *Journal of Fluids and Structures*, Vol. 45, 2014, pp. 79–95.

[53] Noca, F., Shiels, D., and Jeon, D., "A comparison of methods for evaluating time-dependent fluid dynamic forces on bodies, using only velocity fields and their derivatives," *Journal of Fluids and Structures*, Vol. 13, No. 5, 1999, pp. 551–578.

[54] Lamb, H., *Hydrodynamics*, Cambridge University Press, 6th ed., 1932.

[55] Lee, T. and Su, Y. Y., " Unsteady Airfoil with a Harmonically Deflected Trailing-Edge Flap ," *Journal of Fluids and Structures*, Vol. 27, No. 8, 2011.

[56] Garmann, D. and Visbal, M., "Numerical investigation of transitional flow over a rapidly pitching plate," *Physics of Fluids*, Vol. 23, No. 9, 2011.

[57] Eldredge, J. D. and Chong, K., "Fluid transport and coherent structures of translating and flapping wings," *Chaos*, Vol. 20, No. 1, 2010.

[58] Ansari, S. a., bikowski, R., and Knowles, K., "Non-linear unsteady aerodynamic model for insect-like flapping wings in the hover. Part 1: methodology and analysis," *Proceedings of the Institution of Mechanical Engineers, Part G: Journal of Aerospace Engineering*, Vol. 220, No. 2, April 2006, pp. 61–83.

[59] Ansari, S. a., bikowski, R., and Knowles, K., "Non-linear unsteady aerodynamic model for insect-like flapping wings in the hover. Part 2: implementation and validation," *Proceedings of the Institution of Mechanical Engineers, Part G: Journal of Aerospace Engineering*, Vol. 220, No. 3, Jan. 2006, pp. 169–186.

[60] Taha, H. E., Hajj, M. R., and Nayfeh, A. H., "Flight dynamics and control of flapping-wing MAVs: a review," *Nonlinear Dynamics*, Vol. 70, No. 2, 2012, pp. 907–939.

[61] Theodorsen, T., "General theory of aerodynamic instability and the mechanism of flutter," *NACA R-496*, 1935.

[62] Bisplinghoff, R. L., Ashley, H., and Halfman, R. L., *Aeroelasticity*, Dover, 1996.

[63] Leishman, J. G., *Principles of Helicopter Aerodynamics*, Cambridge University Press, 2nd ed., 2006.

[64] Ramesh, K. K., Gopalarathnam, A., Edwards, J., Ol, M. V., and Granlund, K., "An Unsteady Airfoil Theory Applied to Pitching Motions Validated against Experiment and Computation," *Theoretical Computational Fluid Dynamics*, Vol. 1, 2013.

[65] McGowan, G. Z., Granlund, K., Ol, M. V., Gopalarathnam, A., and Edwards, J., "Investigations of Lift-Based Pitch-Plunge Equivalence for Airfoils at Low Reynolds Numbers," *AIAA Journal*, Vol. 49, No. 7, 2011, pp. 1511–1524.

[66] Garrick, I. E., "On some reciprocal relations in the theory of nonstationary flows," *NACA Report*, , No. 629, 1938.

[67] Granlund, K., Monnier, B., Ol, M., and Williams, D., "Airfoil longitudinal gust response in separated vs. attached flows," *Physics of Fluids*, Vol. 26, No. 2, Feb. 2014, pp. 027103.

[68] Pitt Ford, C. W. and Babinsky, H., "Lift and the leading-edge vortex," *J. Fluid Mech.*, Vol. 720, Apr 2013, pp. 280–313.

[69] Brennen, C., "A Review of Added Mass and Fluid Inertial Forces," Tech. Rep. CR 82.010, Naval Civil Engineering Laboratory, Port Hueneme, CA 93043, Jan. 1982.

[70] Ol, M. V., "Vortical structures in high frequency pitch and plunge at low Reynolds number," *37th AIAA Fluid Dynamics Conference and Exhibit*, 2007.

[71] Manar, F. and Jones, A. R., "Transient Response of a Single Degree-of-Freedom Wing at High Angle-of-Attack," *AIAA Journal*, 2017.

[72] Medina, A., Ol, M. V., Mancini, P., and Jones, A., "Revisiting Conventional Flaps at High Deflection Rate," *AIAA Journal*, 2017.

[73] Eldredge, J. D., Wang, C., and Ol, M., "A computational study of a canonical pitch-up, pitch-down wing maneuver," *AIAA*, No. AIAA-2009-3687 in 39th AIAA Fluid Dynamics Conference, San Antonio, TX, June 2009.

[74] Wickenheiser, A. M. and Garcia, E., "Optimization of perching maneuvers through vehicle morphing," *Journal of Guidance Control and Dynamics*, Vol. 31, No. 4, 2008, pp. 815–823.

[75] Carruthers, A. C., G.K., T., Walker, S. M., and Thomas, A. L. R., "Use and Function of a Leading Edge Flap on the Wings of Eagles," *AIAA Paper 2007-0043*, 2007.

[76] Ansari, S., Żbikowski, R., and Knowles, K., "Aerodynamic modelling of insect-like flapping flight for micro air vehicles," *Progress in Aerospace Sciences*, Vol. 42, No. 2, 2006, pp. 129–172.

[77] Reich, G. W., Eastep, F. E., Altman, A., and Albertani, R., "Transient Poststall Aerodynamic Modeling for Extreme Maneuvers in Micro Air Vehicles," *Journal of Aircraft*, Vol. 48, No. 2, March 2011, pp. 403–411.

[78] von Karman, T. and Sears, W. R., "Airfoil Theory for Non-Uniform Motion," *Journal of the Aeronautical Sciences*, Vol. 5, No. 10, Aug. 1938, pp. 379–390.

[79] Ringuette, M., Milano, M., and Gharib, M., "Role of the tip vortex in the force generation of low-aspect-ratio normal flat plates," *Journal of Fluid Mechanics*, Vol. 581, 2007, pp. 453–468.

[80] Manar, F., Mancini, P., Mayo, D., and Jones, A. R., "Comparison of rotating and translating wings: force production and vortex characteristics," *AIAA Journal*, Vol. 54, No. 2, 2015, pp. 519–530.

[81] Mancini, P., Manar, F., Granlund, K., Ol, M. V., and Jones, A. R., "Unsteady aerodynamic characteristics of a translating rigid wing at low Reynolds number," *Physics of Fluids*, Vol. 27, No. 12, 2015, pp. 123102.

[82] Graftieaux, L., Michard, M., and Grosjean, N., "Combining PIV, POD and vortex identification algorithms for the study of unsteady turbulent swirling flows," *Meas. Sci. Technol.*, Vol. 12, 2001, pp. 1422–1429.

[83] Baik, Y. S., Bernal, L. P., Granlund, K., and Ol, M. V., "Unsteady Force Generation and Vortex Dynamics of Pitching and Plunging Airfoils," *Journal of Fluid Mechanics*, Vol. 709, 2012, pp. 37–68.

[84] Maskew, B., "Prediction of subsonic aerodynamic characteristics: a case for low-order panel methods," *Journal of Aircraft*, Vol. 19, No. 2, 1982, pp. 157–163.

[85] Smith, M., Wilkin, P., and Williams, M., "The advantages of an unsteady panel method in modelling the aerodynamic forces on rigid flapping wings," *Journal of Experimental Biology*, Vol. 199, No. 5, 1996, pp. 1073–1083.

[86] Katz, J. and Plotkin, A., *Low Speed Aerodynamics*, Cambridge University Press, 2001.

[87] Jones, R. T., "The Unsteady Lift of a Wing of Finite Aspect Ratio," Tech. Rep. 681, NACA, 1940.

[88] Beckwith, R. and Babinsky, H., "Impulsively Started Flat Plate Wing," *47th AIAA Aerospace Sciences Meeting including The New Horizons Forum and Aerospace Exposition*, Jan. 2009, pp. 1–13.

[89] Lind, A. H. and Jones, A. R., "Unsteady aerodynamics of reverse flow dynamic stall on an oscillating blade section," *Physics of Fluids*, Vol. 28, No. 7, 2016, pp. 077102.

[90] Ellington, C. P., "The novel aerodynamics of insect flight: applications to micro-air vehicles." *The Journal of experimental biology*, Vol. 202, No. Pt 23, Dec. 1999, pp. 3439–48.

[91] Tucker, V. A., "Gliding birds: reduction of induced drag by wing tip slots between the primary feathers," *Journal of Experimental Biology*, Vol. 180, No. 1, 1993, pp. 285–310.

[92] Wang, S., He, G., and Zhang, X., "Lift enhancement on spanwise oscillating flat-plates in low-Reynolds-number flows," *Physics of Fluids*, Vol. 27, No. 6, 2015, pp. 061901.

[93] Bousman, W. G., "Airfoil Dynamic Stall and Rotorcraft Maneuverability," Tech. rep., Army/NASA Rotorcraft Division, 2000.

[94] Yu, H.-T., Bernal, L. P., and Ol, M. V., "Effects of Planform Geometry and Pivot Axis Location on the Aerodynamics of Pitching Low Aspect Ratio Wings," *43rd Fluid Dynamics Conference*, American Institute of Aeronautics and Astronautics, Jun 2013.

[95] Herbst, W. B., "Supermaneuverability," Tech. rep., MESSERSCHMITT-BOELKOW-BLOHM GMBH MUNICH (GERMANY FR), 1984.

[96] Lang, J. D. and Francis, M. S., "Unsteady aerodynamics and dynamic aircraft maneuverability," Tech. rep., AIR FORCE AVIONICS LAB WRIGHT-PATTERSON AFB OH, 1985.

[97] Weis-Fogh, T., "Energetics of hovering flight in hummingbirds and in Drosophila," *Journal of Experimental Biology*, Vol. 56, No. 1, 1972, pp. 79–104.

[98] Tang, J., Viieru, D., and Shyy, W., "Effects of Reynolds number and flapping kinematics on hovering aerodynamics," *AIAA Journal*, Vol. 46, No. 4, April 2008.

[99] Rennie, R. and Jumper, E., "Experimental measurements of dynamic control surface effectiveness," *Journal of Aircraft*, Vol. 33, No. 5, 1996, pp. 880–887.

[100] Rennie, R. and Jumper, E. J., "A Case for Pseudo-Steady Aerodynamic Behavior at High Motion Rates," *AIAA paper*, 1997, pp. 97–0617.

[101] Rennie, R. and Jumper, E., "Gust alleviation using trailing-edge flaps," *37th Aerospace Sciences Meeting and Exhibit*, 1999, p. 649.

[102] Phillips, E. and Wygnanski, I., "Use of sweeping jets during transient deployment of a control surface," *AIAA journal*, 2013.

[103] Woo, G. and Glezer, A., "Transitory control of dynamic stall on a pitching airfoil," *Active Flow Control II*, 2010, pp. 3–18.

[104] Anderson Jr, J. D., *Fundamentals of aerodynamics*, Tata McGraw-Hill Education, 2010.

[105] Mathew, S. and Philip, G. S., *Advances in wind energy and conversion technology*, Vol. 20, Springer, 2011.